EVALUATION OF SAND TREATED WITH COLLOIDAL SILICA GEL

A Dissertation
Presented to
The Academic Faculty

by

Laura Marie Spencer

In Partial Fulfillment
of the Requirements for the Degree
Doctor of Philosophy in the
School of Civil and Environmental Engineering

Georgia Institute of Technology
December 2010

EVALUATION OF SAND TREATED WITH COLLOIDAL SILICA GEL

Approved by:

Dr. Glenn J. Rix, Advisor
School of Civil and Environmental Engineering
Georgia Institute of Technology

Dr. Jianmin Qu
Department of Mechanical Engineering
Georgia Institute of Technology

Dr. Susan E. Burns
School of Civil and Environmental Engineering
Georgia Institute of Technology

Dr. J. Carlos Santamarina
School of Civil and Environmental Engineering
Georgia Institute of Technology

Dr. Dominic Assimaki
School of Civil and Environmental Engineering
Georgia Institute of Technology

Date Approved: August 26, 2010

For Coleman, the light of my life and Todd, the man who I am blessed to share my life with. Also for my parents, who have provided countless support and unconditional love.

ACKNOWLEDGEMENTS

This material is based on work supported by the National Science Foundation under Grant Nos. CMS-0530478 and CMS-0402490. Any opinions, findings, and conclusions or recommendations expressed in this material are those of the authors and do not necessarily reflect the views of the National Science Foundation.

I would like to thank my advisor, Dr. Glenn J. Rix, for providing me with the opportunity to see and experience the world in a way few others are given. My experiences abroad have made me a better, more informed engineer and I thank you for providing me that chance. I would also like to thank the members of my committee, Dr. Susan Burns, Dr. Carlos Santamarina, Dr. Dominic Assimaki and Dr. Jianmin Qu. On a personal level, I would like to thank Dr. Haiying Huang for her support and advice over the last two years. I would also like to thank Carol Maddox for her help over the past few years.

I would like to thank my fellow geotechnical graduate students over the past few years that have provided me with endless hours of discussions, both personal and engineering related. It was a pleasure to have had such a wonderful group to work with, Veronica Rebata-Landa, Catherine McGillivray, Andrew Fuggle, Joan Larranhondo, Nortey Yeboah, Douglas Cortes, Nico Espinoza, Gence, Bate, Varun and HoSung Shin. I am indebted to Alec McGillivray for his enormous amount of support in technical, mechanical and experimental matters. My air pluviator would still be non-functional if it were not for you. A very gracious thanks to HoSung Shin, who helped with the bender element testing. A special acknowledgement to my friends Lindsay and Derek Burden, and Robert Hurt, without whom I would not have enjoyed Georgia Tech quite as much. And a special thank you to Jen Yeboah, Lindsay Burden and most importantly, my mom, for watching Cole before the defense.

A special thank you to Lindsay for being the most amazing friend, for doing all that you do and for always being there for me. My family will miss yours dearly. I would also like to thank my friends from the Green-Blue soccer team for being the best teammates and supporters anyone could ask for. Thank you for being a sounding board, a shoulder to lean on, an outlet of frustration and the best drinking buddies a girl could ever want. You have made my time in Atlanta exciting and memorable and I thank you from the bottom of my heart for all you have done for me.

I would like to thank my parents for their unconditional love and support over the last 29 years. Especially in the first "last push", without you, there would have been no original thesis. And mostly, I would like to thank my husband Todd, for inspiring me to get my doctorate in the first place. I can say with honesty that without the encouragement you provided daily, this thesis would never have been completed. Our life at Georgia Tech has been amazing and I thank you for all you do to challenge me, inspire me, tease me and love me. And finally, I would like to thank Coleman for being the little man that smiles at me at the end of the day.

TABLE OF CONTENTS

LIST OF TABLES

LIST OF FIGURES

SUMMARY

Liquefiable soils are common at ports due to the use of hydraulic fills for construction of waterfront facilities. Liquefaction-induced ground failure can result in permanent ground deformations that can cause loss of foundation support and structural damage. This can lead to substantial repair and/or replacement costs and business interruption losses that can have an adverse effect on the port and the surrounding community. Although numerous soil improvement methods exist for remediating a liquefaction-prone site, many of these methods are poorly suited for developed sites because they could damage existing infrastructure and disrupt port operations. An alternative is to use a passive remediation technique. Treating liquefiable soils with colloidal silica gel via permeation grouting has been shown to resist cyclic deformations and is a candidate to be used as a soil stabilizer in passive mitigation.

The small-strain dynamic properties are essential to determine the response to seismic loading. The small-to-intermediate strain shear modulus and damping ratio of loose sand treated with colloidal silica gel was investigated and the influence of colloidal silica concentration was determined. The effect of introducing colloidal silica gel into the pore space in the initial phase of treatment results in a 10% to 12% increase in the small-strain shear modulus, depending on colloidal silica concentration. The modulus reduction curve indicates that treatment does not affect the linear threshold shear strain, however the treated samples reduce at a greater rate than the untreated samples in the intermediate-strain range above 0.01% cyclic shear strain. It was observed that the treated sand has slightly higher damping ratio in the small-strain range; however, at cyclic shear strains around 0.003% the trend reverses and the untreated sand begins to have higher damping ratio.

Due to the nature of the colloidal silica gelation process, chemical bonds continue to form with time, thus the effect of aging on the dynamic properties is important. A parametric study was performed to investigate the influence of gel time on the increase in small-strain shear modulus. The effect of aging increases the small-strain shear modulus after gelling by 200 to 300% for the 40-minute-gel time samples with a distance from gelation (time after gelation normalized by gel time) of 1000 to 2000; 700% for the 2-hour-gel time sample with a distance from gelation of 1000; and 200 to 400% for the 20-hour-gel time samples with a distance from gelation of 40 to 100.

The treatment of all potentially liquefiable soil at port facilities with colloidal silica would be cost prohibitive. Identifying treatment zones that would reduce the lateral pressure and resulting pile bending moments and displacements caused by liquefaction-induced lateral spreading to prevent foundation damage is an economic alternative. Colloidal silica gel treatment zones of varying size and location were evaluated by subjecting a 3-by-3 pile group in gently sloping liquefiable ground to 1-g shaking table tests. The results are compared to an untreated sample. The use of a colloidal silica treatment zone upslope of the pile group results in reduced maximum bending moments and pile displacements in the downslope row of piles when compared to an untreated sample; the presence of the treatment zone had minimal effect on the other rows of piles within the group.

1. INTRODUCTION

1.1. Motivation

Liquefaction-induced ground failure can cause large deformations and settlements, resulting in structural damage, floating of buried structures and loss of foundation support. Certain soils are more susceptible to liquefaction, such as loose sand deposits, hydraulic fills, and mine tailings. Lateral spreading is the lateral displacement of large, surficial soil blocks as a result of liquefaction in a subsurface layer. Gently sloping waterfront areas are most susceptible to lateral spreading (Gallagher et al. 2006). Liquefaction and lateral spreading caused billions of dollars of damage to port facilities during the 1995 Kobe earthquake (Gallagher et al. 2002; Hamada et al. 1996).

The liquefaction susceptibility of loose fills and liquefaction-related ground deformations may be reduced by a variety of soil improvement methods. Generally, these soil improvement methods rely on one or more of the following mechanisms to mitigate liquefaction hazards: densification of loose soils, rapid dissipation of excess pore pressures via drainage so that the excess pore pressure ratio ($\Delta u/\sigma'_v$) remains below about 0.6, stiffening of the soil mass to limit the development of strains and thus excess pore pressures within the soil mass, and reinforcement of the soil mass via stiff inclusions that limit ground deformations even if liquefaction occurs.

At ports, traditional soil improvement methods can be used to treat soils in the backland, but these methods are difficult, impractical, and expensive to treat soils beneath existing wharf structures due to lack of access or sufficient clearance. In addition, traditional soil improvement methods are often poorly suited for developed sites such as port facilities because of adverse effects on adjacent structures due to vibration, densification, or increased lateral stresses as well as the disruption of ongoing port operations during construction.

Passive soil improvement methods are an attractive alternative for situations requiring minimal disruption. Passive site stabilization involves slow injection of stabilizing materials at the up-gradient edge of a site and delivery of the stabilizer to the target location using natural or augmented groundwater flow. Prior studies of candidate stabilizing materials (Gallagher and Mitchell 2002; Gallagher et al. 2006; Persoff et al. 1999) have identified colloidal silica as an ideal, environmentally benign grouting material with low initial viscosity, controllable gel times, and good long-term mechanical stability. Colloidal silica gelation is induced by adjusting the pH and ionic strength of the suspension. Upon delivery to the target location, the stabilizer starts to gel or set rapidly at a predetermined time to stabilize the soil mass.

Previous work on the applicability of colloidal silica gel as a passive liquefaction mitigation method has focused on the ability of the gel to resist deformations. However, little research has been conducted on the shear modulus and material damping ratio of sand treated with colloidal silica gel in the small and intermediate strain range. To accurately characterize the response of the sand and gel mixtures to seismic loading, these dynamic properties of the mixture are essential. In addition, previous work has shown an increase in the small-strain shear modulus of colloidal silica gel over time and therefore the effect of aging on the small-strain shear modulus of treated sand should be investigated to identify the magnitude of this change with time. A large change in the small-strain dynamic properties with time can affect the site-response analysis and should be taken into account.

Ideally, passive mitigation with colloidal silica grout would treat all of the liquefiable soils at a site. However, the treatment of the entire backland area at a port would likely be cost prohibitive and therefore partial treatment of a zone adjacent to the wharf is suggested as an economic alternative. The goal of partial treatment is to reduce the damage to piles caused by liquefaction-induced lateral spreading. It is necessary to evaluate whether partial treatment can still be effective in reducing the lateral forces and

bending moments experienced by the pile group, such that liquefaction-induced damage is minimized.

1.2. Overview of thesis

Chapter 2 presents a brief review of factors that affect the dynamic properties of soils. Liquefaction-mitigation methods are addressed with a focus on treatment of sand with colloidal silica gel. A background of colloidal silica gel properties is presented and the experimental research on sand treated with colloidal silica gel is reviewed.

Chapter 3 describes the resonant column testing performed to identify the small-to-intermediate strain range dynamic properties of loose sand treated with colloidal silica gel immediately following permeation and gelation. Varying weight percent colloidal silica concentrations are investigated to determine the effect of colloidal silica concentration on the shear modulus and damping ratio. The treated samples are compared to the dynamic properties of untreated sand.

Chapter 4 evaluates the effect of aging on the small-strain shear modulus by means of resonant column and bender element testing. The influence of gel time on the rate of shear modulus increase is investigated. Two alternative models are considered that allow one to estimate the shear modulus of the sand-gel mixture based on the properties of the individual components.

Chapter 5 presents the findings of shaking table tests performed on a 3-by-3 pile group in loose, saturated sand to evaluate the efficacy of a partial treatment of the sands with colloidal silica gel to reduce the bending moments and lateral forces on the pile group. Varying dimensions of the treatment zone and distances upslope of the pile group are investigated and the results are compared to a test with untreated sand sand subjected to the same input accelerations.

Chapter 6 presents the conclusions arising from the research and provides recommendations for future work.

2. LITERATURE REVIEW OF COLLOIDAL SILICA GEL

2.1. Introduction

The small-strain shear modulus and damping ratio of soils are essential to characterize the behavior of soils for both static and dynamic loading conditions. Of particular interest is the response of loose, saturated sands subjected to dynamic loads and the treatment of these loose sands to mitigate their liquefaction susceptibility. Typical soil improvement methods to mitigate liquefaction damage are not suitable for developed sites and a passive means of mitigation must be employed, as described in Chapter 1. The use of colloidal silica gel, which has been identified as a potential stabilizing material (Gallagher 2000), has resisted deformations due to dynamic loading. However, the small-strain dynamic properties are necessary to characterize the response of sand treated with colloidal silica gel to dynamic loading conditions.

2.2. Factors Affecting the Dynamic Properties of Soil

Several factors affect the dynamic properties of soil. Hardin and Black (1968) performed parametric studies on intact and reconstituted soils and concluded that the shear modulus, G, is a functional relationship that can be written as:

$$G = f\left(\sigma_0', e, H, S, \tau_0, C, A_p, f, T, O, K\right) \qquad 2.1$$

where:

σ_0' = isotropic component of ambient effective stress

e = void ratio

H = ambient stress history

S = degree of saturation

τ_o = deviatoric component of ambient stress

C = is the grain characteristics (grain shape, grain size, gradation)

A = strain amplitude

f = frequency of vibration

T = secondary effects that are a function of time

O = soil structure

K = temperature

Hardin and Drnevich (1972) evaluated the importance of these factors on the shear modulus and damping ratio. The results grouped the parameters into three categories: very important, less important and relatively unimportant. They concluded that the very important factors are the strain amplitude, effective mean principle stress, void ratio, number of cycles of loading, and degree of saturation. Dobry and Vucetic (1987) studied the effect of several factors on the small-strain shear modulus, G_{max}, the normalized shear modulus, G/G_{max}, and material damping ration, D, of cohesive soils and their findings are summarized in Table 2.1.

Table 2.1 Effect of increase of various factors on shear modulus and damping ratio of normally consolidate and moderately overconsolidated clays (from Dobry and Vucetic 1987; Meng 2003)

Increasing Factor	**G_{max}**	**G/G_{max}**	**Damping Ratio**
Effective confining pressure	Increases	Stays constant or increases	Stays constant or decreases
Void ratio	Decreases	Increases	Decreases
Overconsolidation, OCR	Increases	Not affected	Not affected
Plasticity Index	Increases is OCR>1; stays constant if OCR = 1	Increases	Decreases
Strain rate (frequency of cyclic loading)	Increases	G increases; G/G_{max} probably not affected	Stays constant or may increase
Number of loading cycles	Decreases after N cycles of large strain but recovers later with time	Decreases after N cycles of large strain	Not significant for moderate shear strain and N

The discussion below will address the factors of strain amplitude, effective stress, void ratio and frequency, focusing on sands because this study is concerned with coarse-grained soils treated with colloidal silica grout to reduce liquefaction susceptibility.

2.2.1. Strain Amplitude

Shear strain amplitude is widely observed to have a dominant effect on the dynamic properties of soils, including sands, as shown in Figure 2.1, and clays. As the shear strain amplitude increases, the shear modulus decreases and the damping ratio increases. Two cyclic threshold shear strains were defined (Vucetic 1994) as shown in Figure 2.2. Before the linear threshold strain, γ_{tl}, the soil behaves essentially as a linear viscoelastic material. The shear modulus at strains less than γ_{tl} is the maximum shear modulus, G_{max}. For strains between the γ_{tl} and the volumetric threshold strain, (γ_{tv}, $\gamma_{tl} < \gamma < \gamma_{tv}$) the soil behaves non-linearly with negligible permanent microstructure changes. However, at strains greater than γ_{tv}, the soil becomes more nonlinear and inelastic with irrecoverable microstructure changes. Dynamic properties are not affected by the number of loading cycles when the strain amplitude is lower than γ_{tl} (Meng 2003).

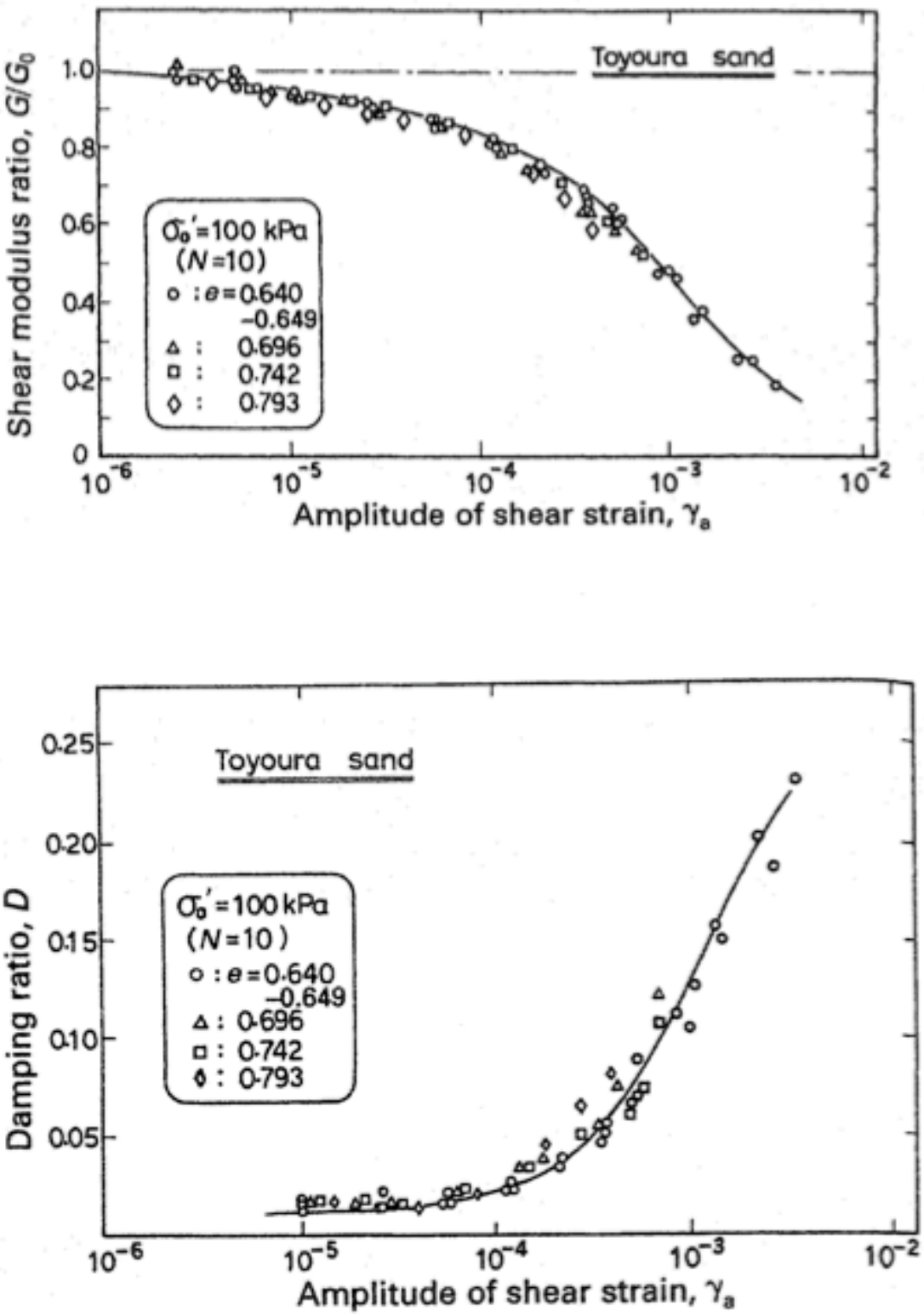

Figure 2.1 Shear strain amplitude effect on sand (from Ishihara 1996)

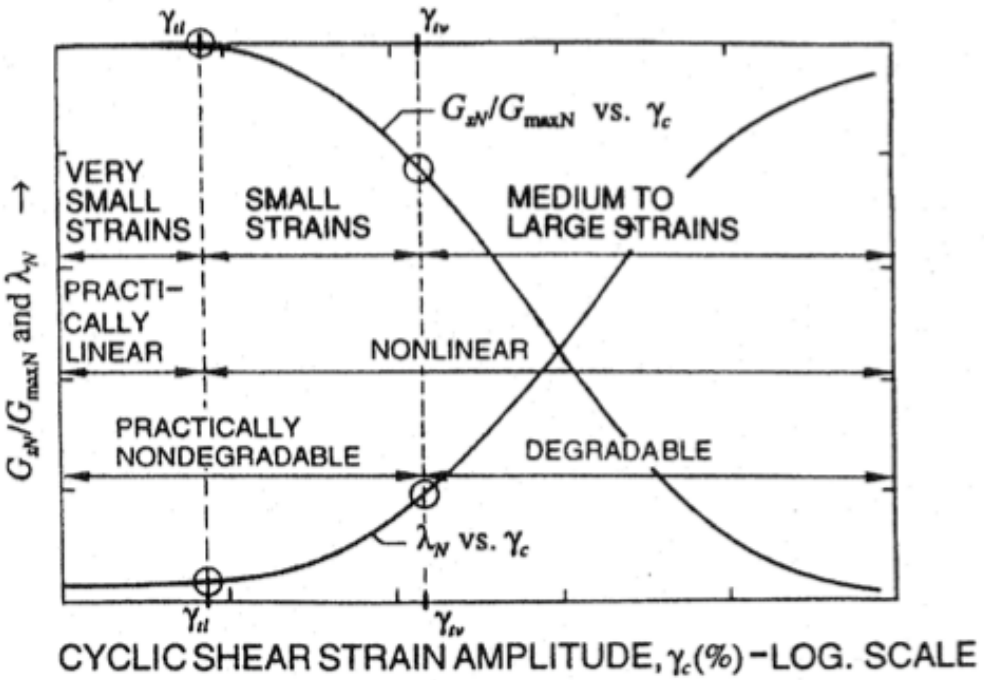

Figure 2.2 Typical modulus reduction curves with threshold shear strains delineated (from Vucetic 1994)

2.2.2. Effective Stress

Research has been conducted that observes the influence of effective stress on the dynamic properties of soils. The shear modulus increases with increasing effective stress, as shown with Ottawa sand in Figure 2.3. The damping ratio is not as affected by effective stress, as indicated in Table 2.1. Research performed using resonant column, torsional shear and bender element tests show that small-strain shear modulus increases with increasing effective stress as shown in Figure 2.4. Effective stress affects shear modulus by increasing the particle contacts, which increases the stiffness of the sample (Santamarina 2001). As the effective stress increases, the major particle-to-particle contact chains carrying the applied load become reinforced by the minor chains due to particle rearrangement in the soil matrix caused by increased effective confining stress (Wang and Tsui 2009). The reinforcement of the major soil chains by the supporting minor chains stiffens the overall soil matrix, which results in an increase in small-strain shear modulus. Work done by Stokoe et al. (1985) found the shear modulus is equally

dependent upon the principal effective stress state in the direction of wave and particle propagation.

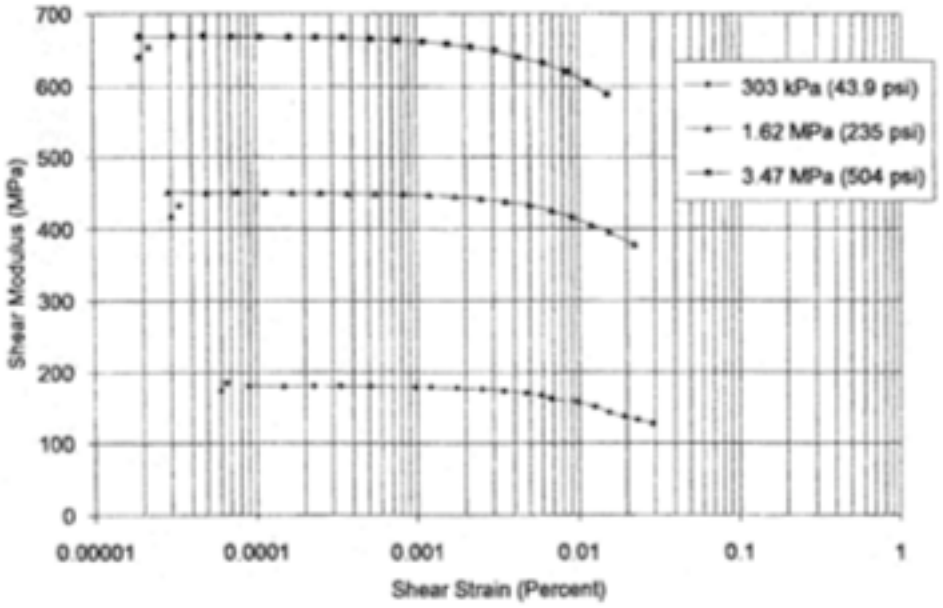

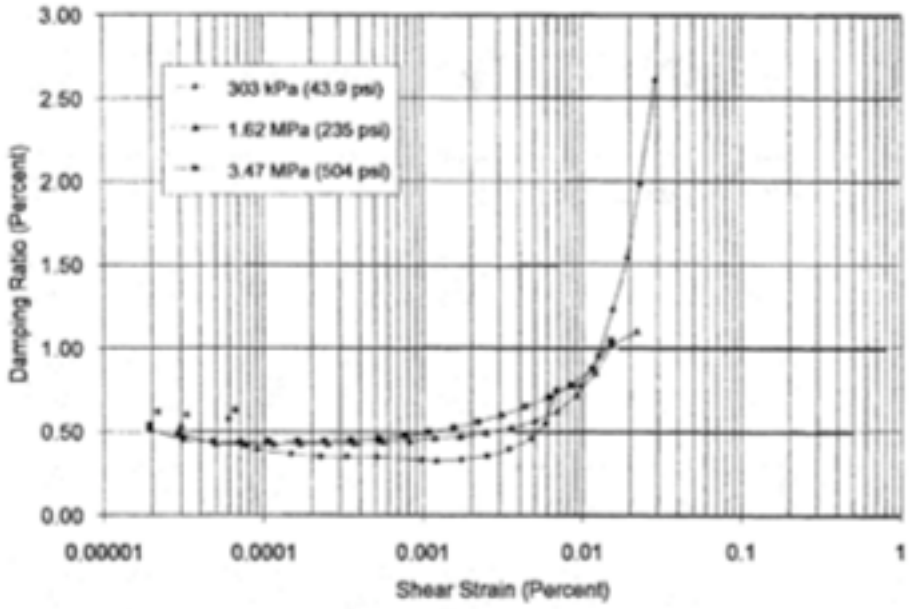

Figure 2.3 Effect of effective stress on dynamic properties of sand (from Hardin et al. 1994)

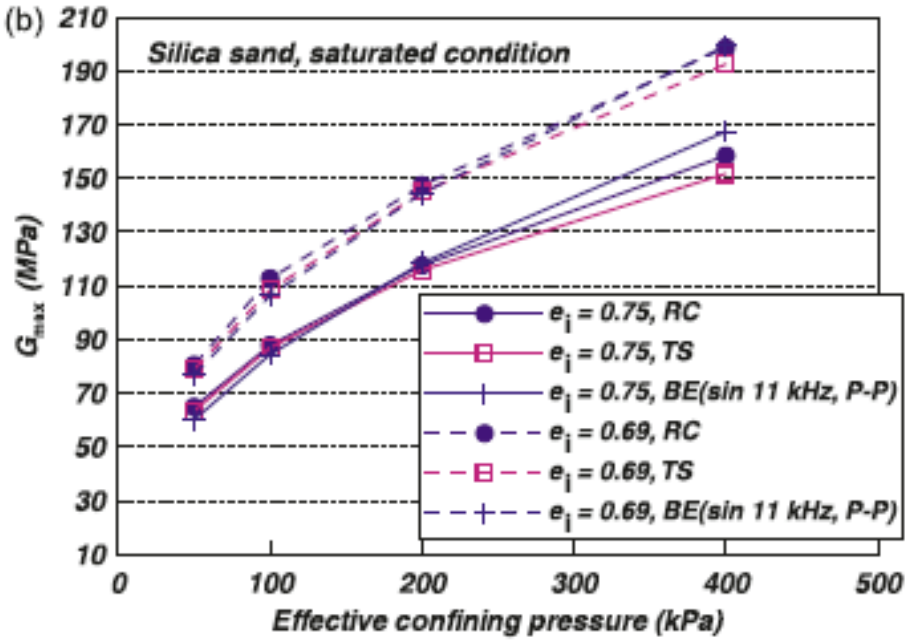

Figure 2.4 Effect of effective stress and void ratio on the small-strain shear moulus of saturated silica sand (from Youn et al. 2008)

2.2.3. Void Ratio

Void ratio is a primary factor influencing the dynamic properties of soils. The typical effect of void ratio on the shear modulus and damping ratio of sand are shown in Figure 2.5. The shear modulus and damping ratio decrease with increasing void ratio. An example of the influence of void ratio on the small-strain shear modulus determined from resonant column, torsional shear and bender element tests is shown in Figure 2.4. Specimens with lower void ratio have a higher number of interparticle contacts and therefore have a higher G_{max}.

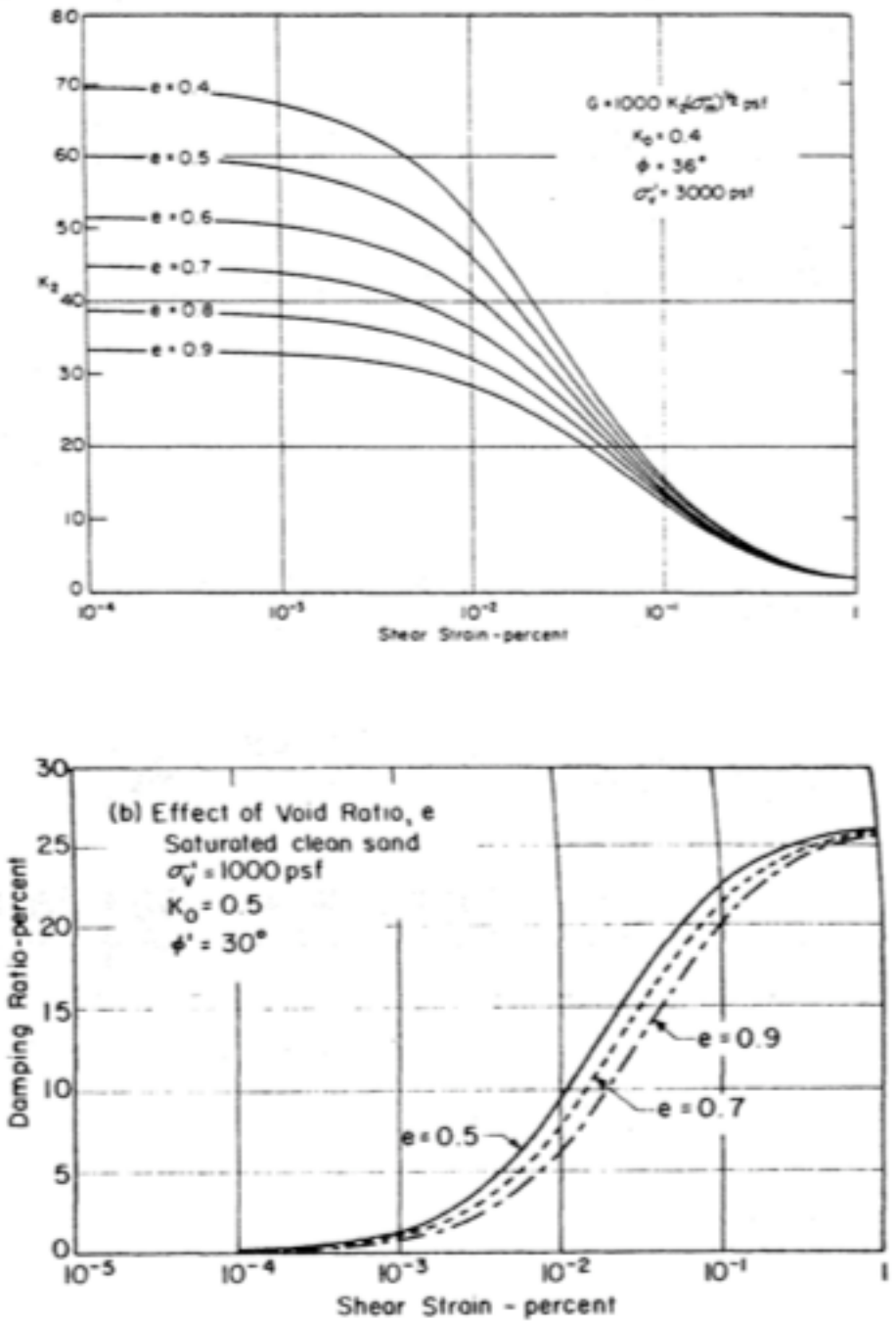

Figure 2.5 Effect of void ratio on dynamic properties of sand (from Seed 1986)

2.2.4. Frequency (at low strain amplitude)

Dynamic loads applied to soils can occur over a broad range of frequencies due to the different loading conditions, such as storms, seismic loading, machine foundations, or

traffic loading and span approximately four orders of magnitude from 10^{-2} to 10^{2} Hz (Ishihara 1996; Meng 2003). However, studies have found there is little effect of loading frequency on the dynamic properties of sand. Hardin and Black (1966) found the shear modulus of sands is essentially independent of frequency from low, quasi-static frequencies to several hundred Hertz. And a comparison of dry and saturated sands subjected to torsional shear and resonant column tests, with test frequencies of 0.1 Hz and approximately 100 Hz, did not show any appreciable difference in the shear modulus (Iwasaki et al. 1978). Kim (1991) showed nearly constant values of dynamic properties of dry sand tested with the torsional shear and resonant column as shown in Figure 2.6.

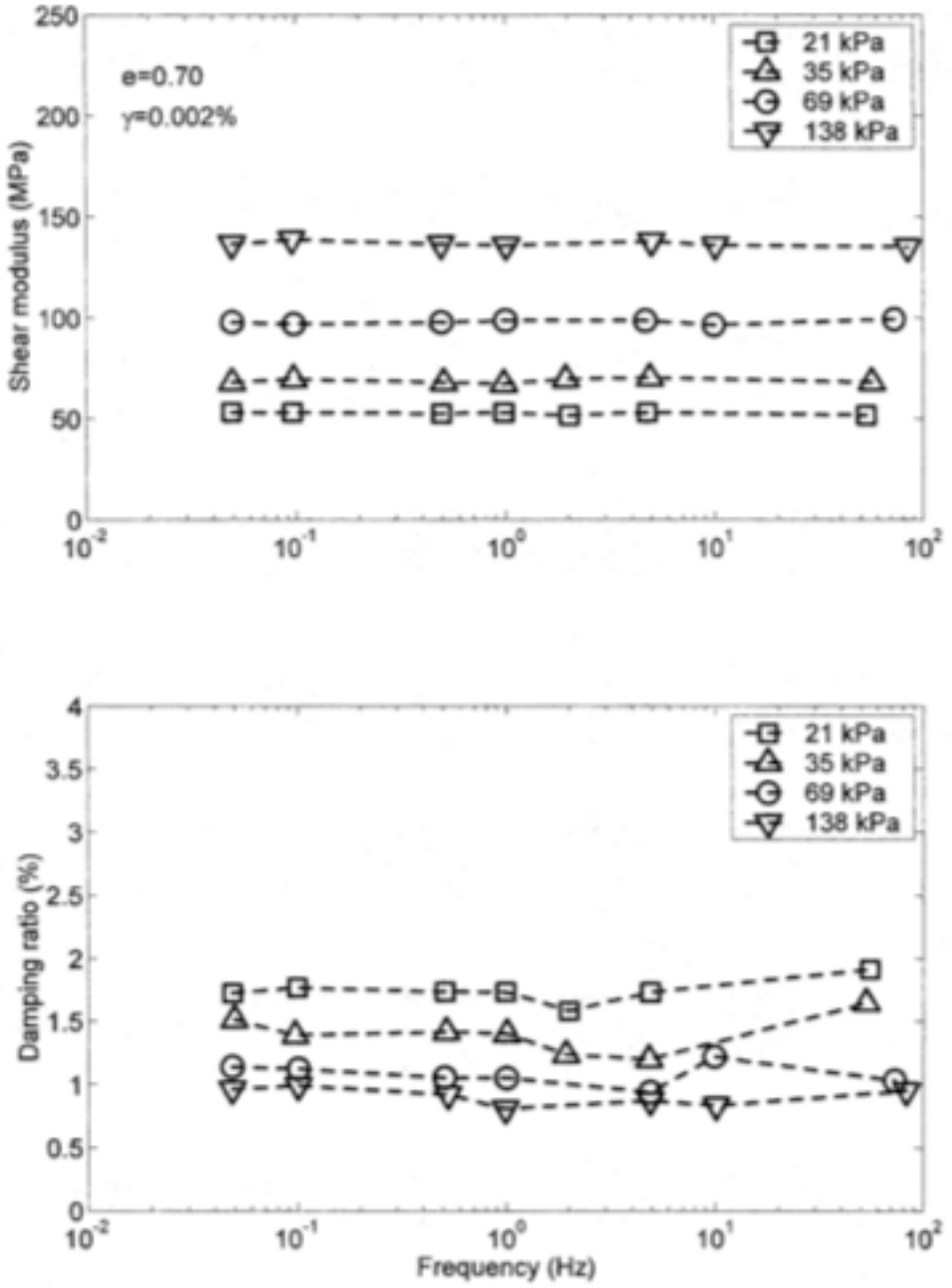

Figure 2.6 Effect of frequency on the dynamic properties for dry sand (Kim 1991)

2.2.4.1.Shear Wave Propagation

Wave propagation in saturated porous materials is affected by the pore fluid (Youn et al. 2008). As frequency of the excitation increases, relative displacements between the pore fluid and particles are caused by differential inertial effects

(Santamarina et al. 2001). A brief explanation of Biot's theory on the elastic wave propagation through fluid-saturated soils is discussed below.

2.2.4.2.Biot's Theory

The shear modulus and mass density of the soil-fluid sample affects the velocity of shear waves in fluid-saturated soils. The frequency equation of Biot's theory can be simplified into three characteristic values for soils when the stiffness of the skeleton (B_{sk}) is much lower than the stiffness of the material that comprises the soil particles (B_g), $B_{sk} << B_g$. If frequencies are low, the soil particles and the fluid move together because of the viscosity of the pore fluid. The inertias of the soil and fluid are added together and the shear wave velocity can be written in terms of total mass density as:

$$V_{s0} = \sqrt{\frac{G_{sk}}{(1-n)\rho_g + n\rho_f}} \qquad 2.2$$

where V_{s0} is the low-frequency limit of the shear wave velocity, G_{sk} is the shear modulus of the skeleton, n is the porosity, ρ_g is the mass density of the soil particles, and ρ_f is the mass density of the pore fluid.

The characteristic frequency that separates the low- and high-frequency velocities is:

$$f_c = \frac{ng}{2\pi k_h} \qquad 2.3$$

where g is the acceleration due to gravity and k_h is the hydraulic conductivity. The high-frequency velocity is calculated by:

$$V_{s\infty} = \sqrt{\frac{G_{sk}}{(1-n)\rho_g + n(1-1/\alpha)\rho_f}} \qquad 2.4$$

where $\alpha = 1$ for tubes, $\alpha = 2$ to 3 for particulate materials and $\alpha = (1+n)/2n$ for spherical particles (Santamarina et al. 2001; Youn et al. 2008).

The low-frequency limit of the shear wave velocity is used when the excitation frequency, f, is ten times lower than the characteristic frequency, $f < 0.1 f_c$. If $f >> f_c$, then the high-frequency shear wave velocity is used. Once the characteristic frequency is established, the corresponding wavelength can be calculated. The wavelength of shear waves approaches the scale of particle size when $f \rightarrow f_c$ and therefore propagation at high frequencies may be affected more by grain scattering effects than Biot dispersion effects (Santamarina et al. 2001).

2.2.5. Aging Effects

Time-dependent property changes in soil are termed aging. Aging has been researched and found to influence several soil behaviors, such as shear strength increase, dilatancy increase, and an increase in cone penetration resistance (Wang and Tsui 2009). The increase of the shear modulus due to aging has also been evaluated (Anderson and Stokoe II 1978; Baxter and Mitchell 2004; Li and Yang 1998; Mesri et al. 1990; Wang and Tsui 2009). Howie et al. (2002) found that aging at any stress ratio resulted in reduced contractive volumetric strain during subsequent shearing, which supports the theory that a change in soil structure occurs during aging due to particle rearrangement during creep (Wang and Tsui 2009). The effect of aging on the small-strain shear modulus of sands is discussed in more detail in Chapter 4.

2.3. Soil Improvement Methods

In an attempt to minimize the damage caused by liquefaction-induced ground deformations, several different soil improvement methods have been investigated and employed over the years (Indraratna and Chu 2005). As noted in Chapter 1, these soil improvement methods rely on one or more of the following mechanisms to mitigate liquefaction hazards: densification of loose soils, rapid dissipation of excess pore pressures via drainage, reinforcement of the soil mass via stiff inclusions that limit ground deformations even if liquefaction occurs, and stabilization of the soil mass via

permeation grouting to limit the development of strains and thus excess pore pressures within the soil mass.

2.3.1. Densification

Densification increases the relative density of the improved area thus reducing the contractive behavior of the soil and making it less susceptible to liquefaction. Soil densification is a traditional means of soil improvement easily employed at undeveloped sites and methods include vibrocompaction, deep dynamic compaction or explosive compaction (Gallagher and Koch 2003). Compaction grouting has been shown to effectively mitigate liquefaction, especially in sands. However the grouting volume used was larger than theoretically calculated to increase soil density (Miller and Roycroft 2004). Furthermore, vibrations from densification can have adverse effects on the adjacent structures. This type of ground modification is not suitable for use at developed sites due to limited access to the liquefiable target zone, especially in ports, where the liquefiable soils have been developed with operational wharf structures.

2.3.2. Drainage

The use of drainage to rapidly reduce the excess pore pressure build up to maintain an excess pore pressure ratio of less than 0.6 has lead to the development of multiple types of drainage methods. Conventional gravel drains and stone columns have been used for drainage, but these methods have drawbacks such as reduction and variability in hydraulic conductivity with time due to clogging and installation difficulties at developed sites. Prefabricated drains are corrugated, perforated plastic pipes encased in filter fabric and, without effects from soil densification due to drain installation, have been shown to reduce pore pressure generation, increase the rate of dissipation of the pore pressure post-shaking and reduce settlements in loose, liquefiable sand subjected to large dynamic loads (Chang et al. 2004). A new type of prefabricated drain that reduces clogging has been shown to reduce excess pore water pressure generation, decrease

bending moments for earthquake motions up to 0.2 g and aide in maintaining shear strength at shaking levels above that (Harada et al. 2006).

2.3.3. Reinforcement

The use of in-situ columns or walls constructed using either cement deep soil mixing (CDSM) or jet grouting provide vertical compressive reinforcement and lateral shear resistance. In addition, walls can be used to form cells that will provide containment for liquefied soil (Mitchell and Hon 2008). A building was constructed on jet grout columns 0.6-m in diameter and 9-m in depth installed in a primary grid and 2.5-m-deep columns located in the liquefiable stratum installed in a secondary grid. The 1999 Kocaeli (M_w = 7.4) earthquake subjected the site to ground acceleration of 0.24g and no evidence of liquefaction, settlement or structural damage to the building was observed, in comparison to the untreated areas on the site which experienced settlements of 50 to 100 mm (Martin et al. 2004).

2.3.4. Permeation Grouting

Treatment of soils with chemical grouts is becoming a more common practice due to the demand for utilization of reclaimed soils. Permeation chemical grouting is an effective means of improving the soil behavior to loading by modifying the volume stability, permeability and strength (Maher et al. 1994). Chemical grouting is also a viable option of soil improvement when typical densification methods and resulting vibration effects on adjacent structures are not suited for a site, or when the treatment zone is difficult to reach due to development (Maher et al. 1994). This process is termed passive mitigation (Gallagher 2000).

2.3.4.1.Dynamic Response of Chemically Grouted Sand

Investigations on the dynamic properties of sand treated with varying chemical grouts, including sodium silicate, acrylate polymer and microfine cement, have been

performed (Li and Woods 1987; Maher et al. 1994). Sodium silicate is formed by burning silica sand and sodium carbonate at high temperatures and then dissolving in water (Iler 1979). Typical grouting sodium silicate solutions are comprised of 20-30% SiO_2, 5-15% NaO_2 and 60-70% H_2O and are gelled by the addition of a catalyst, such as bi-carbonate; gel times on the order of minutes are controllable but longer gel times are not. Stronger gels are obtained with higher concentrations of silica or organic catalyst (Gallagher 2000). Acrylate polymer grout is a solution of acrylate salts that can polymerize with the addition of a cross-linking agent, a catalyst and an inhibitor; the addition of a retarder can be used to obtain gel times of 6 hours (Gallagher, 2000; Maher et al. 1994). Microfine cement grouts are composed of microfine Portland cement particles, roughly 3 to 4 microns, dispersant, slag, water, and additives used to control the viscosity and rheology of the mixture (Gallagher 2000).

In small-strain dynamic property investigation using the resonant column, it was found that the shear modulus increased, more in loose sands, with the addition of grout and the increase in shear modulus was proportional to the grouting degree and curing time, up to a limiting value (Li and Woods 1987).

The intermediate-to-large-strain dynamic properties of Ottawa 20-30 sand treated with three different chemical grouts, sodium silicate, acrylate grout and polyurethane grout, were investigated using a combination of resonant column and cyclic triaxial tests. The results showed that after 14 days curing time sodium silicate increased the shear modulus and slightly decreased the damping ratio while AC-400 (acrylate grout) had no noticeable effect on the shear modulus but increased the damping ratio in the larger strains as shown in Figure 2.7. The curing time was found to not have an effect on the dynamic properties after a certain curing time, 60 days for sodium silicate and 14 days for both acrylate and polyurethane grouts (Maher et al. 1994).

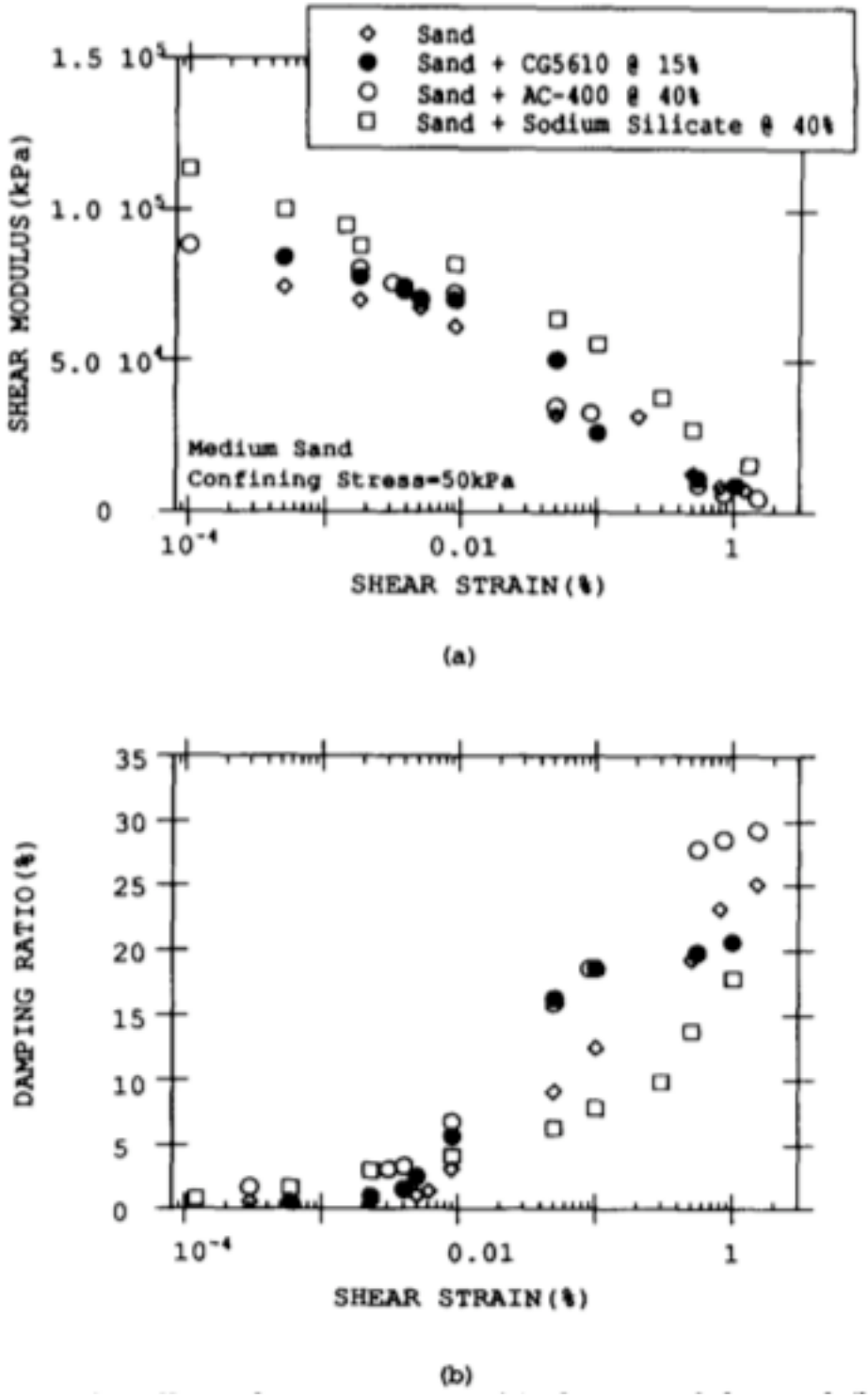

Figure 2.7 Effect of different chemical grouts on the dynamic properties of treated Ottawa 20-30 sand (from Youn et al. 2008)

2.4. Colloidal Silica Gel

A material identified as a potential stabilizer for use in passive soil improvement is colloidal silica gel (Gallagher 2000). Colloidal silica is an aqueous suspension of silica nanoparticles (Iler 1979). The initial particle sizes range from 2 to 100 nm, with a consistent particle size for a given colloidal silica sol suspension. The properties of the colloidal silica sol used in this study are shown in Table 2.2. Colloidal silica particles form when H_4SiO_2 molecules form siloxane bonds (Si-O-Si) because the surface of the particle has an uncombined silanol (SiOH) group. Once particles reach the desired size, the sol is stabilized by increasing the pH to prevent further particle growth. By increasing the pH, the particles ionize and repel each other. Reducing the repulsive forces induces gelation and the rate of particle-to-particle interaction determines the gel time (Gallagher 2000; Iler 1979).

Table 2.2 Properties of Ludox-SM colloidal silica sol (DuPont 1997)

Property	Ludox-SM
SiO_2/Na_2O (by weight)	50
Stabilizing counter ion	Sodium
Particle charge	Negative
Silica (as SiO_2) weight %	30
pH	10.0
Viscosity (cP)	5.5
Average particle size (nm)	7
Specific surface area (m^2/g)	345

Sodium silicate is the starting material to form colloidal silica. The reaction of sodium silicate forms colloidal silica nanoparticles of a predetermined size and also reaction products of water and sodium ions (Iler 1979). The water and sodium ions are removed and the remaining colloidal silica nanoparticles can be dispersed in an aqueous suspension, as is used in this research. Colloidal silica has particles of uniform size and the gelation is more easily controlled whereas sodium silicate gels will have greater particle size distributions. The main advantage of colloidal silica gel over other types of

grout is the controllable gel time over a wide range. Gel times from minutes to weeks can be obtained and the viscosity remains low before gelling, as discussed below. The other chemical grouts mentioned above have shorter gel times, which are insufficient to be used as passive stabilizers. In addition, the above types of grout have drawbacks specific to each. Sodium silicate viscosity doubles before it reaches the gel time, causing difficulty in complete permeation and is prone to shrinkage due to expulsion of water. While sodium silicate is a silica gel, the silica particle size is not controlled, as in colloidal silica. Acrylate grouts have low viscosity until gelation, but the gel time of six hours is not suitable for passive stabilization. Fine cement grout has a similar problem in that a set-retarding admixture is necessary to elongate the set time. In addition, the additives used to stabilize the mix can cause an adverse effect on the rheology of the mixture making penetration of the soil matrix difficult.

2.4.1. Gelation

In this study, the silica particles are approximately 7 nm in size before gelation starts (DuPont 1997) and are polymer spheres with negatively charged surfaces (Scott 1993) as shown in Figure 2.8. Due to the small size and surface charge of the silica particles, electrical interparticle forces dictate the behavior and fabric formation of the particles (Santamarina et al. 2001; Scott 1993). Aggregation, or gelation, is induced by altering the repulsive forces of the silica particles in the suspension. The addition of NaCl to the water used to dilute the silica sol increases the salt concentration of the solution and reduces the double layer thickness of the silica particles. This reduces the repulsive forces and allows the particles to move close enough together to form siloxane bonds and dissociate an H_2O molecule. The dissociated water caused by multiple bonds remains within the pore space of the gelled silica particle network. A simplified chemical bond is shown in Figure 2.9.

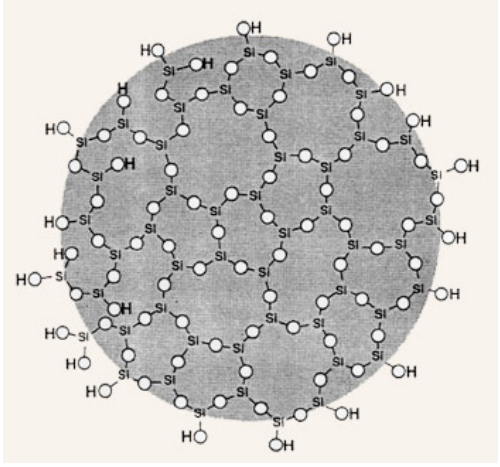

Figure 2.8 Schematic of colloidal silica particle with negatively charged surface (Silco 2005)

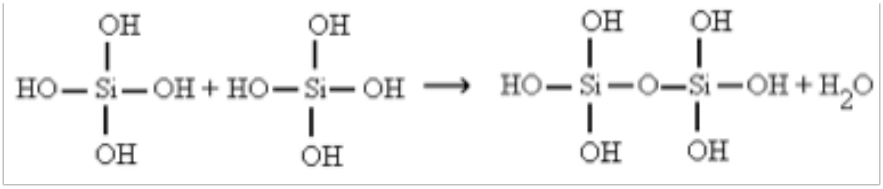

Figure 2.9 Simplified schematic of siloxane bonding

Gel time is dependent on several variables, including the silica solids concentration, the size or surface area of the silica particles, the pH, the charge on the particles and the salt concentration. Gel time increases with decreasing silica solids concentration and increasing silica particle size. Minimum gel times occur in the pH range of 5 to 6, and gel times can be longer if outside of this pH range (Gallagher 2000). As discussed above, salt is added to decrease the double layer size and reduce the repulsive forces to allow bonding to occur; therefore the gel time decreases with increasing salt concentration as shown in Figure 2.10, where the viscosity versus time plot for varying salt concentrations shows the influence of salt concentration on the decrease in gel time. Gel times of 20 minutes to 49 days can be obtained using five percent weight Ludox sol in pH range of 5 to 9.5 and longer gel times occur at lower sol concentrations, lower salt concentrations and higher pH (Gallagher 2000; Persoff et al. 1999).

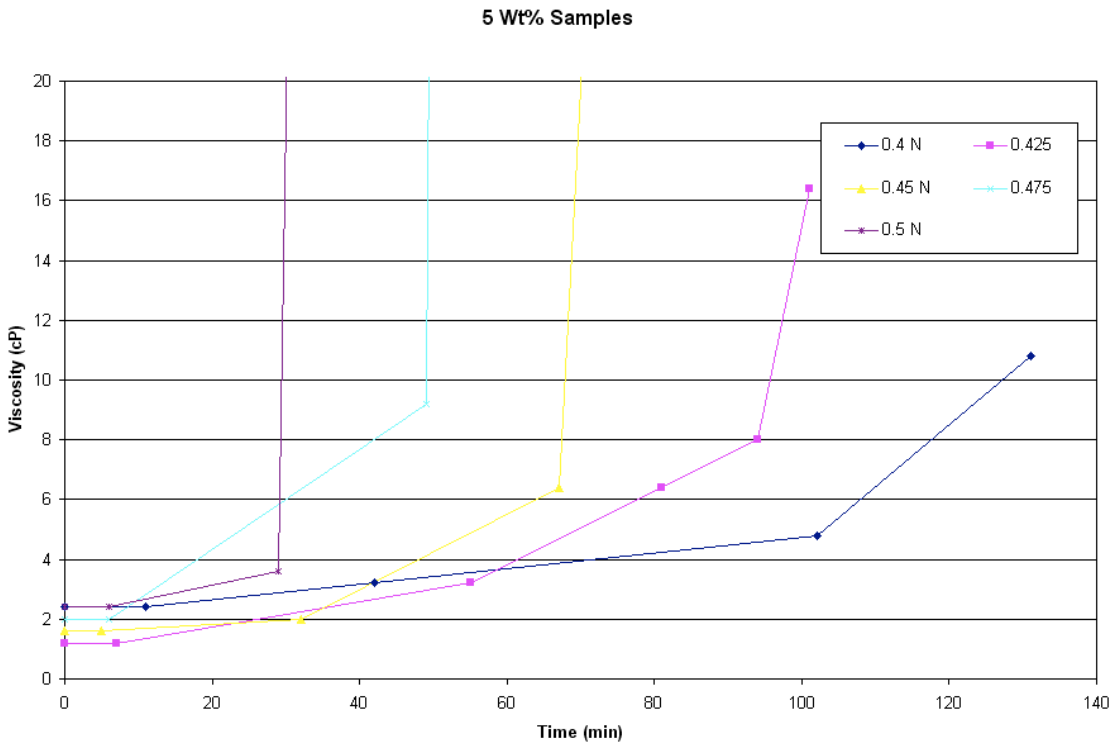

Figure 2.10 Typical gel time curve for 5% weight colloidal silica with varying salt concentrations, increasing concentration from left to right (after Gallagher 2000)

Gelation is the transition from a viscous-fluid behavior to a viscoelastic solid behavior. The chemical evolution of the system is essentially unaffected by gelation, the structure and properties of the gel evolve with time in a process called aging (Scherer 1988). Because the gel continues to change over time from a sol to a gel to a rigid non-ringing gel, a chart of gel states has been developed as shown in Table 2.3. The gel time occurs within the gel state 4 or 5, however a rigid gelled structure is not evident until later gel stages.

Table 2.3 Gel states of colloidal silica (from Gallagher 2000)

Gel State	Description
1	No detectable gel formed. Gel appears to have same viscosity (fluidity) as original polymer solution and no gel is visually detectable.
2	Highly flowing gel. Gel appears only slightly more viscous than original polymer.

3	Flowing gel. Most of obviously detectable gel flows to bottle cap upon inversion.
4	Moderately flowing gel. Small portion (5-15%) of gel does not readily flow to bottle cap upon inversion.
5	Barely flowing gel. Gel slowly flows to bottle cap and/or significant portion (>15%) of gel does not flow upon inversion.
6	Highly deformable non-flowing gel. Gel does not flow to bottle cap upon inversion (el flows to just short of reaching bottle cap).
7	Moderately deformable non-flowing gel. Gel flows about halfway down bottle upon inversion.
8	Slightly deformable non-flowing gel. Only gel surface deforms slightly during inversion.
9	Rigid gel. There is no gel-surface deformation upon inversion.
10	Rigid ringing gel. Tuning-fork-like mechanical vibration can be felt or heard after bottle is tapped.
11	Rigid gel no longer ringing. No tone or vibration can be felt or heard, because natural frequency of gel has increased.

2.4.1.1.Colloidal Silica in a Marine Environment

The gelation and fabric formation of colloidal silica gel is determined by particle-to-particle interaction which is dependent on the percent silica, silica particle size, the pH and the ionic strength. The presence of cations in the groundwater or exchangeable cations in the soil or the introduction of organics or increased groundwater salt concentrations can have an effect on the gel time and the resulting gelled fabric structure. These factors may affect the use of colloidal silica grout in a marine environment such as exists at ports near oceans.

The typical molar composition of seawater contains the components shown in Table 2.4. The ion valence affects the double layer thickness, thus affecting the gel time by changing the rate of the particle-to-particle interaction; for example, a higher valence will decrease the double layer thickness and decrease the gel time. Studies have confirmed the effect of valence on the gelation time of colloidal silica suspensions (Frith et al. 2008; Shani et al. 2008). Another concern is hydrocarbons, but they are less dense (ρ=0.89-0.93) than water and in general only a concern on the surface of water. A more

detailed discussion of the effect of marine pollutants or minority concentration ions on the gelation of colloidal silica gel is outside the scope of this work.

Table 2.4 Composition of seawater

Component	Concentration (mol/kg)
Cl^-	0.546
Na^+	0.469
Mg^{2+}	0.0528
SO^{2-}_4	0.0282
Ca^{2+}	0.0103
K^+	0.0102

2.4.1.2.Microstructure of Colloidal Silica in Suspensions

Research on colloidal silica gel often involves the effect of additives, such as clay particles. Structural development of kaolinite suspensions combined with varying concentrations of salt and colloidal silica were studied by Baird and Walz (2006). A phase change diagram shows a boundary of concentrations of salt and colloidal silica particles needed to transition to a solid gel state as shown in Figure 2.11. The diagram indicates the smaller the initial colloidal silica particle size, the smaller the volume fraction required to produce the sol-gel transition. Scanning electron microscope (SEM) analysis showed the 14% volume kaolinite, 500 mM NaCl and 7% volume Ludox SM (7 nm) gelled supernatant was a porous sponge like structure with average pore sizes of 0.4 μm. Colloidal silica and salt mixtures were also investigated and SEM photos indicated the microstructure was more rounded as shown in Figure 2.12 and did not exhibit the "ordered sponge-like" structure found with kaolinite suspensions. In addition, mixtures containing kaolinite formed a gel in less than an hour, displayed shear-thinning behavior and upon vigorous shaking the gel completely broke up; whereas the silica and salt mixtures took longer to gel, did not exhibit shear-thinning behavior and large lumps of gel material were dispersed upon vigorous shaking.

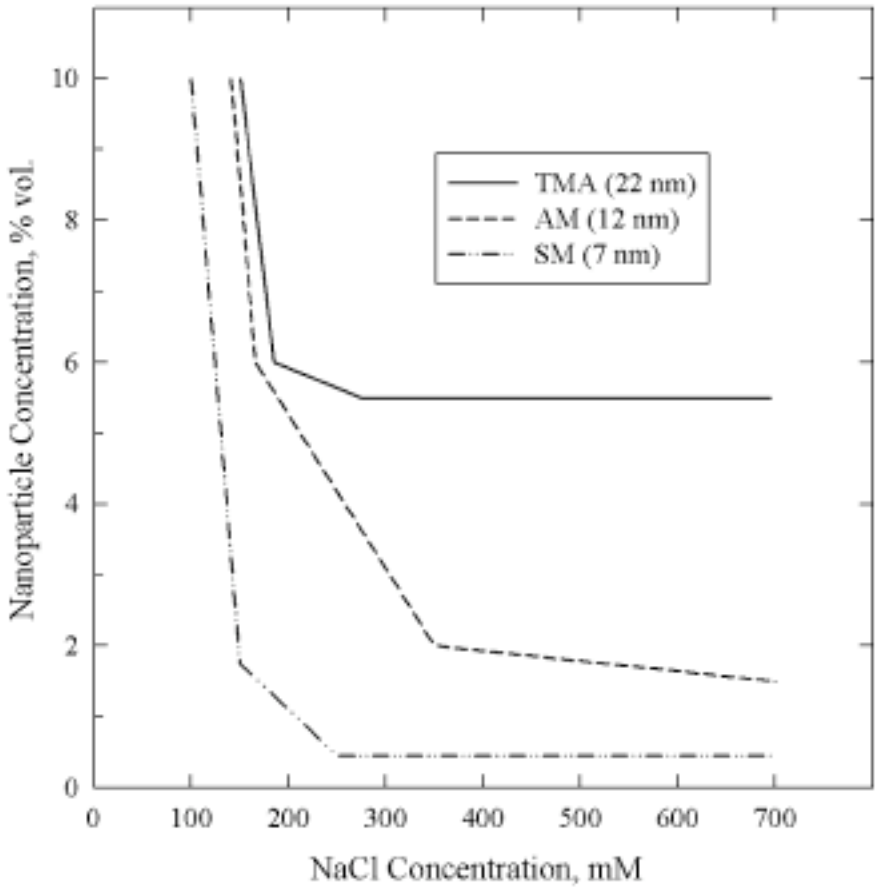

Figure 2.11 Sol-gel phase change diagram for varying Ludox colloidal silica types (colloidal silica particle size), the colloidal silica concentration and salt concentration combinations that fall above the line form a solid while below the line remains liquid (from Baird and Walz 2006)

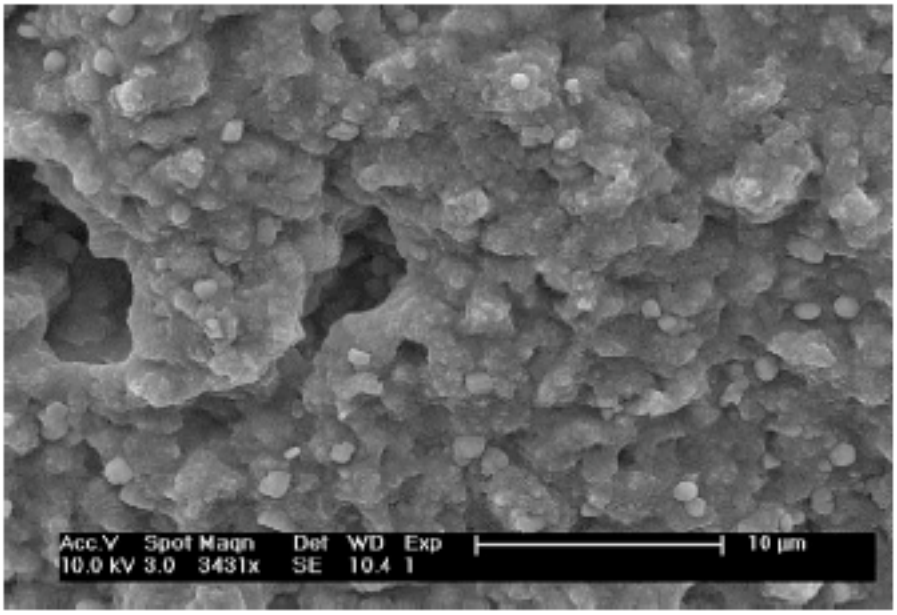

Figure 2.12 SEM photo of colloidal silica gel formed from 7% volume TMA (22nm) colloidal silica and 500 mM NaCl (from Baird and Walz 2006)

2.4.1.3.Strength

The work by Baird and Walz (2007) shows the addition of colloidal silica and salt to kaolin suspensions result in the development of a substantial yield stress, especially for the smaller sized silica particles (Ludox-SM) as shown in Figure 2.13. Oscillatory measurements during gelation indicate an initial rapid rise in viscosity, followed by a period of slower increase continuing through test completion. The work demonstrates that for a given colloidal silica particle size, increasing either the silica particle or salt concentration will increase the yield strength and the long-term complex viscosity. Towhata (2008) identified an unconfined compressive strength of 5.5 kPa on tests of 6.5% weight colloidal silica gel after curing 30 days and also identified the ratio of lateral to axial strains, determining the Poisson's ratio of colloidal silica gel is 0.3 as shown in Figure 2.14. This indicates the gelled silica has volume compressibility and could be the source of increased liquefaction resistance.

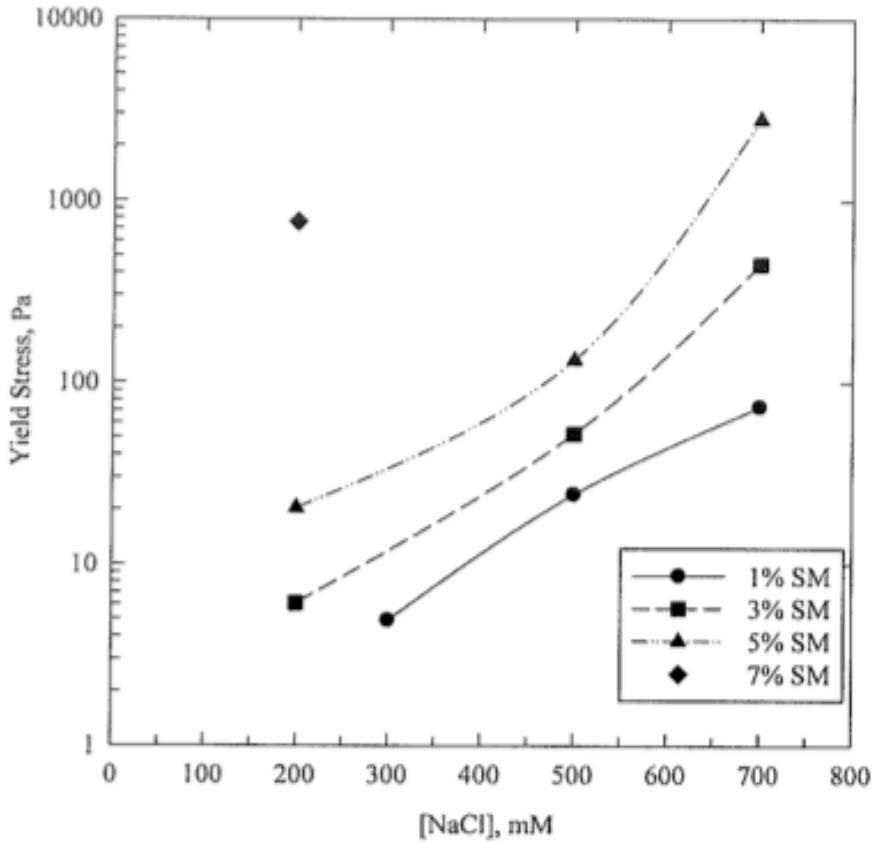

Figure 2.13 Yield stress of 14% kaolinite mixed with different concentrations of SM (7nm) colloidal silica and varying concentrations of NaCl (from Baird and Walz 2007)

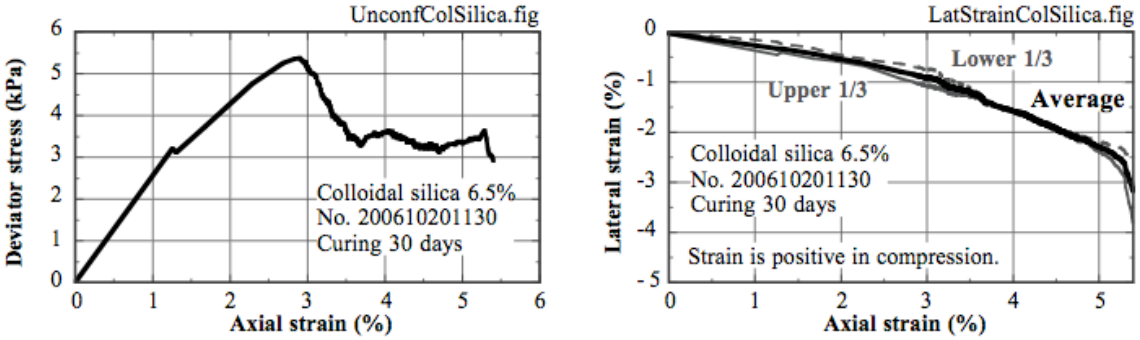

Figure 2.14 Unconfined compressive strength test on 6.5% weight colloidal silica gel (from Towhata 2008)

2.4.2. Colloidal Silica Gel Aging

The properties of gel, and its behavior during subsequent processing are strongly affected by aging. It has been shown by nuclear magnetic resonance (NMR) and Raman spectroscopy that the number of bridging bonds increases long after the gel time (Scherer

1988; Vega and Scherer 1989). The results of ^{29}Si NMR scans for three different water content colloidal silica gels with time after gelling is shown in Figure 2.15. The Q^n represents a Si atom bonded through a bridging oxygen to *n* other Si atoms, so Q^0 is a monomer, $SiOH_4$, and Q^4 is Si surrounded by 4 bridging oxygens. The degree of crosslinking is greater in gels made with more water. The relative amount of Q^3 and Q^4 increase with time, indicating the process of aging (Scherer 1988). As new bonds form, the gel network continues to evolve after gelation and results in a steady increase in the elastic modulus and in spontaneous contraction known as syneresis (Scherer 1996). The continuing chemical bonding also causes an increase in the strength of the gel over time (Axelsson 2006; Hench and West 1990; Scherer 1988) as discussed below.

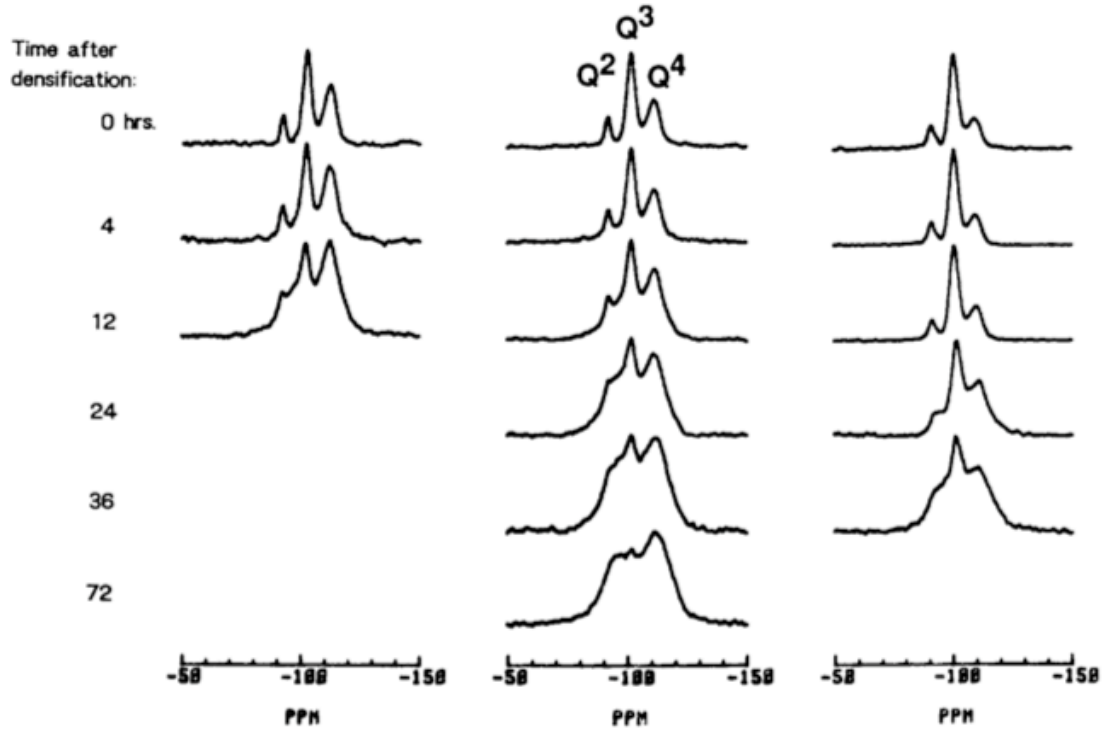

Figure 2.15 Nonspinning ^{21}Si NMR spectra of silica gels prepared with varying water content (16:1, 8:1, 4:1, respectively left to right). Spectra taken at times after solution mixed (from Scherer 1988)

2.4.2.1.Drying

Syneresis is the spontaneous contraction of a gel that occurs without evaporation of a solvent, which is attributed to condensation reactions (the formation of siloxane bonds and dissociated water molecule). A gel is a solid network surrounding a continuous liquid phase; when the solid contracts, the liquid squeezes out of the gel to the gel surface (Scherer 1989b) and the rate of contraction in the gel is equal to the net flux of liquid out of that region (Scherer 1996).

Syneresis is affected by pH, which determines microstructure and therefore the gel stiffness and permeability; therefore the rate of syneresis is affected by permeability and viscoelastic properties (Scherer 1989b). And low permeability causes the rate of syneresis to also depend on the size of the specimen; as liquid near the gel surface can easily escape from the pores, thus the surface shrinks freely. But contraction rate decreases as specimen size increases because a larger fraction of liquid is further from the free surface (Scherer 1996). The incubation (delay before measurable contraction) period that occurs at the start of syneresis experiments is caused by the progressive development of a pressure gradient that drives fluid flow to the gel surface (Scherer 1989b) allowing expulsion of the fluid.

2.4.2.2.Strength

Axelsson (2006) used 35% weight colloidal silica gel to determine the effects of relative humidity at lower temperatures (8°C) and found lower humidity causes strength and shrinkage to increase faster and the failure mode transitions from ductile to brittle as shear strength increases. The shear strength continues to increase over time and there was no limit observed after 6 months of curing as shown in Figure 2.16. The total friction angle of the colloidal silica gel was determined with time and indicates an increase in friction angle with time for all relative humidity curing conditions (Axelsson 2006), as shown in Figure 2.17. Towhata (2008) determined the unconfined compressive strength

of 6.5% colloidal silica gel after 30 days of curing as shown in Figure 2.14, but did not track the change in strength with time.

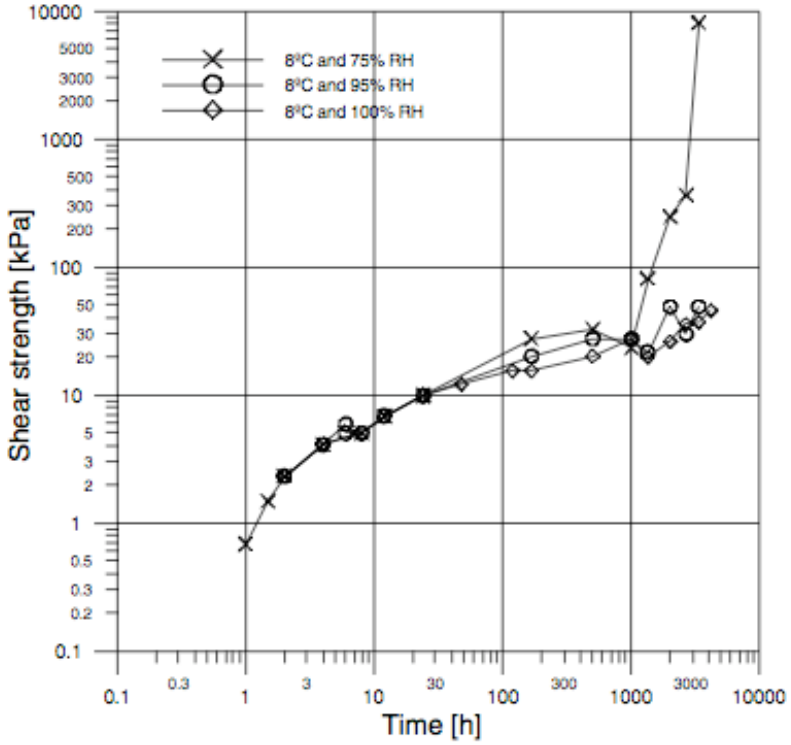

Figure 2.16 Evolution of shear strength over time of 35% weight colloidal silica gel cured at different relative humidities (from Axelsson 2006)

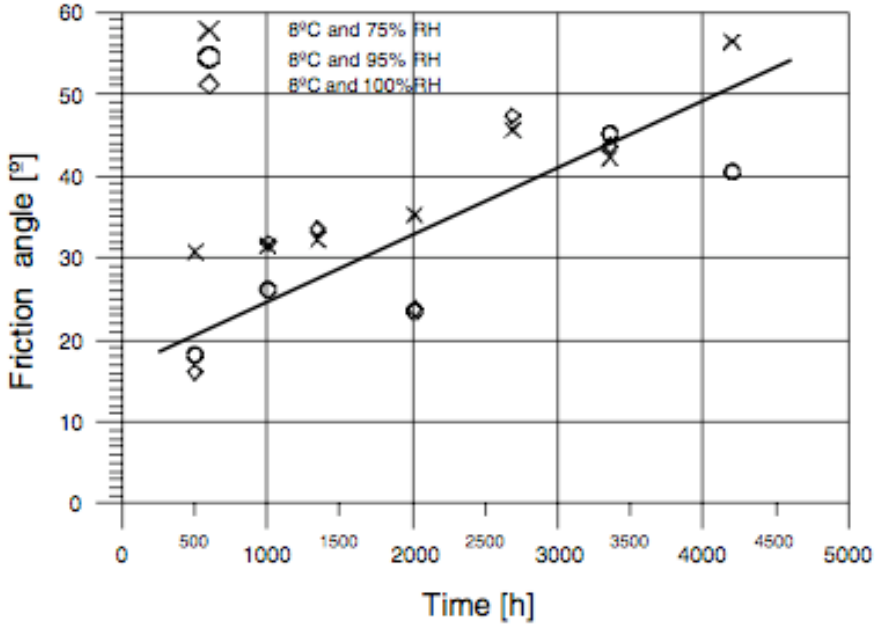

Figure 2.17 Total friction angle over time for different relative humidity curing conditions (from Axelsson 2006)

2.4.2.3.Dynamic Properties

A general increase in shear modulus with time of colloidal silica gel is presented by researchers (Scherer 1989a) and is attributed to the increase in bonds produced by condensation reactions that continue long after gelation. In addition, there is a correlation with shear modulus and diametral strain associated with shrinkage (Scherer 1989a). Dumas et al. (1986) found an increase between the shear modulus at 2 months and 9 months of curing of colloidal silica with varying ethanol concentrations; the maximum percent increase was 50% with the 50% ethanol solution. The influence of frequency on the elastic shear modulus was investigated on suspensions of 14% kaolinite with 7% colloidal silica particles over a period of 10 hours after gelling as shown in Figure 2.18; while the microstructure of the gel and kaolin mixture is different than gel alone, it demonstrates that treated soils also exhibit an increase in the shear modulus with aging. The elastic modulus is independent of frequency four hours after gelation and an increase in the elastic modulus with time after gelling can be seen.

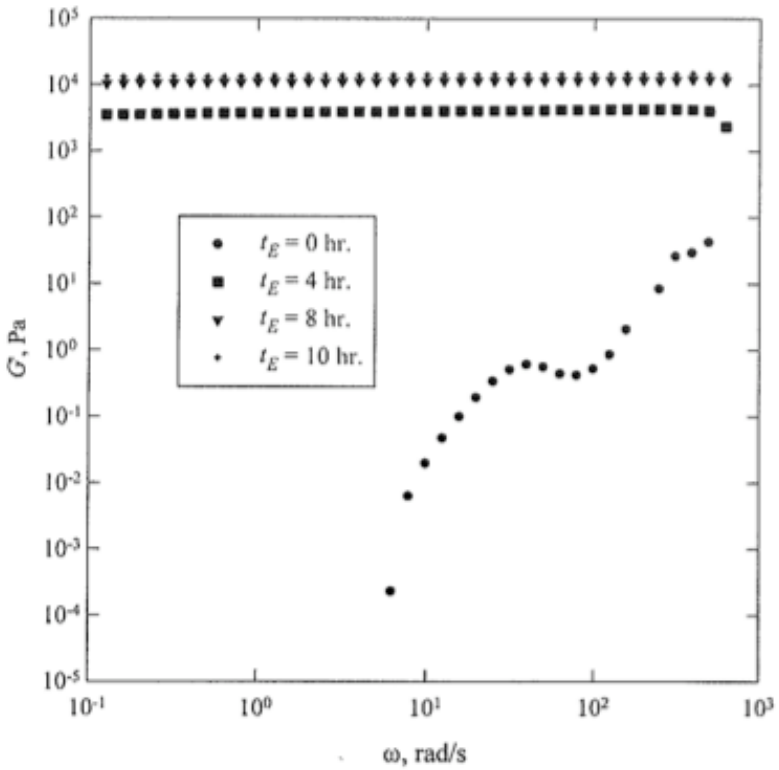

Figure 2.18 Elastic shear modulus of 14% volume kaolinite and 7% volume TMA (22nm) with 500 mM NaCl concentration versus frequency for different time periods after gelling (from Baird and Walz 2007)

The increase in the elastic shear modulus of 10% weight colloidal silica gel over time was fit using an empirical equation, valid for $2 \leq t_c < 30$ days, as shown in Figure 2.19 and the fitted empirical equation is given below (Scherer et al. 1988).

$$G_e(MPa) = -1.4 + 0.96t_c - 0.015t_c^{\,2} \qquad 2.5$$

It was found that the elastic shear modulus and the uniaxial viscosity increased by more than an order of magnitude in the first 14 days of room temperature aging as shown in Figure 2.20 (Scherer et al. 1988). The equation used to fit the elastic shear modulus data shown in Figure 2.20 is shown below.

$$\ln G_e(MPa) = 2.63 - 4.84\exp(-0.194t) \qquad 2.6$$

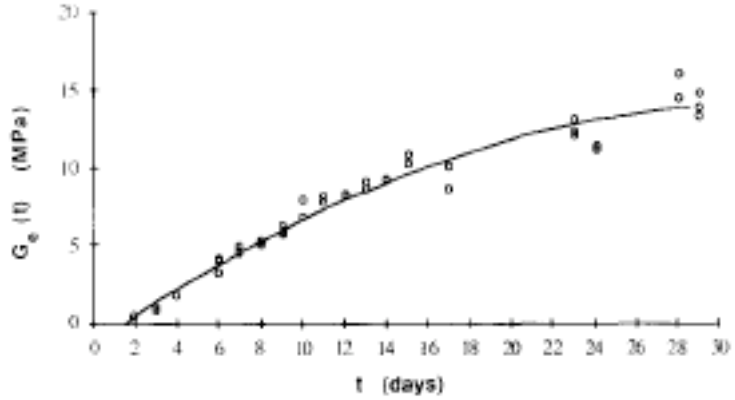

Figure 2.19 Shear modulus of wet gel versus aging time (from Scherer et al. 1988)

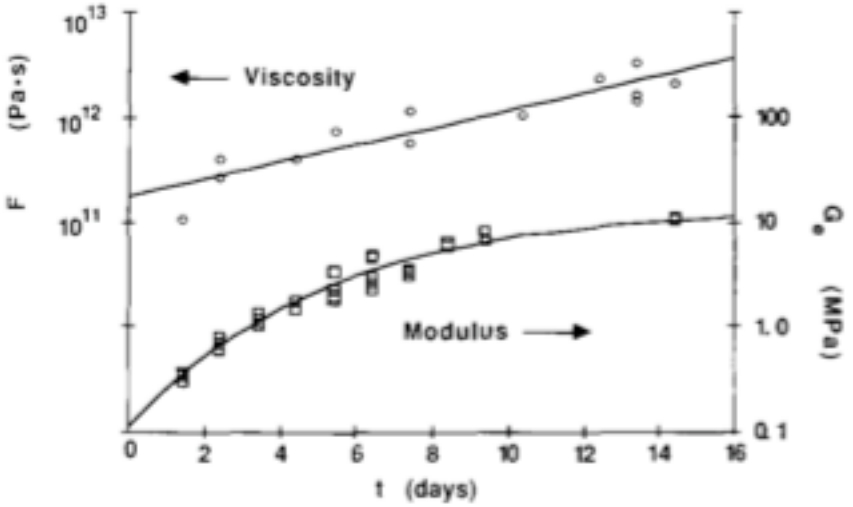

Figure 2.20 Uniaxial viscosity, F, and elastic shear modulus, G_e, versus time after gelation; curve given by Equation 2.6 (Scherer et al. 1988)

Work by Huang et al. (2007), with emulsifiers, organosilicone resin and varying concentrations and sizes of colloidal silica particles indicates that the smaller the particle size and higher the concentration, the higher the storage modulus and lower the loss modulus became. The tan δ increases with increasing particle size and displays a u-shaped response versus frequency (0.1 to 100 Hz) with a trough between 2-3 Hz, the minimum and maximum loss modulus were 20 to 50 Pa, respectively. Drabeck et al. (2002) used commercially available colloidal silica solutions mixed with hydrogen chloride (HCl) to induce gelation. Samples exposed to constant shearing prior to gelation exhibit rapid increase in both the storage and loss modulus after cessation of the shearing

while the unsheared samples initially increase slowly before a sharp increase in the moduli. However, despite different microstructure evolution, upon aging, presheared and unsheared samples display similar viscoelastic properties.

Work done to investigate the effect of relative humidity during curing was done on 35% weight colloidal silica gel at 8°C. The evolution of the Young's modulus with time at three different curing relative humidities is shown in Figure 2.21 (Axelsson 2006). The effect of relative humidity less than 100% on the Young's modulus increases with time and can be correlated to the increase in shrinkage due to lower relative humidity.

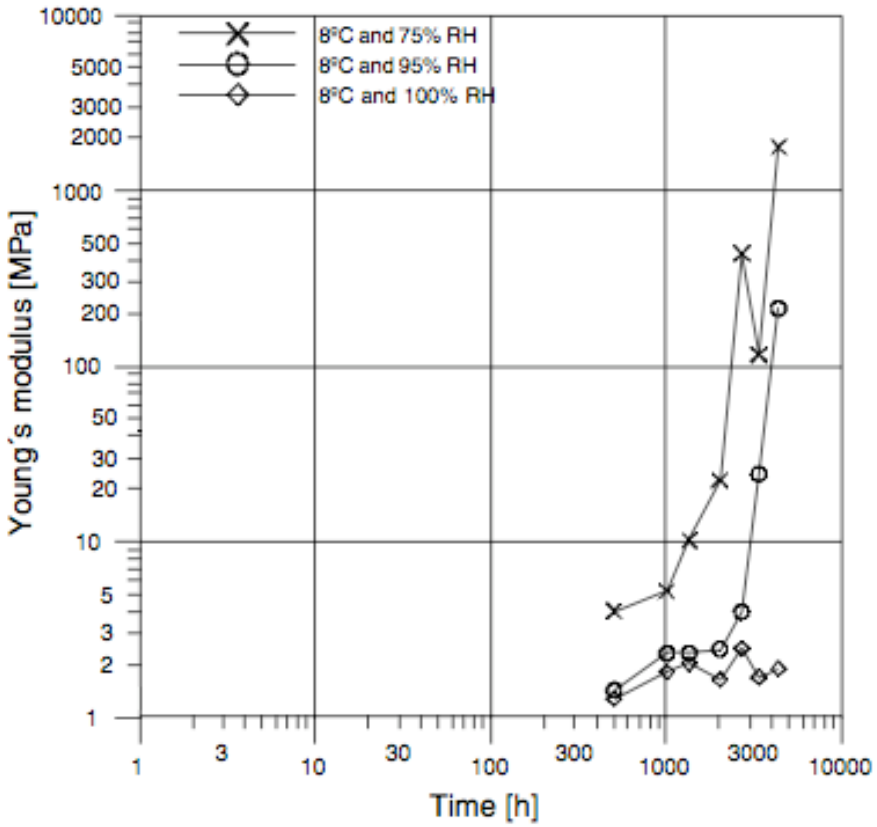

Figure 2.21 Young's modulus over time for samples cured in varying relative humidity conditions (from Axelsson 2006)

Aging of gel while saturated in the pore fluid results in an increase of shear modulus by a factor of two between one month and one year of aging. This reflects the nature of the gel network, as it becomes stiffer it inhibits the approach of labile silanol

groups and once the silanols close to the surface of pores are linked, shrinkage stops and it becomes difficult for bonds to continue at such a rate (Scherer 1989a). If the gel is allowed to dry, the modulus can increase by two orders of magnitude. Two factors contribute to the increase in shear modulus, the reduction in porosity and the stiffening of the solid phase of the gel (Scherer 1989a).

2.5. Sand Treated with Colloidal Silica Gel

Researchers focusing on the strength and large-strain deformation response of the treated sand have performed investigations of sand treated with colloidal silica gel.

2.5.1. Unconfined Compression

The unconfined compression (UC) strength of both Monterrey and Trevino sand grouted with colloidal silica (Ludox-SM) increases proportional to the increase in silica concentration to a maximum of ~400 kPa (for Monterey sand) and the hydraulic conductivity decreased with increasing silica concentration shown in Figure 2.22. Similar experiments performed by Gallagher and Mitchell (2002) confirmed the increase in UC strength with increasing colloidal concentration. Soil samples of 40% relative density Nevada No 120 sand treated with 5% weight colloidal silica had UC strengths ranging from 47-67 kPa with standard deviation of 6-18 (Gallagher and Lin 2005). The effect of cyclic loading or aging on the UC strength of treated sands has been investigated. It was found that samples experiencing high strains during cyclic loading experienced UC strength degradation (Gallagher and Mitchell 2002) as shown in Figure 2.23. Treated samples continued to gain strength for over a year when immersed in water, which prevents drying (Persoff et al. 1999), as shown in Figure 2.24.

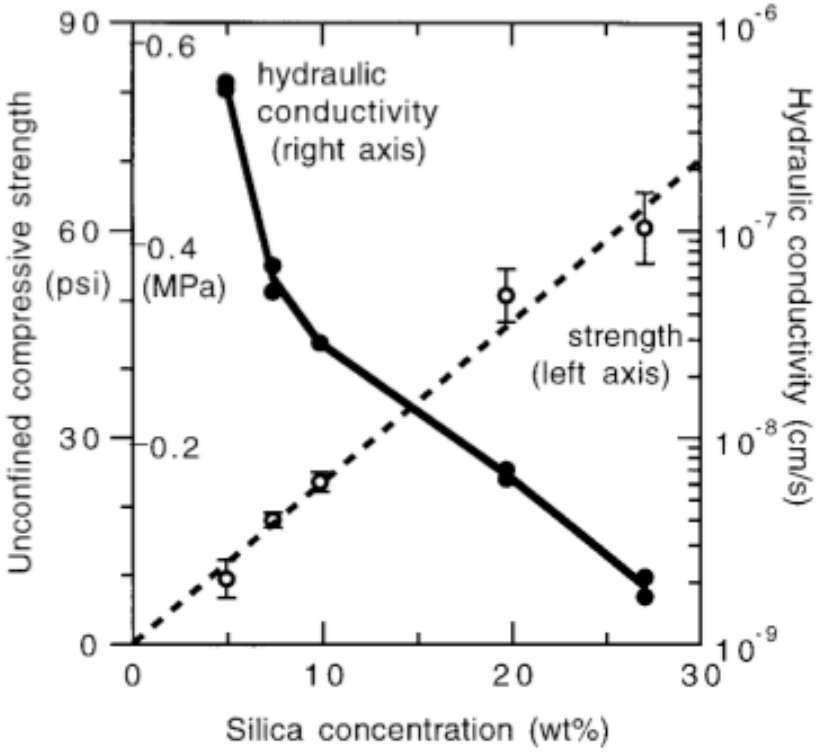

Figure 2.22 Unconfined compressive strength and hydraulic conductivity of Monterey sand treated with varying concentrations of Ludox SM colloidal silica gel (from Persoff et al. 1999)

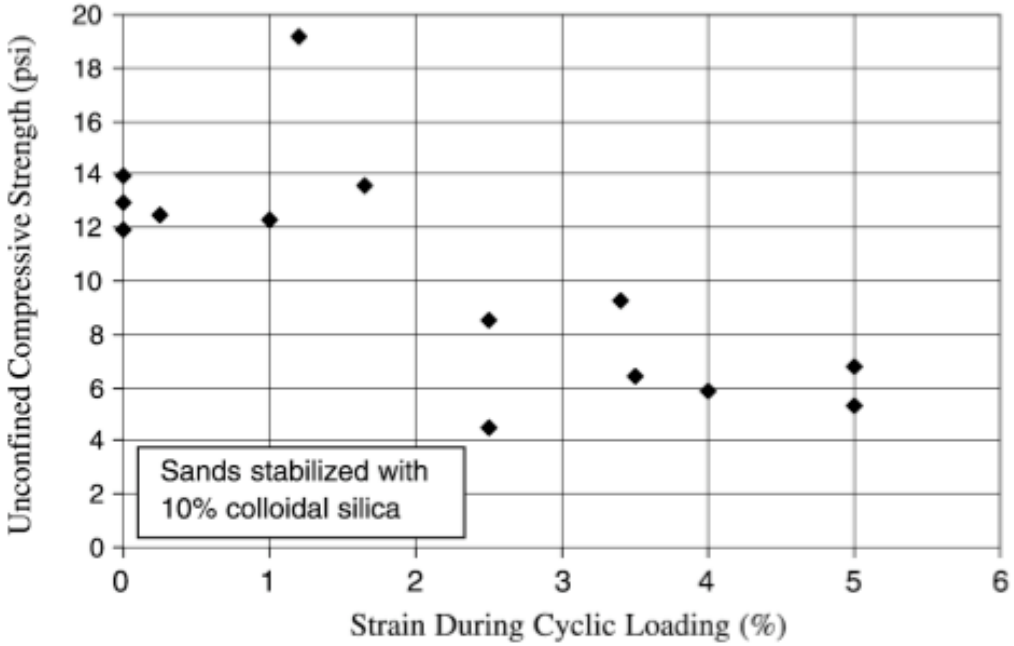

Figure 2.23 Unconfined compressive strength of 10% weight colloidal silica treated Monterey sand after cyclic loading (from Gallagher and Mitchell 2002)

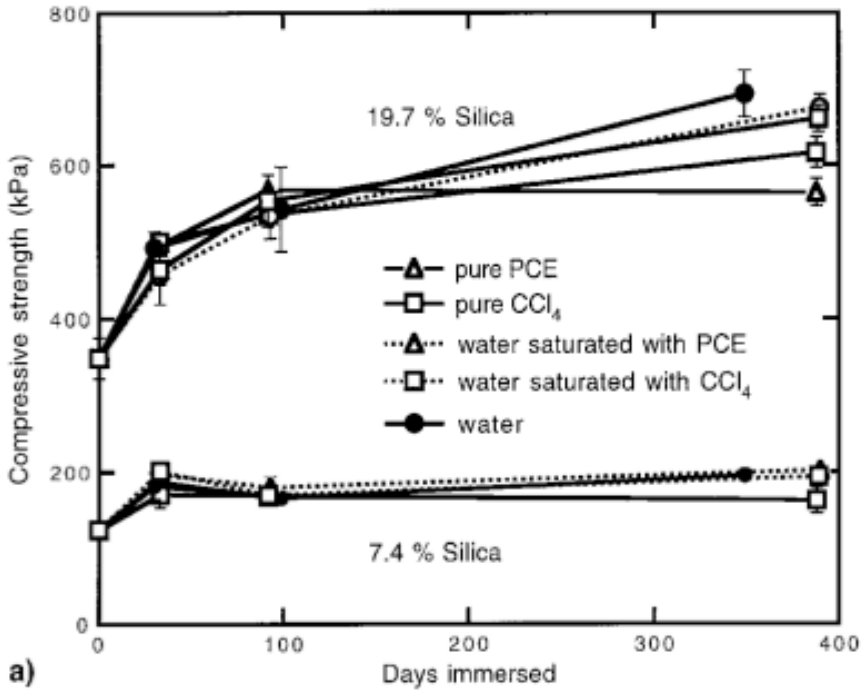

Figure 2.24 Compressive strength of 19.7% and 7.4% weight Ludox SM colloidal silica gel treated Monterey sand after immersion in water, pure chlorinated organics and water saturated with chlorinated organics (from Persoff et al. 1999)

2.5.2. Liquefaction Resistance

Multiple researchers have shown treatment with dilute concentrations of colloidal silica gel increases the liquefaction resistance when compared to untreated sand. Towhata (2008) found that 40% relative density Toyoura sand treated with 4.5% colloidal silica and cured for five weeks, though no gel time was given, shows an increase in liquefaction resistance compared to untreated 50% relative density Toyoura sand as shown in Figure 2.25. It is shown that the treated sand has a higher cyclic stress ratio for the number of cycles it takes to reach liquefaction, defined by 1%, 2% and 5% double amplitude strains or 95% pore pressure generation, when compared to the untreated sand.

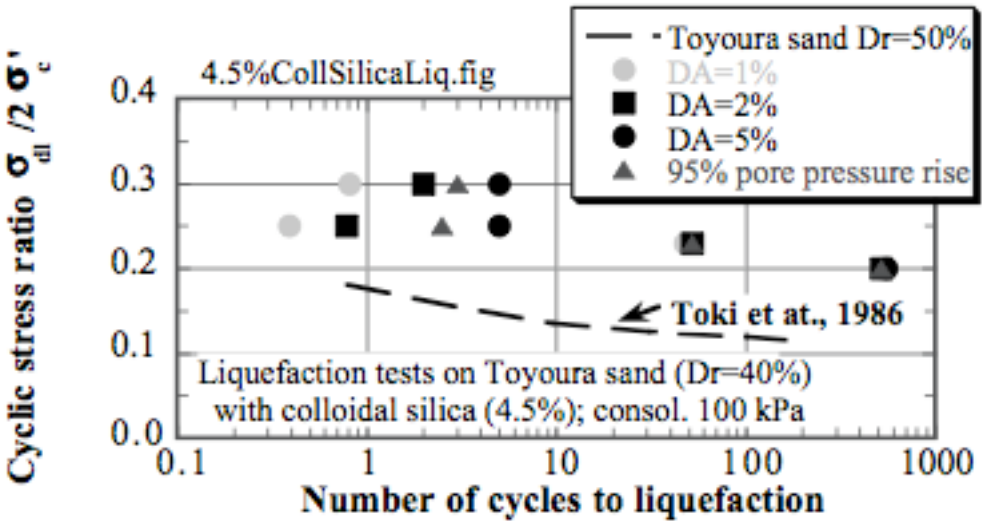

Figure 2.25 Resistance of sand against liqefaction increased by colloidal silica treatment (from Towhata 2008)

Similar conclusions were found by cyclic direct simple shear tests on Nevada sand treated with 5% weight colloidal silica gel, where the treated sand shows an improvement in cyclic resistance ratio over untreated sand and the cyclic resistance ratio of the treated sand increases with increased curing time as shown in Figure 2.26 (Corral and Whittle 2007). The cyclic resistance ratio after the treated sand was cured for 55 times the gel time increased by more than 75% over the treated sand tested at 18 times the gel time at the same number of cycles. This indicates the importance of curing time when identifying increased liquefaction resistance, or other properties such as strength, of treated sands.

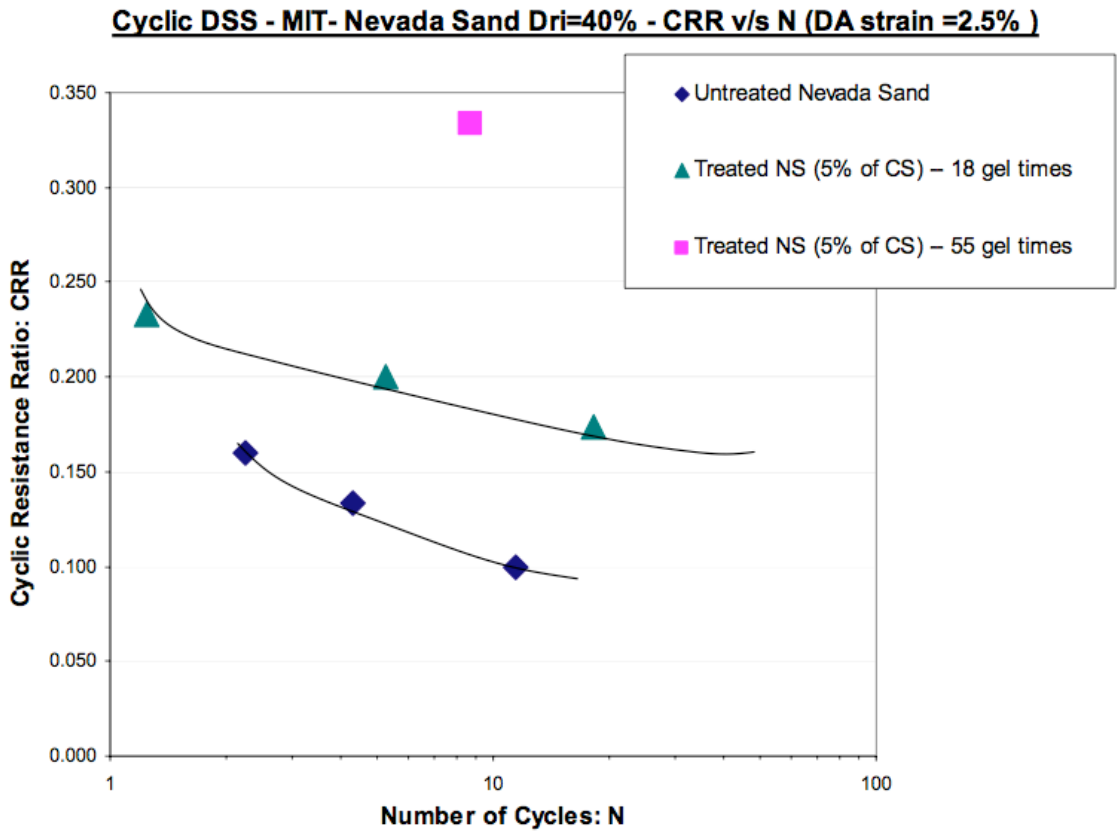

Figure 2.26 Cyclic resistance ratio of sand treated with 5% weight colloidal silica gel (from Corral and Whittle 2007)

In concentrations as low as 5% by weight, colloidal silica significantly improves the deformation resistance of loose sands to cyclic loading (Gallagher 2000; Gallagher and Mitchell 2002). At comparable cyclic stress ratios (CSR), 40% relative density Toyoura sand underwent large stains quickly followed by liquefaction, whereas sand treated with 4% CS does not reach 1% double amplitude strain after 100 cycles; however, at larger CSR the treated samples (untreated samples were not tested at the higher CSR) experienced large strain in early stages of loading but liquefaction did not occur (Kodaka et al. 2005). Treated sand subjected to cyclic loading followed by monotonic shearing indicates that the stiffness of the improved sand after cyclic loading is better than untreated sand as shown in Figure 2.27, indicating the cyclic loading does not destroy already formed bonds (Towhata 2008). The level of strain reached during cyclic loading

decreased as curing time of the samples increased, again indicating the effect of aging on treated sands (Gallagher and Mitchell 2002).

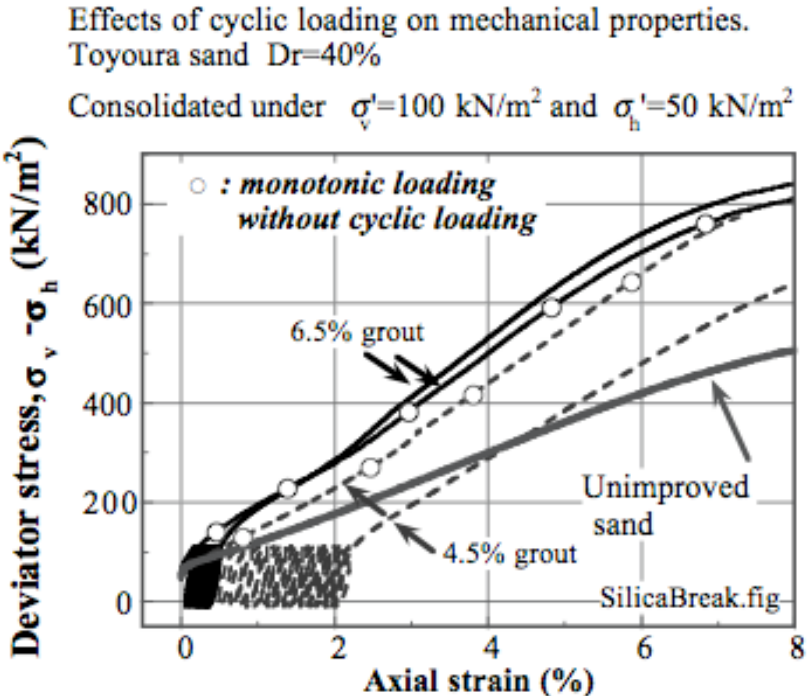

Figure 2.27 Sand treated with colloidal silica gel to cyclic loading followed by monotonic loading compared to unimproved sand (from Towhata 2008)

The use of colloidal silica grouting versus soil densification as a treatment was investigated and showed that 4.5% colloidal silica was equivalent to approximately 80% relative density (Towhata 2008) as shown in Figure 2.28.

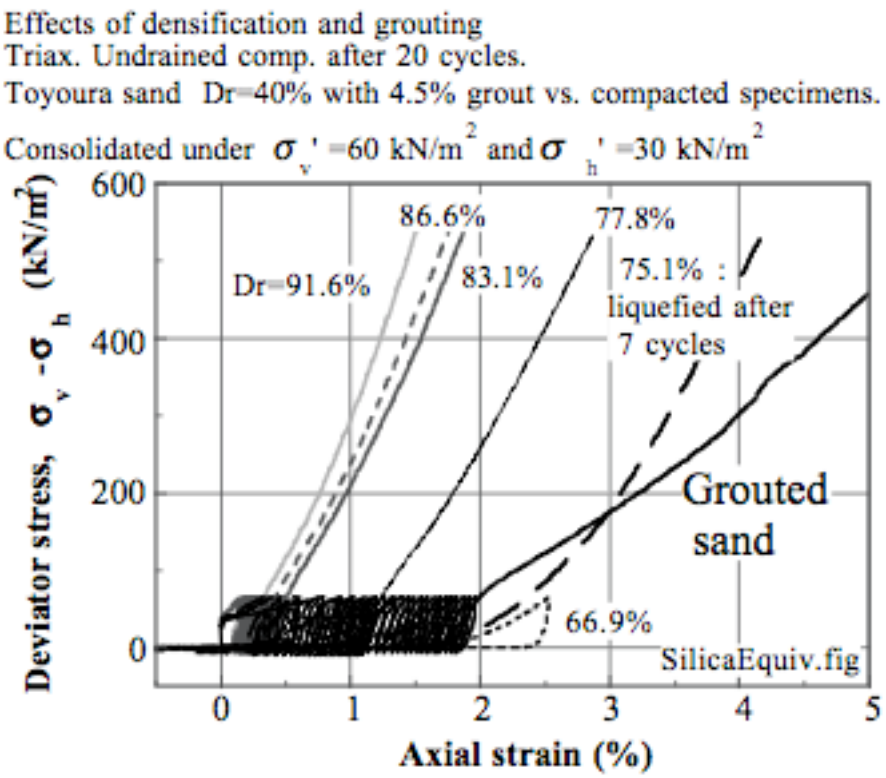

Figure 2.28 Comparing densification of sand to sand treated with 4.5% weight colloidal silica gel (from Towhata 2008)

2.5.3. Settlement and Lateral Displacements

Research on 40% relative density Nevada No 120 sand treated with 6% weight colloidal silica (T_{gel} = 56 hr, tested at 4*T_{gel}), subjected to two shaking events of sinusoidal input with duration of 20 cycles at 2 Hz with an uniform peak amplitude of 0.2g and 0.25g (prototype), in a centrifuge showed that the treated soil did not liquefy, and experienced 0.5% and 1% lateral shear strain, and settlement of 0.3% and 0.1% strain at the model center, respectively for each shake. These treated sand settlements are less than similar untreated sand tests which experienced 3% to 6% strain, however lateral strains were not compared (Gallagher et al. 2006; Gallagher et al. 2002).

A centrifuge test investigating a 2-by-2 end bearing pile group and pile cap with 40% relative density saturated Nevada sand between slightly cemented sand layers was performed (Abdoun et al. 2005; Pamuk et al. 2007). Both the treated, using 6% weight

colloidal silica and untreated model experienced monotonically increasing lateral displacements and pile bending moments through the completion of shaking. However, the treated model did not liquefy, experienced reduced free field and foundation displacements and drastically decreased the pile bending moments. The reduction in free-field displacement is shown in Figure 2.29, where the lateral displacement versus soil depth at different times during lateral spreading for the untreated (Model 1) and treated (Model 2) models is compared. A reduction from 70 cm prototype surface lateral displacement compared to the treated 5 cm prototype surface lateral displacement is a difference of 92%; the reduction in lateral spreading due to treatment with colloidal silica resulted in a 90% reduction in lateral-spreading-induced axial compressive and tensile forces along the pile (Pamuk et al. 2007). The pile bending moments for the untreated and treated models are shown in Figure 2.30, where the upslope and downslope piles of the treated model shows a 90% reduction in bending moments along the pile. It was found that the untreated model passively failed around the pile cap whereas the treated model did not fail (Abdoun et al. 2005).

2.5.3.1.Field Testing of Colloidal Silica Gel Treatment

Gallagher et al. (2007) performed field testing using 7% weight colloidal silica by injection into a 2-m thick target area of sand to silty sand with an estimated relative density of 40 to 45% using 8 injection wells spaced equally with a central extraction well. Blast-induced liquefaction was used to demonstrate the increased deformation resistance and resulting reduction in settlement by treating liquefiable soil with colloidal silica gel. The study found that the excess pore pressure ratio of the treated area still reached 1.0, however the treatment area experienced 0.3 m of settlement in comparison to the untreated 0.5 m. The settlement that occurred on the treated site is attributed to having only partial treatment of the liquefiable layer and the untreated portion is responsible for

the measured settlement. Cracking was observed at the treated site, indicating differential settlement between more and less effective zones of treatment.

CPT testing was performed 27, 131 and 216 days after the blast-induced liquefaction to identify the tip resistance and shear wave velocity of the treated site. Unfortunately, the soundings comparing the treated and untreated site were inconclusive and did not show enough difference to allow CPT testing to be used to detect treatment areas.

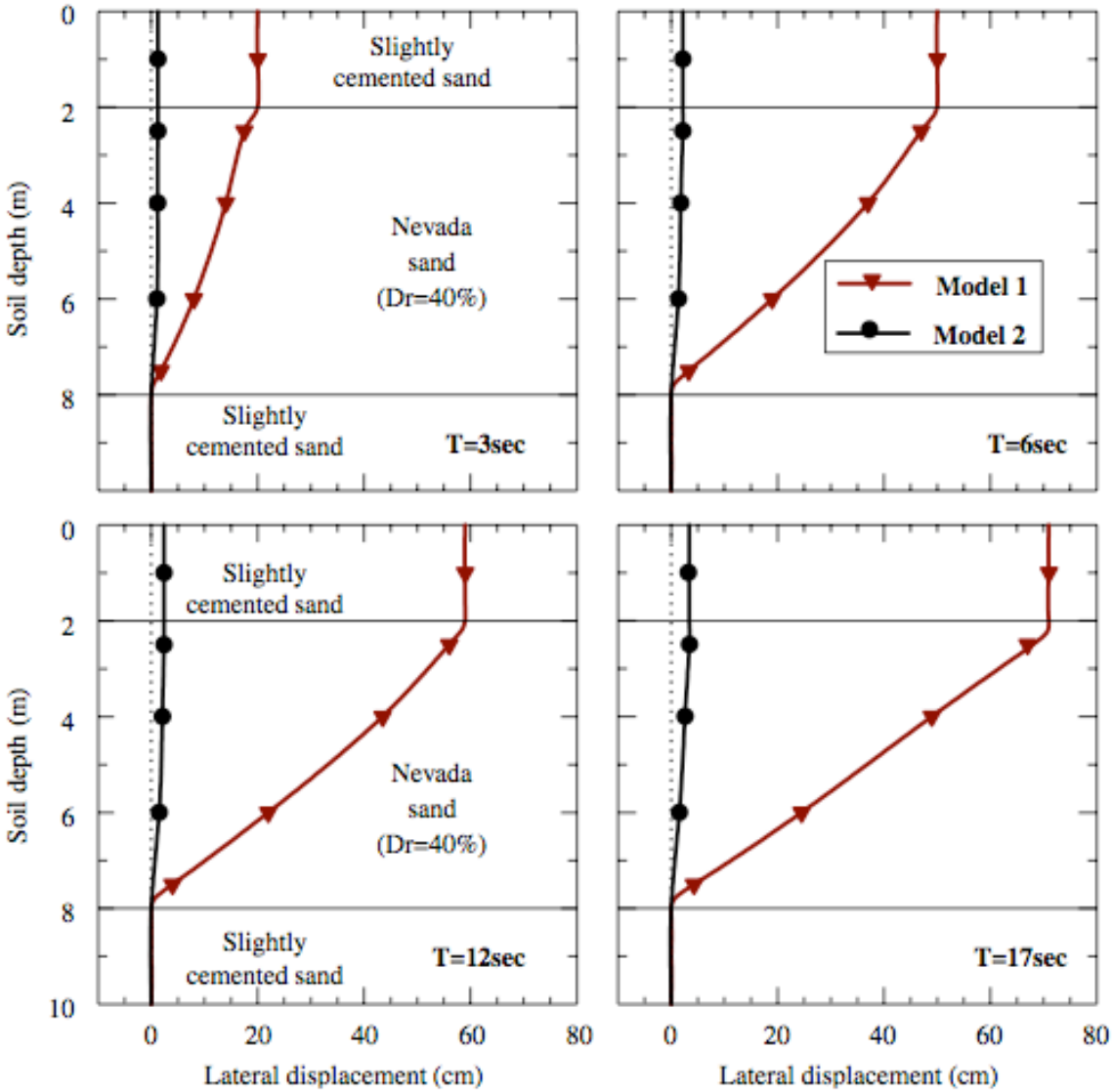

Figure 2.29 Comparing lateral displacements with soil depth of untreated (Model 1) versus treatement (Model 2) with 6% weight colloidal silica gel at different time intervals during lateral spreading (from Pamuk et al. 2007)

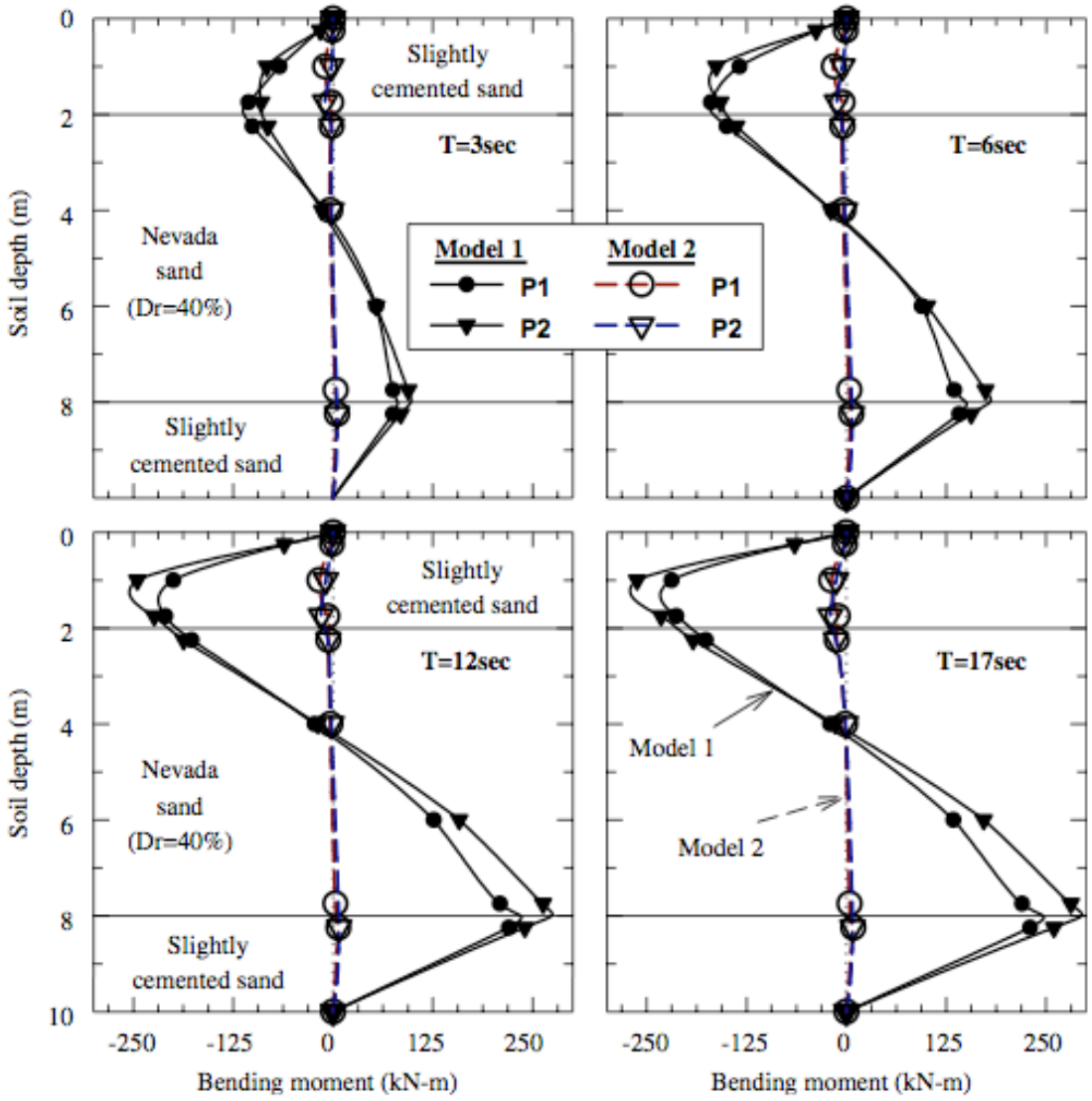

Figure 2.30 Comparing pile bending moments with soil depth of untreated (Model 1) versus treatement (Model 2) with 6% weight colloidal silica gel at different time intervals during shaking (from Pamuk et al. 2007)

2.5.4. Dynamic Properties

The shear modulus and damping ratio of sand treated with colloidal silica gel has not been investigated. However, research has been performed on sand treated with other types of grout, and the following section focuses on sodium-silicate grouts. Work done by Delfosse-Ribay et al. (2004) on Fountainebleau sand treated with three types of grout show an increase in shear modulus with an increase in confining stress; however, the

effect is less significant for sodium silicate grouts than micro-fine cement or mineral grouts. At small strains, treatment with any grout increases the shear modulus over the untreated sand, with the sodium silicate grout shear modulus values lying between the untreated sand and other grouted samples and shows an increase of 350% over untreated sand; however, at large strains, the behavior of treated sands is similar to untreated and it is speculated the cause is due to bonds between the grout and sand particles being altered. The linear threshold strain of the untreated sand is the largest, followed closely by the silicate grout as shown by the normalized shear modulus versus cyclic shear strain plot in Figure 2.31. The damping ratio increases with increasing shear strain and confining stress has little effect on both the treated and untreated samples. The damping ratio of the silicate grout is similar to untreated sand in the low strain region, but deviates once into the larger strains where sand is higher than the grouts, though no reason was given, as shown in Figure 2.32.

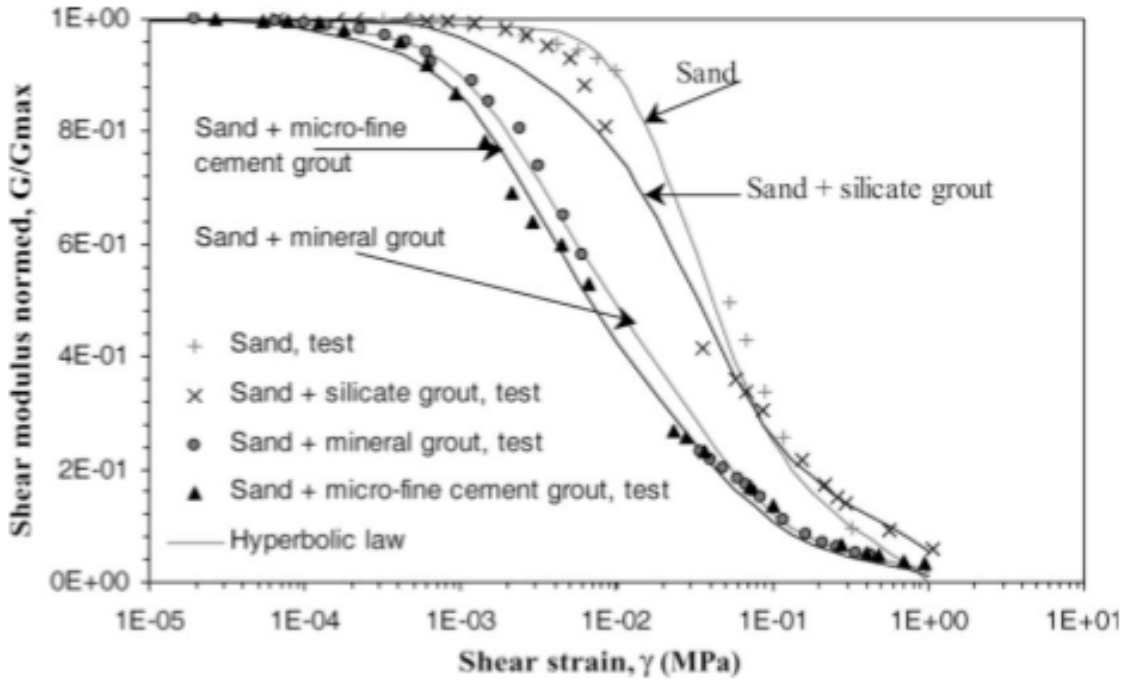

Figure 2.31 The normalized shear modulus of untreated and grouted sand (from Delfosse-Ribay et al. 2004)

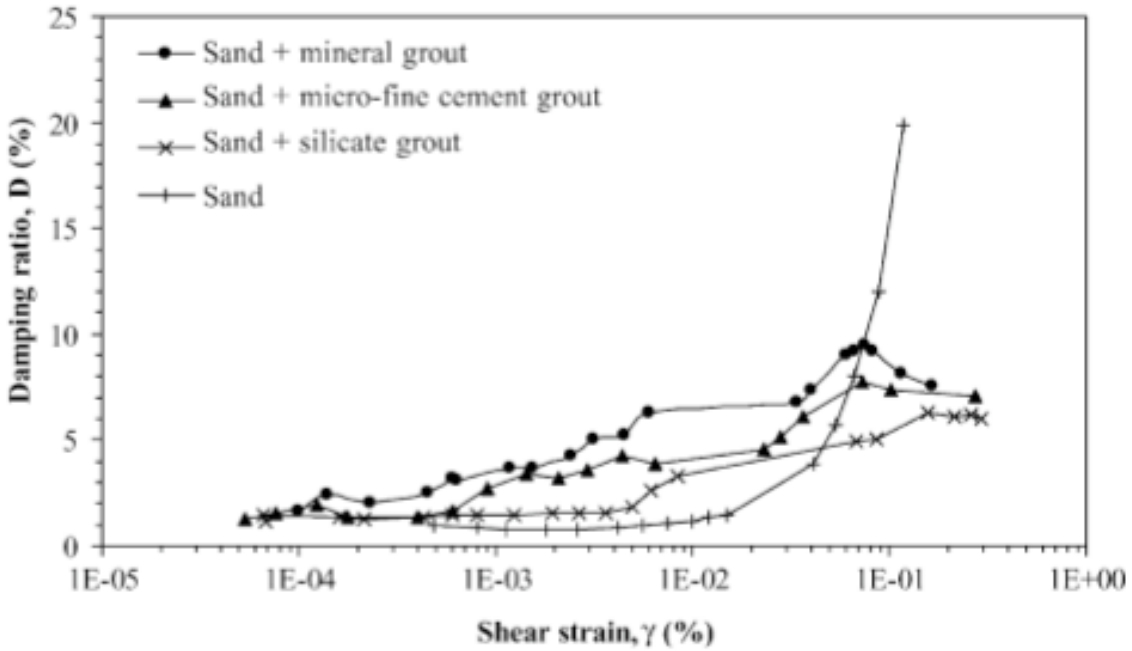

Figure 2.32 The damping ratio versus cyclic shear strain of untreated and grouted sand (from Delfosse-Ribay et al. 2004)

Similar work has been performed by Vipulanandan and Ata (2000) to investigate the change in initial tangent Young's modulus, or E_{max}, with time of silicate-grouted Ottawa 20-30 sand as shown in Figure 2.33. Vipulanandan and Ata (2000) measured both the "static" modulus using cyclic triaxial tests with a loading frequency of 1.0 Hz and the "dynamic" modulus using impact-echo tests. For the latter, the resonant frequency was several kHz. Both tests indicate a rapid increase in Young's modulus initially. The dynamic modulus continues to increase through the entire duration (750 days) of the measurements; the static modulus appears to reach a constant value after approximately 200 days. The effect of aging demonstrates a decrease in the damping ratio of the grouted sand, with an ultimate level reached around 100 days of aging as shown in Figure 2.34. Maher et al. (1994) also investigated the dynamic properties of Ottawa 20-30 sand treated with sodium silicate grout using cyclic triaxial tests and found that the small-strain shear modulus increases and the intermediate-strain range damping ratio decreases with increasing sodium silicate concentration as shown in Figure 2.35. An investigation of the effect of curing time on the dynamic properties was also performed and found no

significant change in small-strain shear modulus and intermediate-strain damping ratio between one and six weeks of curing as shown in Figure 2.36.

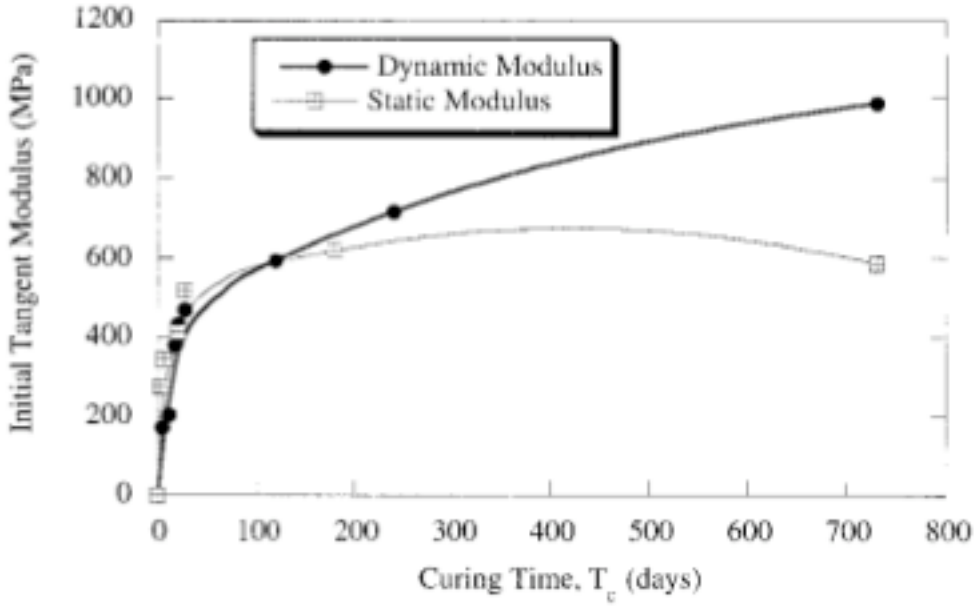

Figure 2.33 The dynamic shear modulus with time of sodium-silicate grouted Ottawa 20-30 sand (from Vipulanandan and Ata 2000)

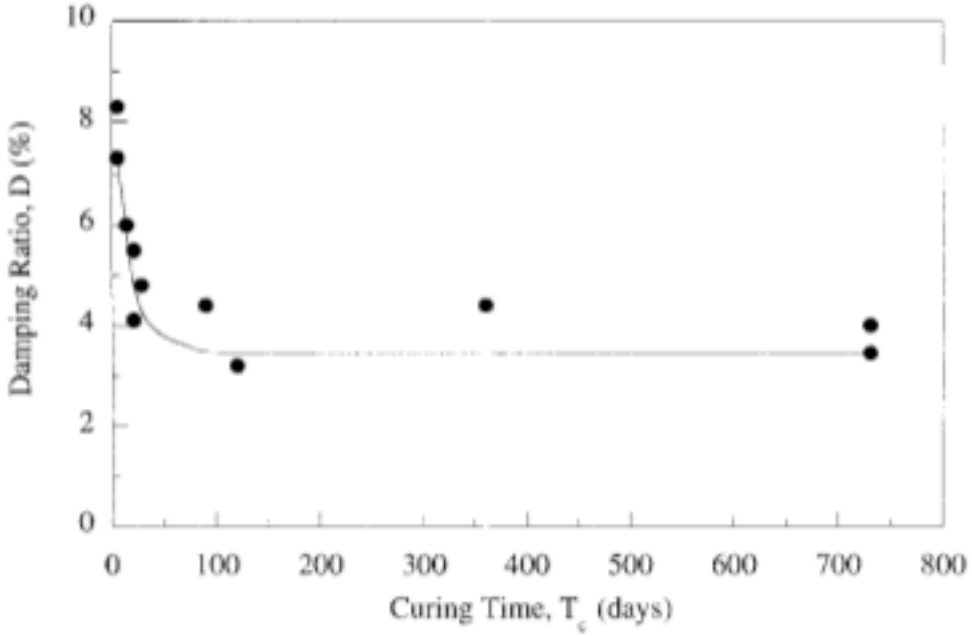

Figure 2.34 The damping ratio with time of sodium-silicate grouted Ottawa 20-30 sand (from Vipulanandan and Ata 2000)

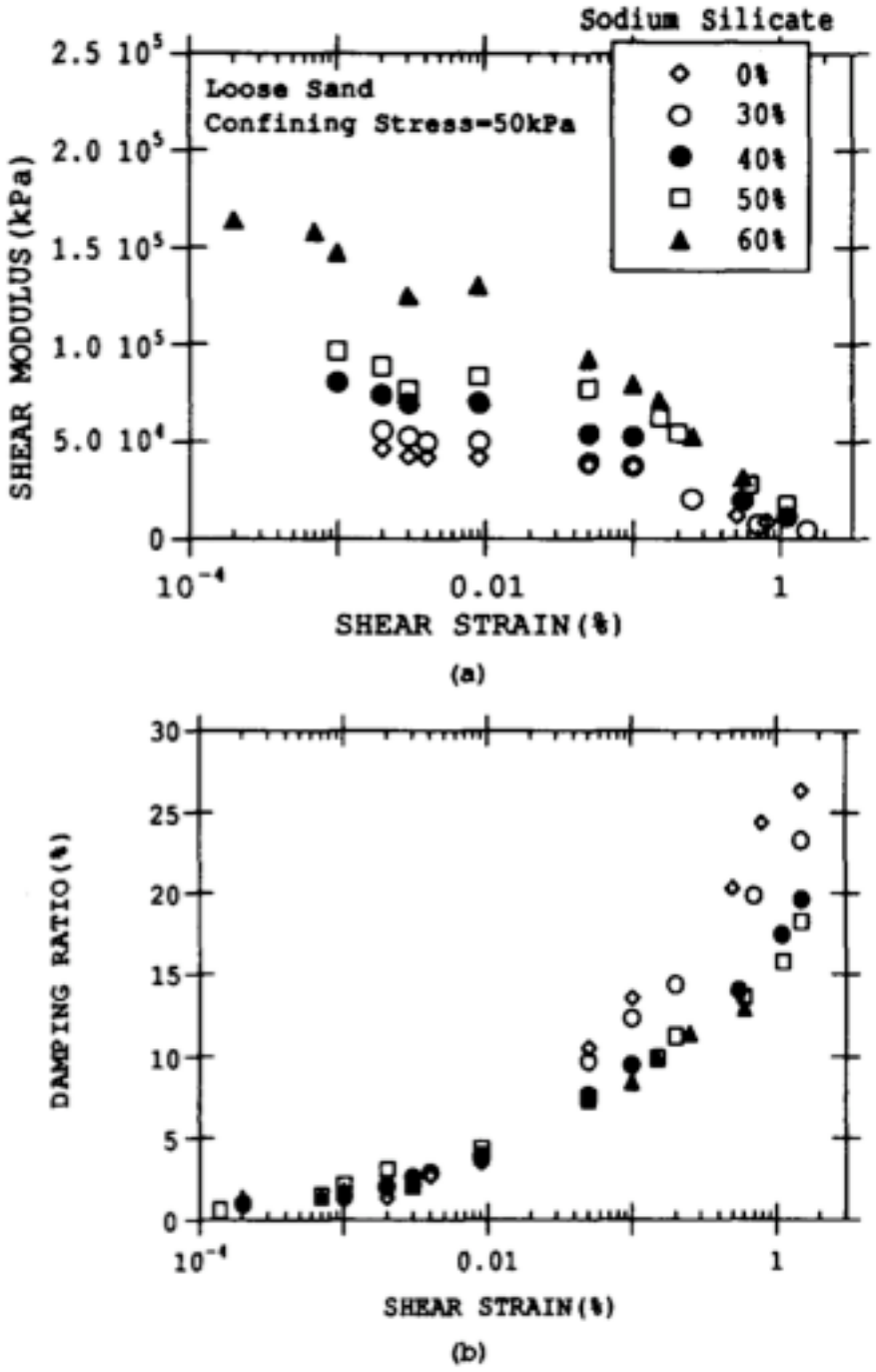

Figure 2.35 The shear modulus and damping ratio versus shear strain of sodium-silicate grouted Ottawa 20-30 sand (from Maher et al. 1994)

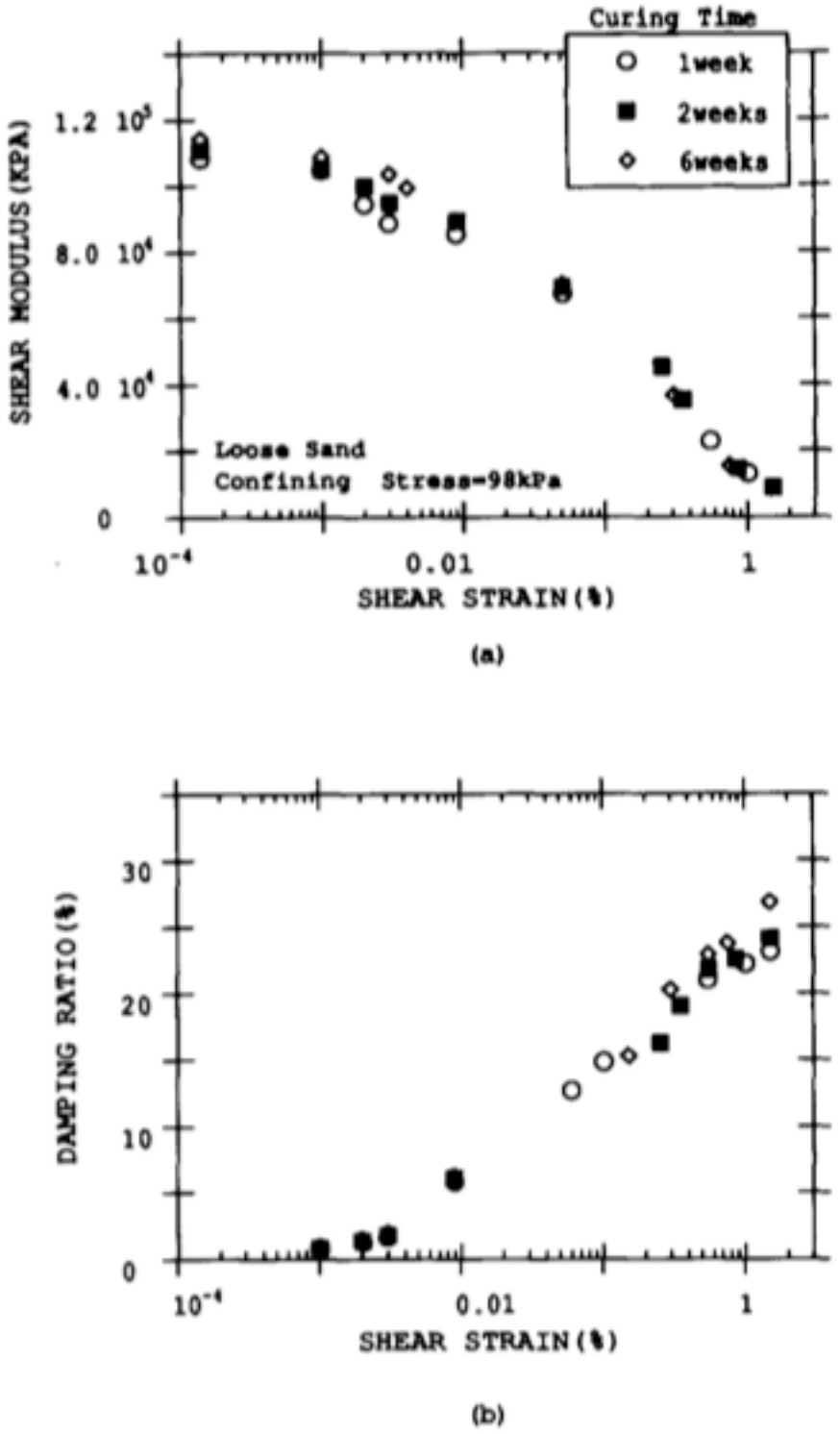

Figure 2.36 The shear modulus and damping ratio versus shear strain at different curing times of sodium-silicate grouted Ottawa 20-30 sand (from Maher et al. 1994)

2.6. Summary

Colloidal silica gel has been identified as a possible candidate for passive soil stabilization for the mitigation of liquefaction and resulting liquefaction-induced damage. A background of colloidal silica gel properties was presented and the experimental research of colloidal silica gel alone and sand treated with colloidal silica gel was reviewed. It was determined the unconfined compressive strength of sand treated with colloidal silica gel increases with increasing silica concentration. Aging of colloidal silica gel results in continued siloxane bonding and has been shown to have an increasing effect on the Young's and shear modulus of gel alone. Aging also has been identified to have an effect on treated sand, resulting in an increase of the unconfined compressive strength and the liquefaction resistance. Centrifuge tests performed on liquefiable soils treated with colloidal silica gel demonstrated treatment successfully reduced the soil lateral displacements and settlement and the pile bending moments and axial forces were reduced by approximately 90% in comparison to the untreated model. Unfortunately, no work has been done to identify the effect of treatment with colloidal silica gel on the dynamic properties of sand; however, sand treated with sodium silicate grout has shown an increase in shear modulus over untreated sand and aging increases the shear modulus with time.

3. DYNAMIC PROPERTIES OF SAND TREATED WITH COLLOIDAL SILICA GEL: PERMEATION AND INITIAL GELATION

3.1. Introduction

Passive soil improvement for liquefaction mitigation of developed sites involves treatment of liquefiable soils with a stabilizing material via permeation grouting. Colloidal silica gel is an inert, non-toxic material with low initial viscosities and good long-term stability and has been identified as a good candidate for use as a stabilizing material in loose sands (Gallagher 2000; Persoff et al 1999). Additional studies have demonstrated that sands treated with colloidal silica gel have greater compressive strength, greater resistance to liquefaction and smaller vertical and lateral deformations than the corresponding untreated soil (Abdoun et al. 2005; Corral and Whittle 2007; Gallagher and Lin 2005; Gallagher and Mitchell 2002; Gallagher et al. 2002; Gallagher et al. 2006; Gallagher et al. 2007; Kodaka et al. 2005; Towhata 2008; Pamuk et al. 2007; Conlee 2010).

While colloidal silica gel has been shown to improve the response of treated soils at large strains, no studies to date have examined the effect of treatment with colloidal silica gel on the small-to-intermediate-strain dynamic properties (i.e., shear modulus and material damping ratio). These properties strongly influence ground motion amplification and other site response phenomena. To evaluate the effect of permeation and initial gelation of colloidal silica gel in loose sands on the shear modulus and damping ratio, a series of resonant column tests were performed on specimens treated with varying weight percentage solutions of colloidal silica gel and the results were compared to untreated specimens.

3.2. Resonant Column Test

The resonant column test is used to determine the small-to-intermediate-strain shear modulus and material damping ratio of specimens (D4015 2001; Woods 1994). The test is based on one-dimensional wave propagation theory and is used to measure the specimen's first-mode resonant frequency under torsional excitation, which depends on the dynamic properties and the geometry of the specimen.

3.2.1. Derivation of the Wave Equation in Torsion

The method of analysis of the resonant column test is derived from the theory of elasticity (Isenhower 1979). The cylindrical soil specimen is excited in the first mode of torsional vibration and is idealized in Figure 3.1. A specimen is fixed to the base pedestal and top cap and a drive plate is attached to the top cap as shown in Figure 3.2. The top cap and drive plate are free to move during the application of cyclic torque. Harmonic torsional excitation is applied to the top of the specimen over a range of frequencies and the variation of angular acceleration amplitude at the top of the specimen is obtained as shown in Figure 3.3. The resonant frequency and maximum amplitude of vibration are determined from the response curve. These values are used in conjunction with equipment and specimen characteristics to determine the shear wave velocity, shear modulus and shearing-strain amplitude (Hwang 1997; Ni 1987).

3.2.2. Shear Modulus

The governing equation of motion is derived from the one-dimensional wave propagation equation that is based on the theory of elasticity. For the torsional resonant column test with fixed-free boundary conditions, the equation is (Hwang 1997):

$$\frac{I}{I_o} = \frac{\omega_n \times L}{V_s} \times \tan\left(\frac{\omega_n \times L}{V_s}\right) \qquad 3.1$$

where:

I = mass polar moment of inertia of the specimen

I_o = mass polar moment of inertia of the top cap and drive plate

L = length of the specimen

V_s = shear wave velocity of the specimen

ω_n = undamped natural angular frequency of the system (= $2\pi f_n$).

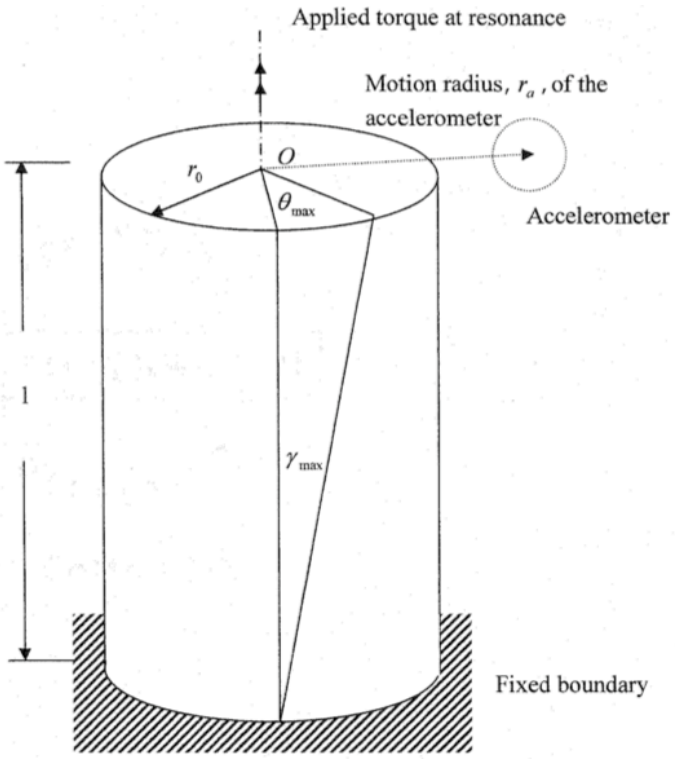

Figure 3.1 Idealized fixed-free resonant column test (from Meng 2003)

The values of I, I_o and L are easily determined from the calibration of the drive plate described subsequently and the weight and dimensions of the specimen. Once the first-mode resonant frequency, f_r, is determined, the shear wave velocity can be calculated using Equation 3.1 by assuming f_r and f_n are equal. Because the resonant frequency is measured, the shear wave velocity of the specimen is calculated using f_r. The relationship between f_r and f_n is:

$$f_r = f_n \times \sqrt{1 - 2D^2} \qquad 3.2$$

where D is the material damping ratio of the specimen. For the small values of D typical of many soils at small-to-intermediate strains, the difference between the resonant and natural frequencies is negligible and the error is small (Hwang 1997). Once the shear wave velocity is determined, the shear modulus is calculated using:

$$G = \rho \times V_s^{\,2} \qquad 3.3$$

where ρ is the total mass density of the soil.

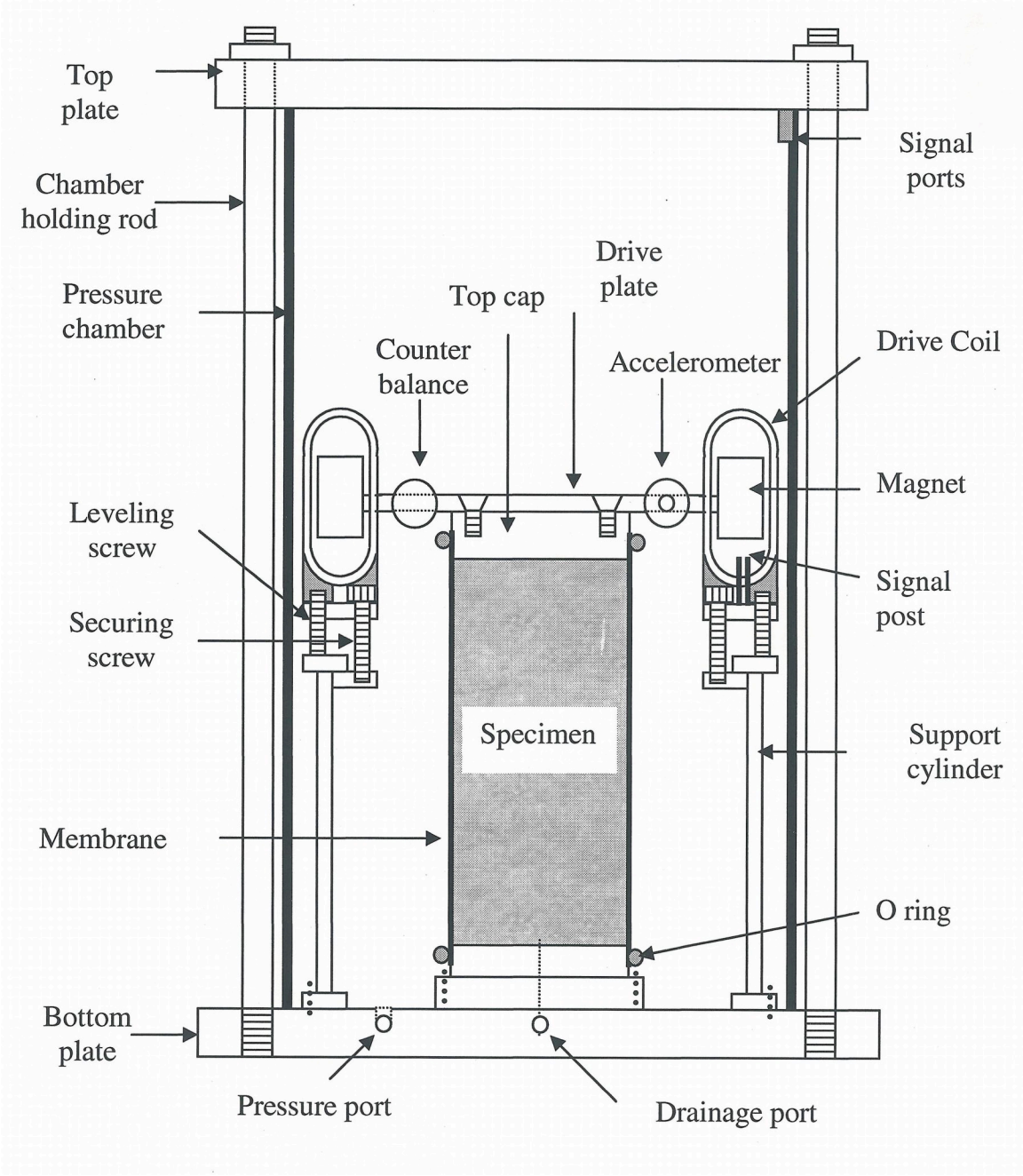

Figure 3.2 Schematic of Stokoe-type resonant column device (from Meng 2003)

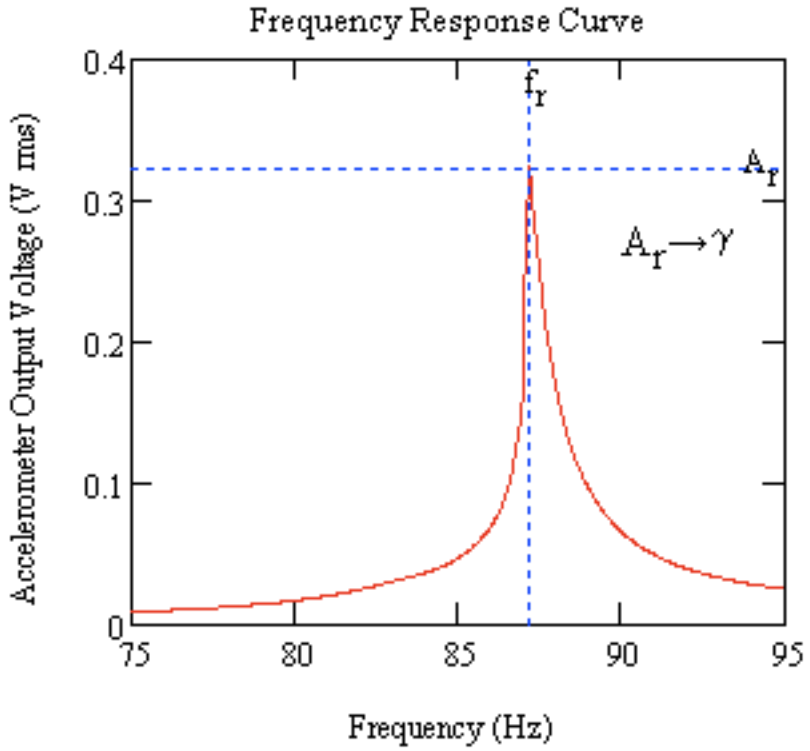

Figure 3.3 Typical frequency response curve from resonant column

3.2.3. Damping Ratio

The calculation of the material damping ratio is based on the vibration of a single-degree of freedom system with equivalent viscoelastic damping (Hwang 1997; Isenhower 1979). The equation of motion is:

$$m\ddot{x} + c\dot{x} + kx = 0 \qquad 3.4$$

where:

m = mass

c = viscous damping coefficient

k = elastic spring constant

$\ddot{x}$, $\dot{x}$ and x are the acceleration, velocity and displacement, respectively.

Using the relationships:

$$D = \frac{c}{c_c} \tag{3.5}$$

$$c_c = 2\sqrt{k \cdot m} \tag{3.6}$$

$$\omega_n{}^2 = \frac{k}{m} \tag{3.7}$$

where:

D = viscous damping ratio

c_c = critical damping coefficient

ω_n = undamped natural angular frequency

Equation 3.4 can be written as:

$$\ddot{x} + 2D\omega_n \dot{x} + \omega_n{}^2 x = 0 \tag{3.8}$$

The equation has three general solutions corresponding to overdamped, critically damped and underdamped systems. Soil specimens are usually underdamped and the corresponding general solution is:

$$x(t) = e^{-\omega_n D t}\left[A \cdot \cos(\omega_n \sqrt{1 - D^2}\, t) + B \cdot \sin(\omega_n \sqrt{1 - D^2}\, t)\right] \tag{3.9}$$

where A and B are constants determined by the boundary conditions.

The material damping ratio in resonant column tests is determined using either the half-power bandwidth method in the forced-vibration mode or the logarithmic decrement method in the free vibration decay mode (Hwang 1997; Ni 1987).

3.2.3.1.Free-Vibration Decay Method

A free-vibration decay curve is generated by exciting the soil specimen at first-mode resonance until steady-state vibration is reached. The driving current to the coils is stopped and the free-vibration decay curve shown in Figure 3.4 is used to calculate the damping ratio as.

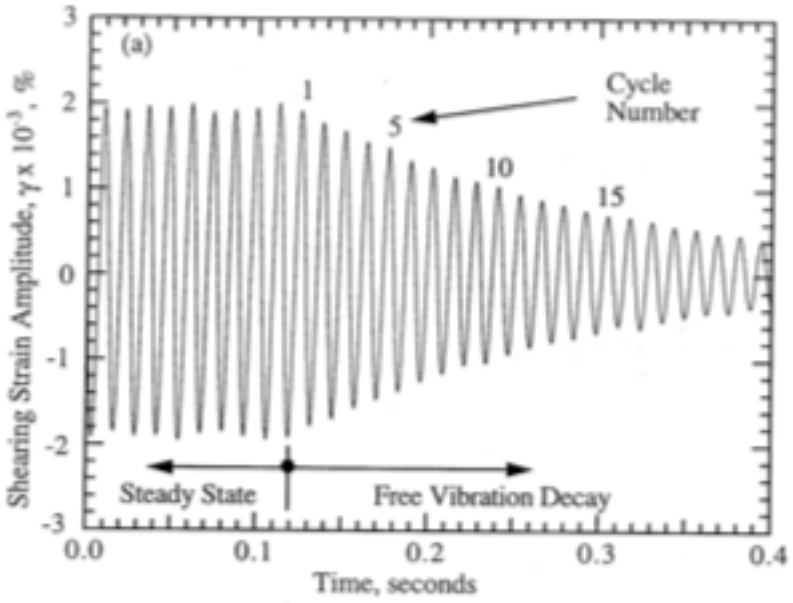

Figure 3.4 Typical free-vibration decay curve (from Hwang 1997)

As a consequence of the first term in Equation 3.9, the ratio of the natural logarithm of the ratio of the amplitudes of two successive cycles is constant and is called the logarithmic decrement, δ (Hwang 1997; Isenhower 1979):

$$\delta = \ln \frac{x_n}{x_{n+1}} \tag{3.10}$$

where x_n and x_{n+1} are the amplitudes of two successive peaks. Two successive peak amplitudes at time t_0 and $t_0+2\pi/\omega_d$ can be obtained and expressed as follows:

$$\delta = \frac{c}{m \cdot \omega_d} \tag{3.11}$$

Dividing both sides by c_c and rearranging results in:

$$\delta = \frac{2\pi D}{\sqrt{1 - D^2}} \tag{3.12}$$

Thus, the material damping ratio can be determined from measured values of the logarithmic decrement:

$$D = \sqrt{\frac{\delta^2}{4\pi^2 + \delta^2}} \tag{3.13}$$

3.2.3.2.Half-Power Bandwidth Method

The half-power bandwidth method assumes a single-degree-of-freedom system and is based on the measurement of the width of the frequency response curve near the resonant frequency as depicted in Figure 3.5. Find the frequencies, ω_1 and ω_2, at which the amplitude is equal to $\frac{1}{\sqrt{2}}$ times the peak amplitude at the resonant frequency, ω_r. Assuming material damping is small and neglecting the second-order term, the material damping ratio is:

$$D \cong \left(\frac{\omega_1 - \omega_2}{2 \cdot \omega_n} \right) \qquad 3.14$$

where, as noted previously, the resonant frequency is used instead of the natural frequency with negligible error. The half-power bandwidth method is generally more preferable than the free-vibration decay method for small-strain damping measurements (Hwang 1997).

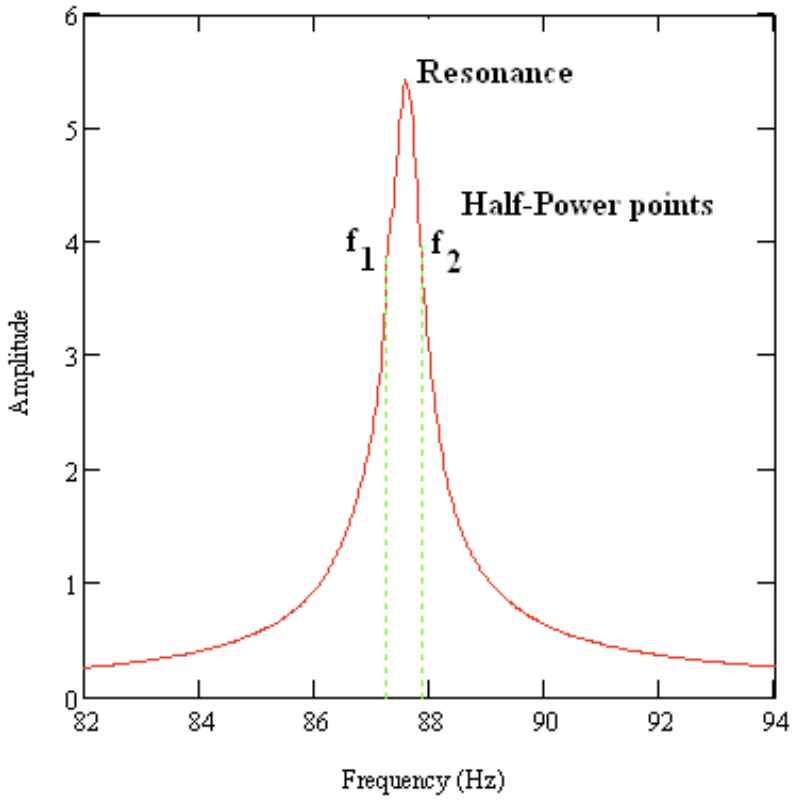

Figure 3.5 Material damping ratio measurement using the half-power bandwidth method

3.2.4. Shearing Strain

At resonance, the specimen vibrates in the first torsional mode and the deformation along the length of the specimen is linear if the ratio of the mass polar moment of inertia of the specimen and the drive system is small (Isenhower 1979). However, shearing strain varies radially from zero at the center of the solid specimen to a maximum at the outer radius of the specimen and can be expressed as a linear function of the distance from the longitudinal axis. An equivalent radius, r_{eq}, can be used to calculate a representative value of the shearing strain in the specimen (Hwang 1997):

$$\gamma_{eq} = C \cdot \gamma_{\max} \qquad 3.15$$

where:

γ_{eq} = equivalent shear strain of the specimen

$$C = \frac{r_{eq}}{r_o} = 0.79 \text{ for a solid specimen}$$

r_{eq} = equivalent radius of specimen

r_o = radius of specimen

$$\gamma_{max} = \frac{r_o \cdot \theta_{max}}{L}$$

L = height of specimen

θ_{max} = maximum rotation at the top of the specimen.

3.2.5. Equipment

The testing was performed using a fixed-free resonant column designed by Dr. Kenneth H. Stokoe, II of the University of Texas at Austin and constructed by Structural Behavior Engineering Laboratories (SBEL). The device is comprised of a confining chamber and a mechanical drive system. A picture of the device is shown in Figure 3.6. The drive system shown in Figure 3.7 consists of eight copper coils with four magnets centered in these coils. The magnets are attached to the specimen top cap by a longitudinal loading plate with four arms, known as a magnet spider. Torsional excitation is applied using sinusoidal voltage applied to the drive mechanism, inducing a magnetic field in the coils which results in reversible oscillation of the magnets that is transferred to the top cap of the specimen through the magnet spider (Ni 1987; Valdes 1999). An accelerometer is mounted on one arm of the spider to measure the angular displacement at the top of the specimen. A counter-weight is located opposite the accelerometer to prevent eccentric loading of the specimen.

Figure 3.6 Resonant column apparatus used during this study (shown with a calibration specimen)

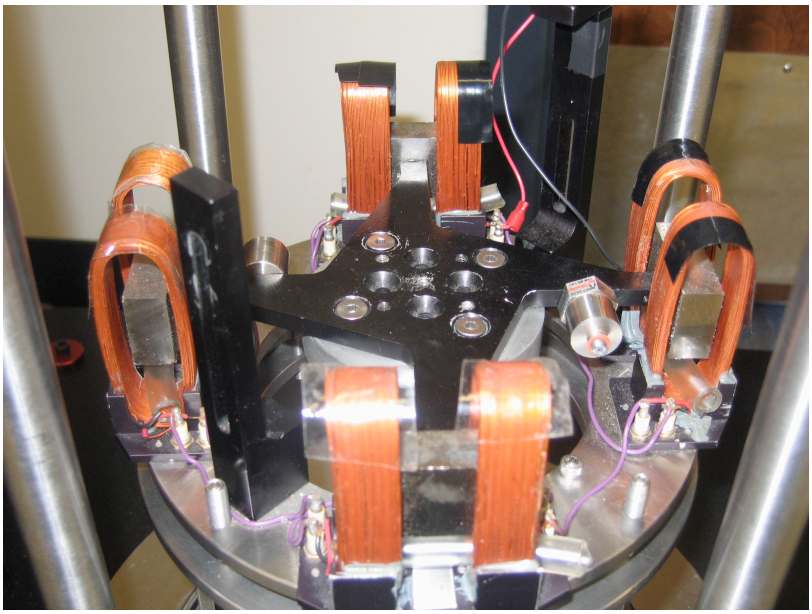

Figure 3.7 Resonant column drive plate

The electronic components utilized in these experiments consisted of a Hewlett-Packard Model 3562A dynamic signal analyzer, a Columbia Research Laboratories Model 3026 accelerometer and Model 4102M charge amplifier, and a Hewlett-Packard Model 9122C data storage system. The dynamic signal analyzer was used to generate the input voltage applied to the coils and to record the output of the accelerometer. The charge amplifier produces an output voltage from the response generated by the accelerometer. A schematic of the experimental set-up is shown in Figure 3.8. Testing was performed on a Minus K Technology isolation table to reduce the adverse effects of ambient vibrations.

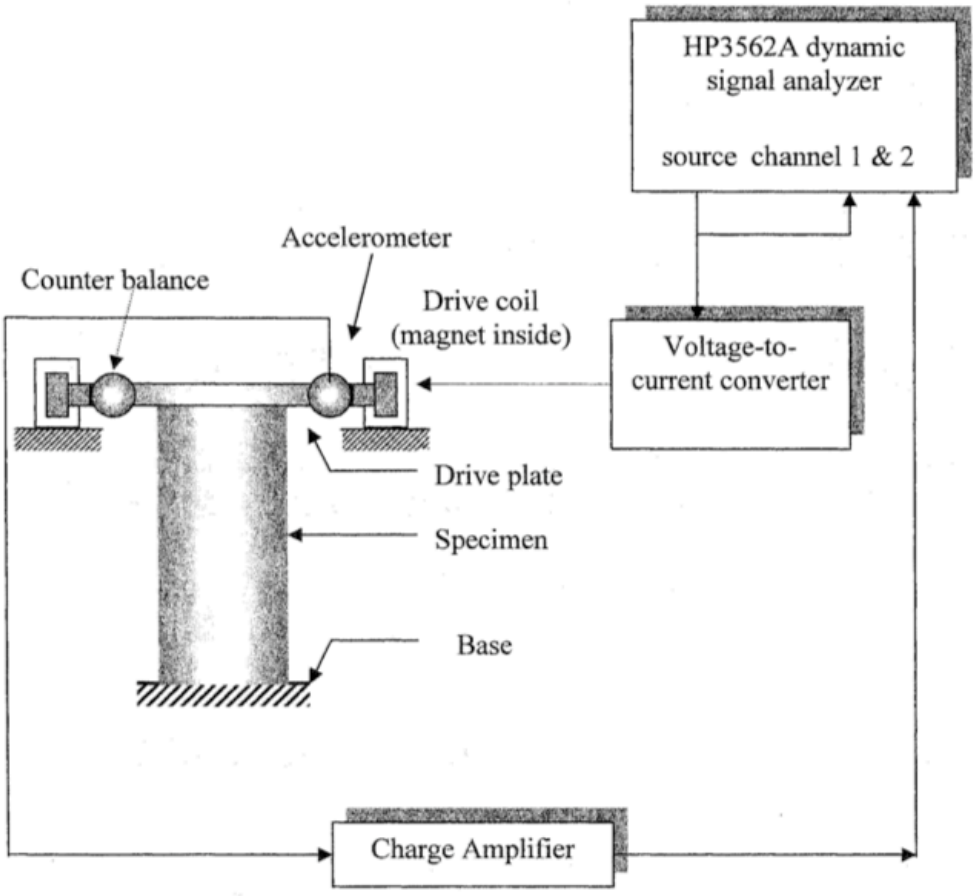

Figure 3.8 Schematic of experimental set-up (after Meng 2003)

Equipment-generated damping in the resonant column test due to the interaction between the magnets and solenoids results in a bias error in the measurement of material damping ratio. Studies have shown that a current-mode source can significantly reduce the amount of equipment-generated damping in comparison to a conventional voltage-mode source. In addition, the current-mode source eliminates the need for post processing. It has been shown that equipment-generated damping can be reduced by more than three orders of magnitude compared with a conventional voltage-mode source (Meng 2003; Meng and Rix 2003). Therefore a current-mode source was utilized via a voltage-to-current converter to perform this research.

3.2.6. Equipment Calibration

The resonant column device requires calibration prior to testing to determine the dynamic soil properties accurately. Calibration is performed to obtain the mass polar moment of inertia of the drive system, which includes the top cap and magnet spider. Because of the irregular shape of the magnet spider, the mass polar moment of inertia is determined by experimental means. The experimental procedure requires the solution of a system of two equations and two unknowns. The unknowns are the mass polar moment of inertia of the magnet spider and the torsional stiffness of the calibration specimen. The two equations of motion are shown below:

$$(I + I_{tcc}) \cdot \omega_1^2 - K = 0 \qquad 3.16$$

$$(I + I_{tcc} + I_{AM}) \cdot \omega_2^2 - K = 0 \qquad 3.17$$

where:

I = mass polar moment of inertia of the spider magnet

I_{tcc} = mass polar moment of inertia of top cylinder of calibration specimen

I_{AM} = mass polar moment of inertia of the added mass

ω_1 = resonant frequency without added mass

ω_2 = resonant frequency with added mass

K = torsional stiffness of calibration specimen.

To obtain K and I directly, the following equations are used:

$$I = \frac{(I_{tcc} + I_{AM}) \cdot \omega_2^2 - I_{tcc} \cdot \omega_1^2}{\omega_1^2 - \omega_2^2} \quad 3.18$$

$$K = \frac{I_{AM} \cdot (\omega_2 \cdot \omega_1)^2}{\omega_1^2 - \omega_2^2} \quad 3.19$$

The mass polar moment of inertia of the top cap, which is easily calculated because of the simple shape of the cap, is then added to the mass polar moment of inertia of the magnet spider to obtain the mass polar moment of inertia of the drive system.

3.2.7. Equipment Modifications

Generally, the desired isotropic confining pressure is applied using pressurized air in the confining chamber; however, for this testing the chamber and specimen top and bottom caps were modified to allow for confinement to be applied using vacuum pressure. This enables the specimen consolidation, permeation and testing to be performed under constant confining pressure to avoid any unload-reload cycle that would occur by using conventional end platens and pressurized air. If air pressurization is used, the resonant column chamber is closed and confining pressure is applied. In order to permeate the specimen under confinement, the chamber would need to be sealed for permeation; however, the chamber must be vented to remove the colloidal silica permeation outlet tube to attach the resonant column drive plate and then re-pressurized to run the test. Due to top cap and drive plate attachment mechanisms, it is not possible to attach the drive plate during specimen permeation or to have the permeation outlet tube hinder the drive plate during testing. Therefore equipment constraints associated with a

traditional resonant column device result in an unload-reload cycle on the specimen, which can be avoided by using vacuum pressure.

To perform specimen permeation, the resonant column cell and end platens were modified so only disposable items were exposed to the colloidal silica solution as shown in Figure 3.9. The top-cap fitting allows plastic tubing to be threaded through to contact the plastic filter. But when the tubing is removed after permeation, the top-cap vent is sealed and vacuum is applied through the bottom platen only.

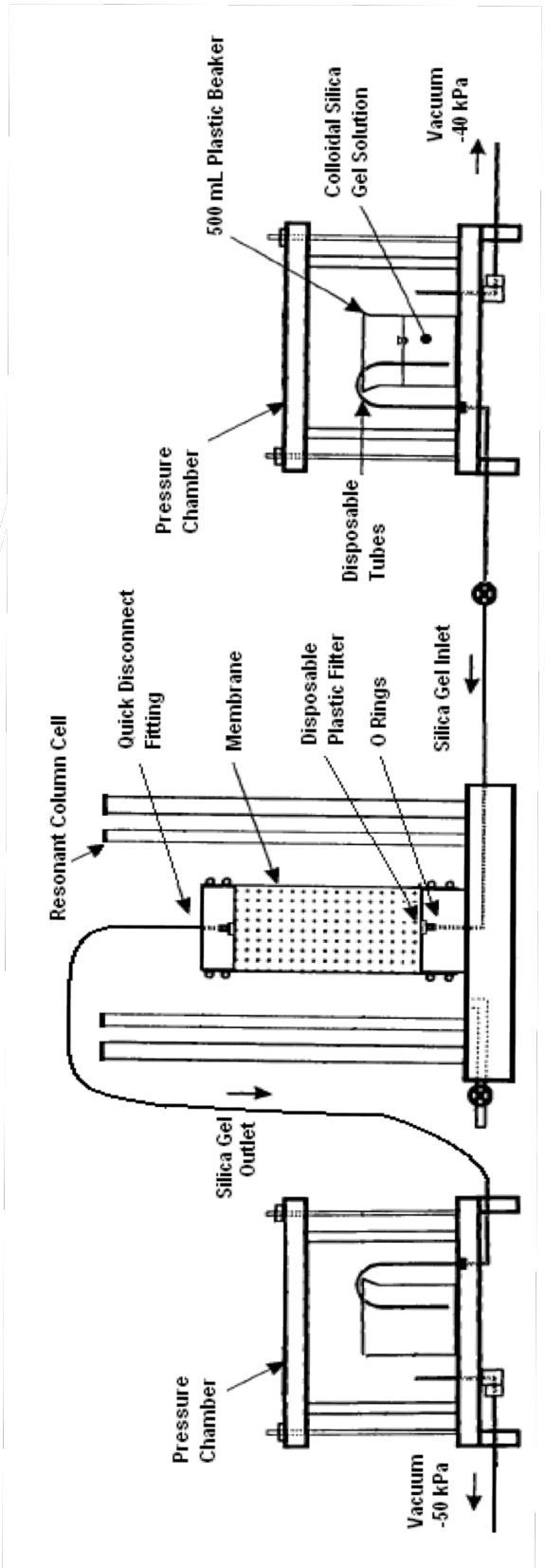

Figure 3.9 Schematic of colloidal silica gel permeation device (after Jang 1997)

3.3. Experimental Procedure

3.3.1. Colloidal Silica Preparation

The colloidal silica gel solution is composed of Ludox SM 30-weight-percent colloidal silica sol, water used to dilute the sol to a desired weight percentage and sodium chloride (NaCl). Gallagher and Mitchell (2002) demonstrated that treatment of loose sand with five-weight percent gel is the minimum value that is effective in increasing liquefaction resistance and reducing deformations. Concentration levels greater than about 10-weight percent become too costly in practice. In this study, five-, seven-, and nine-weight-percent concentrations were evaluated to span this range.

The Ludox SM colloidal silica sol is an aqueous dispersion of 7-nm silica particles at 30-weight-percent; other properties of the sol are shown in Table 2.2. The sodium chloride concentration determines the gel time of the colloidal silica solution; higher salt concentrations reduce the gel time. To prepare the silica solution for permeation, the concentrated silica sol was diluted with the predetermined concentration of salt water. Colloidal silica gel solutions with a gel time of approximately two to three hours were chosen to allow sufficient time for complete specimen permeation during the low-viscosity phase of the gelation process and the ionic strength and gel time for each weight percentage concentration is given in Table 3.1.

Table 3.1 Ionic Strength for Tested Concentrations of Colloidal Silica Gel

Colloidal Silica Concentration (%-weight)	Ionic Concentration (N)	Gel Time (hr)
Five-Weight-Percent	0.4	2
Seven-Weight-Percent	0.35	2.4
Nine-Weight-Percent	0.325	2.7

3.3.2. Soil Specimen Preparation

Tests were performed on specimens of No. 120 Nevada sand with the index properties shown in Table 3.2. Specimens of No. 120 Nevada sand were prepared using air pluviation, which produces specimens that have more uniform local void ratios than other preparation methods (Jang 1997; Park 1999). A schematic of the air-pluviation device is shown in Figure 3.10. To maintain a constant fall height during pluviation, the container of sand was raised at the same rate as the rise in the surface of the sand being deposited in the specimen mold. The fall height was calibrated to obtain the desired relative density, 50%, for the specific sand, Nevada No 120, used in this testing. The specimens have nominal diameter of 7.1 cm and height of 14.2 cm.

Table 3.2 Nevada No 120 Sand Index Properties

Supplier	Gordon Sand Co., Compton, CA
USCS Classification	Uniform, fine sand, SP
D_{50} (mm)	0.15
Coefficient of Uniformity, C_u	1.6
Maximum dry unit weight (kN/m^3)	16.76
Minimum dry unit weight (kN/m^3)	13.98

Following pluviation, the specimen was consolidated under vacuum to an effective confining pressure of 50 kPa. The confining stress was chosen to replicate the in-situ vertical effective stress for a typical liquefiable layer in generalized port soil profile. While under confinement, colloidal silica gel solution was permeated into the specimen under a low differential vacuum pressure of 10 kPa. Permeation was considered complete when two pore volumes of colloidal silica solution were permeated through the specimen. Figure 3.11 shows a photo of a sand specimen permeated with five-weight percent colloidal silica gel that was dyed with red food coloring to demonstrate the uniform treatment obtained using this permeation method. After permeation, the vacuum pressures at the inlet and outlet were equalized to stop the flow and the quick-disconnect fitting on the top platen was released, leaving the vacuum confinement applied via the

bottom platen. The specimen was pluviated, permeated and tested directly on the modified resonant column device to minimize disturbance of the specimen.

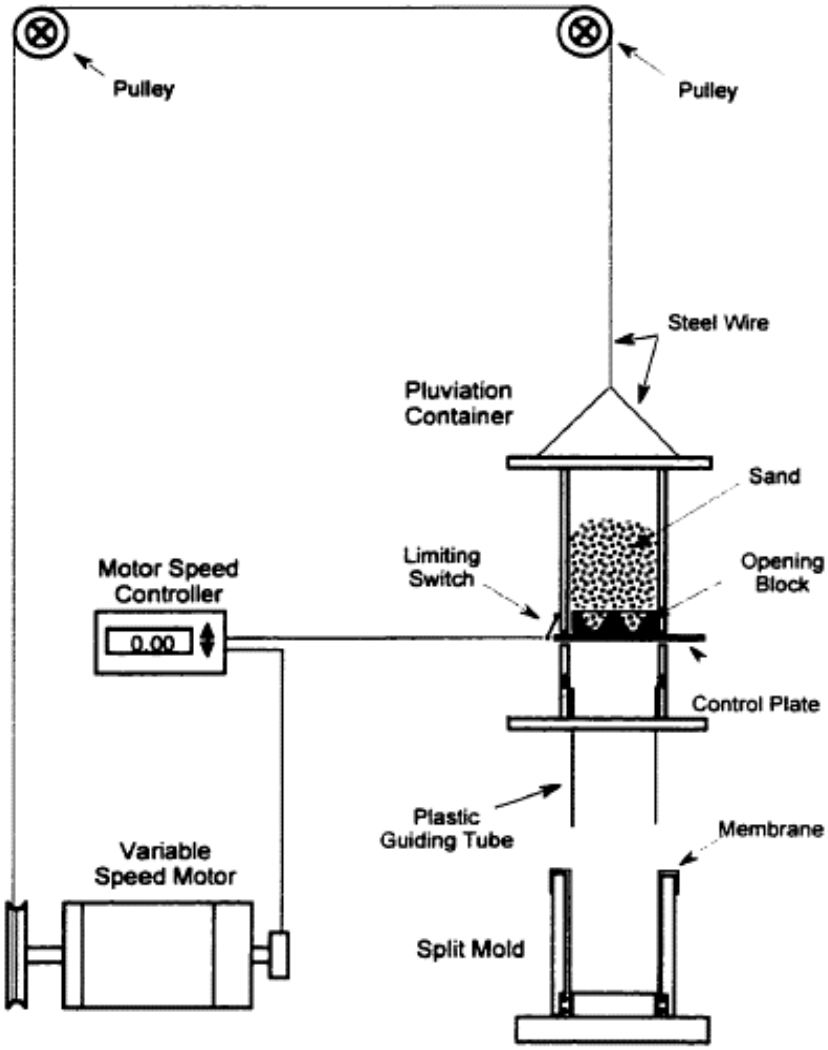

Figure 3.10 Schematic of air pluviation device (after Park 1999)

Figure 3.11 Photo of colloidal silica gel (colored pink) treated sand specimen to demonstrate uniformity of coverage with colloidal silica throughout sand specimen with a disected treated specimen in the background

After permeation, the specimen was left to cure for a period of 10 times the gel time to ensure the specimen was at a resonating gel state before testing and to test each specimen at the same progression of bond formation to make accurate comparisons between the different colloidal silica concentrations (Gallagher 2000).

3.3.3. Resonant Column Tests

Three specimens were tested at each weight percentage to evaluate repeatability of the measurements. Three untreated sand specimens were also tested. The resonant column tests were performed starting at low cyclic shear strain amplitudes and increasing to a maximum strain of approximately 0.03%, depending on the stiffness of the specimen.

According to Alarcon-Guzman et al. (1989) the shear moduli at shear strain amplitudes larger than the previous maximum strain are not affected by cyclic prestraining. The specimens were subjected to a final small-strain test after the intermediate-strain testing was complete to verify that changes in soil structure did not occur during testing.

3.4. Influence of Colloidal Silica Concentrations on Small-Strain Dynamic Properties

Table 3.3 summarizes the relative density and measured values of G_{max} and D_{min} of each untreated and treated specimen. Complete numerical results for each specimen are provided in Appendix A.

Table 3.3 Relative Density of Specimens of Nevada No 120 Sand Treated with Varying Concentrations of Colloidal Silica Gel

Colloidal Silica Concentration (%-weight)	Specimen Number	Relative Density (%)	G_{max} (MPa)	D_{min} (%)
Five-Weight-Percent	CS5_1	47	63.5	0.31
	CS5_2	50	65.9	0.30
	CS5_3	53	66.1	0.27
Seven-Weight-Percent	CS7_1	53	66.3	0.36
	CS7_2	52	66.3	0.36
	CS7_3	61	70.5	0.36
Nine-Weight-Percent	CS9_1	50	64.4	0.45
	CS9_2	54	66.9	0.49
	CS9_3	55	68.0	0.47
Untreated	UN_1	64	62.1	0.30
	UN_2	55	58.0	0.29
	UN_3	54	57.9	0.28

The shear modulus and damping ratio as a function of cyclic shear strain for the specimens treated with five-weight percent colloidal silica gel are shown in Figure 3.12. The trend is similar for each specimen with slight differences between the shear modulus values at each cyclic shear strain and a maximum difference in G_{max} of 4% between the specimens. Part of the observed differences are likely due to the variation in the relative density of each specimen relative to the target value of 50 percent. The damping ratio

values of all three specimens follow the same trend and are close in value up to about 0.01% cyclic shear strain. The maximum difference in material damping ratio between the specimens occurs at the largest cyclic shear strain, where the skewed shape of the frequency response curve caused by non-linear soil behavior can lead to overestimation of the damping ratio.

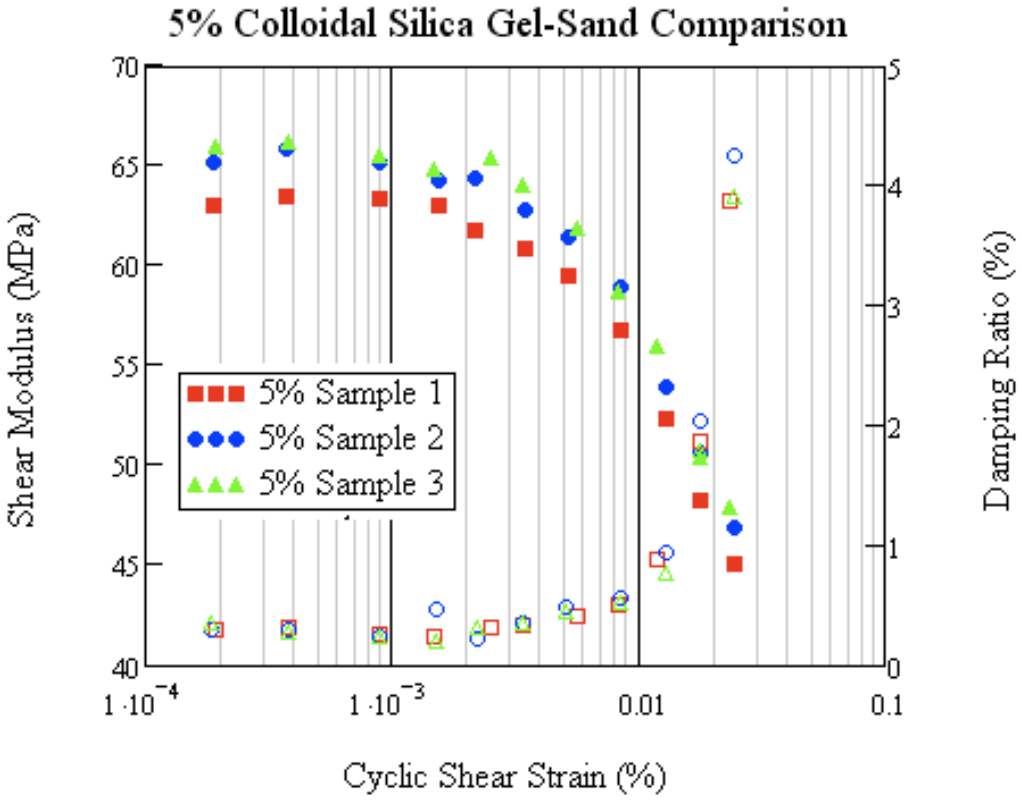

Figure 3.12 Comparison of three 5% weight concentration colloidal silica specimens

Results for the three specimens treated with seven-weight-percent colloidal silica gel are shown in Figure 3.13. Specimen 1 and Specimen 2 have similar shear moduli values while Specimen 3 has slightly higher values. This increase can be attributed to a higher relative density for Specimen 3, which was caused by the use of the incorrect fall height during specimen preparation. There is a 6.3% difference in the G_{max} values between the specimens. The difference between the shear modulus values for the less dense Specimen 1 and Specimen 2 and the denser Specimen 3 decreases as cyclic shear

strain increases, following the trend shown in Figure 2.5. The damping ratio values are similar for all three specimens up to approximately 0.01% cyclic shear strain. Due to the error during specimen preparation, the results for Specimen 3 are not included in subsequent comparisons between different concentrations of colloidal silica gel or between treated and untreated sands.

Figure 3.14 shows the values of shear modulus and material damping ratio vs. cyclic shear strain for the specimens treated with nine-weight-percent colloidal silica gel. There is slight variance in the shear modulus values between the three specimens tested that can be attributed to the small difference in relative densities of the specimens. As noted above, the difference in the shear modulus reduces as cyclic shear strain increases. A maximum difference in G_{max} values of 5.7% was observed among the specimens. The damping ratio values are similar up to approximately 0.01% cyclic shear strain.

The results of the untreated specimens are shown in Figure 3.15. Samples 2 and 3 plot together well and the difference in the G_{max} value between these specimens and Sample 1 can be attributed to relative density. The maximum difference between the G_{max} values is 7%. The damping ratio values are similar, with some scatter in the intermediate cyclic strains.

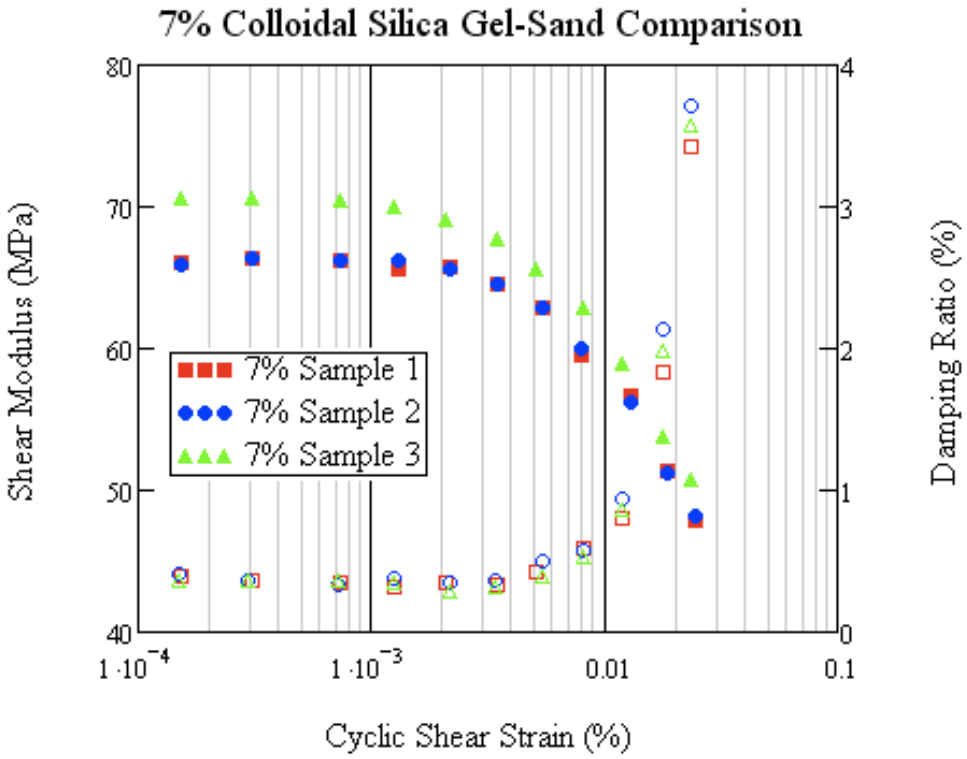

Figure 3.13 Comparison of three 7% weight concentration colloidal silica specimens

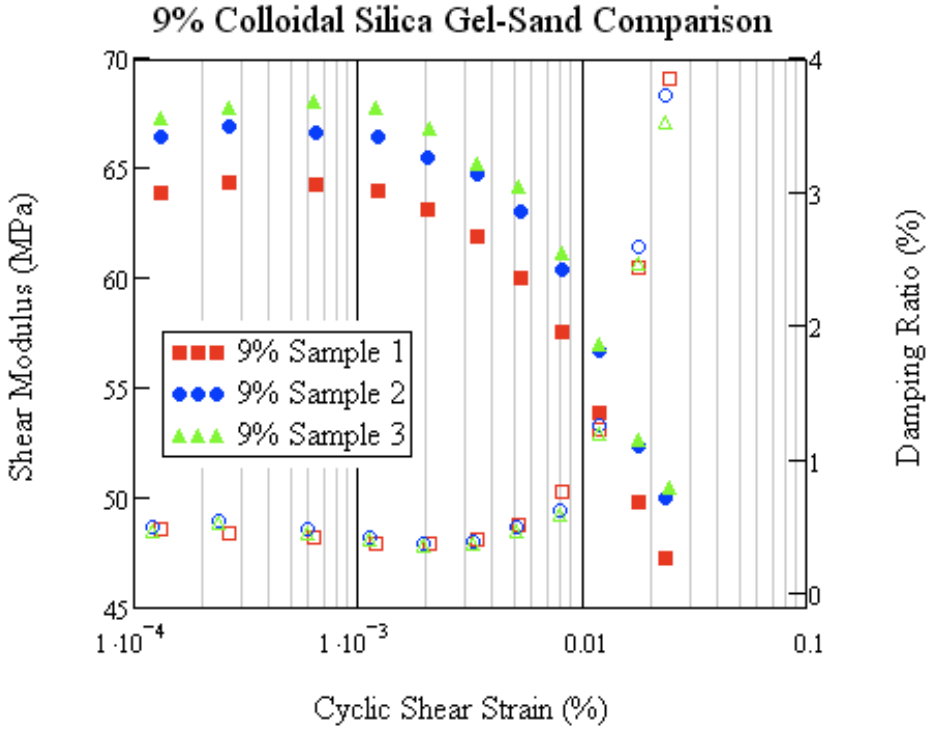

Figure 3.14 Comparison of three 9% weight concentration colloidal silica specimens

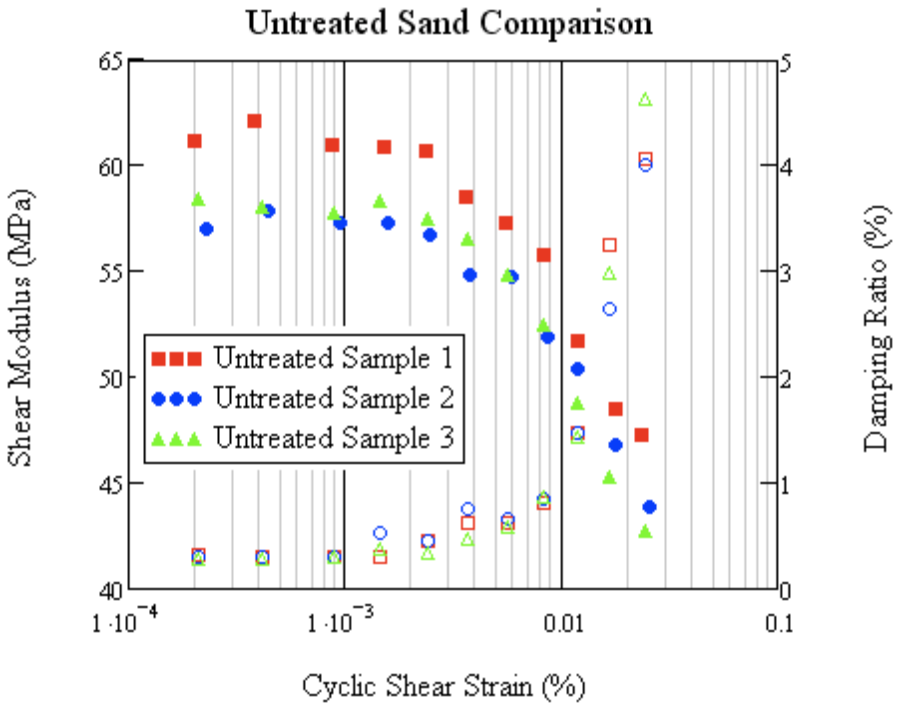

Figure 3.15 Comparison of three untreated sand specimens

3.4.1. Comparison of Treated and Untreated Specimens

For subsequent comparisons, the average of the three specimens (except for the seven-weight-percent specimens) for each concentration (including untreated) is used because the variation among specimens with the same concentration is small. The modulus reduction curves of the treated specimens are compared with the untreated sand specimens Figure 3.16. It is observed that the presence of colloidal silica gel at gel state 10 (rigid ringing gel) slightly increases the shear modulus compared to the untreated sand. The percentage increase in G_{max} for each colloidal silica concentration compared to the untreated sand is shown in Table 3.4. However, it is observed that the difference between the treated and untreated sand decreases as the cyclic shear strain increases, indicating the influence of treatment with colloidal silica gel on the shear modulus is greatest in the small-strain range.

3.4.2. Comparison of Different Gel Concentrations

As shown in Figure 3.16, a difference of only 1.7% in the initial tangent shear modulus is observed between the different concentrations of colloidal silica gel, with the seven-weight and nine-weight-percent resulting in nearly identical values. Gallagher and Mitchell (2002) showed that cyclic strain reached during cyclic triaxial testing on 22% relative density Monterey sand treated with 5-, 10-, 15-, or 20-weight-percent colloidal silica gel decreased with increasing colloidal silica concentration. However, there was overlap between the 5- and 10-weight percent specimens as well as with the 10- and 15-weight-percent specimens. Thus individual specimen results can vary but still demonstrate an overall trend. Previous work has not investigated colloidal silica concentrations with such close proximity, but work by Gallagher and Mitchell (2002) on the unconfined compressive strength of treated specimens also found the 5-weight and 10-weight-percent colloidal silica concentrations to be close and completely overlap for the 10- and 15-weight percent concentrations. This indicates it is reasonable that the difference would be small or negligible (in the case of 7- and 9-weight-percent) between specimens with small differences in concentrations.

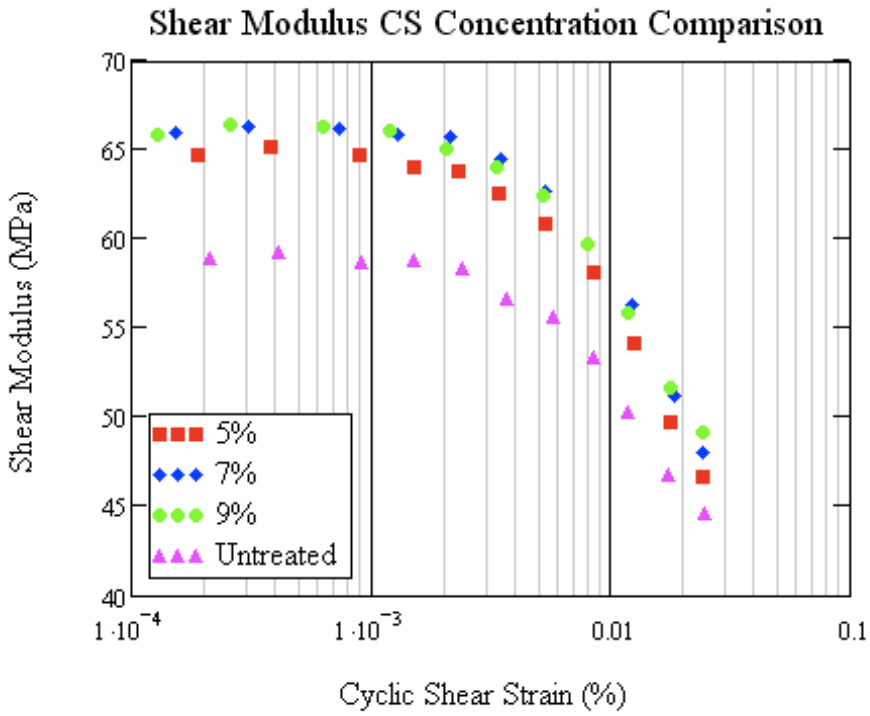

Figure 3.16 Shear modulus comparison of different weight % colloidal silica gel specimens and untreated sand

Table 3.4 Percent Increase in G_{max} for Varying Concentrations of Colloidal Silica Gel when Compared to Untreated Sand

Colloidal Silica Concentraion (wt-%)	Average G_{max} (MPa)	Percentage Increase over Untreated Sand
5	65.2	9.9%
7	66.3	11.9%
9	66.4	11.9%
Untreated	59.3	N/A

3.4.3. Comparison of Normalized Modulus Reduction Curves

The normalized shear modulus of the treated and untreated sands is shown in Figure 3.17. It was observed that the presence of colloidal silica does not affect the shape of the modulus reduction curve. The treated and untreated sand have approximately the same linear threshold shear strain. However, a slight difference between treated and untreated sand was observed in the slope of the nonlinear portion in the intermediate-

strain range greater than approximately 0.01%; the treated specimens have a steeper slope and are reducing at a rate greater than the untreated sands. However, the difference is only about 5%, which is the same variability found between the specimen repeatability tests on a specific concentration.

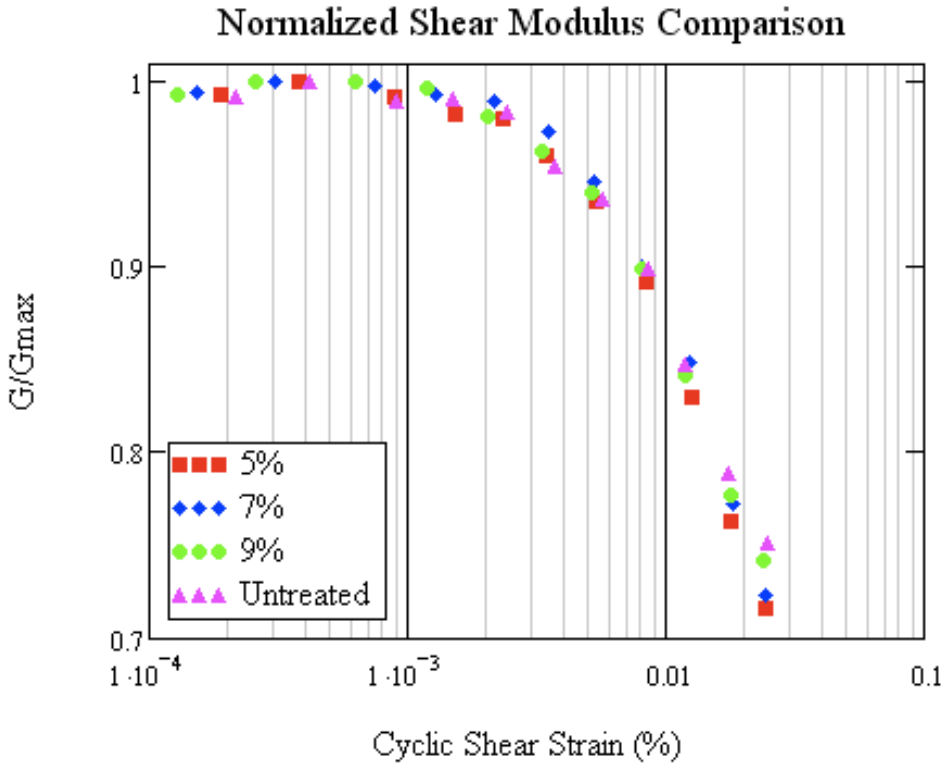

Figure 3.17 Normalized shear modulus comparison of different weight % colloidal silica gel specimens and untreated sand

3.4.4. Comparison of Material Damping Ratio

The damping ratio and the normalized damping ratio, D/D_{min}, of the varying colloidal silica gel concentrations and untreated specimens are shown in Figure 3.18. It was observed that the treated sand has slightly higher damping ratio in the small-strain range. However, at cyclic shear strains around 0.003% the trend reverses and the untreated sand begins to have higher damping ratio and the difference between the treated and untreated increases with increasing strain amplitude. This can be attributed to the energy dissipation due to frictional interparticle forces in the untreated sands, whereas it

is hypothesized that the treated sands can rotate more easily due to an interaction between the gel and sand particles and thus less energy is dissipated at the interparticle contacts.

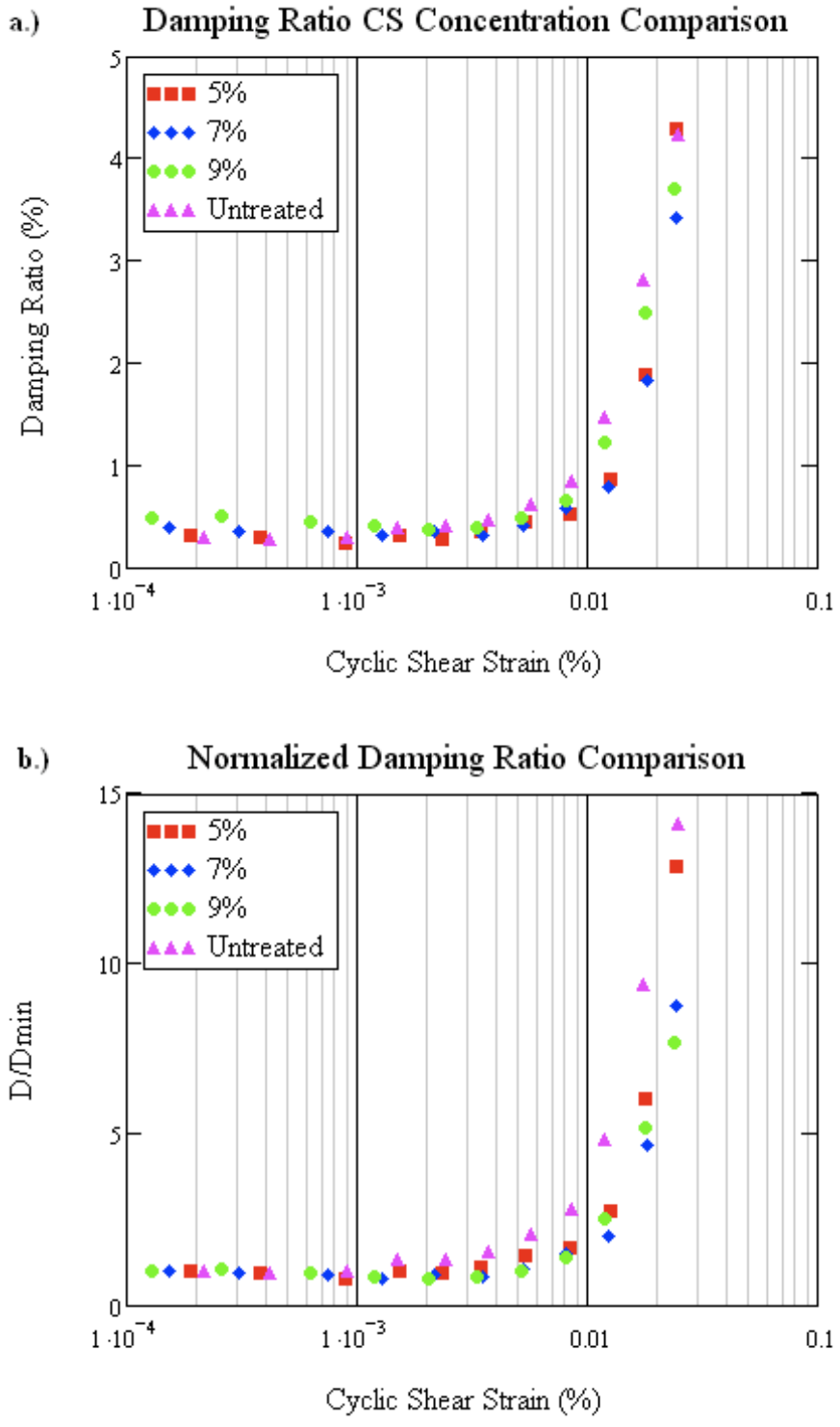

Figure 3.18 Damping ratio (a.) and normalized damping ratio (b.) comparison of different weight % colloidal silica gel specimens and untreated sand

3.5. Summary

An investigation of the effect of colloidal silica gel on the dynamic properties of loose sands was presented. The effect of colloidal silica gel in the initial phase of treatment (permeation through gelation and initial curing to allow development of a resonating gel) is a small increase on the dynamic properties of loose sand. The effect of colloidal silica concentration on the small-strain shear modulus showed a 10% increase in five-weight-percent concentration and a 12% increase in seven- and nine-weight-percent concentrations. The percent increase determined in this study for treatment with colloidal silica gel is applicable in short curing periods, within the $10*T_{gel}$ range. The increase in small-strain shear modulus associated with treatment is time dependent and the increase over the untreated sand shear modulus is expected to continue as curing of the colloidal silica gel occurs. These effects are examined in Chapter 4.

4. DYNAMIC PROPERTIES OF SAND TREATED WITH COLLOIDAL SILICA GEL: AGING EFFECTS

4.1. Introduction

The term aging applies to the phenomenon of time-dependent property changes. The effect of aging on the dynamic properties of soils has been researched and the results show an increase in the small-strain shear modulus with time (Anderson and Stokoe II 1978; Baxter and Mitchell 2004; Howie et al. 2002; Li and Yang 1998; Mesri et al. 1990; Wang and Tsui 2009). Research has also been done to study the effect of time on the properties of colloidal silica gels (Scherer et al. 1988) where modulus values increase due to continued siloxane bond formation. Therefore, it is expected that sand treated with colloidal silica gel will experience an increase in the small-strain shear modulus caused by changes in the soil structure (particle contact network) and the gel occupying the pore space.

It was demonstrated in Chapter 3 that the introduction of colloidal silica gel into the pore space of a sand matrix slightly increases the small-strain shear at times greater than the gel time, but less than the time required to reach a rigid non-ringing gel state, $T_{GelState4}<t<T_{GelState11}$. However, the evolution of the gel within the pore space due to continued siloxane bonding can increase the difference between the initial tangent shear modulus of the treated and untreated sand with time. Because the time horizon of passive soil stabilization may be many years, the colloidal silica gel will continue to cure and the evolution of the initial tangent shear modulus of treated sand with time is important to identify because of the effect that it may have on earthquake site response.

The effect of aging on the dynamic properties of sand treated with colloidal silica gel has been investigated using resonant column and bender element tests performed over a period of 28 to 82 days and the evolution of the small-strain shear modulus with time is

presented. Varying gel times of the same weight-percentage colloidal silica gel were investigated to identify the influence on aging. The small-strain shear modulus values of the colloidal silica treated sand are compared to published values of untreated sand subjected to aging.

4.2. Aging of Colloidal Silica Gel

The term gel is applied to systems with a continuous solid skeleton made of colloidal particles or polymers enclosing a continuous liquid phase (Bergna and Roberts 2006). Gelling is "where the particles are linked together in branched chains that fill the whole volume of sol so that there is no increase in the concentration of silica in any macroscopic region in the medium. Instead, the overall medium becomes viscous and then is solidified by a coherent network of particles that, by capillary action, retains the liquid" (Iler 1979). The transition from the viscous fluid state to a solid gel state is called the gel time and marks a difference in the rheological behavior (Scherer 1996; Warlus et al. 2003). However at the molecular level, there are still many monomers and clusters available to form siloxane bonds. As time passes and the sol continues to gel, polymeric chains come into contact with one another and form siloxane bonds, which stiffens the gel network (Hdach et al. 1990). New bonds continue to form well after the gel time and the gel network continues to evolve which causes a steady increase in the elastic modulus of the gel (Scherer 1996; Scherer et al. 1988). More details of the aging process in colloidal silica gels are given in Section 2.4.1.3.

4.3. Bender Element Experiments

The use of bender elements is becoming a popular means to determine the small-strain shear modulus in soils. Bender elements are piezoelectric transducers that are capable of converting electrical energy to or from mechanical energy (movement). Bender elements are a thin, two-layer plate (Lee and Santamarina 2005). There are two types of bender elements, parallel and series as shown in Figure 4.1. The series type has

poling directions of the two piezoelectric layers opposite each other and is attached to ground as shown in the figure. The parallel type has the same poling directions and the ground is connected to the outer electrodes with the core wire connected to the shim as shown in the figure. For the same applied voltage, the parallel bender element provides twice the displacement as the series type (Lee and Santamarina 2005).

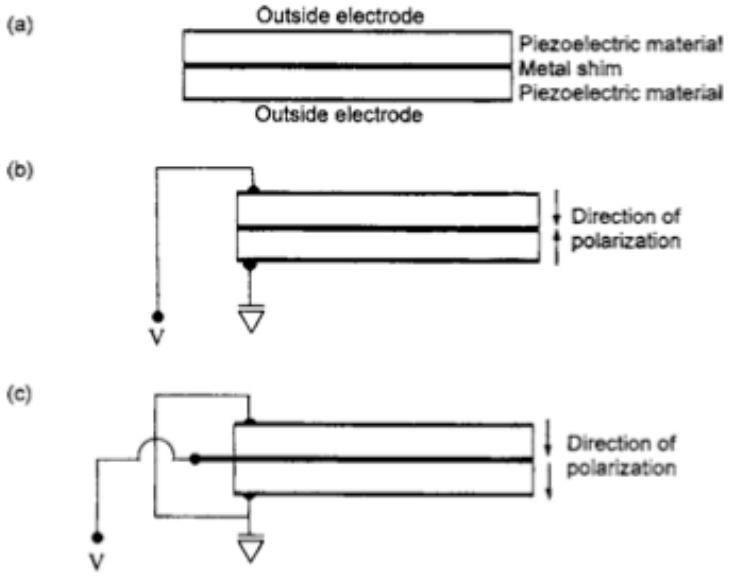

Figure 4.1 Schematic of series (b) and parallel (c) bender elements types (from Lee and Santamarina 2005)

Bender elements produce two compression wave side lobes normal to their plane and one shear wave frontal lobe. The ratio of compression wave to shear wave velocities, V_p/V_s is can be calculated by:

$$\frac{V_p}{V_s} = \sqrt{\frac{2(1-\nu)}{1-2\nu}} \qquad 4.1$$

where ν is the Poisson's ratio. For dry soils with $\nu \approx 0.1$, the velocity ratio is 1.5, but the velocity ratio is stress dependent for saturated soils and can be more than 20 for soils at low effective stress. Due to this, compression wave reflections from the cell wall may interfere with the detection of the arrival time of the shear wave (Lee and Santamarina

2005). Because the velocity ratio depends on Poisson's ratio, the appropriate relative distance between the source and receiver and the receiver to the cell wall boundaries should be used to avoid compression wave interference (Sawangsuriya et al. 2006).

4.3.1. Resonant Frequency

A bender element is essentially a cantilever beam. The embedded bender element has fixed-free boundary conditions where neither rotation or displacement can occur at the fixed end and no moment or shear exists at the free end. The resonant frequency of a cantilever beam is dependent on the elastic modulus, E_b, moment of inertia, I, and the mass per unit length. Taking into account the typical values of modulus and density, ρ_b, of piezoceramic materials, the resonant frequency of the bender element in air for the first mode is (Lee and Santamarina 2005):

$$f_r = 464\left[Hz \cdot m\right]\frac{h}{\left(\alpha L_b\right)^2} \qquad 4.2$$

where:

h = thickness of the bender element (m)

L_b = cantilever length (m)

α = effective length factor, which is affected by the anchor efficiency ($\alpha = 1$ for a perfectly rigid anchor and $\alpha > 1$ for a soft anchor)

The resonant frequency of an anchored bender element in the soil is affected by the soil stiffness and soil density. Soil stiffness can be obtained from Mindlin's solution for a point load within a continuum integrated to a rectangular geometry (Lee and Santamarina 2005):

$$k_s = \eta E_s L_b \qquad 4.3$$

where $\eta \approx 2$ is the mean displacement influence factor at the soil-element interface. The elastic modulus of the soil, E_s, can be determined from the shear wave velocity, V_s, Poisson's ratio, ν, and the soil mass density, ρ_s. Using these properties in Equation 4.3,

and combining the mass and stiffness of the bender element and the affected soil to calculate an equivalent spring constant and equivalent mass, an estimate of the resonant frequency of a bender element in soil can be determined by (Lee and Santamarina 2005):

$$f_r = \frac{1}{2\pi}\left[\frac{1.875^4 \frac{E_b I}{(\alpha L_b)^3} + 2\eta V_s^2 \rho_s (1+\nu) L_b}{\rho_b b h (\alpha L_b) + (\rho_s b^2 L_b)\beta}\right]^{1/2} \qquad 4.4$$

where:

b = width of the bender element

β = experimentally determined coefficient

With a short cantilever length, the resonant frequency is more dependent on the bender element properties, but with a long cantilever length the frequency is controlled by the soil properties (Lee and Santamarina 2005). The effect of soil stiffness on the resonant frequency of the bender element is shown in Figure 4.2.

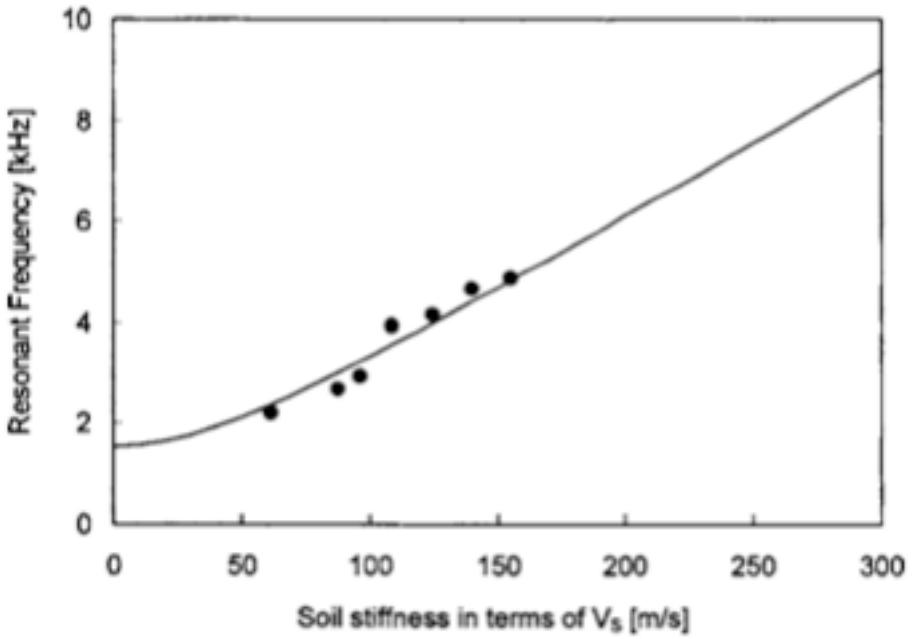

Figure 4.2 Soil stiffness effects on the resonant frequency of bender element installations (from Lee and Santamarina 2005)

4.3.2. Shear Wave Velocity

The determination of the shear wave velocity requires the distance from tip to tip of the source and receiving bender elements and the travel time for the shear wave:

$$V_S = \frac{d}{t} \qquad 4.5$$

The tip-to-tip distance is easy to determine, but the best input signal and method to determine the travel time is debated (Ferreira et al. 2007; Lee and Santamarina 2005; Youn et al. 2008).

4.3.2.1.Input Signal

The form, frequency and amplitude of the input shear wave affect the determination of the arrival time, and thus the accuracy of the travel time (Atkinson 2000). The determination of the arrival time of the shear wave signal has great uncertainty (Ferreira et al. 2007) and the resulting uncertainty in determining small-strain shear modulus G_{max} was 100% (Arroyo et al. 2006). Studies have been performed to determine the most favorable input source signals, which include square waves, single-period sinusoids of various frequencies and distorted sinusoids (Arroyo et al. 2003; Lee and Santamarina 2005; Youn et al. 2008). Conflicting results have been found on the best input signal to use. It was shown that the optimal frequency of a single-period sinusoid input wave is that of the soil sample. However, a square wave is favored because it includes all frequencies and has a clear response regardless of soil stiffness (Lee and Santamarina 2005). Unfortunately, the large number of frequency components in a square wave causes distortion (Blewett et al. 2000). It is important to note that the first arrival is not affected by the input frequency, only the ability to detect the arrival time accurately can change (Lee and Santamarina 2005).

4.3.2.2.Arrival Time Determination Methods

The arrival time determination is also controversial. A typical square-wave input signal and output response is shown in Figure 4.3. When determining travel time, there is a question of which point to use as the first arrival: the first deflection (A), the first trough (B), the zero crossing after the first trough (C) or the major first peak (D). In addition to the question of the first arrival of the shear wave, travel time determination affects the shear wave velocity results. Methods of travel time determination including first detected arrival, characteristic input peak to output peak, cross correlation of the input and output signals, multiple reflection arrivals (Lee and Santamarina 2005), and phase-sensitive detection techniques (Blewett et al. 1999) have been used to reduce picking the arrival time point. The accuracy of identifying the chosen arrival point is dependent on other factors discussed in the following section.

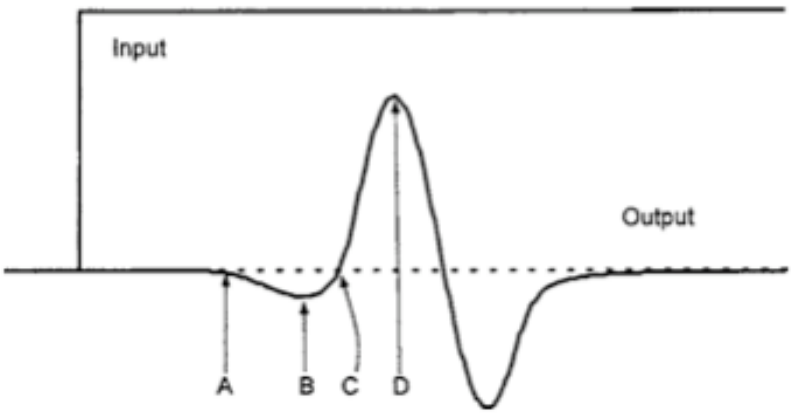

Figure 4.3 Typical shear wave signal from square wave input (from Lee and Santamarina 2005)

Theoretically, the use of the multiple reflections, or the second arrival in the output signal is a robust method to overcome uncertainties in travel time and travel length (Lee and Santamarina 2005) because it is least affected by boundary wave interference or transfer functions relating electric signals to physical waves and is expected to provide a lower bound for the correct shear wave velocity (Arulnathan et al. 1998). Values obtained

using input-output methods resulted in shear wave velocity values up to 9% greater than using the second arrival method, which corresponds to an overestimation of G_{max} by 19% (Arulnathan et al. 1998).

4.3.2.3.Errors in Arrival Time

Arulnathan et al (1998) reviewed errors associated with multiple arrival time methods. It was noted that using characteristic peaks or cross correlation methods are theoretically incorrect because of wave interference boundaries, phase lag or signal distortion, and near-field and non-one-dimensional wave propagation effects. The travel time errors are dependent on the wavelength-to-bender element-length ratio, the travel distance-to-wavelength ratio, method of travel time determination, relative stiffness of the soil and bender elements, and Poisson's ratio.

Difficulty in accurate determination of the arrival time could be due to electrical crosstalk, near-field effects or signal reflections (Arroyo et al. 2003; Arulnathan et al. 1998; Ferreira et al. 2007; Lee and Santamarina 2005). Cross talk can be reduced by using parallel piezoelectric transducers for the source and signal and ensuring good grounding, properly encased transducers and a leak-free environment (Ferreira et al. 2007; Lee and Santamarina 2005).

Near-field effects are caused by the coupling of waves that have the same particle motion propagating at different velocities and attenuating at different rates due to the spherical wave front spreading from the source (Arulnathan et al. 1998). Near-field effects cause an overestimation of shear wave velocity. The near-field term phase velocity is frequency and distance dependent and therefore the near-field term is dispersive. For a given travel distance, every frequency will propagate with a different velocity. As the normalized distance increases, the dispersion decreases and the phase velocity approaches the corresponding bulk velocity. The near-field term attenuates two orders of magnitude faster than the far-field term (Arroyo et al. 2003). Atkinson (2000)

stated that single sine waves are favored because square step introduces near-field effects. A square wave, which is composed of all frequencies, causing the near-field effect to be present can make correct determination of the arrival time difficult (Jovicic and Coop 1997). Single sine-wave input waves have increasing near-field effects the larger the wavelength is relative to the travel (tip-to-tip) distance (Jovicic and Coop 1997). Far-field conditions are reached by keeping the travel distance greater than 1.6 normalized distances (Arroyo et al. 2003).

A refracted wave occurs when the shear wave travels through the soil to the rigid cell wall boundary, through the cell wall and back through the soil to the receiver. To avoid having the refracted shear wave be the first arrival, the distance of the bender elements to the rigid boundary should be greater than 0.4d, where d is the tip-to-tip distance (Sawangsuriya et al. 2006). Errors in determining the arrival time caused by reflected waves can be minimized by keeping the ratio λ / l_b, where $\lambda = \frac{V_S}{f}$, equal to or less than limits for different input signals. It was found a ratio of eight for first peak output signals, of four for the first trough in the signal, and four for input-to-output, peak-to-peak cross correlation. As these limits are breached, the travel time is underestimated leading to an overestimation of shear wave velocity (Arulnathan et al. 1998). The error in travel time determination depends on the arrival time determination method and increases with increasing λ / l_b ratio and the effect on the error in shear wave velocity increases as specimen length decreases (Arulnathan et al. 1998).

Other factors can affect the accuracy in determining the arrival time, such as bender element and soil coupling, bender element alignment, and oscilloscope and system resolution. Isolation is important in saturated soils subjected to long-term bender element tests, especially in high ionic concentrations. Short-circuits can develop caused by the pore fluid reaching the bender element by diffusion and can result in a diminished output. If both the source and receiver are affected, the output wave rides on a charging

curve (Santamarina and Fam 1997). This can be remediated by using a pulse excitation signal to facilitate arrival time determination.

4.3.3. Test Procedure

A series of five sand samples treated with five-weight-percent colloidal silica gel were subjected to long-term shear wave velocity measurements via bender elements. The gel time for each of the five samples was varied to determine the effect that gel time has on the rate of shear modulus increase.

4.3.3.1.Bender Element Cells

The test cells were composed of a top and bottom cap made of 76.2-mm diameter cast acrylic circles and the cell wall was 6.35-mm thick cast acrylic tube. The top and bottom caps had a hole drilled through the center to allow for placement of bender elements and associated cable as shown in the schematic in Figure 4.4. The top and bottom cap were shaved down to ensure the caps would fit snugly inside the cell walls and the top cap was shaved slightly more to allow the top cap to be placed inside the cell wall and float down evenly to ensure a flat even surface on the top surface of the sand sample. The bottom cap is fitted with an O-ring to ensure a good seal. A schematic of the assembled bender element cells is shown in Figure 4.5 and photos of a completed cell are shown in Figure 4.6. The nominal height of the completed samples was approximately 33 mm. The samples were within the limiting distances to avoid a reflected P-wave arrival and the distance of the bender element from the rigid wall boundary is greater than 0.4d to avoid receiving refracted signals (Sawangsuriya et al. 2006).

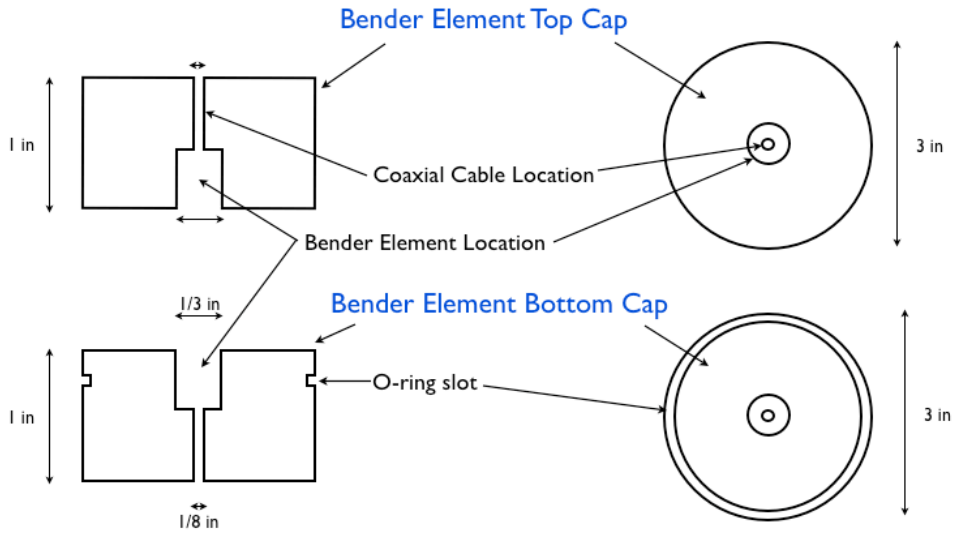

Figure 4.4 Schematic of bender element top and bottom caps

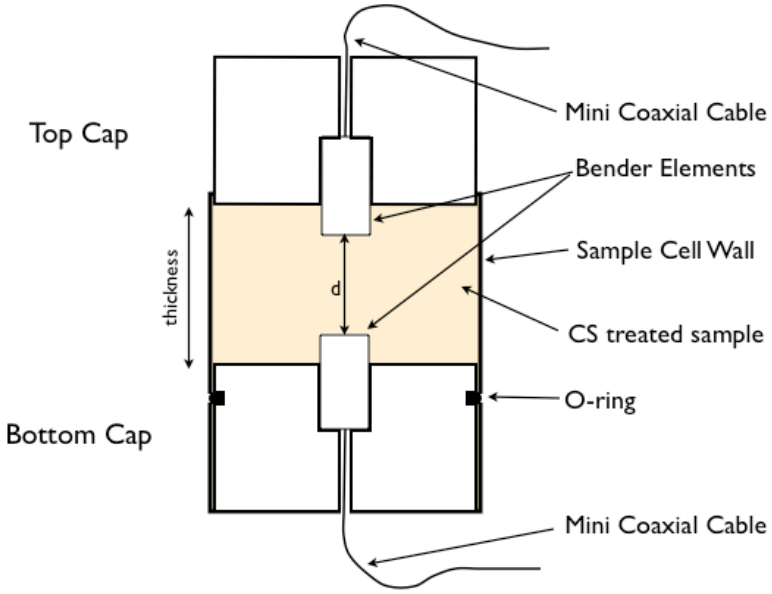

Figure 4.5 Schematic of bender element test cells

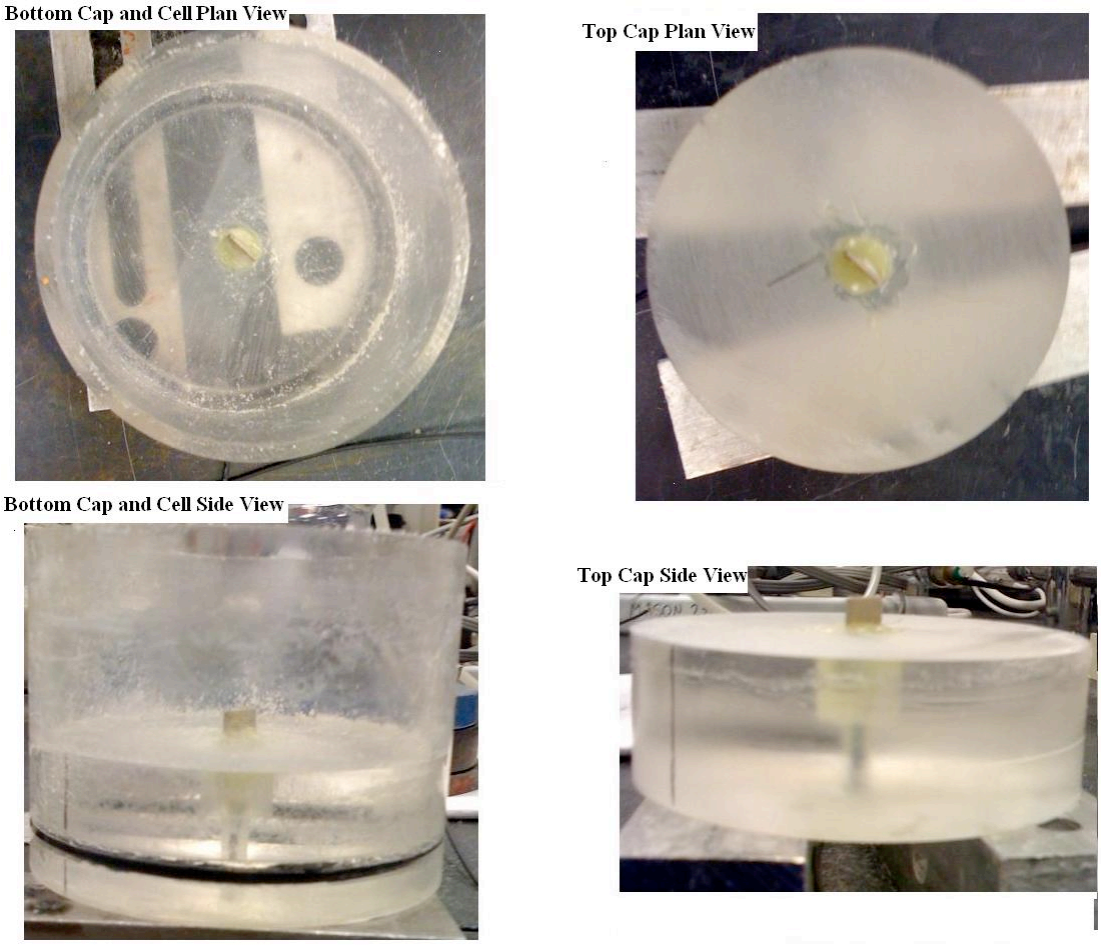

Figure 4.6 Picture of bender element test cell

4.3.3.2.Bender Elements

The piezoceramic crystals used in this testing were the parallel type as shown in Figure 4.1. The bender elements were prepared by connecting the core wire to the intermediate metal shim and the ground to the piezoelectric transducer on both sides of the shim. The bender element was then thinly coated in polyurethane and painted in conductive silver paint. Once the bender element was complete, it was mounted in the top or bottom cap and secured with quick set epoxy. The top and bottom caps were marked to indicate the direction of the bender element within to allow for proper alignment during sample preparation and testing.

4.3.3.3.Soil Sample Preparation

The bottom cap was placed into the acrylic tube so that the bottom was flush. Vacuum grease was used around the O-ring to ensure a waterproof seal. Approximately 100 mL of the colloidal silica solution was placed into the sample cell. Nevada No 120 sand, the properties are given in Table 3.2, was then pluviated through the silica solution to obtain as high a void ratio as possible. The obtained relative densities ranged from approximately 70% to 75%. The sand was filled to the top of the side tube and then the top cap was placed on and any colloidal silica solution that squeezed out was removed. Once the top cap was placed, a weight was placed on the top cap to apply the vertical confining pressure with a nominal value of 25 kPa. The contact area between the top cap and the cell wall was coated with vacuum grease to reduce the diffusion of air into the sample via the sides of the top cap. A completed sample ready for testing is shown in Figure 4.7. No attempt at maintaining a constant humidity was made during the testing. Upon sample deconstruction, it was evident that drying had started to occur at the edges of the samples around the top cap and across the top layer of the sample near the top cap surface as well as along the cell wall. The outer portions of the sample were dry with flaky sand and the drying decreased towards the center of the sample.

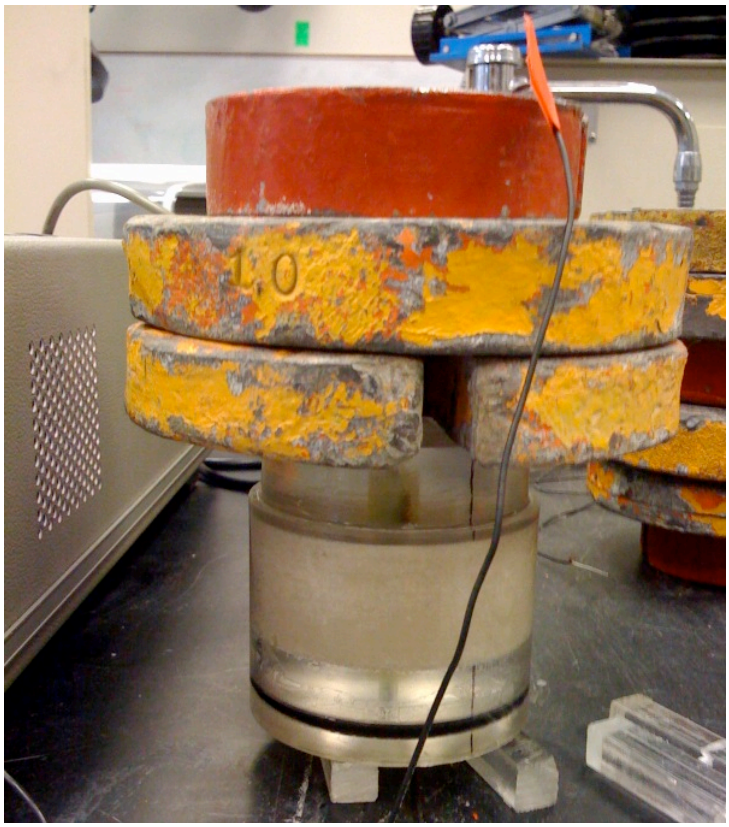

Figure 4.7 Picture of completed bender element sample

Different ionic concentrations of colloidal silica gel were used in the samples to identify the effect the ionic concentration, and therefore gel time, has on the rate of shear wave velocity increase. Two specimens each of two of the tested ionic concentrations were performed to evaluate repeatability. The details for the bender elements test samples are shown in Table 4.1. The test duration was determined by the length of time each set of bender elements continued to function; testing was terminated when the bender elements no longer worked.

Table 4.1 Details of bender element test samples

Sample Number	Ionic Concentration (N)	Approximate Gel Time (hr)	Initial* Relative Density (%)	Test Duration (days)
1	0.5	2/3	75	75
2	0.4	2	69	82
3	0.3	20	71	78
4	0.5	2/3	75	42
5	0.3	20	70	42

* Measurement taken before vertical confining stress was added to the sample

4.3.3.4.Shear Wave Velocity Measurement Procedure

Once a specimen was prepared, the first measurement was taken. A schematic diagram of the bender element test set-up is shown in Figure 4.8. An input square wave with amplitude of five volts peak-to-peak was applied to the bottom cap and the resulting voltage time history of the bender element within the top cap was recorded. The output signal was amplified and a high-pass filter applied before being displayed on the oscilloscope and recorded. The time, Δt, it takes for the shear wave to arrive at the top cap is divided by the distance, d, between the bender elements to calculate the shear wave velocity, V_S, of the sample. This measurement is repeated over time to track the change in V_S.

The shear wave velocity obtained with bender elements can be related to the small-strain shear modulus by $G_{\max} = \rho \cdot V_s^2$, and therefore the shear modulus can be tracked overtime. The arrival time chosen for these tests was the zero after the first trough, point C in Figure 4.3, as explained by Lee and Santamarina (2005). The arrival time was difficult to determine during the initial stages of the test, but a more distinct trend of arrival times is evident once gelation occurred. The relative change in the shear modulus over time is more important than the absolute magnitude when studying aging effects (Baxter and Mitchell 2004), and therefore the same method is used for all samples.

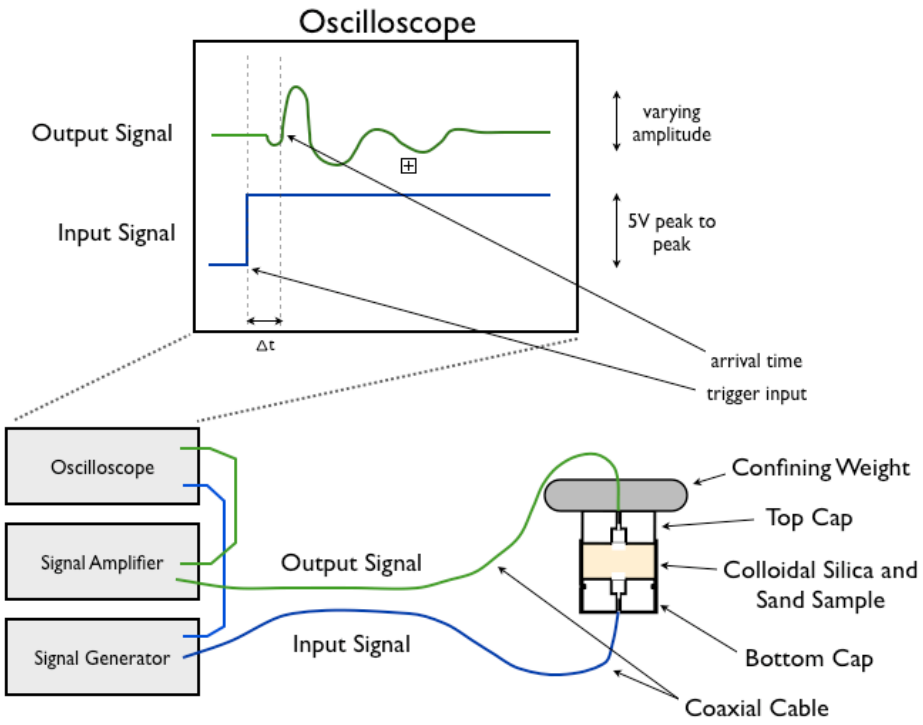

Figure 4.8 Bender element test schematic

4.3.4. Shear Wave Velocity Bender Element Test Results

Typical results for one of the five bender-element specimens are discussed below.

4.3.4.1. Typical Bender Element Test Results

Sample 2 was sand treated with a 0.4 N ionic concentration NaCl colloidal silica gel and tested at a relative density of 69%. The shear wave velocity was tracked over a period of 82 days. The shear wave signal time histories are shown in Figure 4.9. The time histories at the top of the figure are immediately after sample preparation and curing time increases downward along the vertical axis: time zero (t=0) is when the colloidal silica suspension was mixed. The initial time history arrival times are difficult to determine because the colloidal silica is still a colloidal suspension and has not begun to gel. This leads to very low-amplitude peaks and difficulty in identifying the exact arrival time. However, an upward peak can be identified in the time histories by one hour after mixing (T_{gel} = 2 hr), and the large downward arrival can be seen clearly at 1.5 hours. The zero

point before the downward trough (or the zero point after the initial bump) is the arrival time as shown in Figure 4.10 where a close up of the signal arrival is shown with the trend of arrival times added to the time histories.

The time histories show a quasi-single-sinusoidal response at the arrival time of the shear wave. However, the time histories of Sample 2 begin to show additional amplitude peaks and troughs within the response. This trend is found in one other specimen tested and these peaks generally tend to develop further into the curing period. These additional peaks indicate a resonance in the sample. It is possible that as the sample stiffness increases, a higher frequency is amplified and appears as another hump in the time history. Another possibility is due to a second arrival of the input signal due to reflections or refractions, however, using appropriate dimensions of the test cell to reduce this minimized the probability of refractions and reflections arriving before the initial shear wave signal.

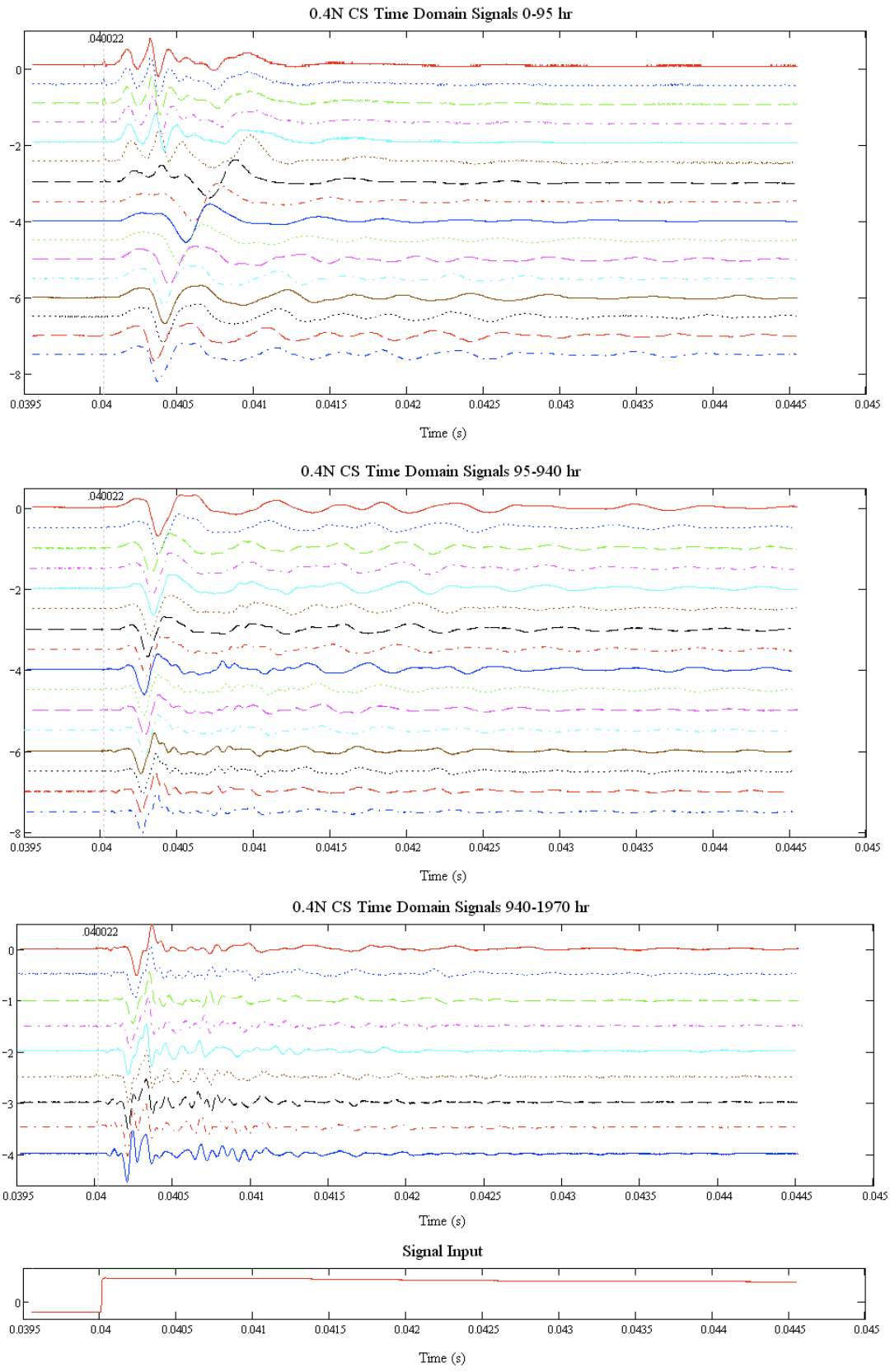

Figure 4.9 Output signal time histories over time of Sample 2

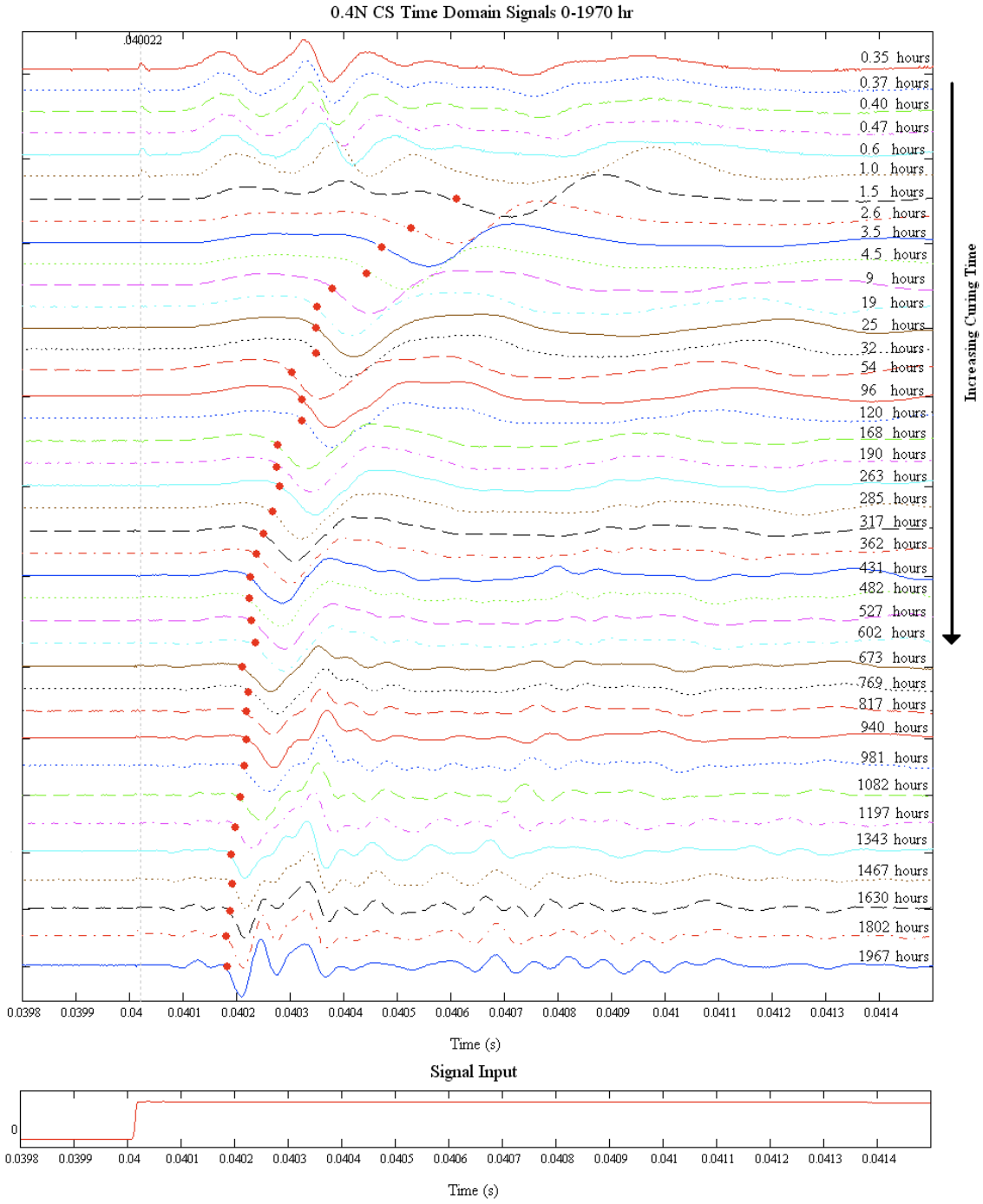

Figure 4.10 Close up of shear wave arrival and arrival time trend of Sample 2

4.3.4.2.Cross-Talk in Sample Results

In Sample 1, the results were affected by cross-talk (Lee and Santamarina 2005) that worsened over time. While precautions were taken to shield and ground the bender elements and to maintain a leak-free environment (Lee and Santamarina 2005; Youn et al. 2008), the conditions deteriorated with time and affected the output signals. The cross-talk resulted in a spike at the input signal trigger time, and in some time histories skewed the determination of the arrival time. The cross-talk noise increased, both in amplitude and duration, over time and the signals most affected by this were the final few time histories recorded. All signals were filtered to remove the spike by using the forward and backward difference and comparing to a threshold value. It is more difficult to identify the arrival times for the time histories recorded after approximately 1000 hours of curing due to the overlap of the cross-talk with the signal arrival. However, even with the exact arrival time difficult to obtain, the trend of the downward trough moving closer to the input trigger is still obvious and indicates an increase in shear wave velocity.

In Sample 3, the later time histories, after approximately 500 hours of curing, are affected by cross-talk and the spike associated with this phenomenon has been removed using a threshold filter. Fortunately, the noise resulting from the cross-talk is of short duration and does not affect the determination of the arrival time. Several time histories have artifacts from the applied filter, but this does not obscure the determination of the arrival time. In Sample 5, most of the signals were affected by cross-talk, however it resulted in a distorted zero value (DC offset) after the trigger time. The cross-talk did not skew the time history curves and therefore did not affect the determination of the arrival time.

4.3.5. Shear Modulus Results

The small-strain shear modulus was determined from the sample density and the measured shear wave velocity from the experiments. The shear modulus evolution of

each sample versus time and log time are shown in Figure 4.11 and Figure 4.12. For Sample 1, the signals towards the end of the testing duration showed signs of electrical leakage, as discussed above, which could have affected travel time determination and results in scatter of the shear modulus values. Each sample displays an increase in the small-strain shear modulus over time. An asymptotic trend can be observed, but Samples 2 and 5 still show an increase, with the asymptote more difficult to establish. However, it is important to note than an asymptotic trend is expected to develop due to the availability of siloxane bonds available within a given matrix and localized pore spaces.

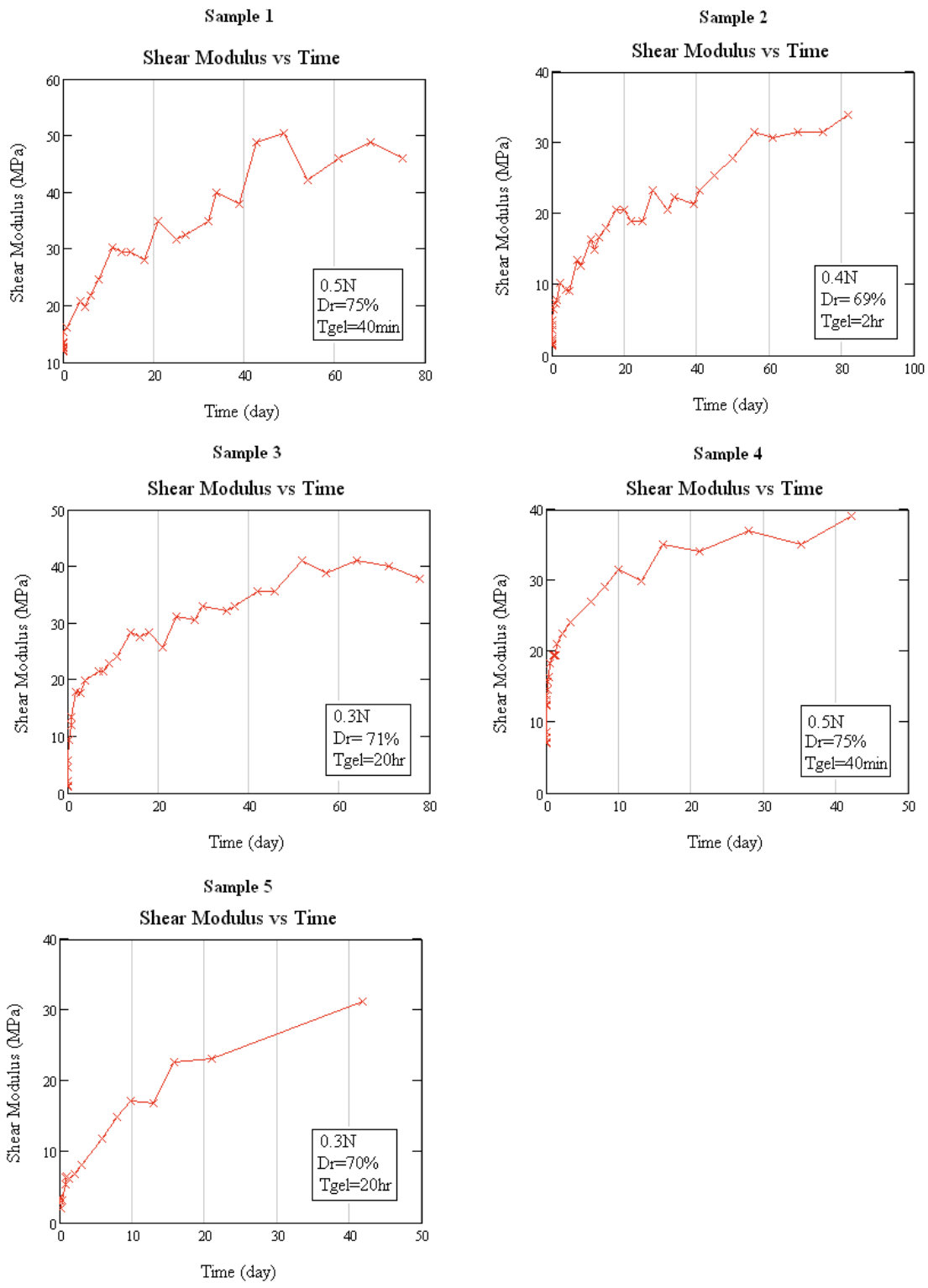

Figure 4.11 Bender element shear modulus evolution over time for each sample

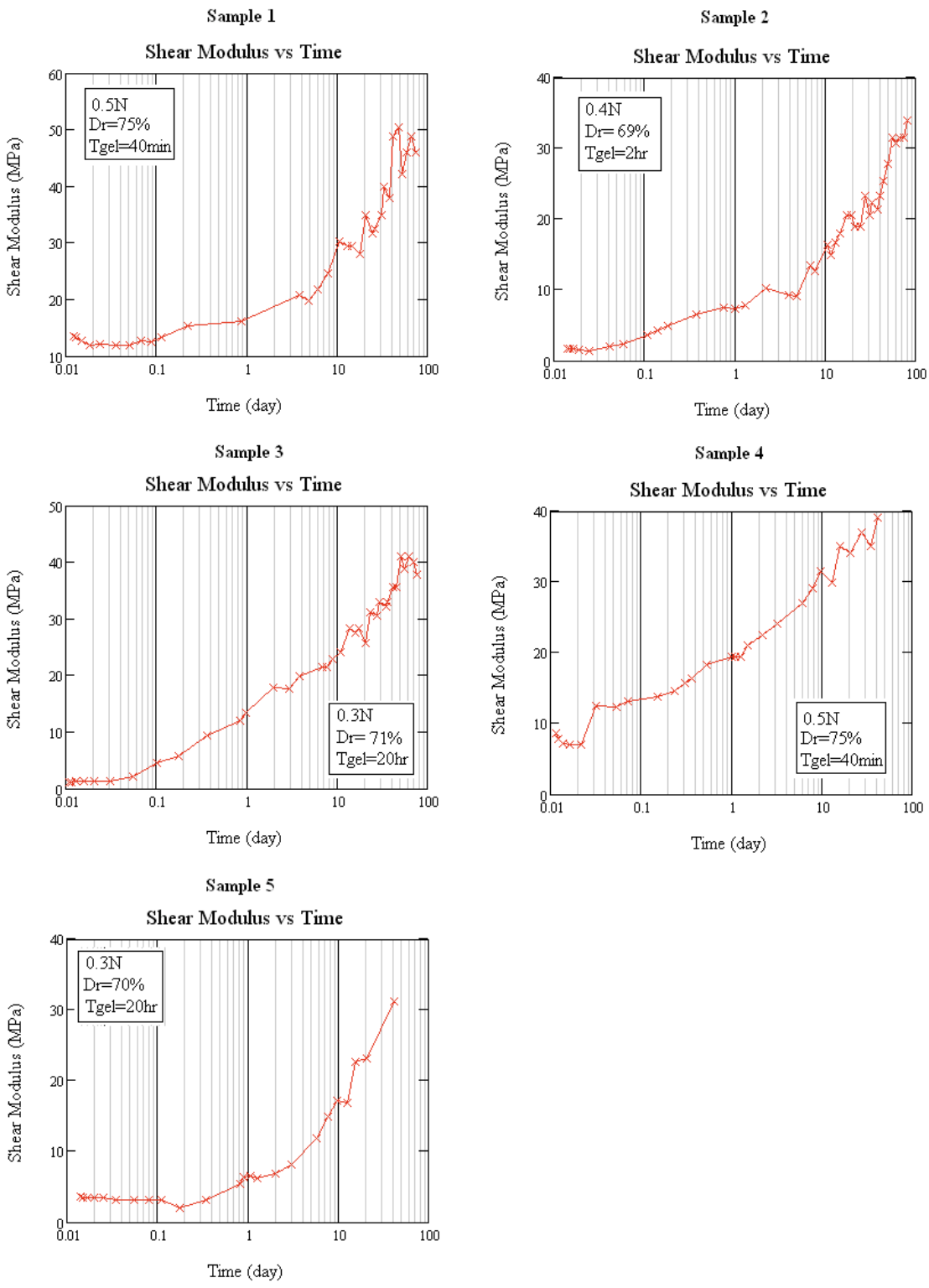

Figure 4.12 Bender element shear modulus evolution over time (log scale) for each sample

4.3.5.1.Repeatability of Bender Element Tests

Two samples each of the 0.3N and 0.5N NaCl ionic concentration colloidal silica gel samples were tested using bender elements. The comparison of the results of the samples is shown in Figure 4.13. Sample 1 and Sample 4 are both 0.5N ionic concentration samples and the data plots together well. The maximum difference of the shear modulus results occurred during the initial testing, but the results are consistent as early as prior to 0.1 days. Sample 3 and Sample 5, both 0.3N ionic concentration, have similar results with more variation than the 0.5N samples. The maximum difference between the samples occurred around 2 days. The difference between the shear modulus values decreases with time. Sample 3 shear modulus increases at a rate faster than Sample 5 during the initial testing period and then levels off at the end of testing. The variability in the 0.3N samples can be attributed to the longer gel time, which results in a slower formation of the gel and the spatial variability associated with the location of the gelled versus ungelled clusters within the sample may result in different shear moduli, up to the time when the gel has become a resonating gel, approximately $10*T_{gel}$, or about 10 days. It can be seen that the difference between the two 0.3N samples is decreased by t=10 days, and the values are similar after this time.

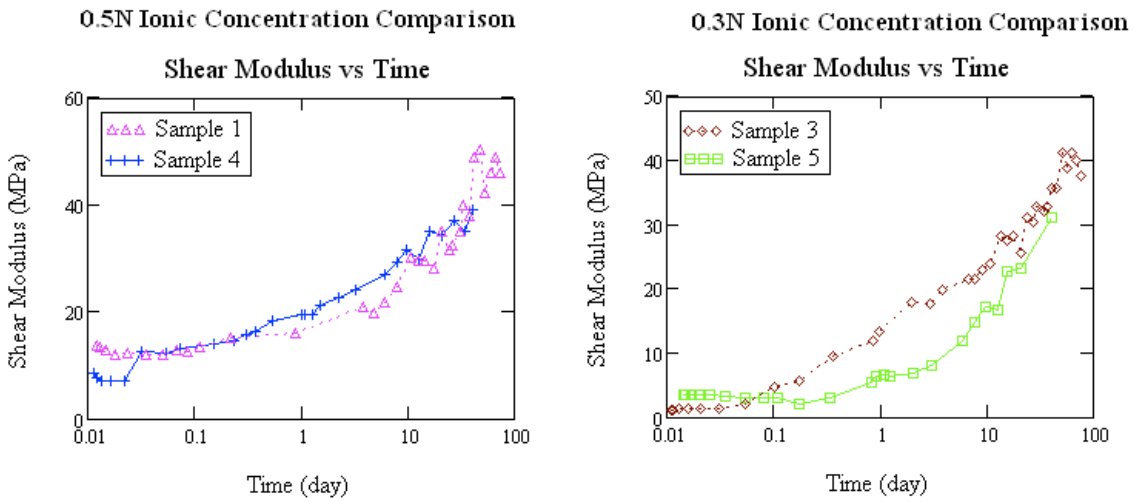

Figure 4.13 Shear modulus versus time of the samples treated with the same ionic concentration soltion of colloidal silica gel, Sample 1 and 4 (0.5N) and Sample 3 and 5 (0.3N)

4.3.6. Shear Modulus Aging Comparison

4.3.6.1. Comparison of Different Ionic Concentrations from Bender Element Tests

The bender element tests investigated the effect the ionic concentration of the colloidal silica gel on the aging of sand specimens treated with colloidal silica gel. The samples were 0.3N, 0.4N and 0.5N NaCl ionic concentration colloidal silica solutions, and the evolution of shear modulus over time is shown in Figure 4.14. The results generally plot within a band, with Sample 1 and 4 forming the upper trend and Sample 2 and 5 forming the lower trend, as shown in Table 4.1. As curing continues, the relative difference between the lowest and highest measured shear modulus decreases to approximately 20%.

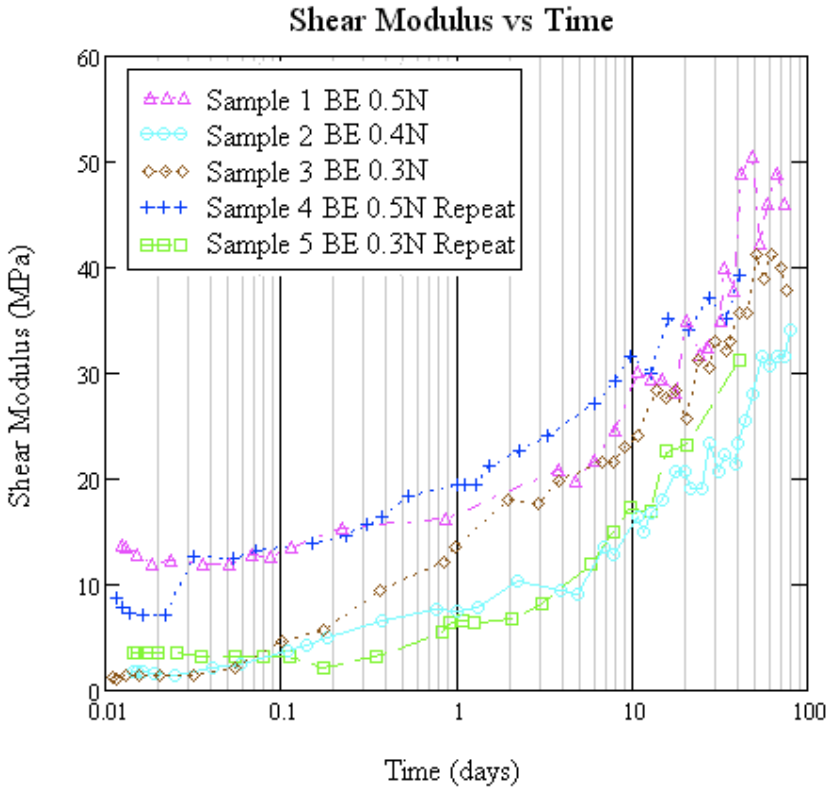

Figure 4.14 Comparison of bender element sample shear modulus evolution over time

4.3.6.2.Comparison of Normalized Results

The change in shear modulus, $\Delta G = G_t - G_{T\,gel}$, is shown versus normalized time, called distance from gelation, defined as $dgel = \frac{t - T_{gel}}{T_{gel}}$ (Warlus et al. 2003) in Figure 4.15. It can be seen that the longer gel time samples have shear moduli that increase at a smaller distance from gelation than the shorter gel time samples. It is has been shown that this is due to the slower gel time resulting in the polymer chains forming to have greater chain mobility which allows restructuring during the formation of siloxane bonds and as a result be highly cross-linked (Drabarek et al. 2002). The faster gel time samples bond rapidly and are unable to rotate or rearrange the polymer chains, which results in a less ordered linked structure with a lower number of cross-links. The greater the number of cross-links, the stiffer the gel within the pore space and the stiffer the resulting treated

sand. The variability in the 0.3N samples can be attributed to the spatial variability of the polymer chain formation within the sample, but the trend is still evident.

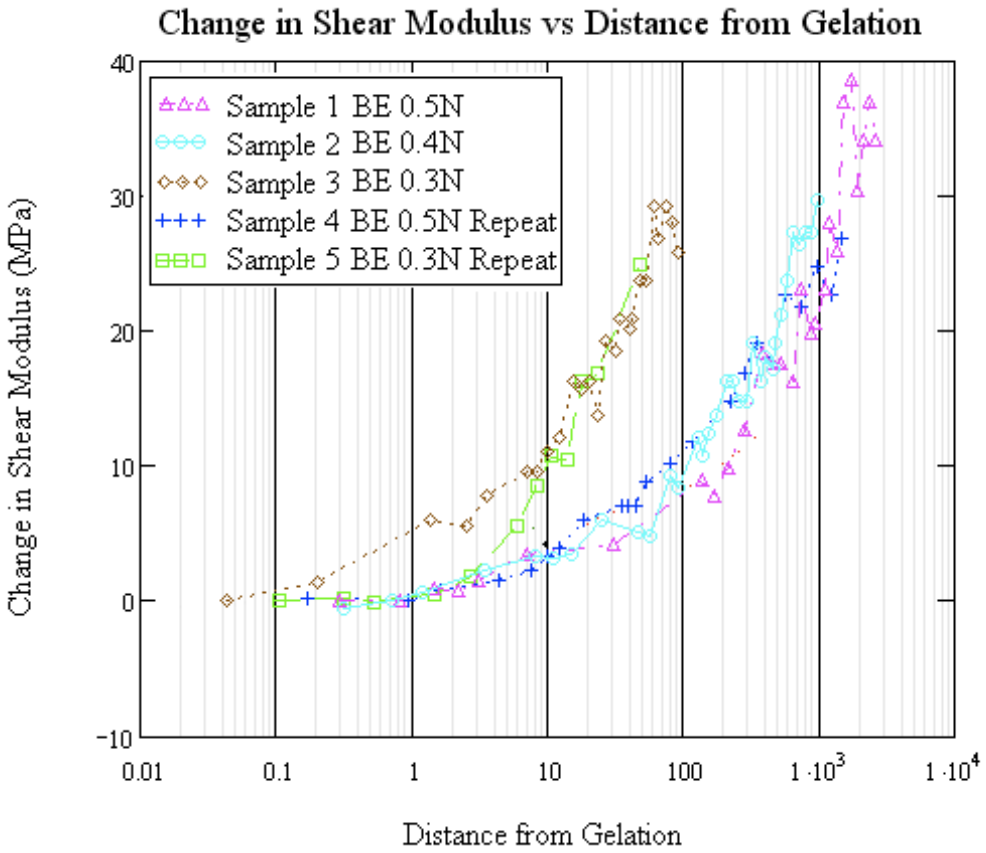

Figure 4.15 Change in shear modulus versus distance from gelation of the bender element samples

4.3.7. Comparison with Untreated Sand

4.3.7.1.Shear Modulus Increase in Untreated Sand

It has been shown that aging of sands increases the initial tangent shear modulus logarithmically, with little change in soil density (Anderson and Stokoe II 1978; Wang and Tsui 2009). It has also been shown that the aging, or curing, of colloidal silica gel increases the strength (Axelsson 2006; Hench and West 1990) and stiffness (Scherer et al. 1988). When investigating the effect of aging on the small-strain shear modulus of sands treated with colloidal silica gel, it becomes difficult to identify the portion of the increase

in G_{max} due to particle rearrangement and contact force homogeneity caused by creep (Mesri et al. 1990; Wang and Tsui 2009) or due to the increased chemical bonds that form overtime. To identify the contribution of the small-strain shear modulus increase due to the colloidal silica gel, a measure of increase used in the literature must be employed.

The increase in shear modulus with time can be estimated by

$$N_G = \frac{\Delta G / \log_{10}(t_2 / t_1)}{G_{1000}} \times 100\% \qquad 4.6$$

where N_G is the normalized change in small strain shear modulus with time, G_{1000} is the shear modulus measured after 1000 minutes of aging and ΔG is the change in shear modulus between times t_1 and t_2 (Anderson and Stokoe II 1978; Baxter and Mitchell 2004; Wang and Tsui 2009). Many researchers have found bias and error when calculating the N_G, some of which result in negative N_G values (Baxter and Mitchell 2004; Howie et al. 2002; Wang and Tsui 2009). To calculate the N_G for this research, it is difficult to determine what value should be used for G_{1000} when the soil has been treated with colloidal silica gel that has time-dependent stiffness increase. The gel time, or T_{gel}, of the samples investigated have a range of 40 minutes to 1200 minutes, thus the G_{1000} value is well into the curing stage of the 0.4N and 0.5N samples, but still before the gel time of the 0.3N samples. This makes using an arbitrary time to determine the shear modulus value introduce bias into the comparison of the colloidal silica treated samples due to the influence of the gel time. Therefore, it is suggested that a shear modulus value that has a normalizing effect on the data is used, and this is the value of the shear modulus at the gel time, G_{Tgel}. The value of N_G and the percent increase from the gel time through the duration of the test for each sample is shown in Table 4.2.

Table 4.2 Comparison of N_G and G_{Tgel} for the Colloidal Silica Gel Aging Tests

Sample Number	Approximate Gel Time (hr)	N_G	$\Delta G/G_{Tgel}$[1]	$\Delta G_{7d}/G_{Tgel}$[2]
1	2/3	53.3	288	108
2	2	113.3	702	219
3	20	79.4	215	92
4	2/3	47.0	218	136
5	20	146.4	392	134
Resonant Column	2	9.9	12.1*	5.2

[1]The change in G from the time of gelling to the entire length of the test
[2]The change in G from the time of gelling to 7 days after gelling
*The G_{Tgel} is not within the time period of the test, so $G_{10*Tgel}$ is used

Previous studies investigating the effect of aging on sand reported N_G values ranging from 1-5% for silica sand (Anderson and Stokoe 1978; Baxter and Mitchell 2004). Using the published N_G values, a schematic has been developed comparing a general shear modulus aging trend for untreated sand to the treated bender element samples and is shown in Figure 4.16. The untreated sand increases 5% per log cycle and the bender element test results are increasing at a rate greater than the untreated sands.

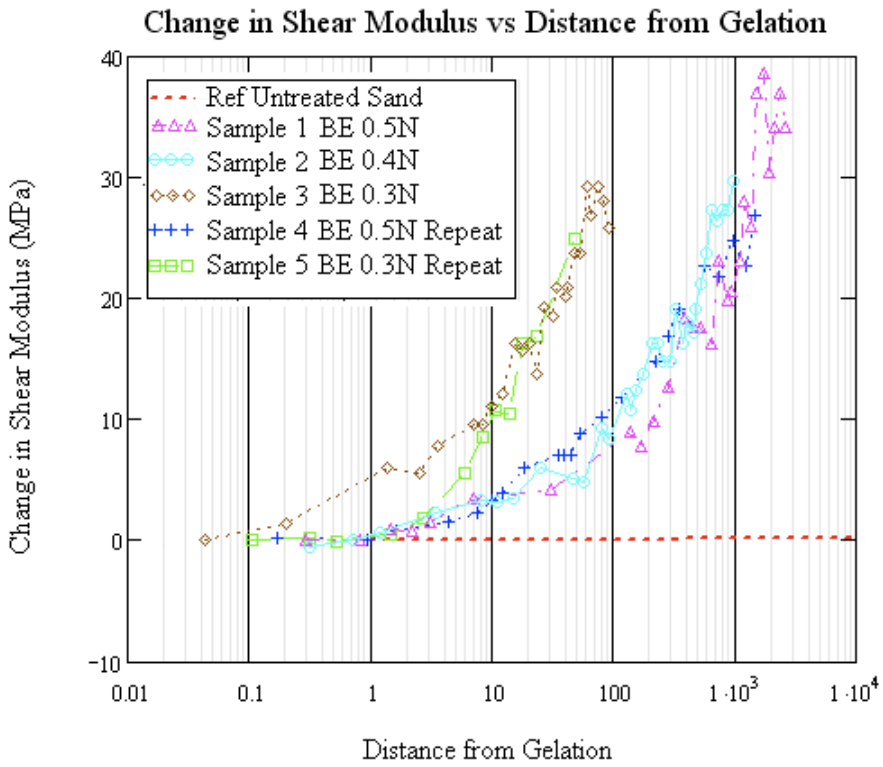

Figure 4.16 Comparison of increase in shear modulus of the treated bender element tests compared to published increasing values, N_G (from Anderson and Stokoe 1978) of untreated sand

Researchers have shown that the reference shear modulus leads to a bias in the N_G value (Howie et al. 2002; Wang and Tsui 2009) and to combat this, Wang and Tsui (2009) have suggested using a different shear modulus normalizing value (Wang and Tsui 2009), as suggested above for this study. The calculation to determine the influence of aging on the shear modulus is $\Delta G_{7d}/G_{in}$, where ΔG_{7d} is the change in shear modulus after the specified aging days (as indicated by the subscript) and G_{in} is the initial state, taken as the shear modulus after aging 1 minute. Using this metric, an increase in the small-strain shear modulus of loose and dense samples of Ottawa and Toyoura sand subjected to constant confining pressure of 35 kPa over 7 days showed an increase ranging from 4 to 7% (Wang and Tsui 2009). The percent increase values over 7 days have been calculated for the BE samples and are shown in Table 4.2. The change in the shear modulus over 7 days was calculated using the shear modulus at gel time as the

normalizing value and the aging was calculated 7 days after gelling occurred. The $\Delta G_{7d}/G_{Tgel}$ for the BE samples are much higher than any results found by Wang and Tsui (2009) for clean sands.

The BE values of percentage increase and N_G are much larger than published values for clean sands. Therefore, it can be concluded that the influence of the increasing chemical bonds caused by the curing of the colloidal silica contributes to the aging phenomenon that increases the small-strain shear modulus overtime.

4.3.7.2.Comparison of Results to Empirical Values

The sample shear wave velocity values were compared to empirical estimated shear wave velocities calculated from Hardin and Black (1968) using Equation 4.7 and Seed and Idriss (1970) using Equation 4.8 (Chung et al. 1984; Hardin and Black 1968; Hardin and Drnevich 1972; Seed et al. 1986).

$$G_{\max} = 1230 \cdot \frac{(2.973 - e)^2}{1 + e} \cdot OCR^K \cdot \sigma'^{0.5}_o \qquad 4.7$$

where

G_{max} = small-strain shear modulus, in psi

K = 0 for cohesionless soils

σ'_o = mean effective confining stress, in psi

$$G = 1000 \cdot K_2 \cdot \sigma'^{1/2}_m \qquad 4.8$$

where

G = shear modulus, in psf

K_2 = soil modulus coefficient (ranging from 30 to 75 for loose to dense sands)

σ'_m = mean effective confining stress, in psf

The results of the BE tests and the calculated shear wave velocities from the empirical equations above are shown for each sample in Figure 4.17. All of the BE test samples

have an initial shear wave velocity below the calculated empirical values. All, but Sample 2, of the BE tests approach the lower empirical shear wave velocity, calculated by the Hardin and Black equation, around approximately 40 days into testing.

The empirical formulas correlate well with the small-strain shear modulus values obtained by resonant column testing that was presented in Chapter 3. Therefore, the empirical formulas are a good estimate of the expected values. As such, it would be expected for the shear modulus around the gel time to correlate with the empirical values, however this is not the case. A possible explanation for the discrepancy between the empirical values and the bender element specimens is the order of applying the load and treating with colloidal silica. The resonant column specimens were consolidated before colloidal silica gel was permeated through the specimen and the BE samples were pluviated through the colloidal silica solution and then confinement was applied. Santamarina et al. (2001) discussed how at the same cement content at low confining pressures, the tangent modulus is greater for the loading-before-cementation because larger particle contacts develop before cementation. The process of colloidal silica gelation includes bonding at the particle contacts and is similar to cementation and this could be a consideration in why the resonant column shear modulus values correlate well with the empirical values while the bender elements are less than the empirical values.

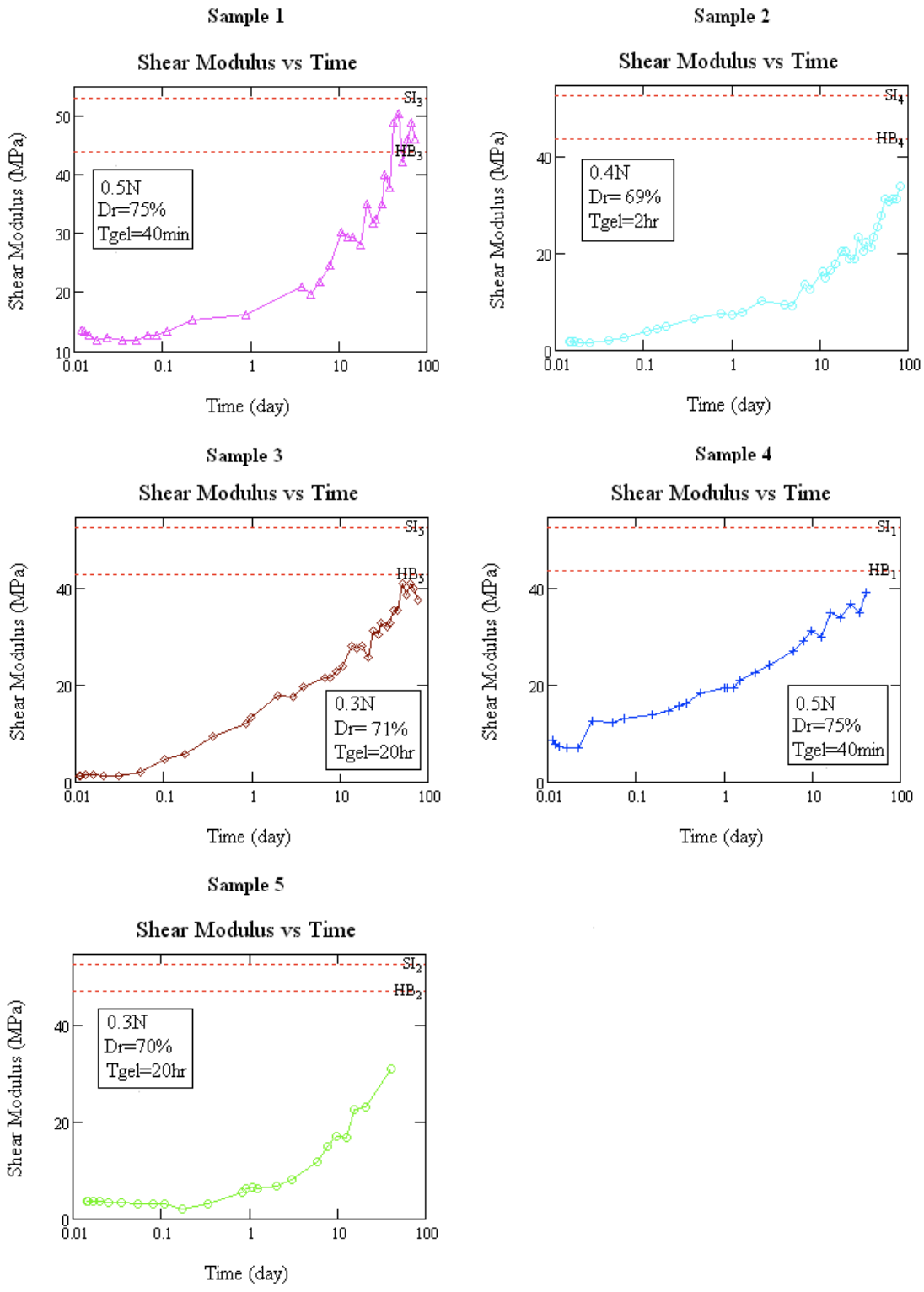

Figure 4.17 Comparison of shear modulus values to empirical values for all BE samples

4.3.8. Colloidal Silica Gel Experiments

Multiple attempts were made at measuring the shear modulus of colloidal silica gel alone. A picture of the first test configuration is shown in Figure 4.18. The measurements were unsuccessful because the signal traveled through the testing apparatus as opposed to the colloidal silica gel. The test configurations used in subsequent attempts were similar, with varying types of support structures to avoid the signal traveling through the bender element housing device. However the different bender element housings were unsuccessful.

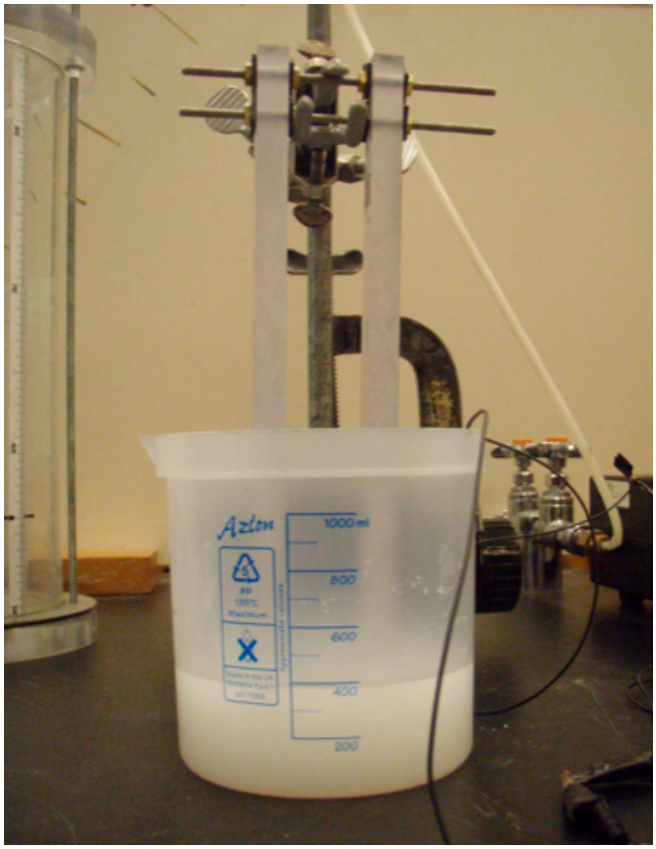

Figure 4.18 Colloidal silica gel bender element test set-up

4.4. Resonant Column Experiment

The effect of aging on the small strain dynamic properties was investigated by subjecting a five-weight percent colloidal silica gel treated sand sample to resonant column tests over a period of 28 days.

4.4.1. Test Procedure

Nevada No 120 test sand was air pluviated to a relative density of 50%. The properties of Nevada No 120 sand are shown in Table 3.2. The sample was consolidated and then treated with five-weight percent colloidal silica solution and allowed to cure for 10 times the gel time before subjected to resonant column tests. The same resonant column equipment was used as described in Section 3.2. The sample was pluviated, consolidated and permeated on the modified end platens as shown in Figure 3.9 to reduce sample disturbance. The resonant column tests were performed over a period of 28 days. Three trials were run at each time interval to identify the repeatability of the measurements; the resonant frequency identified during each trial was the same. The testing was performed at an effective confining pressure of 26 kPa. The tests were run at the smallest cyclic shear strain achievable by the signal generator, a 5mV swept sine that resulted in a cyclic shear strain amplitude of 2.5×10^{-4}% for each of the measurements.

4.4.2. Resonant Column Results

The small-strain shear modulus, G_{max}, results obtained from resonant column tests over a period of 28 days on 50% relative density sand treated with five-weight-percent colloidal silica are shown in Figure 4.19. The small-strain damping ratio over time is shown in Figure 4.20. The shear modulus increases 6.5 MPa, or 12%, over 28 days. Due to resonant column sample preparation, the first measurement was taken at $10*T_{gel}$ and this is the reference value used for percentage increase. The increase in shear modulus follows a logarithmic trend. The damping ratio slightly increases, a total of 0.1%, over 28 days. The trend is clearly increasing, however, all the damping ratio values, except the first and last data point, plot within +/- one standard deviation of the mean damping ratio. The frequency resolution of the resonant column data affects the accuracy of the calculated damping ratio and therefore could have caused error in the values. The increase in damping ratio is contrary to the trend found by Wang and Tsui (2009), that

small-strain damping ratio of sand decreases approximately 11% to 20% overtime, due to the stiffening of the sample and reduced energy loss.

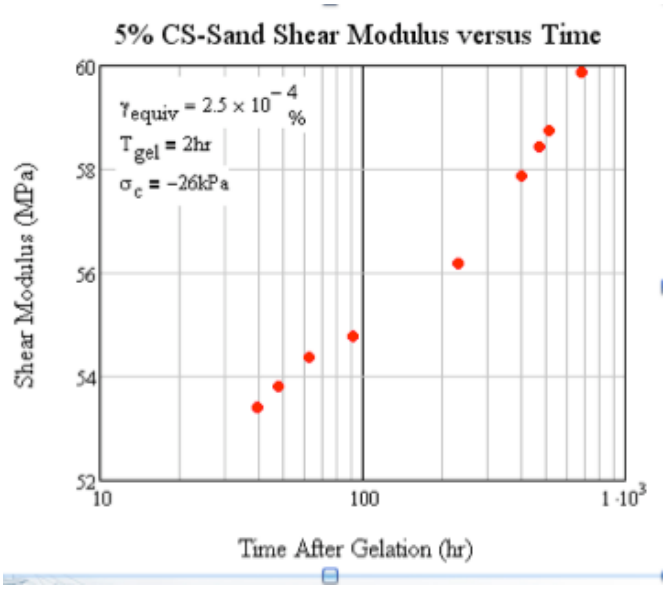

Figure 4.19 Shear modulus versus time of 5% weight colloidal silica treated sand

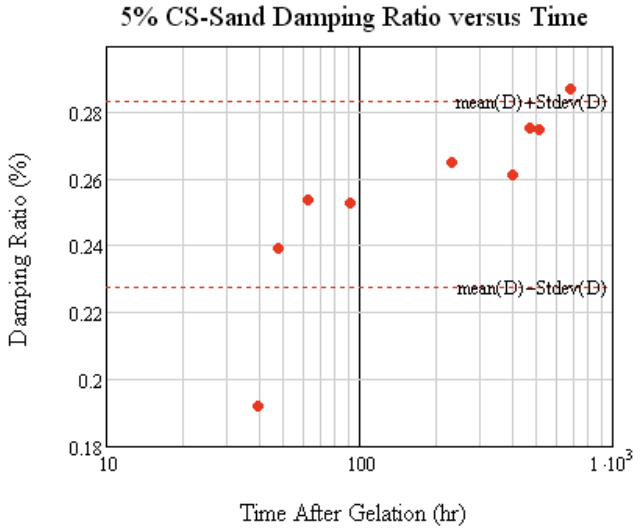

Figure 4.20 Damping ratio versus time of 5% weight colloidal silica treated sand

4.4.2.1.Comparison of Resonant Column and Bender Element Samples

Previous work has been done comparing bender element and resonant column tests results performed on the same samples and have found good agreement (Dyvik and Madshus 1985; Ferreira et al. 2007; Youn et al. 2008). However, some research by Youn

et al. (2008) showed that bender element tests on saturated samples will result in higher G_{max} values due to the frequency of excitation used in the bender elements to impart the initial shear wave. This is due to the Biot's theory on the dispersion of a shear wave (Santamarina et al. 2001; Youn et al. 2008) as described in Section 2.2.4.2.

The change in shear modulus obtained in the resonant column test is compared to the bender element results in Figure 4.21. The resonant column sample was permeated with 0.4N NaCl ionic concentration colloidal silica solution, and plots well with the 0.5N and 0.4N bender element data.

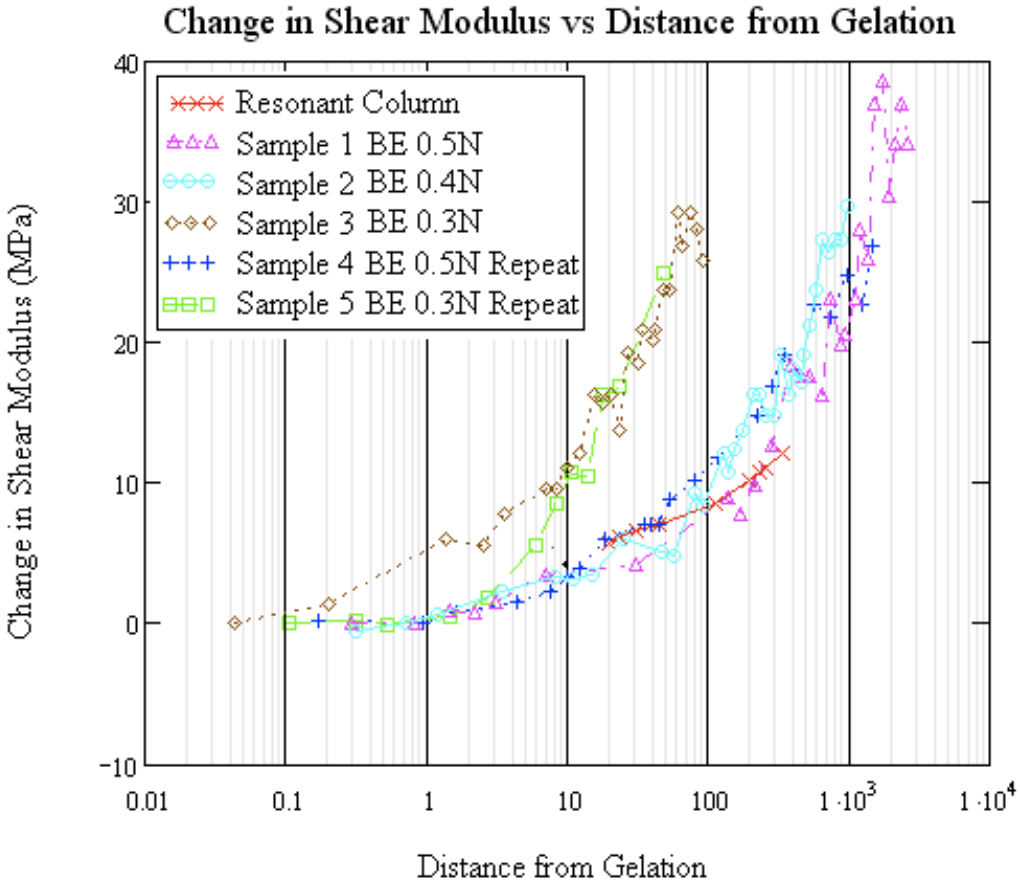

Figure 4.21 Comparison of RC and BE sample change in shear modulus versus distance from gelation

The percentage increase and N_G for the resonant column test results are shown in Table 4.2. When looking at the small-strain shear modulus increase of the resonant

column sample over the first 7 days (168 hours) of the test, there is an increase of approximately 5%, which is on the order of the increase found by Wang and Tsui (2009) for dense Ottawa sand at low confining pressures. More than 50% of the aging effect due to stiffness increase occurs within the first 2 days of aging for sands (Wang and Tsui 2009), therefore an aging period of 7 days to compare the literature values and the resonant column test is adequate. However, the due to sample preparation in resonant column testing, the first point was used as the value of G_{in}, which occurred 24 hours after permeating the sample with the colloidal silica solution, at approximately $T = 10*T_{gel}$. Therefore, the value of G_{in} could be lower if there were data available earlier than $10*T_{gel}$, which would increase the percentage change over the seven day period. The percentage increase in the shear modulus by resonant column test is on the order of the clean sand aging tests, however the N_G value is larger than published values.

Research has shown that denser samples experience a greater increase in stiffness (Baxter and Mitchell 2004; Li and Yang 1998), which corresponds to the differences in rate of increase between the RC (loose) and BE (dense) samples in this study. However, Wang and Tsui (2009) demonstrated that at low confining stress, aging-induced increase in small-strain shear modulus is more significant in loose samples than in dense samples. It has also been found that isotropic stress states, such as the resonant column, results in a slower rate of increase in stiffness (Howie et al. 2002).

To identify if the change in shear modulus (ΔG) versus distance from gelation is a good normalization for treated sand data, the average shear modulus value for five-percent-weight colloidal silica (0.4N ionic concentration) treated sand obtained at $10*T_{gel}$ from the results in Chapter 3 are shown with the aging resonant column and bender element tests in Figure 4.22. The shear modulus value obtained in Chapter 3 falls along the 0.4N line and fits the trend well on the plot.

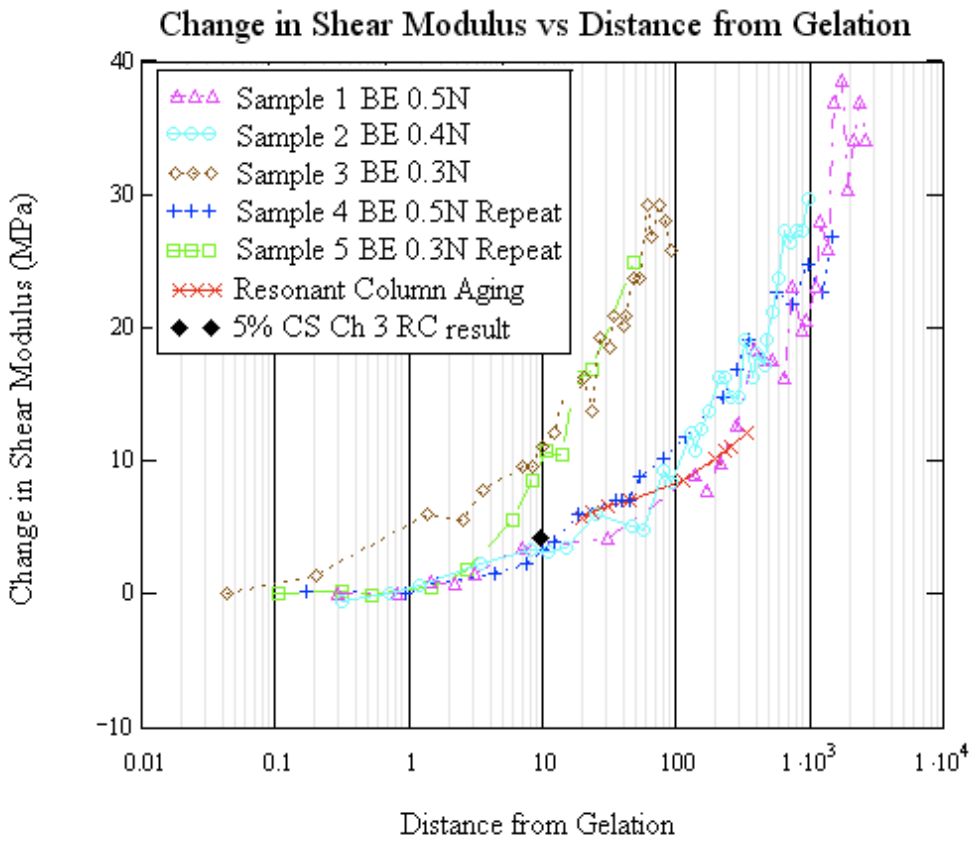

Figure 4.22 Comparison of aging RC and BE sample change in shear modulus versus distance from gelation with Chapter 3 5% weight colloidal silica gel result

4.5. Estimation of Treated Sand Shear Modulus

4.5.1. Heuristic Model

It has been shown that the bulk and shear moduli of fluid and particle mixtures can be determined by summing the contribution of each material to the modulus. The bulk modulus of sand with fluid-filled pore space can be determined using the simplified Gassmann equation (Santamarina 2001), as shown below.

$$B_{mix} = B_{sk} + \frac{1}{\frac{n}{B_f} + \frac{1-n}{B_g}} = B_{sk} + B_{sus} \qquad 4.9$$

where:

B_{sk} is the bulk modulus of the soil skeleton,

B_g is the bulk modulus of the grain within the suspension fluid,

n is the porosity, and

B_f is the bulk modulus of the fluid, which is defined as:

$$B_f = \frac{1}{\frac{S}{B_w} + \frac{1-S}{B_a}} \tag{4.10}$$

where:

B_w is the bulk modulus of water,

B_a is the bulk modulus of air, and

S is the saturation of the fluid phase, $S = V_w/V_f$.

The simplified Gassmann equation is applicable in particulate materials at low confinement, where the $B_{sk} << B_g$. However, when the fluid within the pore space is replaced with colloidal silica instead of water, the bulk modulus of the matrix becomes the sum of the bulk modulus of the soil skeleton and the bulk modulus of the colloidal silica suspension. Upon gelling, the colloidal silica gel forms a skeleton of silica particles with water in the gel pore space, so the bulk modulus of the sand and colloidal silica gel matrix is

$$B_{matrix} = B_{sk} + B_{CSmix} = B_{sk} + B_{CSsk} + B_{CSsus} \tag{4.11}$$

where:

B_{CSsk} is the bulk modulus of the colloidal silica particle (gel) skeleton, and

B_{CSsus} is the bulk modulus of the fluid within the gel skeleton pore space.

However, the shear modulus is of interest when considering the shear wave velocity of the sand and gel matrix, and Berryman (1999) showed that the shear modulus is the same for a dry or fluid-filled medium at low frequencies (Santamarina 2001). Therefore, the shear modulus of the sand and gel matrix is composed of the modulus of the sand skeleton and the modulus of the colloidal silica gel skeleton, as shown below

$$G_{matrix} = G_{sk} + G_{CSsk} \quad (4.12)$$

where:

G_{sk} is the shear modulus of the sand skeleton, and

G_{CSsk} is the shear modulus of the colloidal silica gel skeleton.

4.5.1.1. Comparison of Results to Heuristic Model

To estimate the shear modulus of the treated sand using the heuristic model proposed in Equation 4.12, the measured shear modulus of dry untreated sand is used to for G_{sk} (obtained either from resonant column or bender element testing) and the shear modulus of the colloidal silica gel can be estimated by using Equation 2.6 given by Scherer et al. (1988) for the elastic shear modulus of 10-weight-percent colloidal silica gel. The shear modulus estimated from Equation 4.12, G_{matrix}, is compared to the results of the five-weight-percent colloidal silica treated sand (T_{gel} = 40 min) bender element results and is shown in Figure 4.23. The estimated modulus matches very well with the bender element test results for the initial 30 days and then the bender element test results continue to rise at a rate faster than the estimated modulus, indicating the method is a good approximation of treated sand shear modulus for the initial period. It is hypothesized that the drying of the sample that occurred during the bender element experiments resulted in an increase in the rate of shear modulus increase towards the end of testing, which can explain the deviation from the trend after 30 days.

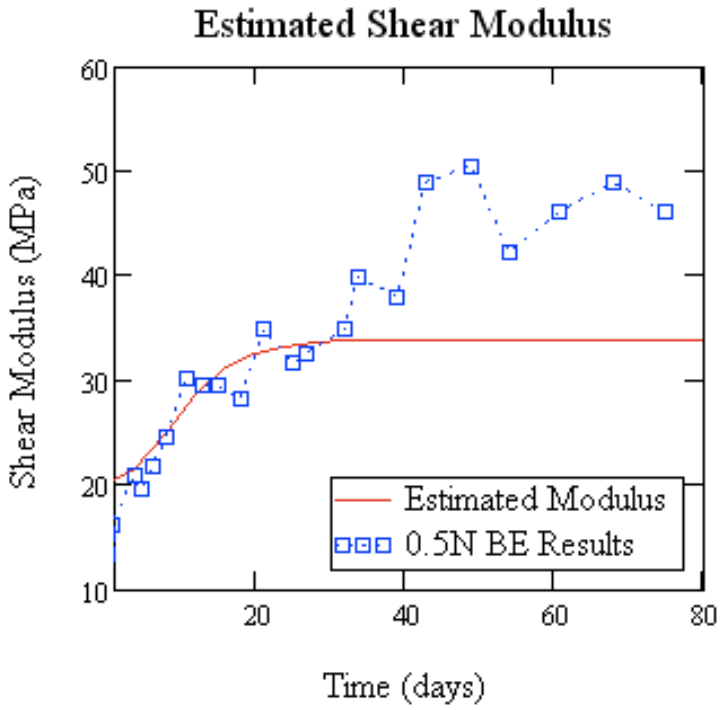

Figure 4.23 Estimated shear modulus of colloidal silica gel and sand mixtures versus aging time compared to the aging bender element test results. The estimated shear modulus aging was calculated using the Scherer et al. (1988) equation of shear modulus aging (T_{gel} = 14 hr).

The estimated shear modulus from Equation 4.12, using the shear modulus of the sand skeleton, determined from untreated dry sand resonant column test, and colloidal silica gel, determined using Equation 2.6, is compared to the small-strain resonant column aging test results in Figure 4.24. The resonant column data has been fit with a logarithmic curve. The value at zero days is the shear modulus of the sand skeleton only. The resonant column results increase at a rate much faster than the estimated modulus but the rate of modulus increase levels off before the estimated modulus. The estimated and observed small-strain shear modulus value at 30 days is within 3%, indicating a good estimation at the end of the resonant column testing duration.

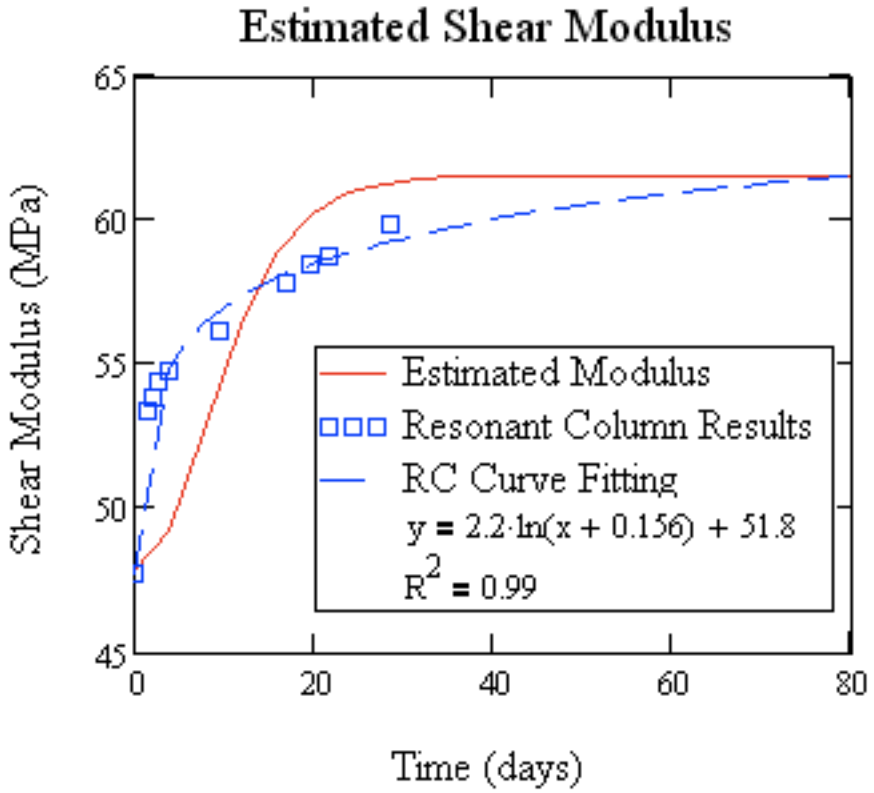

Figure 4.24 Estimated shear modulus of colloidal silica gel and sand mixtures versus aging time compared to the aging resonant column test results, 5% wt T_{gel} = 2hr. The estimated shear modulus aging was calculated using the Scherer et al. (1988) equation of shear modulus aging (T_{gel} = 14 hr).

The estimated modulus curve obtained by summing the modulus of the sand skeleton with the modulus of the gel results in a good estimation of the treated sand shear modulus. Both the bender element and resonant column data fit the estimated modulus well, with slight variation in the initial portion of the curve (found in the resonant column) or past 30 days, where the bender elements increase faster. The variation can be attributed to the loading-permeation order of the samples. The rate of increase in the initial portion of the curve of the resonant column data can be attributed to the confinement being applied before permeation, because as gelation occurs, the existing particle contacts are being reinforced by the gel skeleton structure, so the interaction of the sand skeleton and gel skeleton result in a quick increase in shear modulus immediately after gelling. Whereas the estimated modulus does not account for the

particle-gel-interaction; however, as the gel ages and becomes stiffer, the particle contacts are already supported by the gel within the pore space and the rate of increase slows as the main source of modulus increase becomes the increase in the gel itself. On the contrary, the bender element samples were pluviated through the silica sol, so initial particle contacts were not created before introduction of the sol into the pore space. This leads to the initial portion of the bender element data matching very well with the estimated modulus because the particle-contact network was undeveloped prior to testing and the resulting measured modulus increases at the rate of the of the increase in gel alone.

4.5.2. Ciz and Shapiro Model

Work by Ciz and Shapiro (2007) developed a modified Gassmann equation for the shear modulus of a porous material saturated with a solid material. These equations are capable of capturing the contribution of a solid (or quasi-solid) pore-filling material to the mixture shear modulus, such as the case in sand treated with colloidal silica gel. The solid-saturated shear modulus for the isotropic case can be determined using

$$G_{matrix}^{-1} = G_{sk}^{-1} - \frac{(G_{sk}^{-1} - G_{gr}^{-1})^2}{n(G_{CS}^{-1} - G_n^{-1}) + (G_{sk}^{-1} - G_{gr}^{-1})} \qquad 4.13$$

where:

G_{matrix} is the solid-saturated mixture shear modulus,

G_{sk} is the drained shear modulus of the porous frame,

G_{gr} is the shear modulus of the grain material making up the porous frame,

G_{CS} is the shear modulus of the solid body pore infill,

G_n is the shear modulus of the pore space of the porous frame, and

n is the porosity of the porous frame.

4.5.2.1.Comparison of Results to Ciz and Shapiro Model

To estimate the shear modulus expected from a porous sand matrix saturated with a shear modulus contributing solid material, or colloidal silica gel, the shear modulus of dry sand obtained by the resonant column or bender element test is used as the G_{sk} and the respective porosity, *n*, of the resonant column or bender element sample. The shear modulus of the sand grain, G_{gr}, is $3.8x10^4$ MPa (Richardson et al. 2002) and $G_{gr} = G_n$. The shear modulus of the colloidal silica gel can be estimated using Equation 2.6, given by Scherer et al. (1988). The estimated shear moduli values of the sand treated with colloidal silica gel are compared to the resonant column and bender element aging results in Figure 4.25 and Figure 4.26. The Ciz and Shapiro model overestimates the resonant column results in the long-term. The 0.5N bender element specimen (Sample 1) compares well with the Ciz and Shapiro model. The initial portion of the bender element data that falls below the sand only shear modulus is due to the pluviation-before-confinement, however the estimated model is the upper bound for the bender element data.

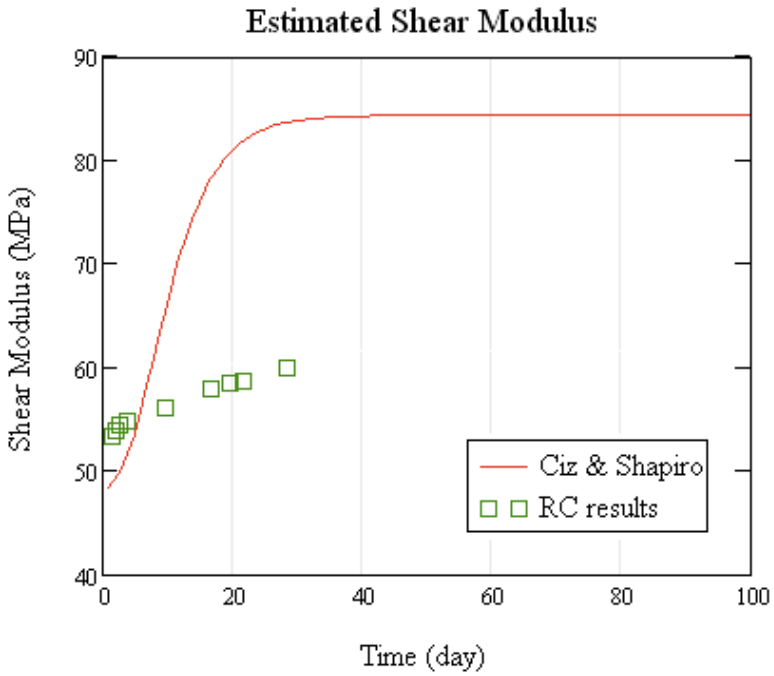

Figure 4.25 Ciz and Shapiro (2007) estimated shear modulus of colloidal silica gel and sand mixtures versus aging time compared to the aging resonant column test results, 5% wt T_{gel} = 2hr. The estimated shear modulus aging was calculated using the Scherer et al. (1988) equation of shear modulus aging (T_{gel} = 14 hr).

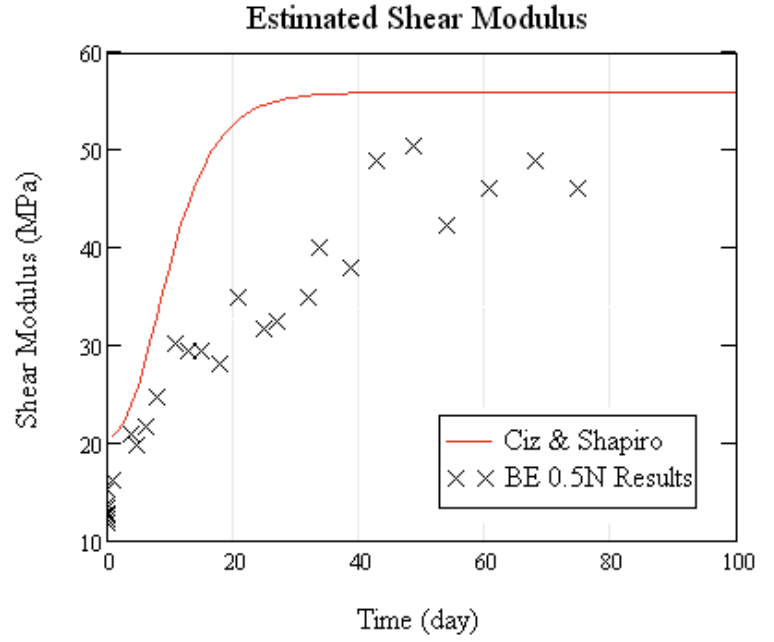

Figure 4.26 Ciz and Shapiro (2007) estimated shear modulus of colloidal silica gel and sand mixtures versus aging time compared to the bender element aging test results, 0.5N T_{gel} = 40 min. The estimated shear modulus aging was calculated using the Scherer et al. (1988) equation of shear modulus aging (T_{gel} = 14 hr).

4.5.2.2.Comparison of Shear Modulus Estimation Models

The estimated shear moduli with time using the heuristic and Ciz and Shapiro (2007) models have been determined and are plotted with the results from the resonant column and 0.5N bender element (Sample 1) tests. It is evident that the two models form an upper (Ciz and Shapiro model) and lower (heuristic model) bound for the estimated shear modulus of sand treated with colloidal silica gel. The resonant column results fall close to the lower bound while Sample 1 of the bender elements begins on the lower bound and rises towards the upper bound however it never reaches it.

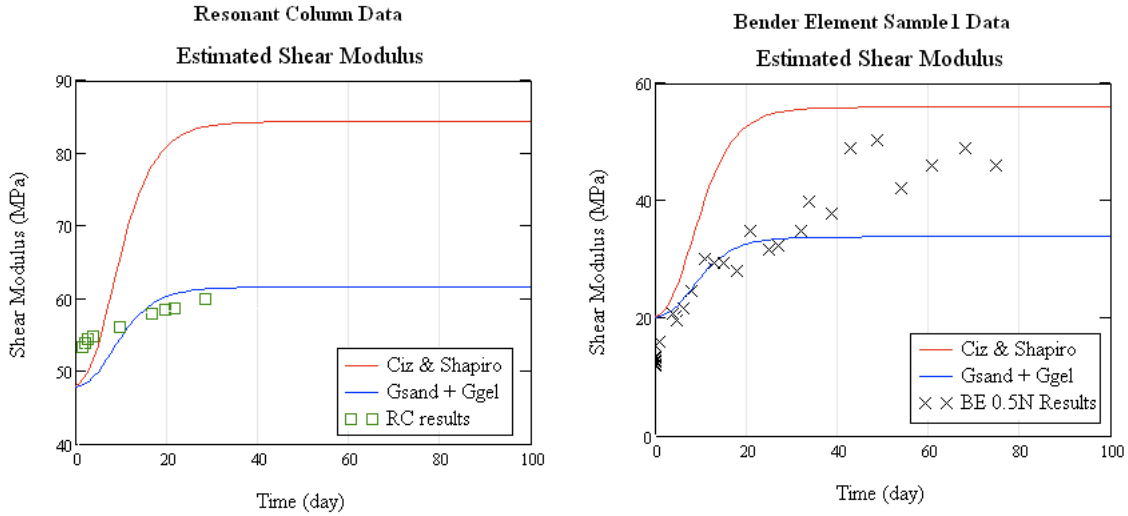

Figure 4.27 Comparison of Ciz and Shapiro estimated shear modulus and heuristic estimated shear modulus of colloidal silica gel and sand mixtures versus aging time compared to the bender element and resonant column aging test results

4.6. Conclusions

A passive method of liquefaction mitigation involves the treatment of saturated loose sands with colloidal silica gel. The introduction of colloidal silica gel into the pore space of loose sands slightly increases the small-strain shear modulus in short time frames. However, the time horizon for liquefaction mitigation treatment requires the long-term small-strain shear modulus of treated sands to be identified for use in characterizing the treated soil over time. Research has shown that both untreated sands

and colloidal silica gel experience an increase in shear modulus with time, however the effect of aging on the small-strain shear modulus of treated sands has not previously been studied.

A comparative study of the influence of colloidal silica gel on the effect of small-strain dynamic properties due to aging was presented. One resonant column test and five bender element tests were performed over a period of time to track the evolution of the shear wave velocity over time to identify the change in shear modulus due to aging. Three different ionic concentration colloidal silica solutions were used to treat the sand samples and identify repeatability of the measurements. Resonant column tests over 28 days determined that initial tangent shear modulus increased 12% and small-strain damping ratio slightly increased due to aging in the first 28 days. The bender elements test results showed an increase in small-strain shear modulus ranging from 200 to 700% over the duration of the tests, ranging from 42 to 82 days.

By comparing published results of the increase in small-strain shear modulus of silica sands, it was concluded that the siloxane bonds that continue to form overtime due to the curing of the colloidal silica gel affect the increase in G_{max} with time. A heuristic approach to estimate the treated shear modulus, by summing the shear modulus of the sand skeleton and the shear modulus of the colloidal silica gel within the pore space, was shown to fit the increase in shear modulus with time of the treated sands measured in the resonant column well. The bender element results plot towards the upper bound of the shear modulus that is estimated by the model developed by Ciz and Shapiro (2007).

5. EVALUATION OF PARTIAL COLLOIDAL SILICA TREATMENT TO REDUCE LIQUEFACTION-INDUCED DAMAGE TO PILES

5.1. Introduction

Research has shown that treatment of loose sands with five-weight-percent colloidal silica gel resists deformations and mitigates liquefaction risk (Gallagher and Mitchell 2002). However, treatment of an entire liquefaction-prone site may be cost prohibitive and it has been demonstrated that there is a limiting width of treatment around or under a structure beyond which additional treatment will not substantially reduce the movements of the structure (Cooke and Mitchell 2003). To reduce the cost of treatment but still maintain the ability to reduce liquefaction-induced damage to the structure, the use of a partial treatment zone upslope of a pile group, as illustrated in Figure 5.1, will be investigated to identify the efficacy of partial treatment with colloidal silica gel.

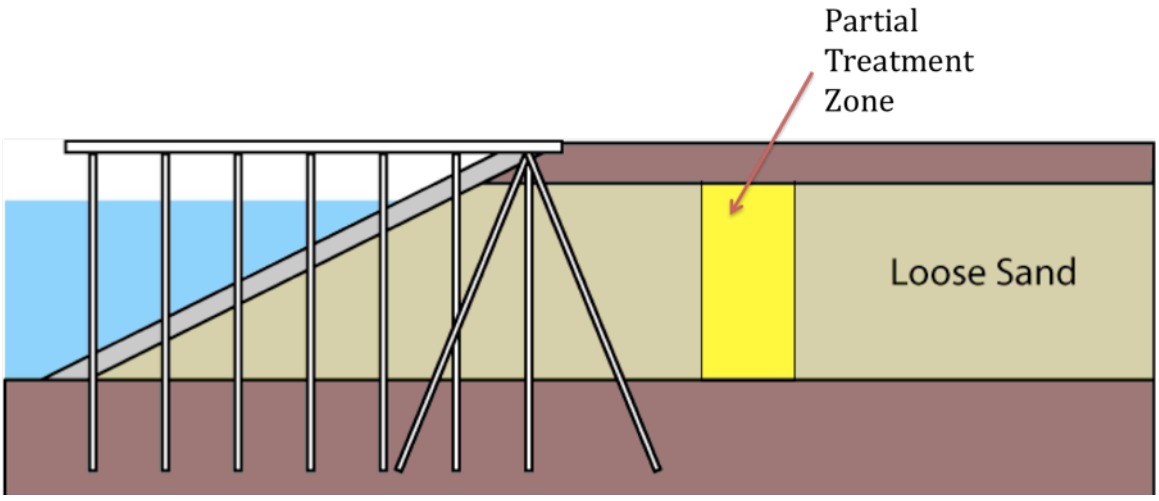

Figure 5.1 Schematic of partial treatment zone in wharf structure

It is important to consider the access to the target partial treatment area of a wharf structure when determining the best location for treatment. Abdoun et al. (2005) and Pamuk et al. (2007) have shown a pile group in a three-layer soil profile consisting of slightly cemented top and bottom layers with a loose sand layer in the middle treated with

six-weight-percent colloidal silica gel experienced a reduction in the bending moments and lateral spreading. However, it is not feasible to treat the area surrounding the piles of a marginal wharf due to lack of access for equipment to perform the grout injection. Therefore, it is necessary to identify another partial treatment zone that would adequately reduce the lateral-spreading-induced pile damage.

A series of 1-g shaking table tests were conducted at the University of Tokyo on loose sand to determine the efficacy of partial treatment with colloidal silica gel to mitigate damage to pile groups caused by liquefaction-induced lateral spreading. In each of the tests, a block of treated sand of varying dimensions was located upslope of the pile group. The response of the piles with the partial treatment zone is compared to the response without any treatment.

5.2. Liquefaction-Induced Ground Deformation

Liquefaction-induced ground displacements have caused significant damage to pile foundations and buried pipelines; evidence of this damage was observed in the 1964 Niigata, 1984 Nihokai-Chubu, 1989 Loma Prieta and 1995 Kobe earthquakes (Ashford et al. 2006; Jang and Hamada 2007; Motamed 2007). Evidence of deep-foundation damage caused by lateral spreading includes the Yachiyo and Showa bridges in the 1964 Niigata earthquake and the 7th Street Terminal Wharf batter piles in the 1989 Loma Prieta earthquake (Ashford et al. 2006).

5.2.1. Pile Foundations Subjected to Lateral Force of Liquefied Soil

Piles and pile groups are subjected to the inertial effects of the supporting structure and the kinematic effects caused by the lateral loads applied by the liquefied soil (Abdoun et al. 2003).

5.2.1.1.Lateral Displacements

Multiple researchers have performed shaking table tests and found that the magnitude of the lateral soil displacements that occur are dependent on the input ground motion and the relative density of the soil. Similar results were found for shaking table tests on liquefied ground behind both floating-type and gravity-type quay walls and for sloped-ground-surface experiments. As the amplitude of the acceleration input motion increases, so does the lateral soil movement; whereas the lateral soil displacement increases as input acceleration frequency decreases (Motamed 2007; Motamed and Towhata 2010; Toyoto et al. 2004). Lateral soil movement increases as relative density decreases (McVay et al. 1998; Motamed and Towhata 2010).

5.2.1.2.Bending Moments

Many researchers have studied pile bending moments caused by liquefaction-induced ground deformations using shaking table tests either with a centrifuge or at 1-g conditions. Pile bending moments are dependent upon the soil profile and properties, pile boundary conditions and inertial loads, and whether the pile is a single pile or within a pile group. The behavior of a pile within a pile group varies depending on the pile position (McVay et al. 1998; Motamed and Towhata 2010). This is due to the different locations of the piles within a pile group experiencing different lateral ground displacements (Cubrinovski and Ishihara 2006).It has been shown that bending moments increase and then decrease during shaking even though lateral displacements continue, indicating strain softening in the soil around the foundation (Abdoun et al. 2003).

Bending moments are usually large at soil-layer interfaces between a liquefiable and non-liquefiable layer and at the pile cap (Gonzalez et al. 2009; Harada et al. 2006). Larger pile bending moments are also caused by the passive pressure on the pile and pile cap exerted by a shallow non-liquefiable layer atop a liquefied layer when compared to the pressure exerted by the liquefied soil itself (Abdoun et al. 2003). Ashford et al. (2006)

performed a blast-induced lateral spreading, full-scale test and found that the liquefied layer did not produce significant forces on the piles; rather the bending moments were caused by the mobilized clay layer on top of the liquefied soil while the piles were embedded in a dense-gravel sublayer.

Pile-head constraint is also a consideration in determining where the maximum bending moments will occur; a free-head pile will be allowed to displace more at the top and the bending moment will be zero. However a pile cap or a fixed-head condition produces a bending moment in the pile-head opposite of the moment at the base of the pile (Motamed and Towhata 2010). The presence of a pile cap and local soil densification increases the maximum pile bending moment due to an increased foundation area exposed to the lateral pressures. This problem is compounded by the pile cap providing resistance to rotation (Abdoun et al. 2003). End-bearing pile groups experience reduced bending moments in comparison to single end-bearing piles and the moment reduction is dependent upon the axial forces on piles within the group (Abdoun et al. 2003).

5.2.2. Mitigation of Liquefaction-Induced Lateral Spreading Damage Using Colloidal Silica Gel

Abdoun et al. (2005) and Pamuk et al. (Abdoun et al. 2005; 2007) performed a centrifuge test investigating the treatment of a liquefiable layer consisting of 40% relative density saturated Nevada sand treated with 6%-by-weight colloidal silica gel between slightly cemented sand layers on the response of a 2-by-2 end bearing pile group. The models were subjected to 30 cycles of input motion with a peak amplitude of 0.25g (prototype) and a frequency of 2 Hz (prototype). Both the treated and untreated models experienced monotonically increasing lateral displacements and pile bending moments through the completion of shaking. However, the treated model did not liquefy, experienced reduced free-field and foundation displacements and drastically decreased the pile bending moments. The reduction in free-field displacement was 92% between the

treated and untreated model and the treatment with colloidal silica gel resulted in a 90% reduction in lateral-spreading-induced axial compressive and tensile forces along the pile (Pamuk et al. 2007). The upslope and downslope pile bending moments of the treated model were reduced by 90% in comparison to the untreated model. It was found that the untreated model failed passively around the pile cap whereas the treated soil did not fail (Abdoun et al. 2005).

5.2.3. University of Tokyo Shaking Table Testing

The University of Tokyo has a history of performing shaking table tests under the advisement of Professor Ikuo Towhata. A study of interest is the investigation of a 3-by-3 pile group within a loose, liquefiable sand performed by Motamed (2007). The materials and dimensions of the tests performed were used as a guide for this research and the details can be found in the following sections. The work by Motamed demonstrated that 30% relative density sand subjected to 0.3 g-amplitude shaking at 10 Hz (model) resulted in repeatable pile response, and therefore these parameters were used for this research. The results of the work demonstrated that the upslope and downslope pile rows experienced the largest bending moments with the middle pile row being the least distressed. Similarly, the outer piles experienced higher bending moments than the center piles within a row.

5.3. Equipment

5.3.1. Shaking Table

The shaking table employed for testing belongs to the Geotechnical Engineering Laboratory of the Civil Engineering Department at the University of Tokyo. It is a 3-m-by-2-m bi-axial shaking table with a loading capacity of seven tons as shown in Figure 5.2. The displacement control system of the shaking table consists of a servo unit that controls the position of the piston, a vibration control unit to regulate the magnitude of

the input motion acceleration, an input equalizer to transfer the input acceleration into displacement signals and a power control unit that regulates the oil pressure in the piston (Motamed 2007). The data acquisition system associated with the shaking table has eight data loggers able to record 120 channels with a sampling frequency up to 1000 Hz.

Figure 5.2 Picture of the shaking table at the University of Tokyo

The container used to construct the models is a rigid container made of transparent acrylic plates with a steel frame and a system of pipes at the bottom for drainage. The box used in testing was 2.65 m in length, 0.40 m in width and 0.60 m in height. The transparent side walls allow for observation of the model during testing.

5.3.2. Soil Characteristics

The sand used for the shaking table tests was Albany silica sand with the index properties shown in Table 5.1. One of the advantages of 1-g shaking table testing is that larger models can be employed at a lower cost than centrifuge tests. However, the reduced stress level under 1-g conditions can affect the stress-strain behavior of the sand

in comparison to the full-scale prototype profile. To overcome this, it is proposed to use looser sand for testing as demonstrated in Figure 5.3. Towhata (2005) showed using data from Verdugo and Ishihara (1996) showed that two specimens with the same void ratio (e=0.908) displayed strain-hardening or strain-softening behavior depending on whether the effective confining pressure was 98 kPa or 1960 kPa, respectively. Therefore it is not appropriate to use the same density under significantly reduced confining pressures. However, a strain-softening response can be achieved at the lower effective stress level with a looser specimen (e=0.949) as shown in Figure 5.3. To achieve strain-softening behavior in the 1-g shaking table tests, the specimens were prepared at a relative density of 30%.

Table 5.1 Index properties of Albany silica sand (Motamed 2007)

Specific gravity, G_s	2.646
Maximum void ratio, e_{max}	0.741
Minimum void ratio, e_{min}	0.470
Mean particle diameter, D_{50} (mm)	0.302
Uniformity coefficient, U_c	2.237

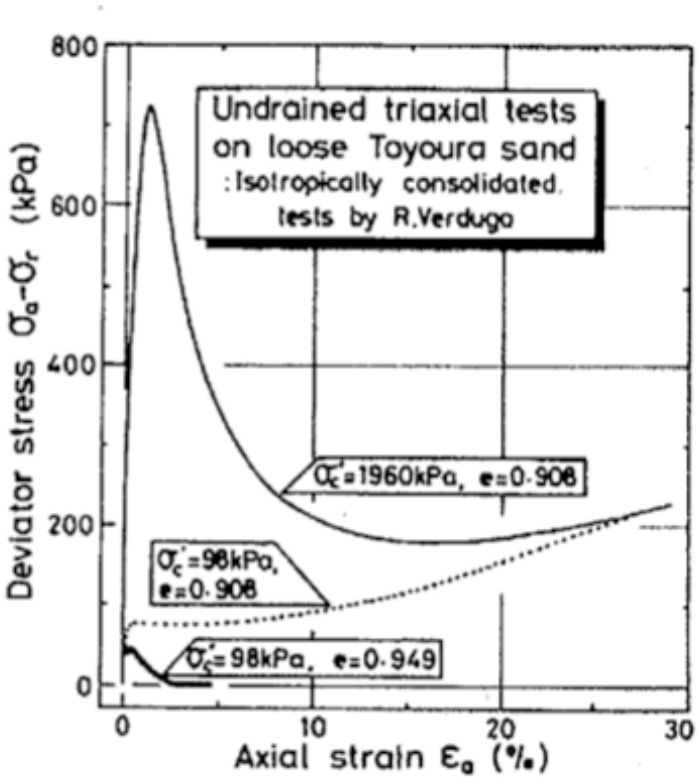

Figure 5.3 Undrained triaxial compression tests under different effective stress levels at different densities (from Towhata 2005)

5.3.3. Model Piles

The properties of the model piles used are summarized in Table 5.2. The piles were fixed at the bottom and free at the top to simulate prototype piles that are embedded into a dense layer. This boundary condition also allows one to back-calculate the force and deformation of the piles more readily. The piles were arranged in a 3-by-3 group with a spacing of 2.8 pile diameters between the piles in both horizontal directions.

Table 5.2 Material properties of pile (Motamed 2007)

Material	Polycarbonate
Height (cm)	53
Outer/Inner Diameter (cm)	3.2/2.7
E (N/cm^2)	270000
I (cm^4)	2.5385

The models have a geometric scaling factor of 30, so the model and prototype pile properties using similitude for 1-g shaking tests (Iai 1989) are shown in Table 5.3. The prototype pile flexural rigidity, EI, is lower than would be expected for common pile materials such as steel or concrete.

Table 5.3 Model and prototype properties of pile

	Model	**Prototype**
Height	53 (cm)	15.9 (m)
Diameter	3.2 (cm)	96 (cm)
EI	68.5 N*m^2	10140 kN*m^2
Input Frequency	10 Hz	1.8 Hz

5.4. Instrumentation

Several different types of instrumentation were used during the experiments to record test data. These sensors include strain gages along the piles, accelerometers, pore water pressure transducers, inclinometers, and a laser displacement transducer.

5.4.1. Strain Gages

Each pile was instrumented with eight pairs of Kwoya SKF-23993 strain gages along the length of the pile to measure the bending strain along the pile during testing and calculate bending moments in the piles. The strain gage locations are shown in Figure 5.4 and a picture of an instrumented pile is shown in Figure 5.5.

5.4.1.1.Strain Gage Calibration

All piles were empirically calibrated to obtain the bending moment from measured strain values. The same boundary conditions of fixed at the bottom of the pile and free at the top were replicated during calibration. Different known forces were applied to the top of the pile and the bending strain was recorded for each strain gage along the pile length. For each strain gage, a plot of recorded bending strain versus the

calculated theoretical bending moments (M_{theory}) was created to obtain an empirical calibration factor for each strain gage as shown in Figure 5.6.

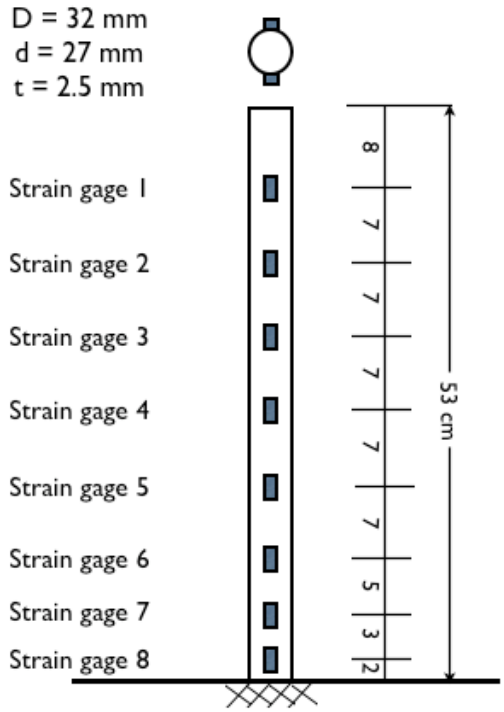

Figure 5.4 Schematic of strain gage location on model pile

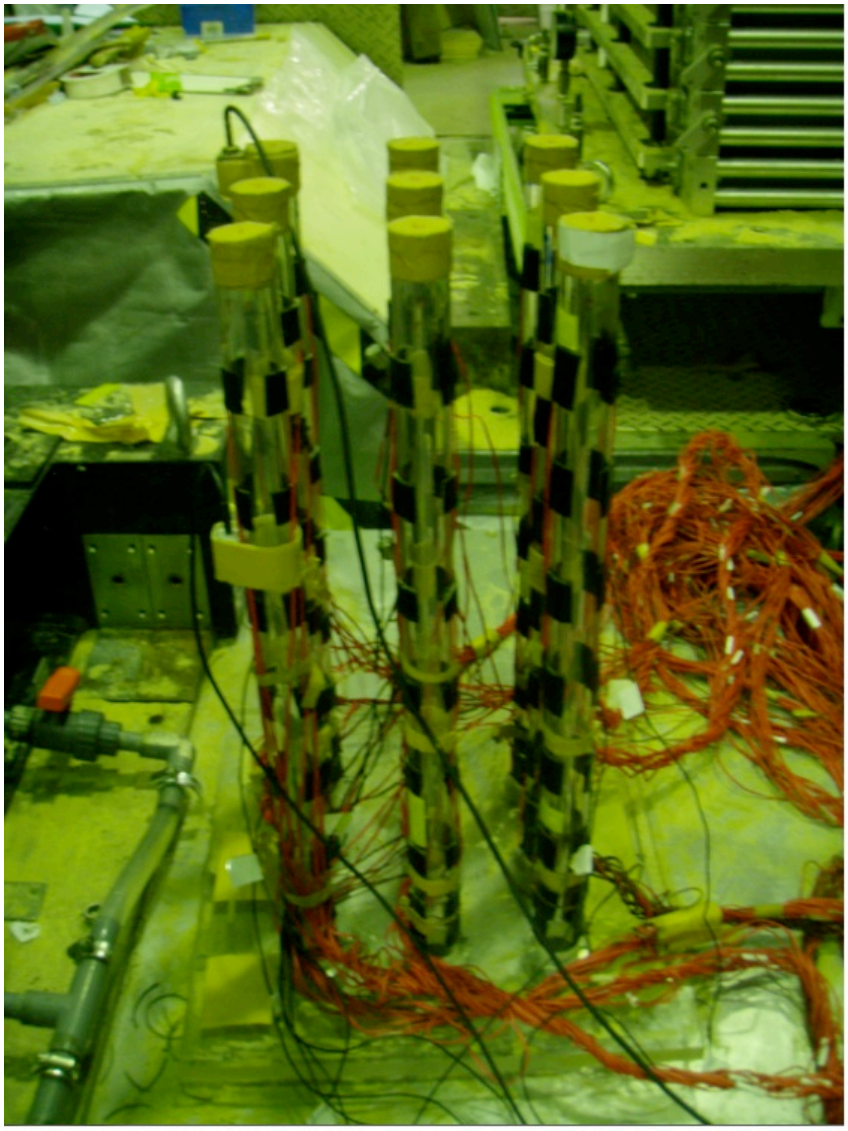

Figure 5.5 Photo of instrumented piles with strain gages (under the black tape)

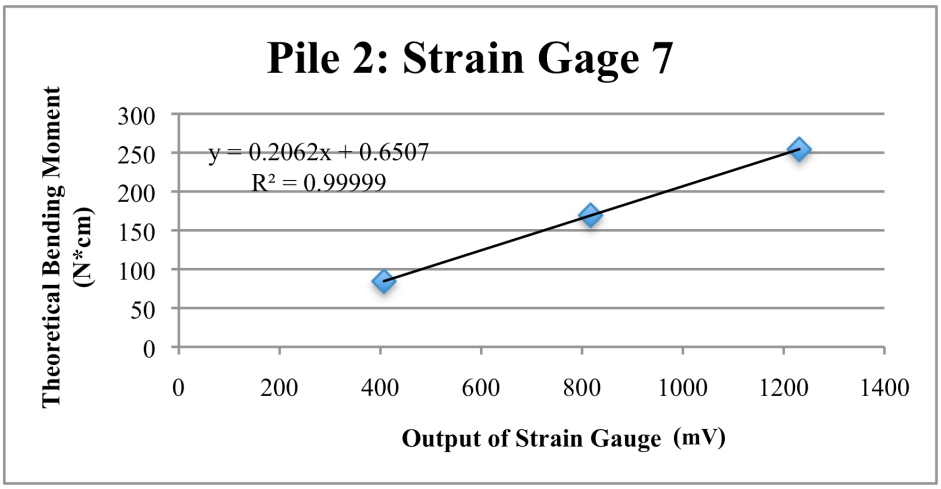

Figure 5.6 Example of empirical strain gage calibration (Strain gage 7 on Pile 2)

It is also possible to obtain theoretical calibration factors by using the material properties of the pile. The relationship between bending strain and bending moment is:

$$M = \sigma \frac{I}{y} = E\varepsilon \frac{I}{y} \qquad 5.1$$

where

M: bending moment

σ: bending stress

I: area moment of inertia about the neutral axis

y: perpendicular distance to neutral axis

E: modulus of elasticity

ε: bending strain

A theoretical calibration factor can be calculated using Equation 5.1, resulting in a calibration factor of 0.42836 (N-cm/mV), which is larger than the empirically determined factors due to assumptions in material properties. The calibration factors employed in this study were all obtained empirically.

5.4.2. Accelerometers

Accelerometers were employed to record horizontal accelerations at different locations throughout the model. The accelerometers used have a 2-g maximum capacity and each accelerometer was checked before testing. To prevent accelerometers from tilting during testing, base plates were attached to the accelerometers for stabilization. However, some sensors tilted as a result of liquefaction-induced lateral movement of the soil. These inclined records were corrected to obtain the true horizontal acceleration by using:

$$Acc_{true} = \frac{Acc_{meas} - g \cdot \sin\theta}{\cos\theta} \qquad 5.2$$

where θ is the angle of tilt from the horizontal.

5.4.3. Inclinometers

Inclinometers were utilized in this study to record liquefaction-induced lateral displacement of the soil. The inclinometers were constructed by arranging a series of accelerometers in a column by attaching them to acrylic plates connected by hinges as shown in Figure 5.7. The relative horizontal displacement between the top and bottom of each plate (S) is obtained using Equation 5.3 and total horizontal displacement (D) is calculated with Equation 5.4.

$$S_k = L \cdot \sin(\theta_k) \qquad 5.3$$

$$D_i = \sum_{k=1}^{i} S_k \qquad 5.4$$

where

S_i: relative displacement at i-th level

L: length of acylic plate

Θ_i: angle of inclination at i-th level

D_i: total displacement at i-th level

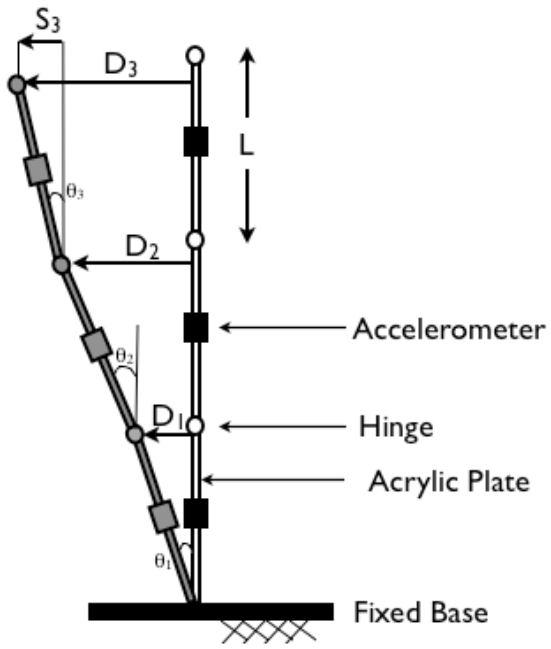

Figure 5.7 Schematic of inclinometer displacement

5.4.4. Pore Water Pressure Transducers

Pore water pressure transducers (PWPT) were used to record excess pore water pressure generation due to shaking and consequent liquefaction. These sensors were located throughout the soil mass and attached at different locations on the piles as shown in the testing configurations that follow for each test sample. The PWPT were secured within the soil mass by using string to suspend them at different heights to prevent subsidence during liquefaction. The PWPT were saturated before testing began by allowing the water level to come above the elevation of the PWPT. The caps were opened and air bubbles were removed to allow full saturation. The caps were then replaced and the sensors remained submerged for the remainder of specimen preparation.

5.4.5. Laser Displacement Transducer

A laser displacement transducer (LDT) was used to measure the displacement time history of one of the corner piles during shaking. The LDT was attached to the container box and a target was attached to the top of the pile. The resolution of the LDT

is +/- 1 mm, so the measurement is used as an estimation of pile displacement time history.

5.5. Model Preparation

5.5.1. Testing Configurations

Five shaking table tests were performed at the same amplitude and frequency of shaking. The height and width of each treated colloidal silica block was the same, nominally 43 cm in height and 24 cm in width. The height was chosen to be at the surface level of the sloping ground at the treatment location and the width was chosen to be 2D larger than the width of the pile group to have a 1D overlap on each side of the group. The thickness of the colloidal silica block and distance upslope from the pile group varied on each test as shown in Table 5.4. The treated silica block thickness dimension was constrained by the need to have the thickness substantial enough to support its own weight and remain stable during sample construction but it still must be small enough to be handled with care during transport and placement into the container. The thickness of the block was chosen to be as close to one and two times the pile spacing (2.8D and 5.6D), respectively, while still meeting the constraints. The distance of the treated block upslope of the piles was one and two times the pile spacing.

Table 5.4 Shaking Table Test Configurations

Test Number	Colloidal Silica Block Thickness (cm)/pile spacing	Distance Upslope of Pile Group (cm)/pile spacing	Relative Density (%)
1	Untreated	N/A	28
2	15/5.4D	18/5.6D	29
3	10/3.1D	18/5.6D	30
4	15/5.4D	9/2.8D	30
5	15/5.4D	9/2.8D	28

5.5.2. Container Set-up

5.5.2.1.Instrumentation Placement

The instrumentation locations for each test are shown in the test configurations in Figure 5.8 through Figure 5.12. Most instrumentation employed during testing was placed before sample preparation began. The strain gages, excess pore water pressure transducers and accelerometers attached to the piles were secured before placement of the pile group into the rigid-wall test container. The inclinometer plates were aligned perpendicular to expected soil flow in a vertical position and securely attached to the base board within the container and attached to a rod across the top of the container as shown in Figure 5.13. Once the specimen preparation was complete, the inclinometer was detached from the top to allow the inclinometer to track the lateral movement of the soil.

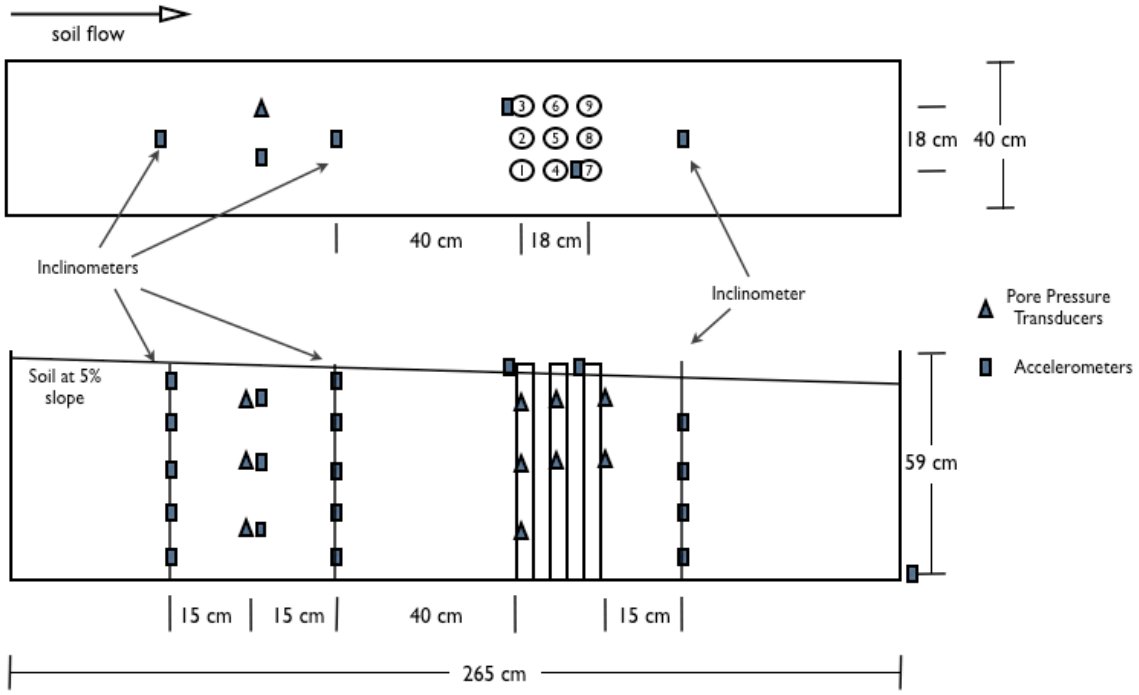

Figure 5.8 Testing congifuration for Test 1

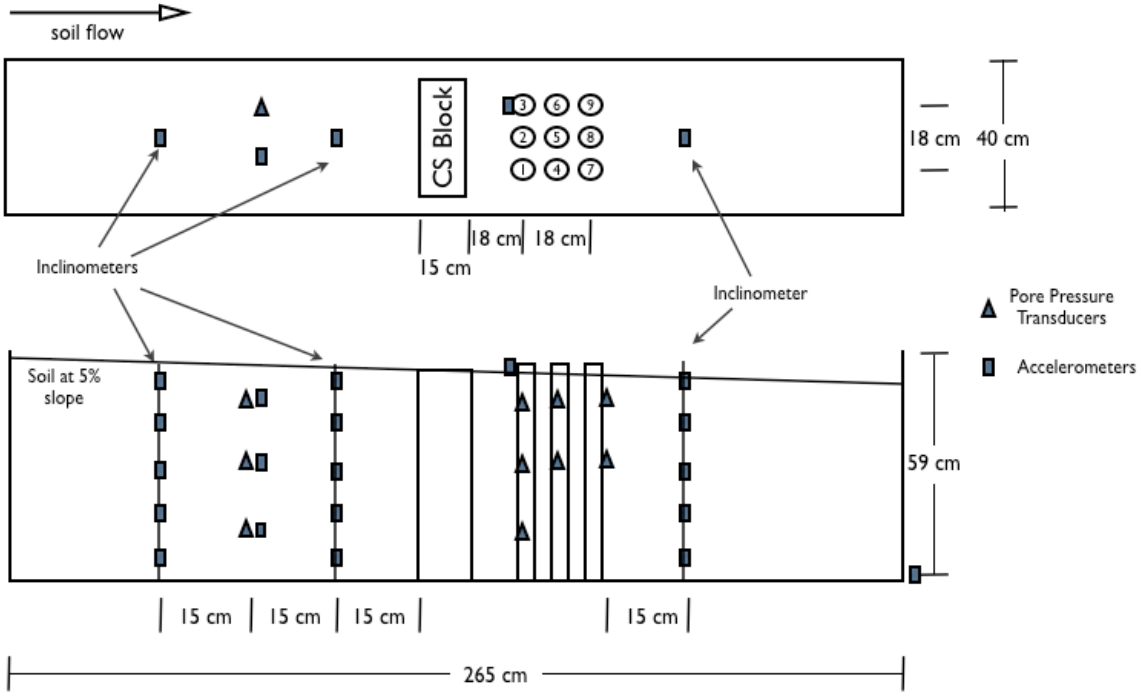

Figure 5.9 Testing congifuration for Test 2

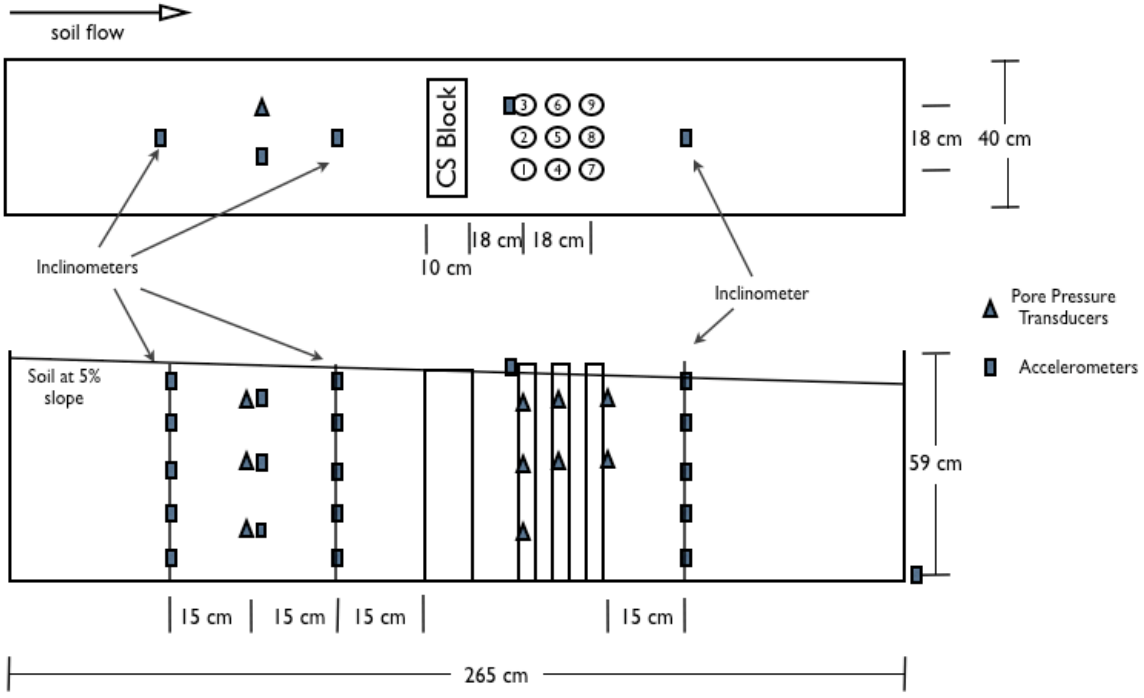

Figure 5.10 Testing congifuration for Test 3

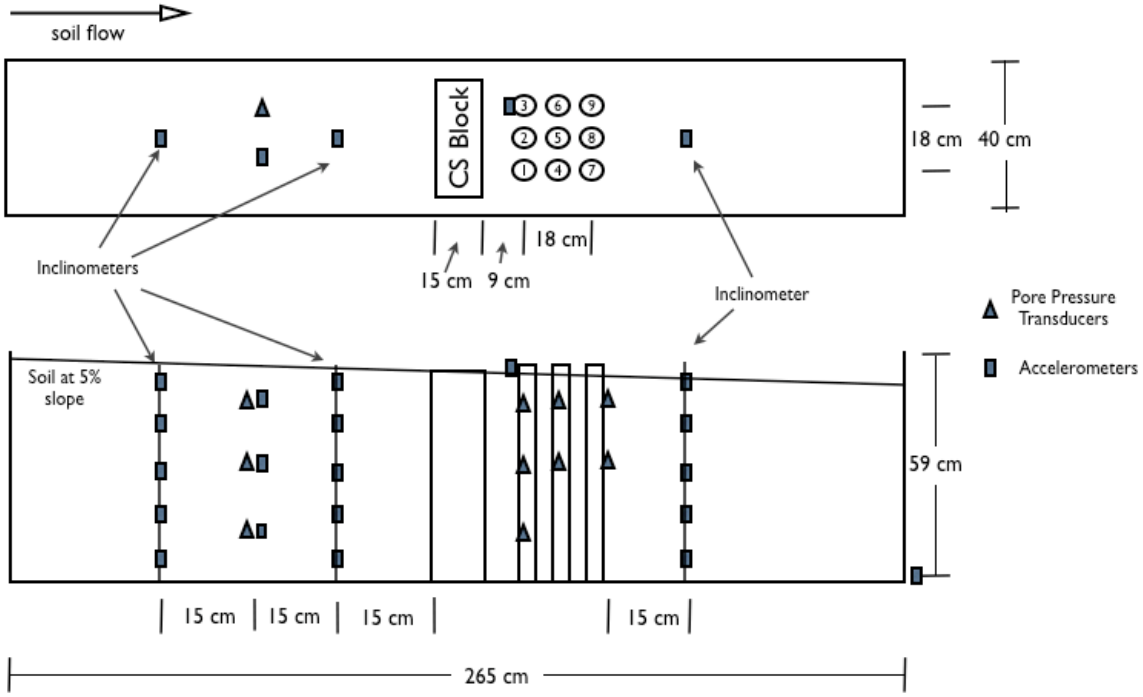

Figure 5.11 Testing congifuration for Test 4

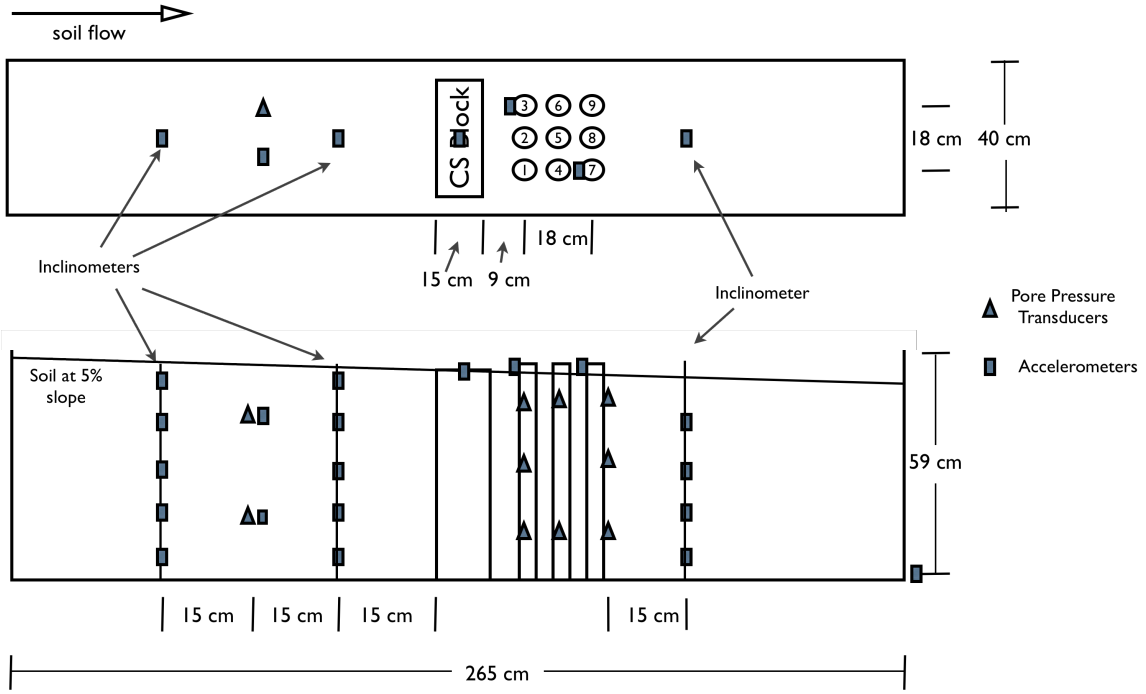

Figure 5.12 Testing congifuration for Test 5

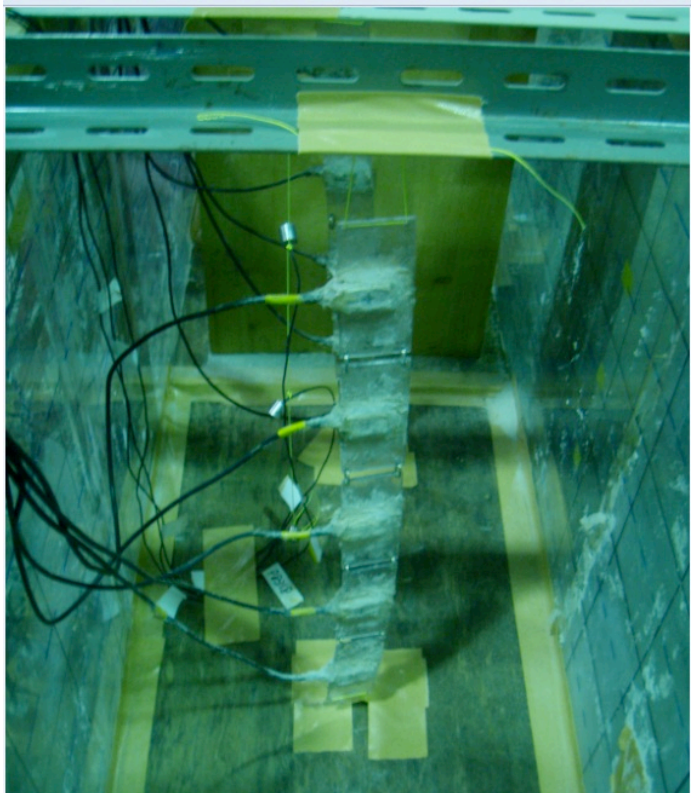

Figure 5.13 Photo of inclinometers in place before sample preparation

The accelerometers used upslope of the pile group were placed during sample preparation; as the target height for the accelerometer was reached by the sand, the accelerometers were aligned correctly and pressed into the level sand and sand was placed over it to reduce the movement during the remainder of sample preparation.

5.5.2.2.Pile Set-up

The 3-by-3 pile group fixed-base boundary condition was accomplished by screwing each pile into a pile base plate as shown in Figure 5.5 and securing with a nut at the bottom of the base plate to prevent pile rotation during testing. The piles were aligned so the strain gages were perpendicular to the flow of the liquefied sand.

5.5.2.3.Sand Placement

The testing container was fitted with wooden boards level with the pile base plate, used to ensure the piles were fixed at the bottom. These boards were then shimmed to

ensure that no movement of the pile base plate would occur. Once the boards were snugly inserted, the drains were closed and the container was filled to 10 cm above the wooden boards with water. The water pluviation method was used to obtain loose, saturated specimens. The weight of the sand was measured before adding it to the container to allow for calculation of the relative density. After every 5-cm lift of sand, the water level was increased such that it was 10 cm above the surface of the sand. This process was repeated until the specimen was completed. The top surface of the specimen was constructed with a slope of 5% to promote lateral spreading of the liquefied soil.

5.5.2.4.Colloidal Silica Treated Sand Block

Due to material constraints at the testing location, the treated sand blocks were constructed outside of the rigid-wall shaking table container and moved into the container before testing. The colloidal silica solution used by the University of Tokyo (a different, proprietary colloidal silica solution than used in the previous laboratory testing) was mixed and poured into a rigid plastic container as shown in Figure 5.14. The plastic container was sprayed with WD-40 and lined with aluminum foil to facilitate removal of the treated sand block as shown in Figure 5.15. The treated sand was left to cure for a period of at least three weeks to reach a resonating gel state (according to the proprietary colloidal silica gel information) before removal. The treated sand block was then trimmed to the desired test dimensions and placed into the rigid-wall test container for specimen preparation as shown in Figure 5.16. Figure 5.17 shows the treated sand block placed adjacent to the model piles in the container.

Figure 5.14 Colloidal silica treated sand block preparation

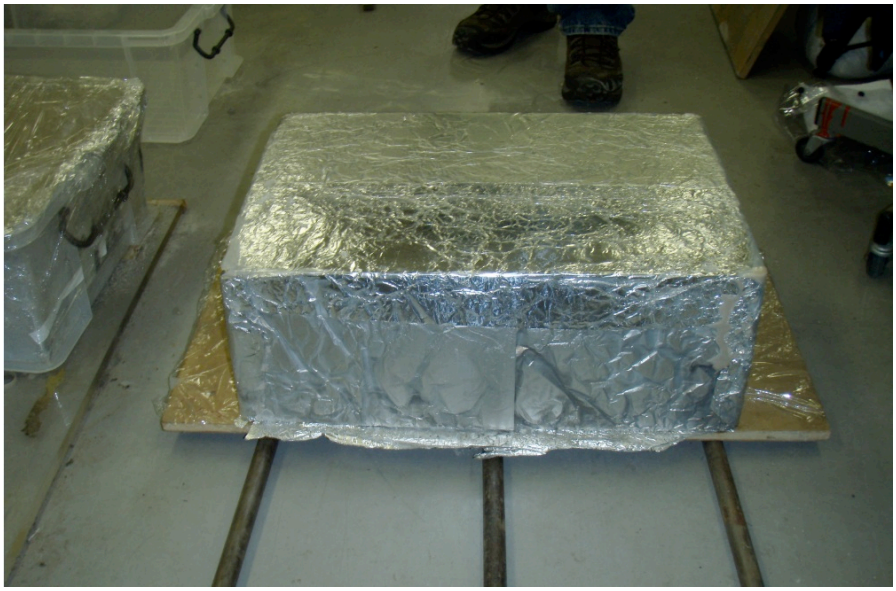

Figure 5.15 Cured colloidal silica treated sand block after removal from plastic container

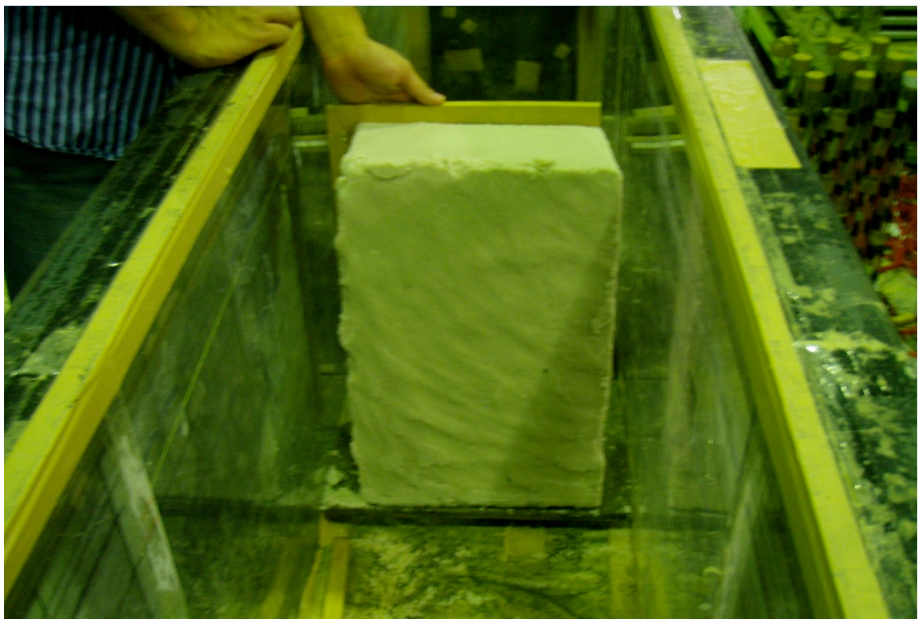

Figure 5.16 Photo of trimmed CS block placed in rigid test box ready for sample preparation

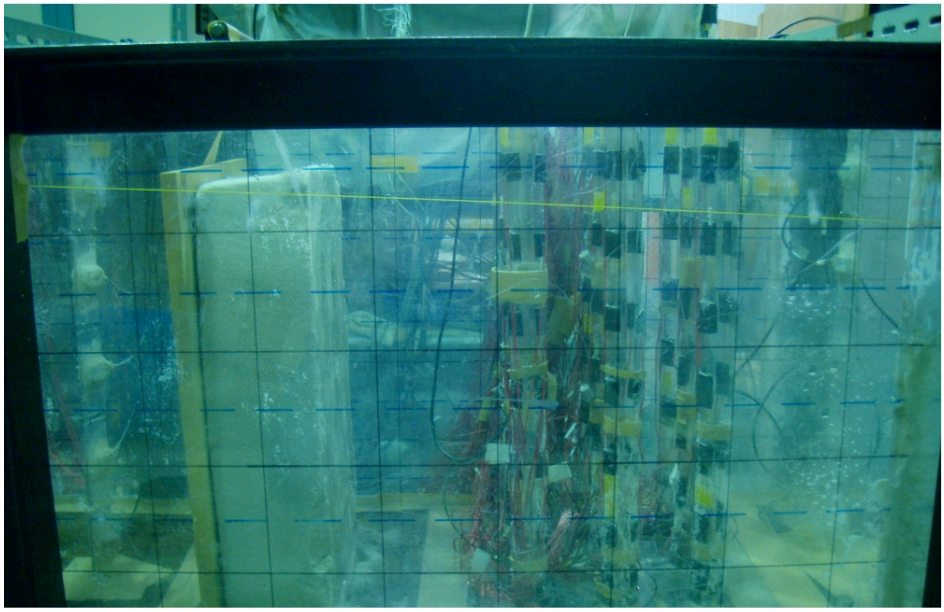

Figure 5.17 Photo of CS treated block with pile group in place before sample preparation

5.5.2.5.Colored Sand Markers

Colored sand was used to visually track the lateral displacement of the soil during testing. The colored sand was placed along the transparent rigid wall of the container and

on the surface of the sand outlining the CS block and the pile rows. The colored sand was placed in dots vertically every 10 cm and horizontally every 20 cm to visually track the lateral displacement throughout the depth of the sample during testing.

5.6. Typical Test Results

Each specimen was subjected to one-dimensional shaking at 10 Hz for a period of 20 seconds with a maximum amplitude of 0.3g. Typical test results are presented below for Test 5, a 15-cm-wide colloidal silica treated block placed 9 cm upslope of the 3-by-3 pile group. Photographs of the specimen before and after the test are shown in Figure 5.18 and Figure 5.19. The black gridlines along the container are 10 cm apart. A schematic diagram in Figure 5.20 shows the nomenclature (pile row designation) and sign conventions as used in the data processing. The results and photographs for the remaining four specimens are provided in Appendix C.

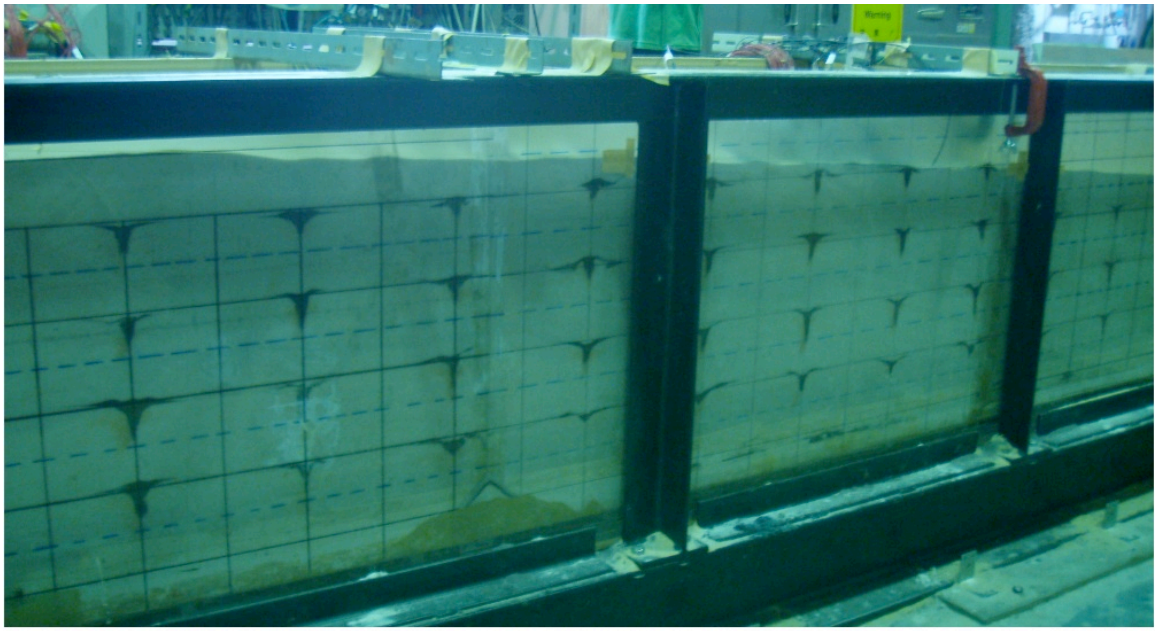

Figure 5.18 Photo of Test 5 before shaking

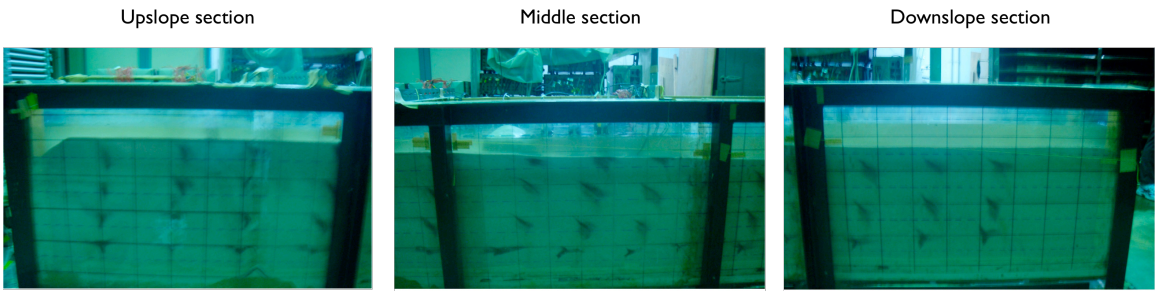

Figure 5.19 Photo of Test 5 after shaking

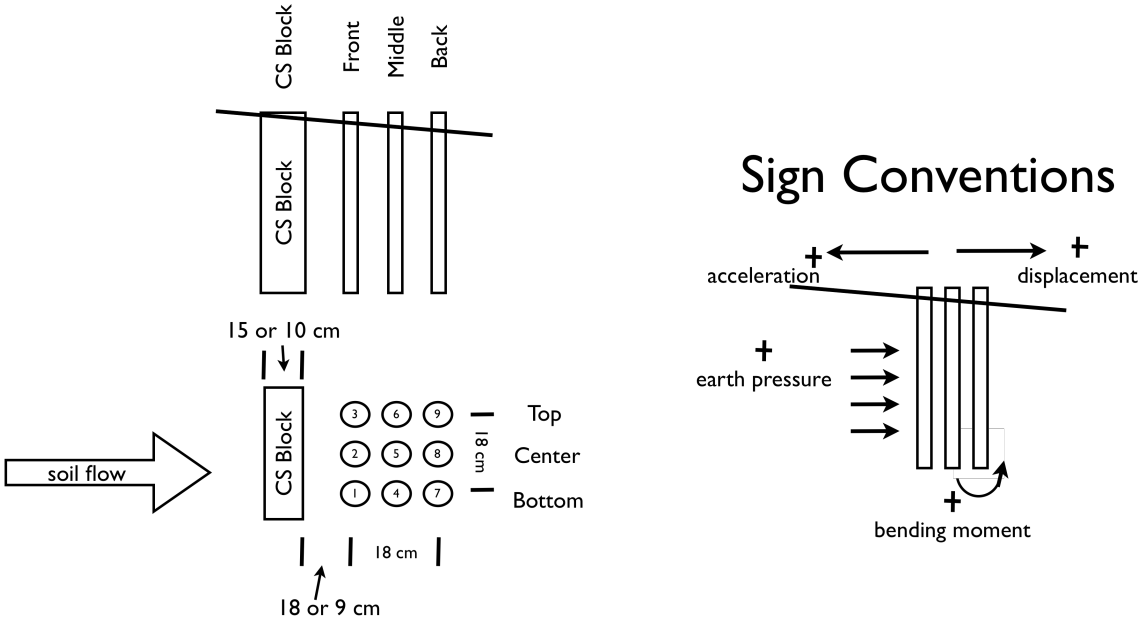

Figure 5.20 Sign conventions and testing nomenclature

5.6.1. Free-Field Response

5.6.1.1.Inclinometer Response

Three inclinometers were used during testing—two upslope of the pile group and one downslope as shown in Figure 5.12. The lateral soil displacements determine from the inclinometers as a function of depth at various times are shown in Figure 5.21. The maximum soil displacement generally occurred at the soil surface and the soil movement started when the excess pore water pressure ratio, $r_u = 100\%$, as shown in Figure 5.22. Soil displacement ceased coincident with shaking, indicating lateral spreading occurred

only during shaking. The surface soil displacement for all the inclinometers is shown in Figure 5.23.

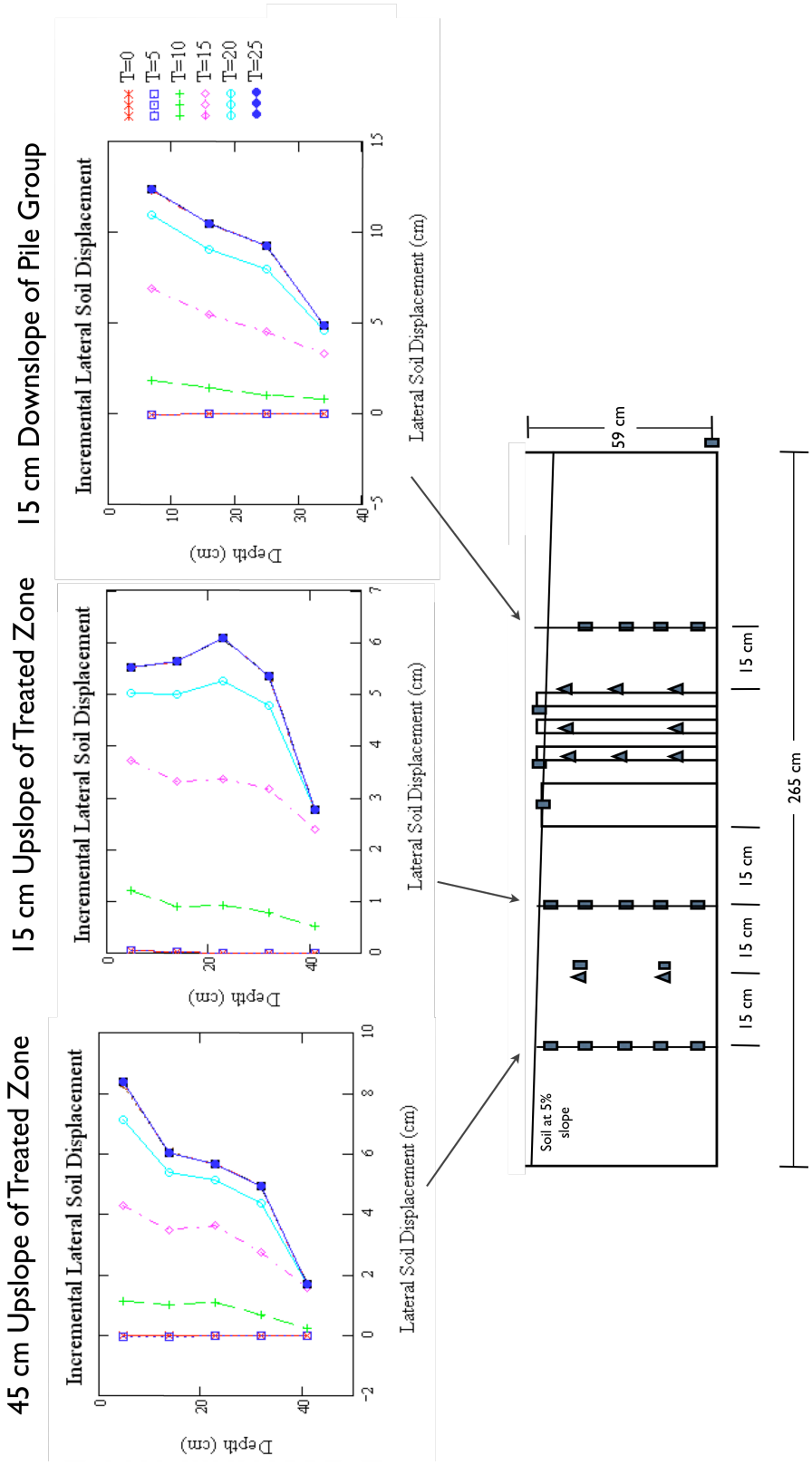

Figure 5.21 Inclinometer response and maximum soil displacement for Test 5

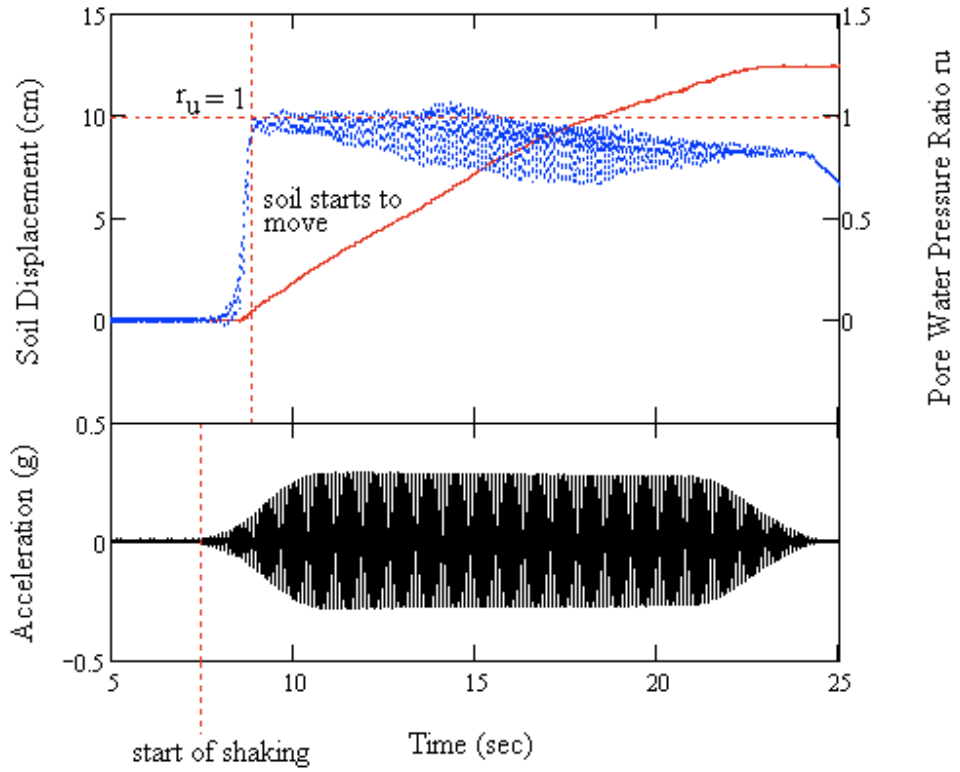

Figure 5.22 Downslope inclinometer surface soil displacement, r_u and input acceleration versus time for Test 5

A comparison of the displacements inferred from the colored sand markers to the measured lateral displacements can be made. The section containing the pile group had lateral displacement ranging from 10 to 20 cm, with the maximum at the top. The downslope inclinometer measured the largest lateral displacements at 12 cm. The displacement along the sidewall is expected to be larger than measured at the inclinometers, which are in the center of the rigid container, due to the soil flowing around the edges of the colloidal silica treated block and the boundary effects of the wall during soil flow.

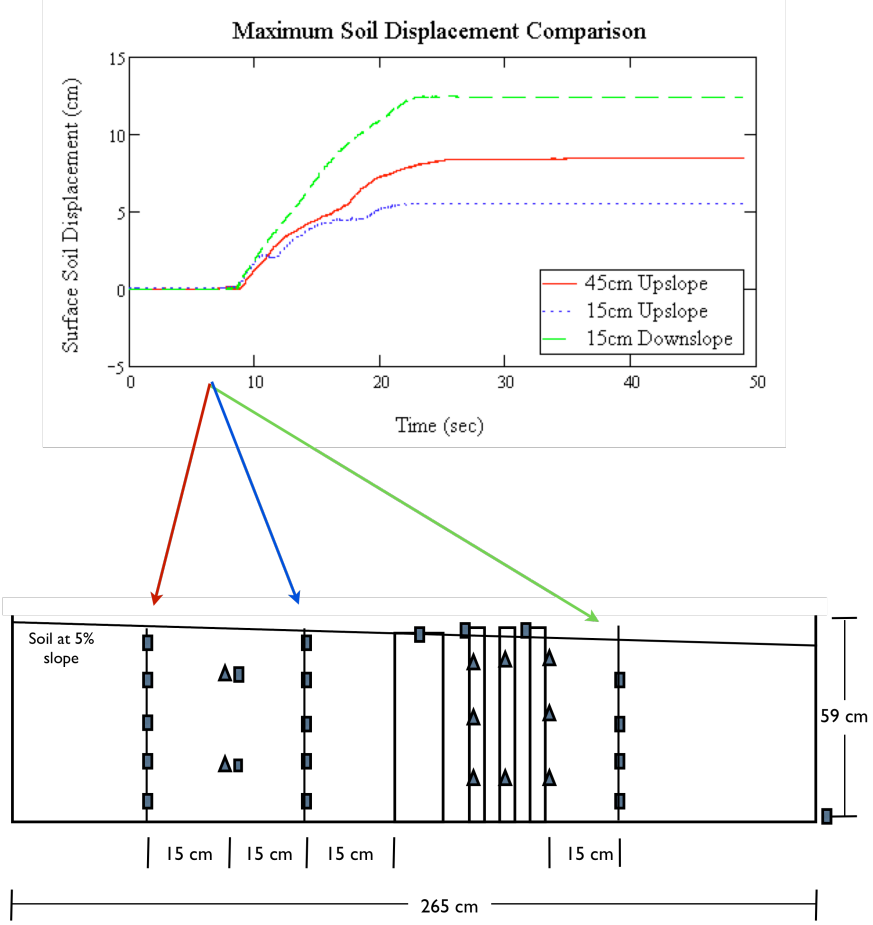

Figure 5.23 Maximum soil surface displacement versus time for Test 5

5.6.1.2.Accelerometer Response

The upslope accelerometer response is shown in Figure 5.24. The bottom accelerometer begins to ramp up acceleration amplitude as shaking begins, but then decreases in amplitude as the excess pore pressure increases causing liquefaction and a subsequent loss of strength. At approximately 15 seconds into shaking, r_u decreases to less than100% and the acceleration amplitude increases to approximately the value of the input acceleration, indicating that soil strength has been regained. The top upslope accelerometer starts to increase as input shaking ramps up and quickly reduces and remains at a low amplitude throughout the remainder of the test, indicating low shear

strength near the top of the specimen. The PWPT indicates that liquefaction did not occur at that level; however, the accelerometer response indicates the loss of soil strength.

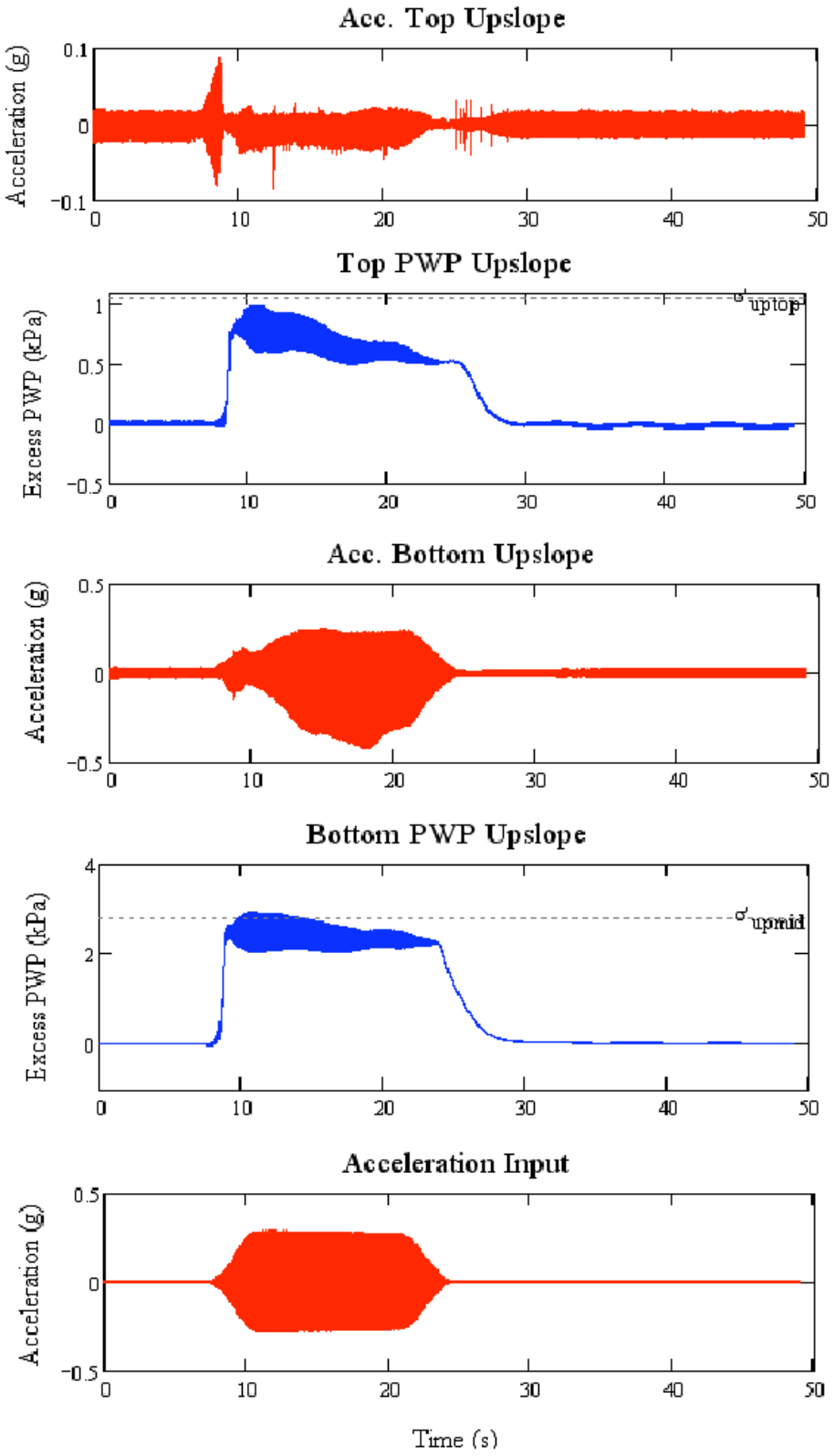

Figure 5.24 Upslope excess porewater pressure, acceleration and soil displacement for Test 5

5.6.2. Pile Response

5.6.2.1.Excess Pore Water Pressure Transducers

Excess pore water pressure transducers (PWPT) were located along the length of the center piles as shown in Figure 5.12. The time history of a PWPT on Pile 2 for Test 5 is shown in Figure 5.25, along with the input motion and the recorded bending moment and measured acceleration at the top of Pile 3. The dashed line shows the estimated effective vertical stress at the level of the PWPT and it is assumed liquefaction occurs when the pore pressure ratio, r_u, is equal to 100% which occurs when the excess pore water pressure equals the effective vertical stress (Kramer 1996).

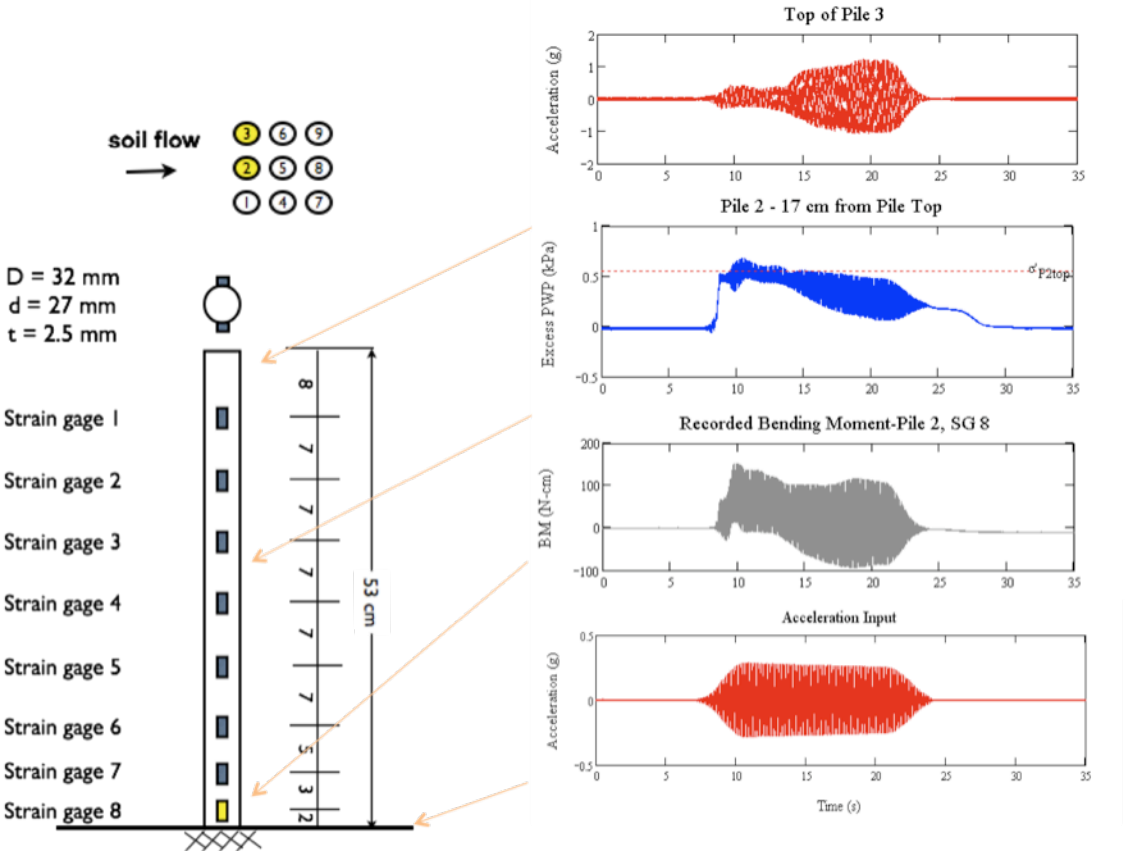

Figure 5.25 Time histories of instruments along the front row piles for Test 5

A contour plot showing the value of the excess pore water pressure ratio at the PWPT locations along the depth of the center piles is shown at 2-second time intervals during the maximum amplitude shaking in Figure 5.26. Each plot shows the r_u value measured along the depth of the pile for the center pile in the front, middle and back pile row. Because the values of the excess pore pressure are limited to the locations of the PWPTs, the surrounding areas have been set equal to r_u=0. The front and middle pile rows reach r_u=1 towards the beginning of maximum amplitude shaking. Throughout the duration of maximum shaking, the front pile row consistently has high r_u values generally $r_u > 0.7$. Similarly, the middle row also experiences $r_u > 0.7$, but the top PWPT begins to have a reduction in pore pressure ratio as shaking continues. The back pile row does not ever reach $r_u = 1.0$, but reaches a maximum of $r_u \sim 0.8$. This trend is consistent for all the samples. Therefore, the sand around the front and middle rows completely liquefied, whereas the soil around the back pile row did not fully liquefy.

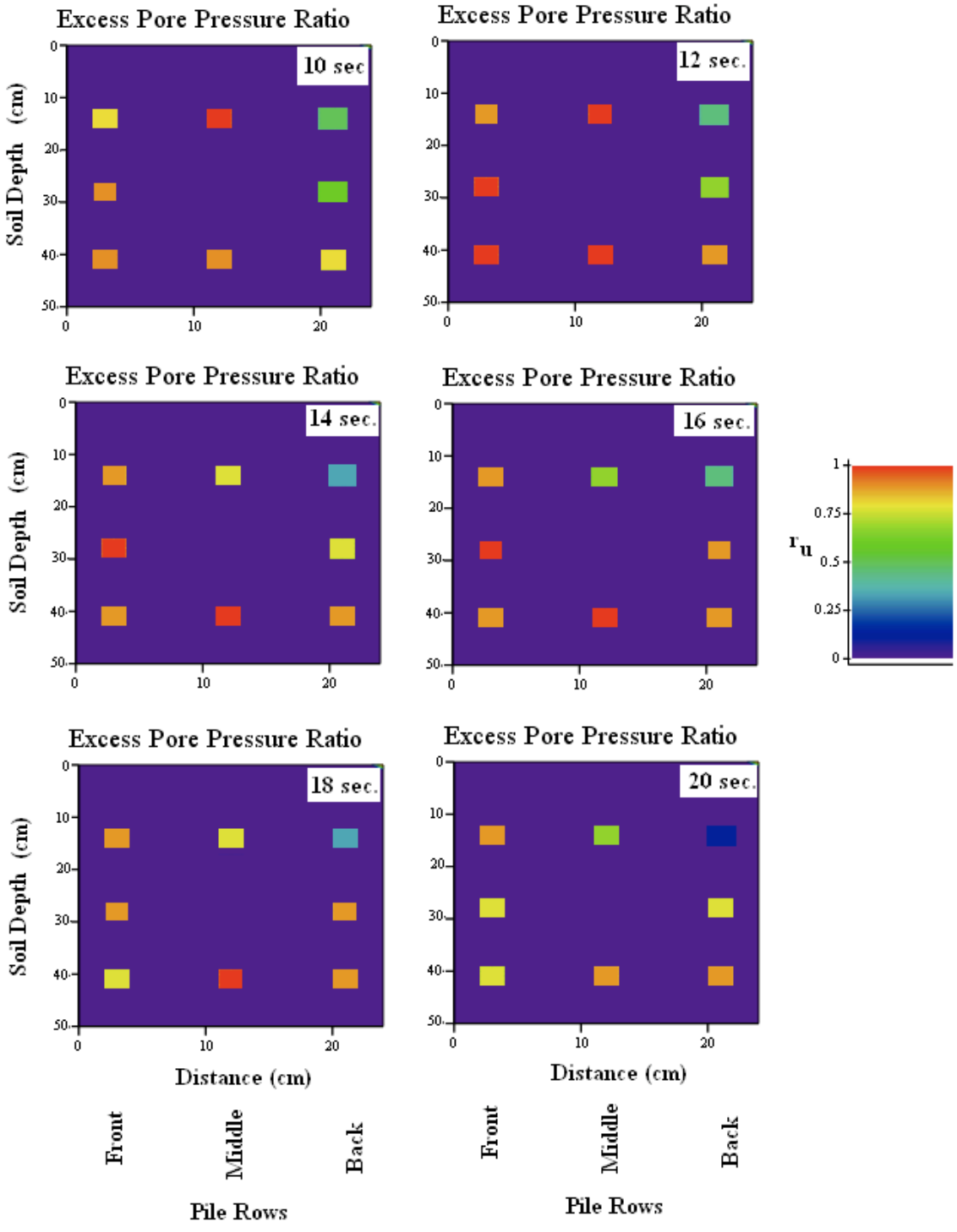

Figure 5.26 Excess pore water pressure ratio along the center piles at time intervals during shaking for Test 5

5.6.2.2.Accelerometer Response

The acceleration time histories at the top of Pile 3 and Pile 7 are shown in Figure 5.27 and shows that there is an amplification at the top of the piles reaching an amplitude of 1 g at 20 seconds of shaking. The amplification at the top of the pile is attributed to liquefaction around the pile and the resulting loss of strength, thus reducing the soil resistance and the pile to displace more. Both Pile 3 and Pile 7 have a similar trend in that the acceleration amplitude increases at the onset of shaking to a value close to the acceleration input and then approximately half way through shaking, the acceleration is amplified. The values of amplitude in the first half of shaking are similar, while Pile 3 is slightly lower. However, the Pile 3 amplification occurs earlier than Pile 7 and slightly increases in amplitude at the end of the shaking, whereas Pile 7 remains at the lower amplitude for a few more seconds before increasing to the peak amplitude, which remains constant throughout the remainder of shaking. This indicates the amplification at the top of the piles occurs sooner in the front row piles than the back row piles. This corresponds to the observation of the front and middle pile rows liquefying to a greater extent than the back pile row.

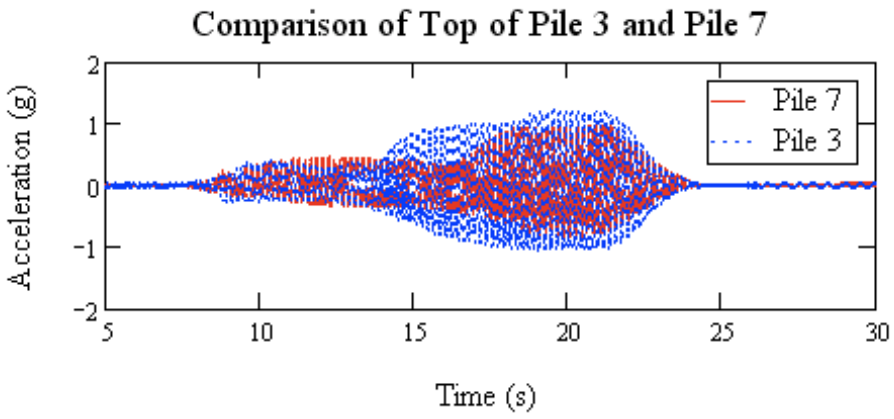

Figure 5.27 Comparison of accelerations at the top of Pile 3 and Pile 7 for Test 5

5.6.2.3.Recorded Bending Moments

The recorded bending moments are a combination of monotonic and cyclic components due to the lateral spreading of soil and the applied shaking, respectively. The recorded bending moments were decomposed into monotonic and cyclic bending moments using a median smoothing kernel. Moving average kernel filtering requires that the filter be significantly shorter than the shortest relevant time period (Santamarina and Fratta 1998). During data processing of the recorded bending moment signals, the kernel length (m) used, between 100 and 500, was kept within the guidelines of $m \leq T/(10 \cdot \Delta t)$, as suggested by Sanatmarina and Fratta (1998). The decomposed bending moments for the bottom strain gage (SG8 in Figure 5.25) for the center pile from the front, middle and back row of piles of Test 5 are shown in Figure 5.28. For most tests, the bottom strain gage reached the maximum bending moment because of its proximity to the fixed end of the pile.

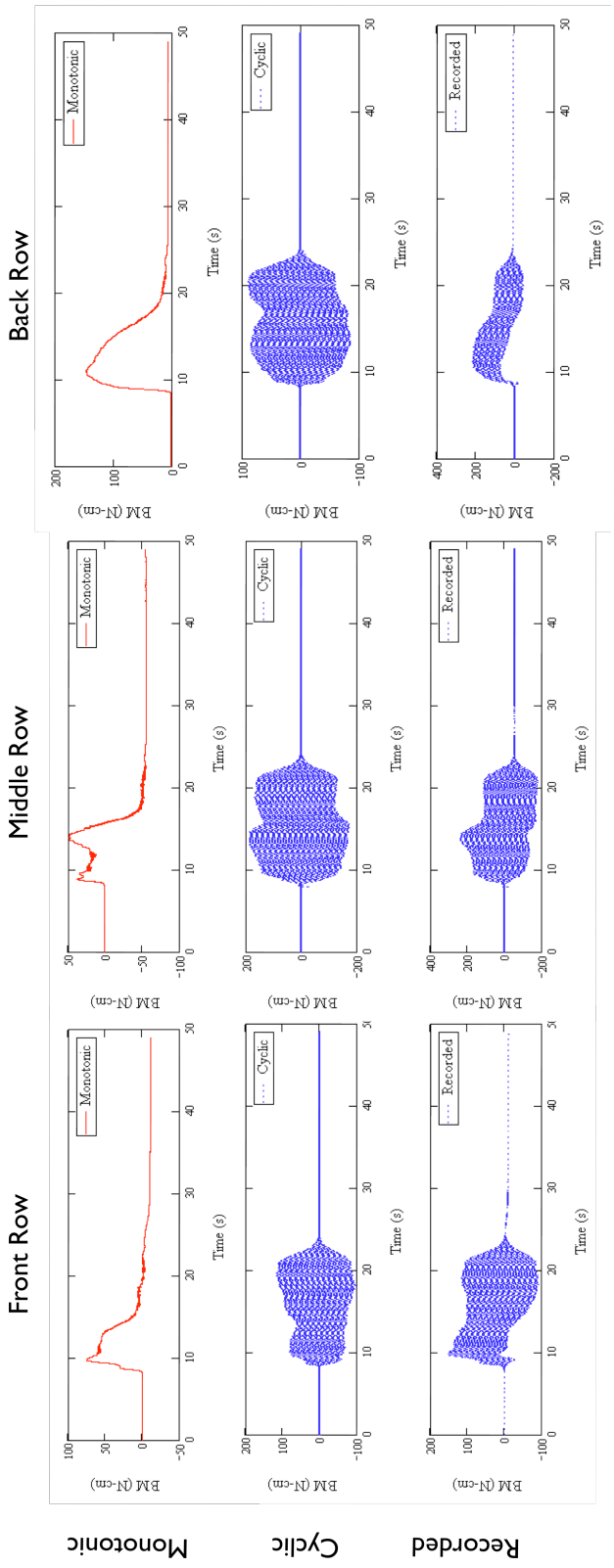

Figure 5.28 Recorded bending moments at the bottom strain gage of the center piles for Test 5

5.6.2.4.Monotonic Bending Moments

The variation of the monotonic component of the bending moments along the length of each pile at various times are shown in Figure 5.29. Each plot represents one of the nine piles and is located in the same position as if looking at the pile group in plan view with soil flow from the left to right. Each plot shows the bending moment along the length of the pile over time.

As noted previously, the maximum bending moment occurs at the base, as expected. In general, the maximum bending moment in each row occurs at one of the outer piles and the center pile experiences the lowest bending moments for each of the pile rows and the maximum bending moments occur in the back pile row for the tests. This corresponds to the larger soil displacements that were measured along the container wall compared to the center, which can be attributed to the liquefied soil flowing around the edges of the colloidal silica treated sand block. In Test 5, both the front and middle row of piles have the same approximate maximum bending moment occurring at approximately 10-15 seconds into shaking, which corresponds to the maximum amplitude shaking input. The maximum occurs in an outer pile for both the front and middle pile rows. The back row has a maximum monotonic bending moment of 250 N-cm, occurring at 10 seconds into shaking. Most of the piles rebound to the origin or have negative bending moments after shaking stopped.

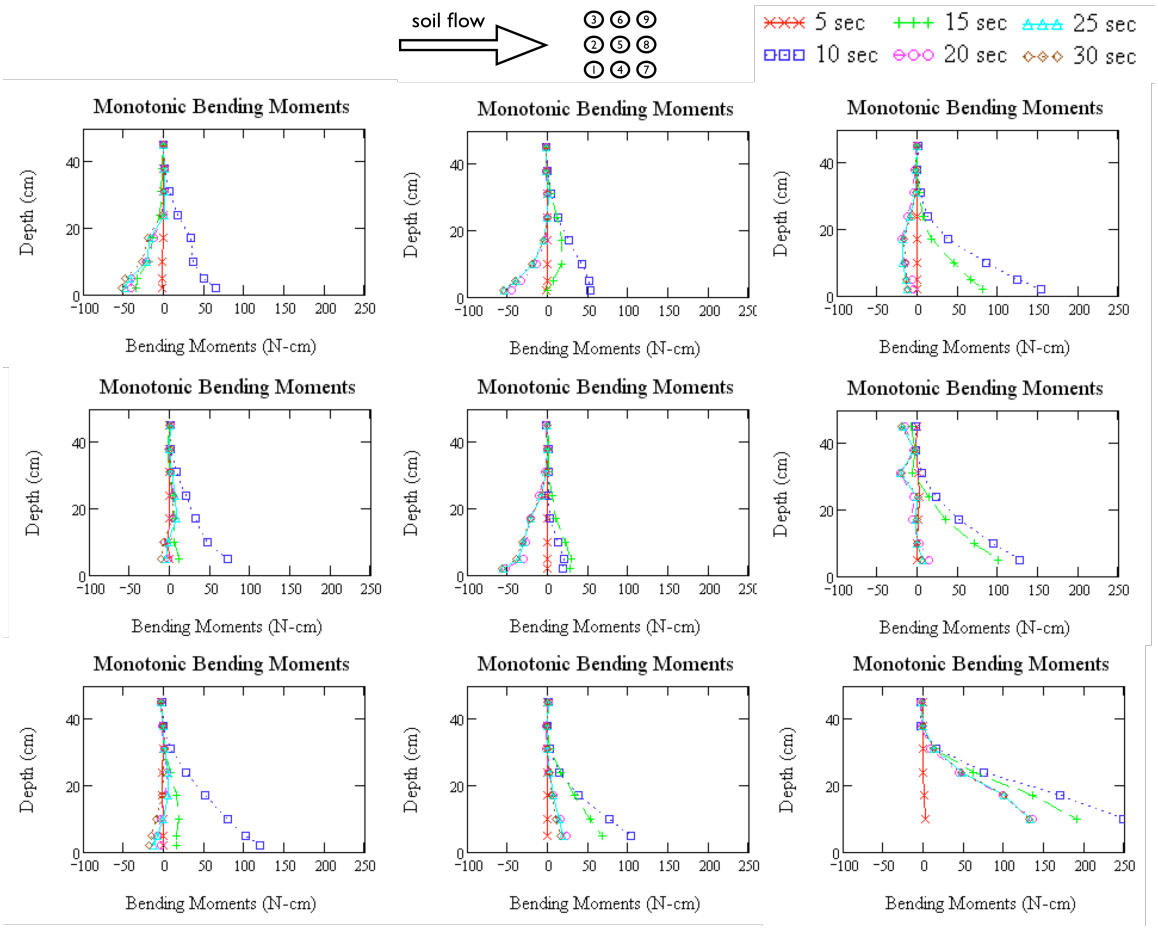

Figure 5.29 Monotonic bending moments for all piles at time steps for Test 5

5.6.2.5.Pile Displacement Response

Pile displacements were calculated by twice integrating the monotonic component of the measured bending moments and assuming no displacement and no rotation at the base of the piles as boundary conditions. The calculated pile displacements along the length of the center pile in each row for Test 5 is shown in Figure 5.30. As expected, the maximum pile displacement occurs at the top of the pile.

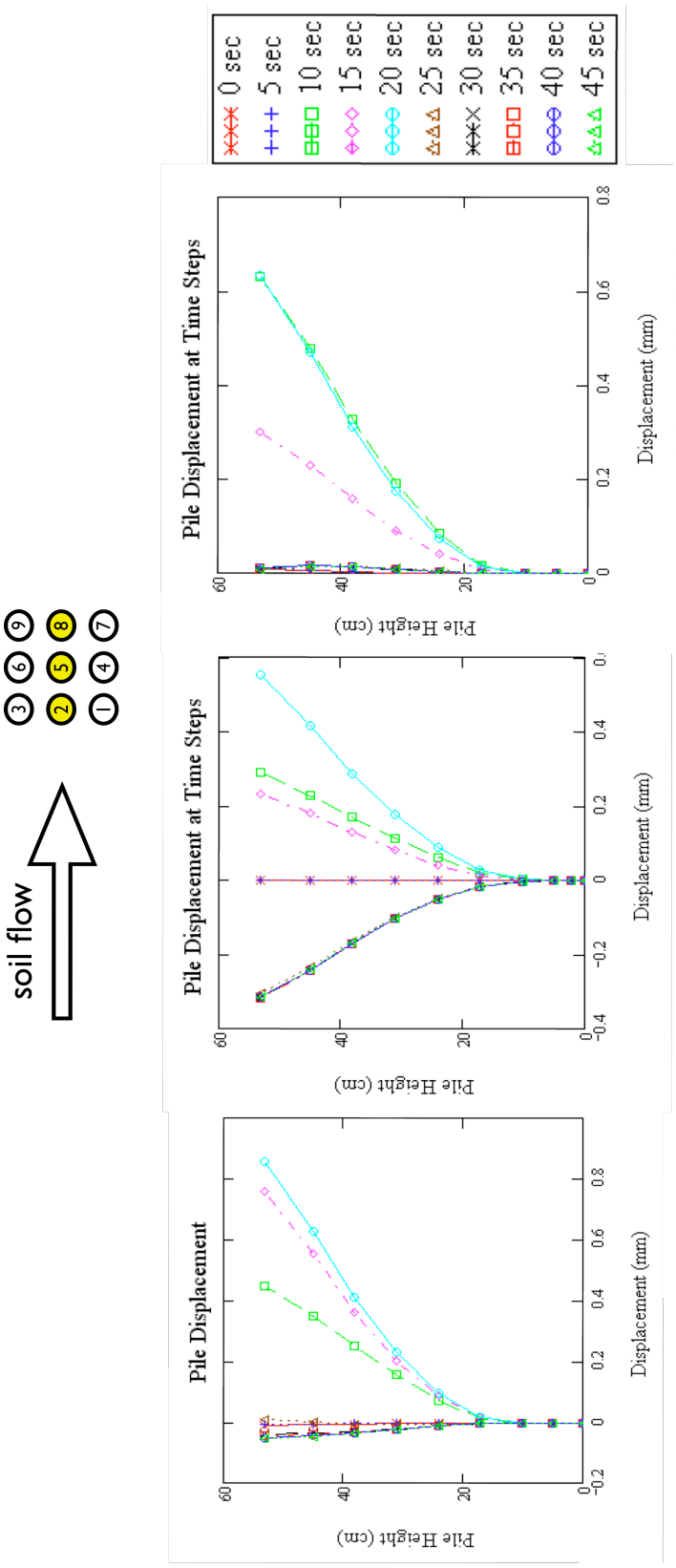

Figure 5.30 Pile displacement response of the center piles at time steps for Test 5

5.6.2.6.Comparison of Laser Displacement Transducer to Pile Displacements

The maximum displacement recorded by the laser displacement transducer (LDT) is compared to the calculated pile displacement for Pile 7 at the same time step in Figure 5.31. The measured maximum monotonic pile displacement was 2.9 mm and occurred at 11 seconds into shaking. The maximum pile displacement calculated using the bending moments in the back row was approximately 1.9 mm, which is less than the displacement measured by the LDT. The maximum displacement occurred at the same time in both methods of determining the pile displacement at the top. In all the tests, the LDT displacements are higher than the calculated displacements. This corresponds to the findings of Motamed (2007) where the LDT consistently recorded larger displacements than the calculated pile displacements. The LDT used in the testing is not very precise and has an error of +/- 1mm.

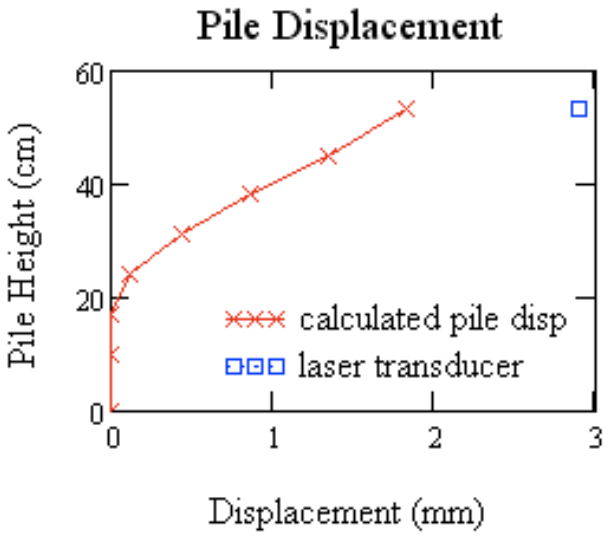

Figure 5.31 Laser transducer vs. calculated pile displacement for Pile 7 for Test 5

5.6.2.7.Lateral Earth Pressure

The lateral earth pressure exerted on the piles is calculated by taking the second numerical derivative of the measured pile bending moments. The numerical derivative is

very sensitive to small errors in bending moment and therefore the calculated lateral earth pressure is highly variable. The calculated lateral earth pressure along the height of the piles within the pile group over time is shown in Figure 5.32.

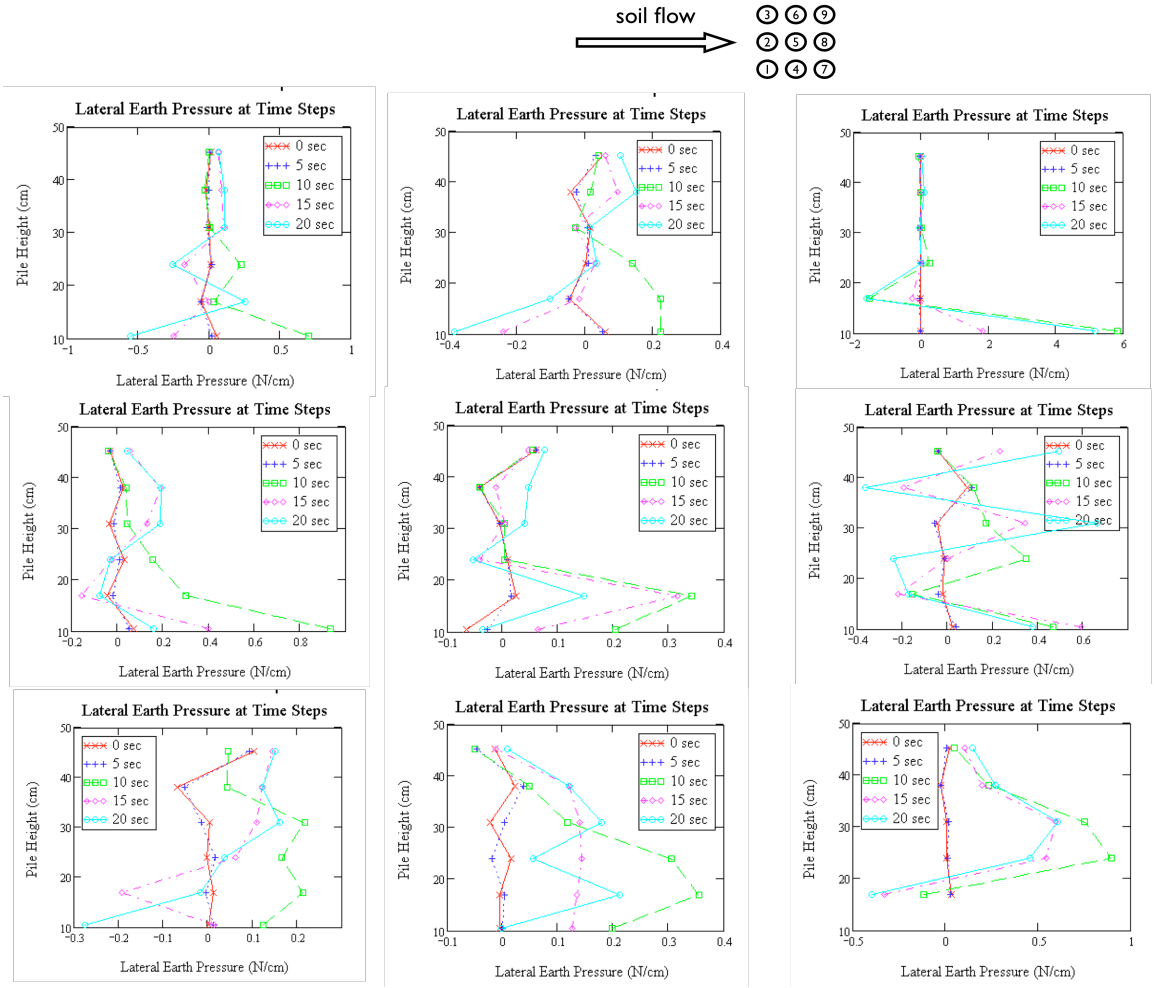

Figure 5.32 Lateral earth pressure for all piles at time steps for Test 5

5.6.3. Variations to the Typical Test Results

In all tests, the treated colloidal silica block slid during shaking to some degree. In Test 3 the colloidal silica treated sand block slid 5.5 to 6 cm towards the pile group during shaking. It is expected that this sliding contributed to the recorded bending moments being approximately equal for all piles within the pile group. This is also the suspected cause of why the maximum displacement occurred in the front row, whereas it

occurred in the back row in the other tests. Additionally, the inclinometers have approximately the same maximum displacement, indicating the entire soil specimen moved in unison.

In Test 5, several additional accelerometers were employed and their locations are shown in Figure 5.12. The accelerometer located on the top of the treated colloidal silica block indicated the treated sand block tilted and slid during testing. The sliding and tilting of the block was visually evident after shaking was complete and during sample deconstruction, these values were measured. The calculated values of tilt and displacement are compared with the visual measurements in Figure 5.33. The measured and calculated final tilting values are very similar, while the measured and calculated displacement at the top of the treated CS block differs by approximately 1 cm. The difference in the displacement value could be due to the assumption that the face of the treated sand block is level and thus the measurement between the block face and piles was accurate.

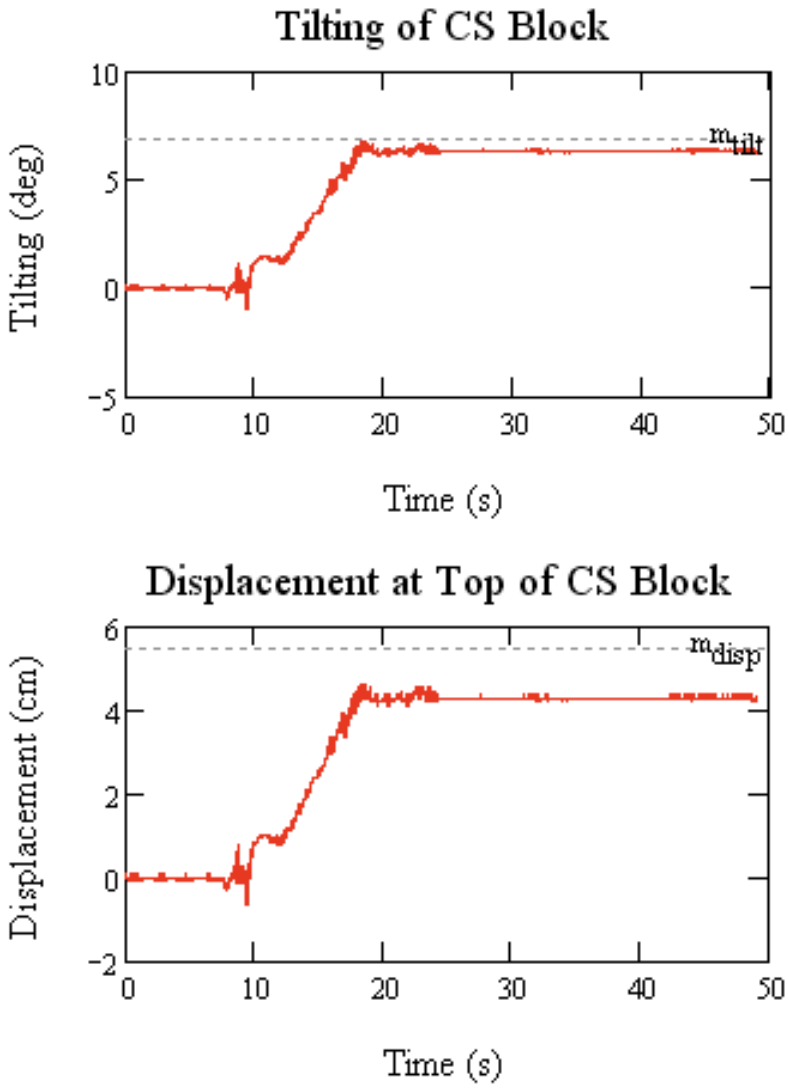

Figure 5.33 Measured versus calculated tilting and sliding of the CS block for Test 5

5.7. Discussion

5.7.1. Free-Field Response

5.7.1.1.Excess Pore Water Pressure

Most of the upslope PWPTs measured excess pore pressures equal to the effective vertical stress levels at the onset of shaking, however most decreased below this level

during the remainder of shaking. In some tests, the excess pore water pressures measured at the upslope PWPT indicated full liquefaction did not occur.

5.7.1.2.Inclinometer Response

The test configuration for Test 4 and Test 5 was the same and the displacements of all three inclinometers are similar for both tests. The maximum surface displacement occurred at the downslope inclinometer and was approximately 11 and 12 cm, respectively. The upslope inclinometer for both tests recorded maximum displacements of approximately 9 cm, while the inclinometer closest to the treated block measured surface displacements of 8 and 5.5 cm, in Test 4 and 5, respectively. The difference in the latter values is likely because in Test 5, the top of the inclinometer was displaced in the upslope direction and the maximum displacement occurred at depth within the soil instead of at the surface as expected. Therefore the soil displacement response was repeatable.

In all tests except Test 2, the upslope inclinometer located closest to the treated CS block had the least maximum surface displacement. The downslope inclinometer experienced the most surface displacement in each of the tests. A comparison of the maximum soil displacement measured for all the tests is shown in Figure 5.34. The downslope inclinometer has a quick rate of surface displacement at the onset of shaking and the rate of displacement remains relatively constant throughout shaking. The upslope inclinometers have a similar rate of displacement to the downslope inclinometer at the onset of shaking, however the rate of displacement slows concurrent to the excess pore water pressures reducing as shown in Figure 5.35.

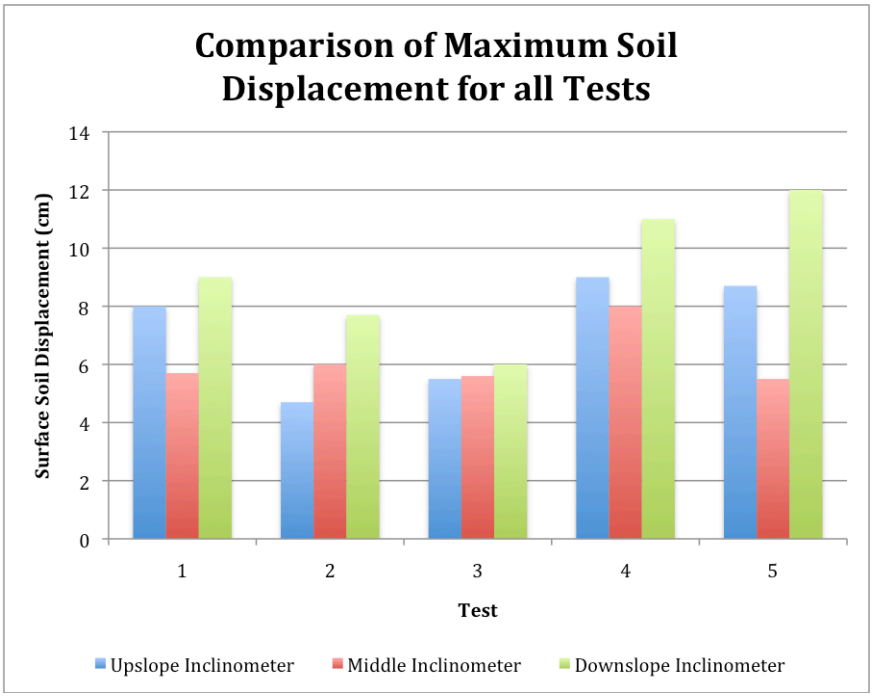

Figure 5.34 Inclinometer maximum soil displacement for all tests

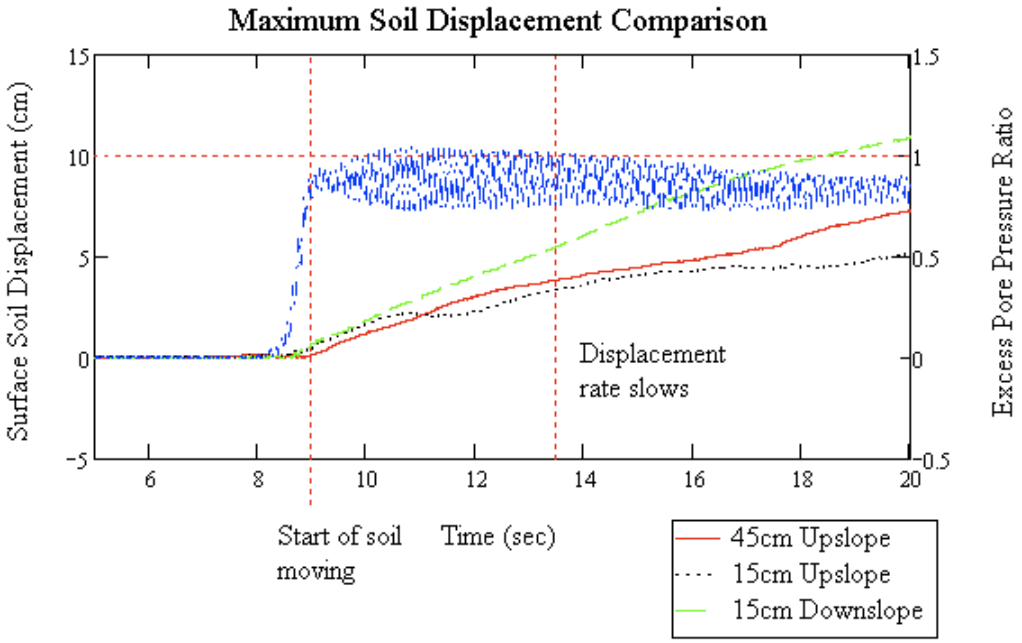

Figure 5.35 Inclinometer displacement versus time with upslope PPT r_u for Test 5

The flow velocity of the soil at the surface has been calculated by taking the time derivative of the inclinometer displacement data from Test 5 at one-second increments.

The difference in the velocity of the soil at the different inclinometer locations is shown in Figure 5.36. At approximately 13 seconds, the velocity of both upslope inclinometers decreases while the downslope inclinometer peaks in velocity, this is confirmed in Figure 5.35 where the downslope inclinometer rate of displacement remains at the same rate while the upslope and middle inclinometer decreases.

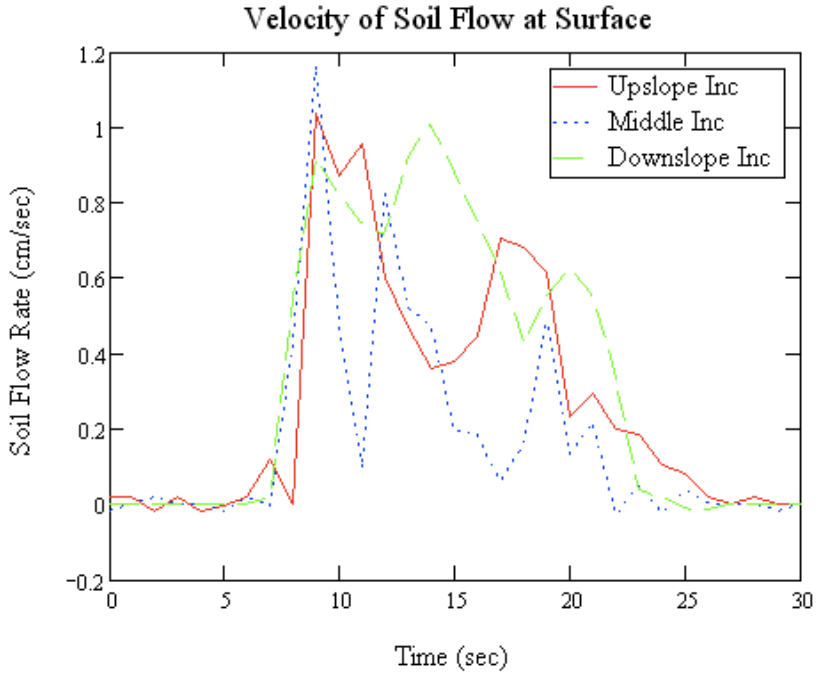

Figure 5.36 Soil flow rate at the inclinometer locations for Test 5

However, in Tests 1 and 3, the upslope inclinometers were similar to the downslope inclinometer displacements. All the inclinometers in Test 3 move at the same rate throughout shaking as shown in Figure 5.37, indicating the upper layer of the soil sample moved as a block downslope all at the same rate of displacement along the length of the sample. However, in Test 1 the upslope inclinometer displaces at a quick rate at the onset of shaking, the displacement rate was greater than the downslope inclinometer displacement rate as shown in Figure 5.38, which occurred only in Test 1. The rate of displacement slowed before the excess pore water pressure dropped below the effective

vertical stress at the upslope PWPTs, but the rate levels out concurrent with r_u less than 1 as shown in Figure 5.39.

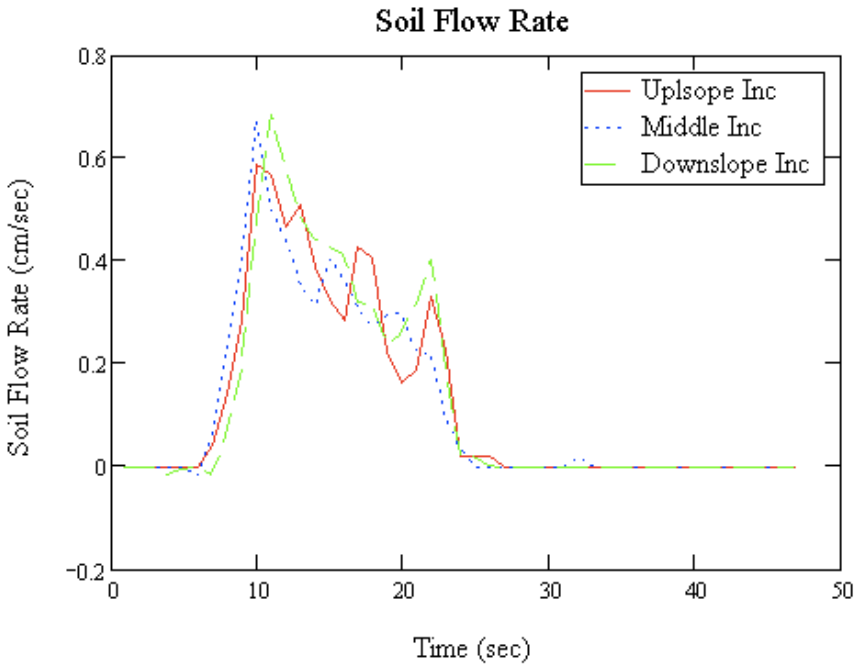

Figure 5.37 Soil flow rate at the inclinometer locations for Test 3

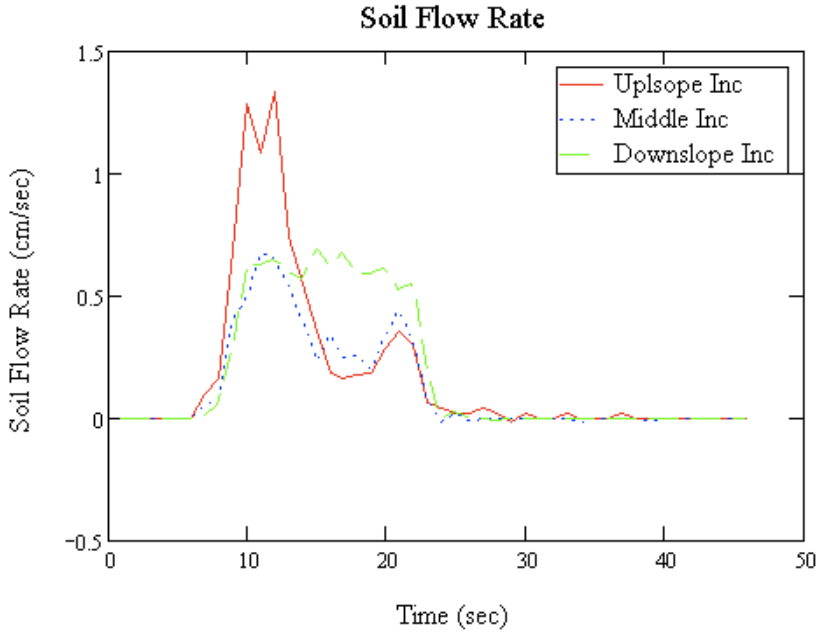

Figure 5.38 Soil flow rate at the inclinometer locations for Test 1

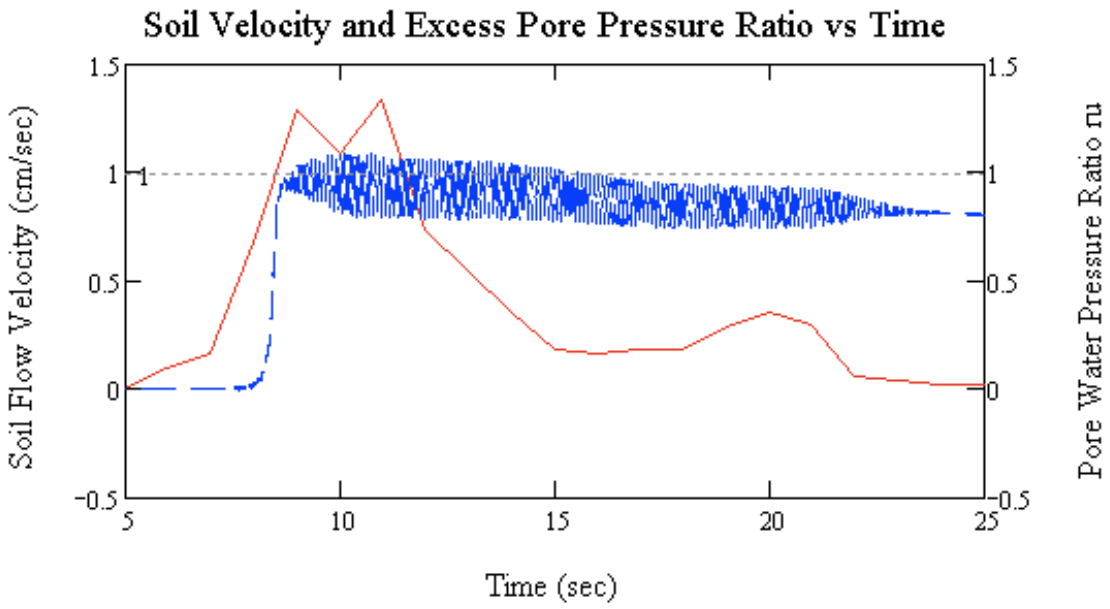

Figure 5.39 Soil flow rate and ru versus time at the upslope inclinometer for Test 1

The velocity of the soil can be compared to the calculated lateral load experienced by the piles. The surface soil flow rate and the lateral load experienced at 10 cm above the pile base of Pile 8 (back row, center pile) are compared in Figure 5.40. The lateral load shows good correlation to the soil flow rate.

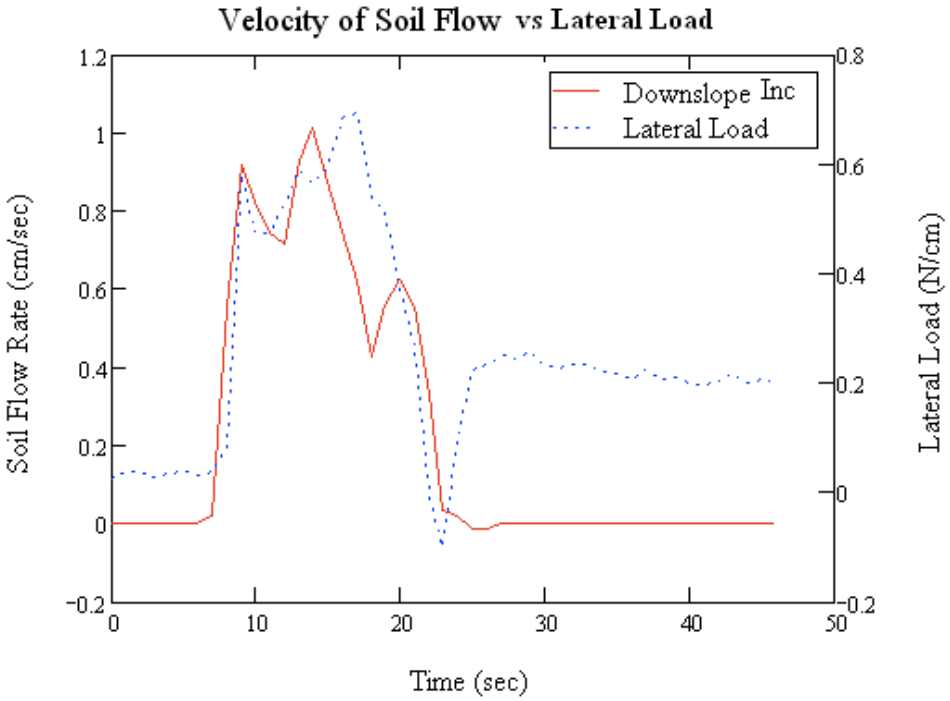

Figure 5.40 Soil flow rate (downslope inclinometer) versus lateral load (Pile 8) for Test 5

5.7.2. Pile Response

5.7.2.1.Excess Pore Water Pressure

The excess pore water pressure response is very similar for the tests. Most excess pore water pressures along the piles reached the effective vertical stress values at the respective PWPT locations. Only Pile 8 did not reach $r_u = 100\%$ in several tests. Most PWPTs along the piles increased at the onset of shaking and maintained elevated levels throughout shaking with a slight decrease to the lower stress levels during the second half of shaking as indicated in Figure 5.26.

5.7.2.2.Maximum Monotonic Bending Moments

The maximum bending moment occurred at the base of the pile due to the fixed-free boundary conditions. The maximum monotonic bending moments generally occurred at the onset of the maximum acceleration amplitude shaking, which varied slightly for

each test but was at approximately 10 seconds. In general, the center piles (Piles 2, 5, and 8) had smaller monotonic bending moments in comparison to the outer piles. In most tests, one row of the outer piles (either Piles 1, 4 and 7 or Piles 3, 6 and 9) reached higher bending moments than the other, and this remained consistent throughout the individual test. The only exception to this is Test 3, where all the piles reached similar monotonic bending moments due to the sliding of the treated block during testing.

Several piles in Test 2 and Test 4 experienced the maximum bending moments at approximately 10 cm from the base of piles during the intense shaking period as opposed to the maximum occurring at the base, this indicates that the soil at the base of the piles did not fully liquefy and provided resistance against the lateral pile movement. The monotonic bending moment for these piles shows similar behavior to that of piles at a soil layer interface, such as a liquefiable layer and a dense sublayer. Unfortunately, the deepest PWPT location for Test 2 and Test 4 was 15 cm above the pile base, which is above the bottom three strain gage locations, where the smaller bending moments were recorded as shown in Figure 5.41, so this hypothesis cannot be confirmed. However, the inclinometers at the base in Test 2 measured a displacement of 1-cm for all inclinometer locations and Test 4 had displacements of 1.5-, 1.5- and 3-cm, for the upslope, middle and downslope inclinometer. This is in comparison to Test 1, which measured 2-, 2- and 5-cm, respectively, and Test 5 measured 2-, 2.8- and 5-cm. Therefore the smaller inclinometer measurements at the base indicate that liquefaction likely did not occur at the base of the soil profile.

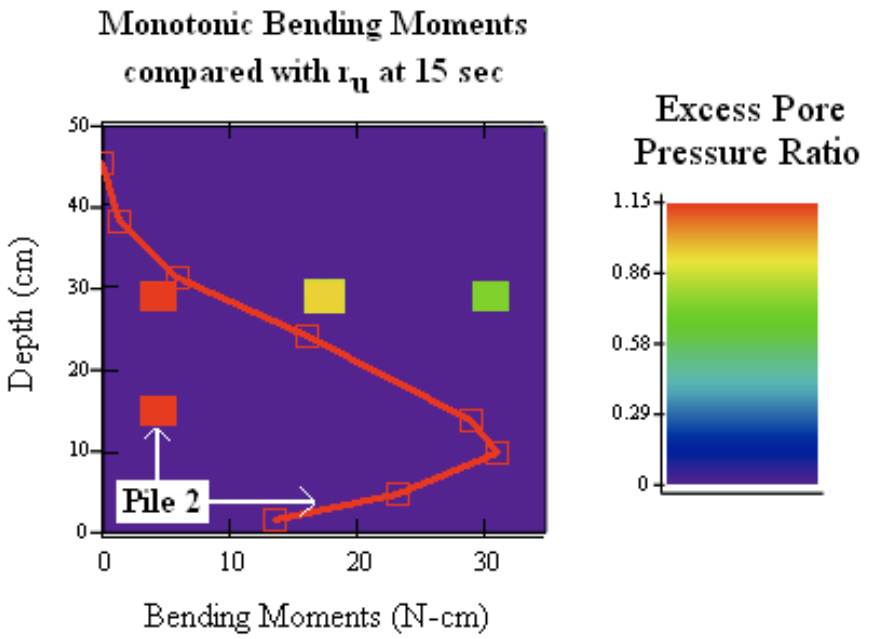

Figure 5.41 Monotonic bending moment and r_u with depth of Pile 2 for Test 2

The maximum achieved monotonic bending moment for the front, middle and back rows of piles each for each of the five tests is shown in Figure 5.42. Test 1, the untreated sample, has the largest bending moments in the middle and back row; however, Test 3 has the largest in the front row which may have been elevated due to the colloidal silica treated block sliding during testing. The results for Test 1 in the middle and back rows have over 100% increase in bending moments over the other tests, whereas Test 3 has an increase of 70% in the front row over the other tests, which can be attributed to the large movement of the treated colloidal silica block.

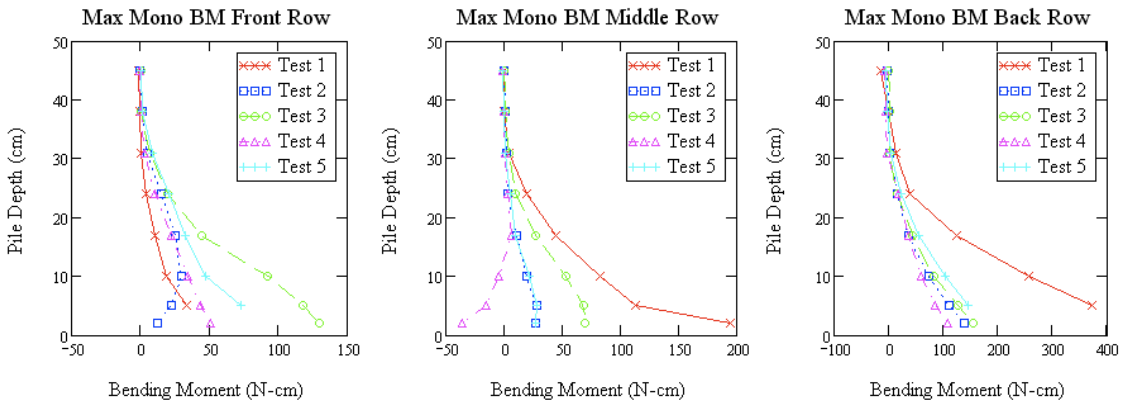

Figure 5.42 Pile row comparison of the maximum monotonic bending moments for all tests

The sample set-up for Test 4 and Test 5 were similar, and the maximum monotonic bending moments achieved in both tests are similar in the front and back rows. The middle row has a negative bending moment for Test 4 and reaches approximately 30 N-cm in Test 5, indicating the middle row was protected by the front row and resulted in lower bending moments during lateral spreading in both tests.

All the treated tests had similar results for the back row, indicating that regardless of block thickness and location upslope of the pile group, the back row experienced the largest monotonic bending moments during shaking. At the onset of lateral spreading, the soil develops a steep slope (much greater than the original 5% slope) at the back pile row, as shown in Figure 5.43. It is hypothesized this occurs only at the back row at the onset of shaking because the soil on the downslope side of the back pile row begins to displace before the soil around the pile group, causing a steep slope at the back row. However, this soil displacement is localized to the back row, as shown in Figure 5.43, where the colored sand markers have not displaced, therefore the localized movement is not visible on the downslope inclinometer, located outside of the displaced localized zone. This causes less soil to be present along the back-side of the piles in comparison to the front-side. The disparity in soil depth results in less resistance on the back-side of the back pile row, which leads to larger bending moments. The steep slope at the onset of lateral spreading

results in a backfill with a slope of approximately 22 degrees, which increases the Rankine active pressure on the upslope side of the pile by 25% and decreases the Rankine passive pressure on the downslope side by 31%. This steep slope levels out as lateral spreading continues.

The maximum monotonic bending moment response indicates that treatment upslope of a pile group reduces the bending moment experienced in the back row in comparison to the untreated samples. However, the thickness and location of the treated block does not influence the degree of bending moment reduction.

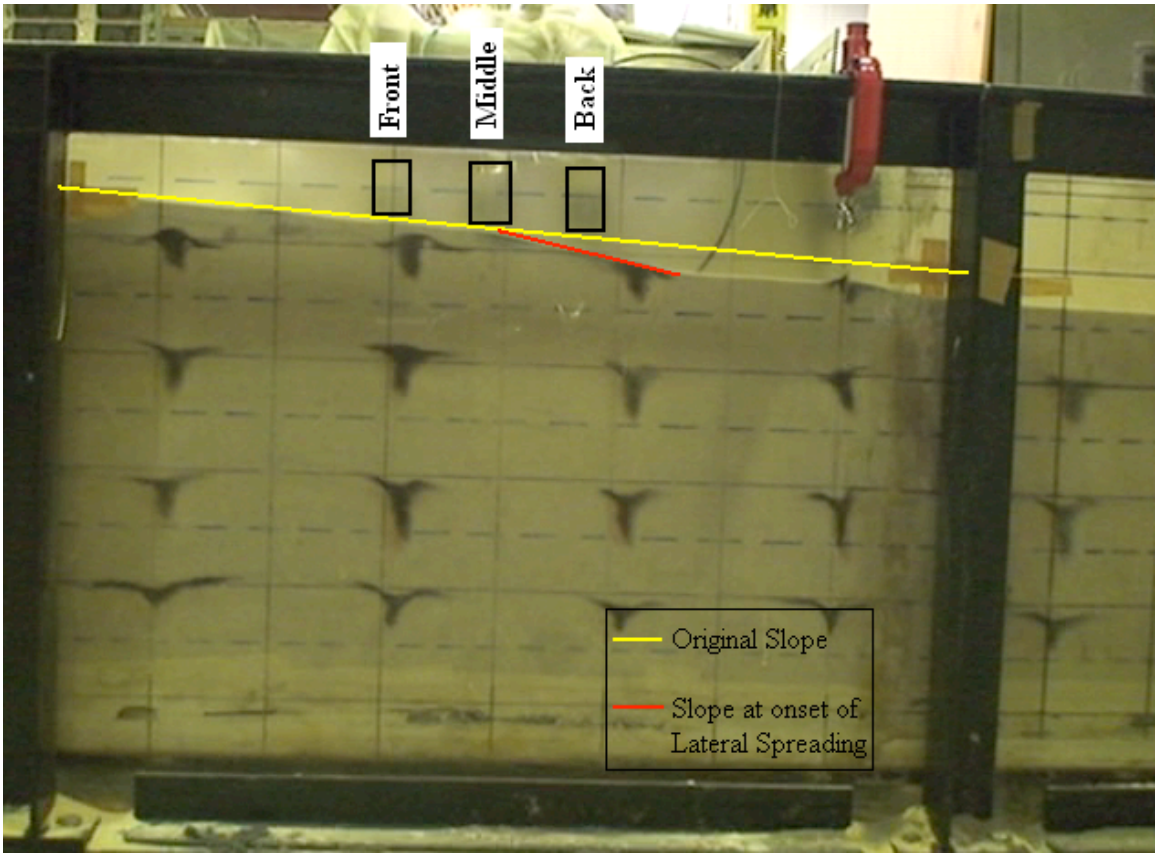

Figure 5.43 Snapshot of sample during shaking highlighting the soil surface slope at the back pile row (pile row locations are labeled)

5.7.2.3.Pile Displacement Response

The pile displacement calculations are dependent on the recorded bending moments. A comparison plot of the maximum pile displacement calculated for the center pile for the front, middle and back rows is shown in Figure 5.44. Test 1, the untreated sample, has the greatest displacements in the middle and back rows, while Test 3 and Test 5 have the largest displacements in the front row, but the elevated displacement could be an effect of the treated colloidal silica block shifting towards the pile group during shaking. The negative pile displacements (during shaking) in Test 4 are of similar magnitude to the other treated tests for the front and middle pile row; the back row in Test 4 is positive and has similar values to the other treated tests. The performance of the center pile in the middle row for all tests is similar, indicating that the protection gained by being the center pile in the 3 by 3 pile group outweighs any benefit using a block of treated soil upslope of the pile group. However, the back row has similar response for all tests except the untreated test, indicating the use of the colloidal silica treated sand upslope of the pile group reduces the pile displacements in comparison to the untreated sample. However, it was expected that treatment upslope would reduce displacements of all the piles, the cause of the reduction being realized only in the back pile row is unknown. The calculated pile displacements are negative for some piles after shaking has concluded and this has been confirmed with the laser displacement transducer, which found Pile 7 to have residual negative displacements after shaking finished.

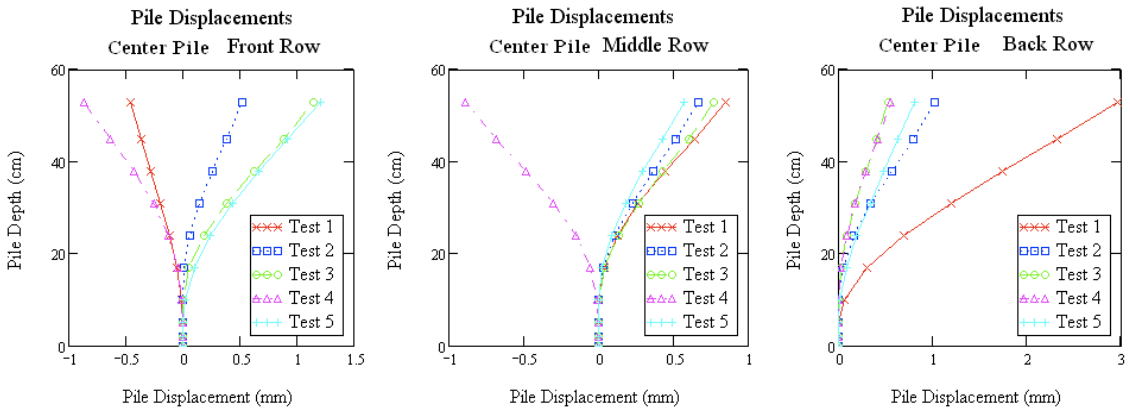

Figure 5.44 Maximum pile displacements of the center pile for the front, middle and back rows for each test

5.7.2.4.Lateral Earth Pressure

An estimate of the ultimate soil resistance can be calculated using the beam on nonlinear Winkler foundation with limit pressures (BNWF-LP). The lateral pressures of the laterally spreading soils reach the limiting values because the soil movements are assumed to be large enough to be independent of free-field soil displacements. The ultimate lateral resistance of a liquefied soil is calculated using (Boulanger et al. 2003):

$$p_{ult} = N_p Sb \qquad 5.5$$

where

N_p is the lateral bearing factor = 9 for plane strain conditions

S is the mobilized shear resistance of the liquefied soil = $0.07*\sigma'_v$

B is the pile diameter

N_p is dependent on depth, but in liquefied sand the dependence is not significant (Boulanger et al. 2003).

The estimated lateral resistance along the depth of the soil profile is shown in Figure 5.45. The calculated lateral earth pressure from the second derivative of the measured bending moments of the center piles (Piles 2, 5 and 8) for each test at 10 seconds into shaking is shown as a comparison. Pile 2 calculated lateral earth pressure are

generally less than the BNWF-LP estimate, with the exception of Test 3 and Test 5 where the lateral pressures equal or exceed the BNWF-LP estimate near the bottom of the soil profile. The calculated lateral earth pressure is smaller than the BNWF-LP estimate for Pile 5 in all tests. Pile 8 calculated lateral earth pressures are close to the BNWF-LP estimate and in all tests except Test are greater than the BNWF_LP estimate at the bottom of the soil profile. Test 1 has high variation in the calculated values about the BNWF-LP line and the trend of the calculated lateral pressure for the other tests matches the trend of the estimated BNWF-LP with the exception of one data point per test; these are likely a consequence of the sensitivity of numerical differentiation.

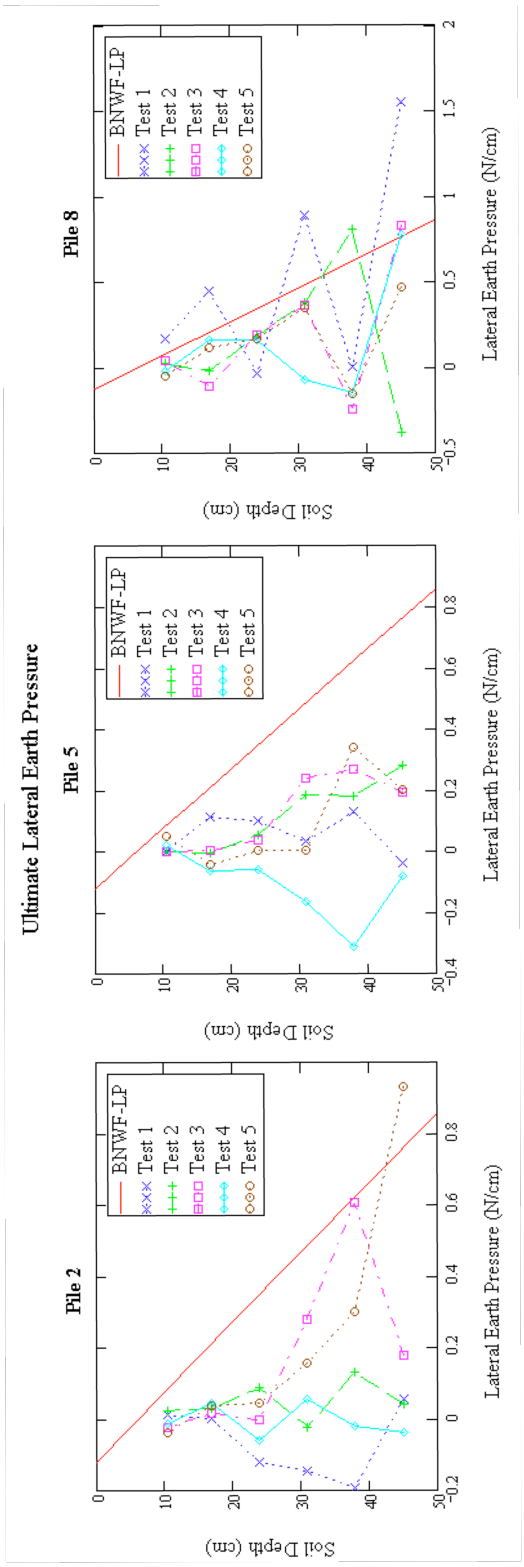

Figure 5.45 Comparison of lateral pressures calculated using BNWF-LP and measured bending moments of Piles 2, 5 and 8 for all Tests.

5.8. Conclusions

Shaking table tests were performed on a 3-by-3 pile group in loose sand samples with a 5% slope that employed a treated colloidal silica gel and sand block upslope of the pile group. The results of the colloidal silica treated block samples were compared to an untreated sample. The results showed that the presence of the colloidal silica treated sand block, regardless of block thickness or location upslope of the pile group, reduced the monotonic bending moments in the back pile row, thus reducing the pile displacements. The presence of the colloidal silica block had a negligible effect on the front and middle pile rows.

6. CONCLUSIONS AND RECOMMENDATIONS

6.1. Summary

Treatment of saturated loose sands with colloidal silica gel is a passive method of liquefaction mitigation that is well suited for use at developed sites. This is the first study to examine the effect of introducing colloidal silica gel into the pore space of loose sands on the dynamic properties of the treated soil, which are essential for characterizing the site response. The time horizon for liquefaction mitigation treatment requires the long-term small-strain shear modulus of treated sands to be identified for use in characterizing the treated soil over time. Treatment of an entire liquefiable area would potentially be cost-prohibitive, so a partial treatment zone was considered to reduce the cost of treatment but still maintain the ability to reduce liquefaction-induced damage to the structure.

An investigation of the effect of colloidal silica gel on the dynamic properties of loose sands was presented. A series of resonant column tests investigating the effect of loose sand treated with varying colloidal silica concentration on the small-to-intermediate strains was performed. A comparative study of the influence of colloidal silica gel on the effect of small-strain dynamic properties due to aging was presented. Varying gel times of the same weight-percentage colloidal silica gel were investigated using resonant column and bender element tests to identify the influence on the evolution of small-strain shear modulus with time. The evaluation of partial treatment with colloidal silica gel to mitigate damage to piles caused by liquefaction-induced lateral spreading by reducing the bending moments experienced by a 3-by-3 pile group was presented. Colloidal silica gel treatment zones of varying size and location were evaluated by subjecting a 3-by-3 pile group in gently sloping liquefiable ground to 1-g shaking table tests and the results were compared to an untreated sample.

6.2. Conclusions

Treatment of loose sands with colloidal silica gel in the initial phase of treatment (permeation through gelation and initial curing to allow development of a resonating gel) results in a small change in the dynamic properties. The effect of colloidal silica concentration on the small-strain shear modulus showed a 10% increase in five-weight-percent concentration and a 12% increase in seven- and nine-weight-percent concentrations. The modulus reduction curve indicates that treatment does not affect the linear threshold shear strain, however the treated samples reduce at a greater rate than the untreated samples in the intermediate-strain range above 0.01% cyclic shear strain. It was observed that the treated sand has slightly higher damping ratio in the small-strain range; however, at cyclic shear strains around 0.003% the trend reverses and the untreated sand begins to have higher damping ratio.

The effect of aging on colloidal silica gel treated sand samples due to continued siloxane bonding of the gel results in an increase of the shear modulus with time. Resonant column tests over 28 days determined that initial tangent shear modulus increased 12% and small-strain damping ratio slightly increased due to aging over a distance from gelation (time after gelation normalized by gel time) of 350. The effect of aging increases the small-strain shear modulus after gelling by 200 to 300% for the 40-minute-gel time samples with a distance from gelation of 1000 to 2000; 700% for the 2-hour-gel time sample with a distance from gelation of 1000; and 200 to 400% for the 20-hour-gel time samples with a distance from gelation of 40 to 100. A heuristic approach to estimate the shear modulus of treated soils, by summing the shear modulus of the sand skeleton and the shear modulus of the colloidal silica gel within the pore space, was shown to fit the increase in shear modulus with time of the treated sands measured in the resonant column well.

Partial treatment with colloidal silica gel was evaluated by performing shaking table tests on a 3-by-3 pile group in loose sand samples with a 5% slope that employed

varying thicknesses and locations of a treated sand block upslope of the pile group. The results of the colloidal silica treated block samples were compared to an untreated sample. The results showed that the presence of the colloidal silica treated sand block, regardless of block thickness or location upslope of the pile group, was effective in reducing the maximum bending moments reached in the back row of piles by 50%. However a negligible effect was seen on the front and middle rows of piles.

6.3. Recommendations

Recommendations for future work to compliment these studies are as follows.

6.3.1. Sample Aging Tests

Future work should include further investigation into the optimal input signal to use over time for bender element tests on specimens treated with colloidal silica. Untreated sand samples should also be subjected to aging tests to determine a baseline aging effect. Further investigation is needed on the sand and colloidal silica gel damping ratio evolution with time to identify the trend, and increase the frequency resolution to reduce the error in measurement.

6.3.1.1.Sample Saturation

Perform both resonant column and bender element tests that address the issue of sample saturation decreasing over time and thus causing an increase in the shear wave velocity. In order to separate this effect from the effect of colloidal silica gel curing on the increase in shear wave velocity, and therefore shear modulus, over time a new experimental set-up should be employed. Keeping the sample saturated during the resonant column test, with the use of vacuum as the confinement, becomes difficult; the sample is being dried by the confinement application in addition to through the diffusion through the sample membrane. However, keeping the bender element samples saturated

would require less experimental ingenuity, but requires an investigation of saturating fluid used to age the samples within.

6.3.2. Shaking Table Tests

The shaking table tests were flawed due to the constraint of having to prepare the treated colloidal silica block outside of the sample and the resulting sliding and tilting of the treated block during shaking. Therefore, it is suggested to replicate field treatment conditions by performing shaking table tests on sand that is treated in-situ by injecting the colloidal silica solution into the sample. The treatment zone is expected to be radial in area from the injection point and the gradient of colloidal silica treatment will vary radially from the source. It is suspected that this treatment zone will act as a part of the soil mass, just with different properties, as opposed to a pseudo-soil wall that is susceptible to sliding and tilting. This difference in soil treatment would more accurately reproduce the full-scale field treatment and would likely affect the effectiveness of the treatment in reducing bending moments and displacements of the piles. This would also facilitate the use of instruments, such as inclinometers and accelerometers, inside the treated soil mass.

APPENDIX A RESONANT COLUMN TEST RESULTS

	Five-Weight-Percent Samples			Seven-Weight-Percent Samples			Nine-Weight-Percent Samples			Untreated Sand Samples		
Sample 1	γ (%)	G (Mpa)	D (%)	γ (%)	G (Mpa)	D (%)	γ (%)	G (Mpa)	D (%)	γ (%)	G (Mpa)	D (%)
	1.91E-04	63.027	0.302	1.54E-04	66.039	0.389	1.34E-04	63.884	0.483	2.05E-04	61.128	0.31
	3.79E-04	63.463	0.316	3.11E-04	66.344	0.359	2.69E-04	64.409	0.452	3.88E-04	62.141	0.292
	9.01E-04	63.318	0.259	7.49E-04	66.191	0.345	6.61E-04	64.296	0.423	8.77E-04	60.984	0.295
	1.57E-03	63.027	0.245	1.32E-03	65.508	0.304	1.23E-03	63.996	0.38	1.54E-03	60.84	0.296
	2.21E-03	61.727	0.32	2.20E-03	65.735	0.346	2.08E-03	63.101	0.368	2.39E-03	60.696	0.444
	3.52E-03	60.867	0.337	3.53E-03	64.526	0.321	3.41E-03	61.918	0.401	3.70E-03	58.56	0.495
	5.27E-03	59.449	0.4	5.52E-03	62.734	0.414	5.33E-03	60.018	0.513	5.66E-03	57.297	0.609
	8.67E-03	56.799	0.501	8.11E-03	59.514	0.576	8.15E-03	57.579	0.755	8.43E-03	55.772	0.802
	0.013	52.341	0.885	0.013	56.519	0.794	0.012	53.809	1.228	0.012	51.717	1.474
	0.018	48.191	1.861	0.019	51.296	1.83	0.018	49.803	2.436	0.018	48.455	2.654
	0.025	45.069	3.866	0.025	47.869	3.417	0.024	47.261	3.845	0.024	47.244	4.058
Sample 2	γ (%)	G (Mpa)	D (%)	γ (%)	G (Mpa)	D (%)	γ (%)	G (Mpa)	D (%)	γ (%)	G (Mpa)	D (%)
	1.97E-04	65.114	0.288	1.53E-04	65.896	0.403	1.22E-04	67.33	0.47	2.32E-04	57.033	0.303
	3.83E-04	65.867	0.301	3.11E-04	66.352	0.359	2.43E-04	67.791	0.525	4.52E-04	57.866	0.286
	8.99E-04	65.114	0.245	7.52E-04	66.2	0.33	6.00E-04	68.099	0.453	9.70E-04	57.31	0.302
	1.49E-03	64.215	0.465	1.28E-03	66.2	0.374	1.15E-03	67.791	0.397	1.60E-03	57.31	0.514
	2.57E-03	64.365	0.218	2.13E-03	65.593	0.346	2.00E-03	66.871	0.357	2.48E-03	56.757	0.44
	3.44E-03	62.732	0.353	3.51E-03	64.537	0.349	3.27E-03	65.2	0.376	3.83E-03	54.843	0.476
	5.74E-03	61.413	0.49	5.20E-03	62.746	0.487	5.14E-03	64.148	0.467	5.95E-03	54.707	0.65
	8.40E-03	58.958	0.561	8.26E-03	59.963	0.574	8.00E-03	61.189	0.597	8.85E-03	51.9	0.842
	0.012	53.925	0.935	0.012	56.116	0.936	0.012	57.022	1.191	0.012	50.33	1.468
	0.018	50.661	2.027	0.018	51.118	2.126	0.018	52.629	2.464	0.018	46.727	2.645
	0.024	46.923	4.256	0.024	48.089	3.709	0.024	50.482	3.519	0.026	43.802	4.011
Sample 3	γ (%)	G (Mpa)	D (%)	γ (%)	G (Mpa)	D (%)	γ (%)	G (Mpa)	D (%)	γ (%)	G (Mpa)	D (%)

	1.89E-04	66.011	0.342	1.51E-04	70.544	0.362	1.32E-04	66.481	0.492	2.13E-04	58.425	0.284
	3.86E-04	66.162	0.271	2.98E-04	70.544	0.362	2.67E-04	66.922	0.549	4.20E-04	58.005	0.27
	9.00E-04	65.56	0.229	7.25E-04	70.387	0.362	6.49E-04	66.628	0.476	9.02E-04	57.727	0.301
	1.55E-03	64.811	0.202	1.27E-03	69.917	0.336	1.21E-03	66.481	0.417	1.46E-03	58.285	0.375
	2.26E-03	65.409	0.315	2.21E-03	68.982	0.282	2.13E-03	65.46	0.376	2.45E-03	57.449	0.332
	3.41E-03	64.066	0.348	3.41E-03	67.591	0.313	3.42E-03	64.735	0.393	3.74E-03	56.482	0.472
	5.17E-03	61.858	0.442	5.47E-03	65.606	0.39	5.27E-03	63.014	0.491	5.71E-03	54.843	0.587
	8.56E-03	58.69	0.515	8.16E-03	62.759	0.517	8.25E-03	60.341	0.628	8.44E-03	52.429	0.869
	0.013	56.021	0.759	0.012	58.821	0.854	0.012	56.65	1.252	0.012	48.783	1.425
	0.018	50.342	1.781	0.018	53.701	1.978	0.018	52.345	2.598	0.017	45.299	2.992
	0.025	47.937	3.902	0.024	50.695	3.563	0.025	49.933	3.73	0.025	42.719	4.622

APPENDIX B BENDER ELEMENT TIME HISTORIES

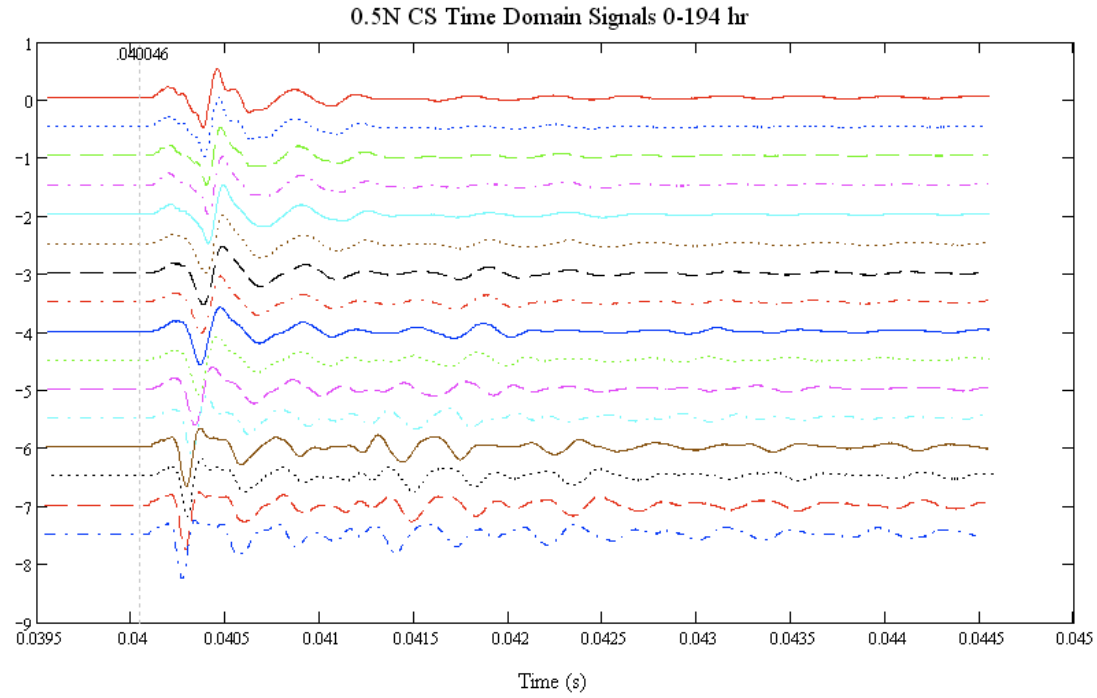

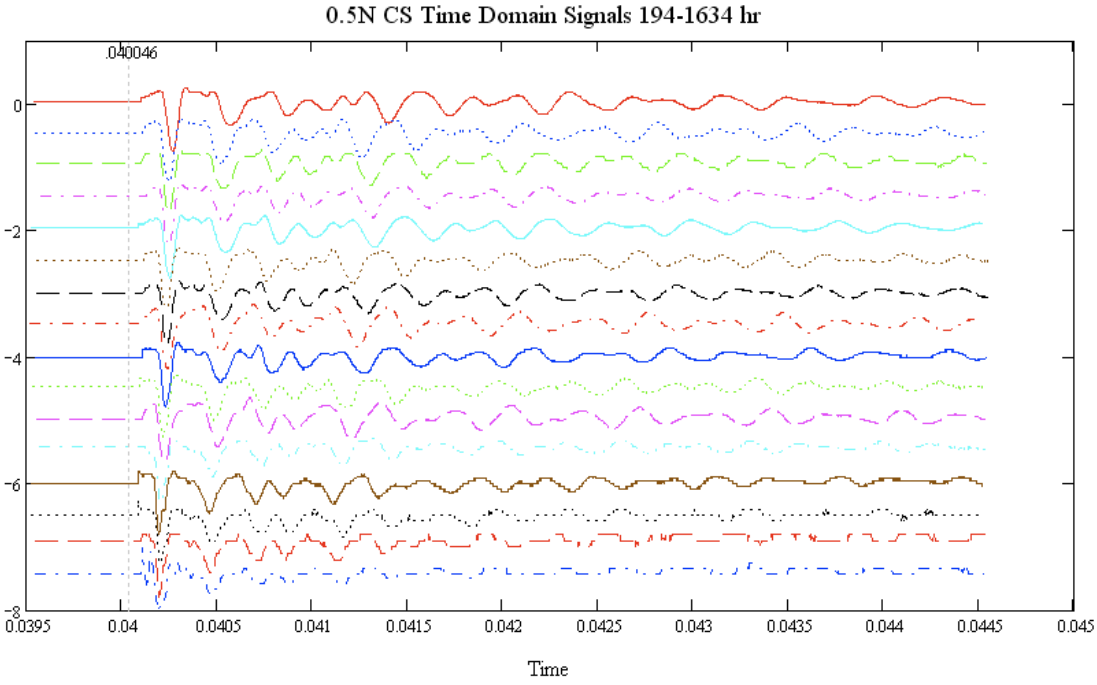

Figure B.1 Output signal time histories over time of Sample 1

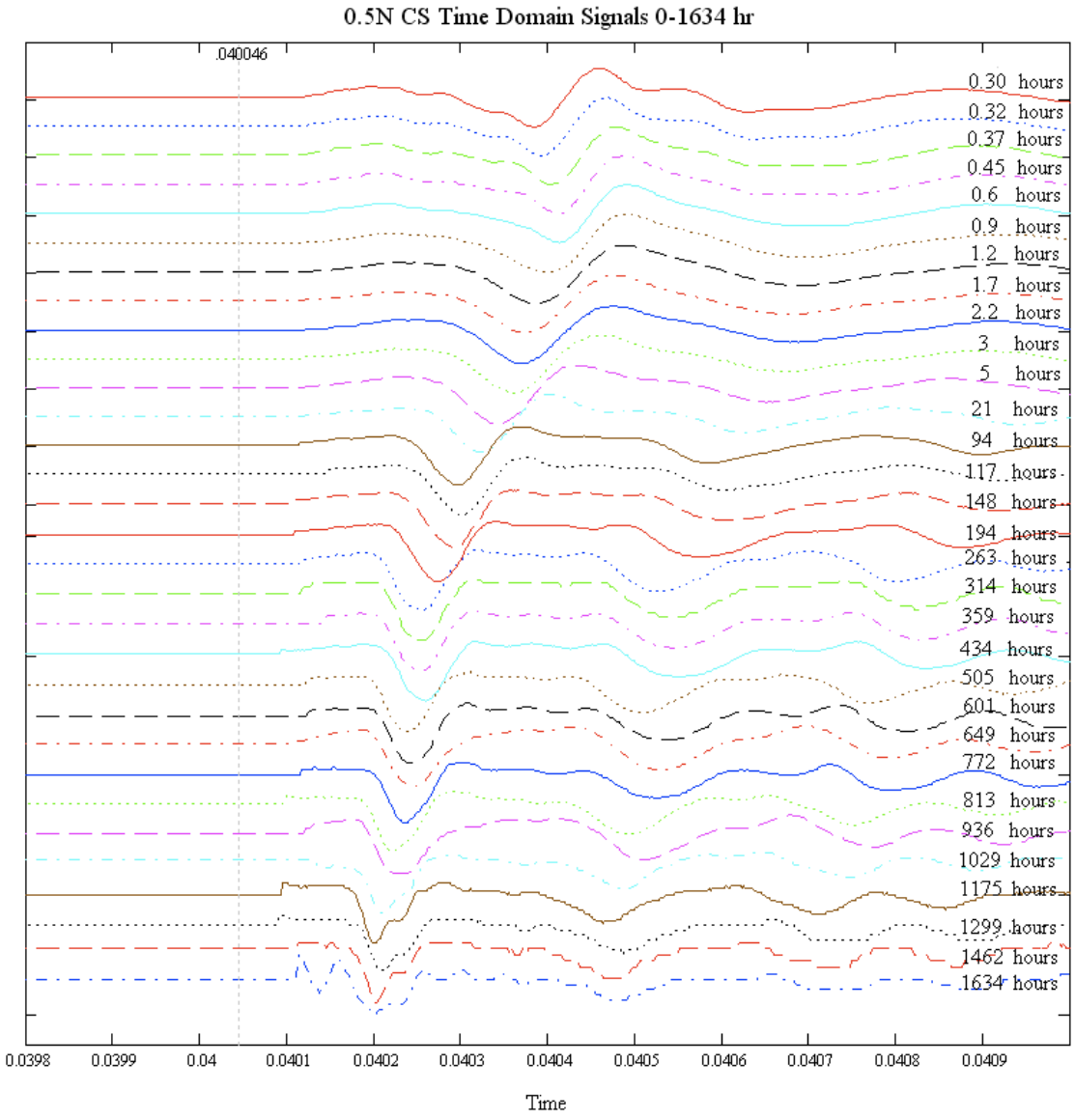

Figure B.2 Close up of shear wave arrival over time of Sample 1

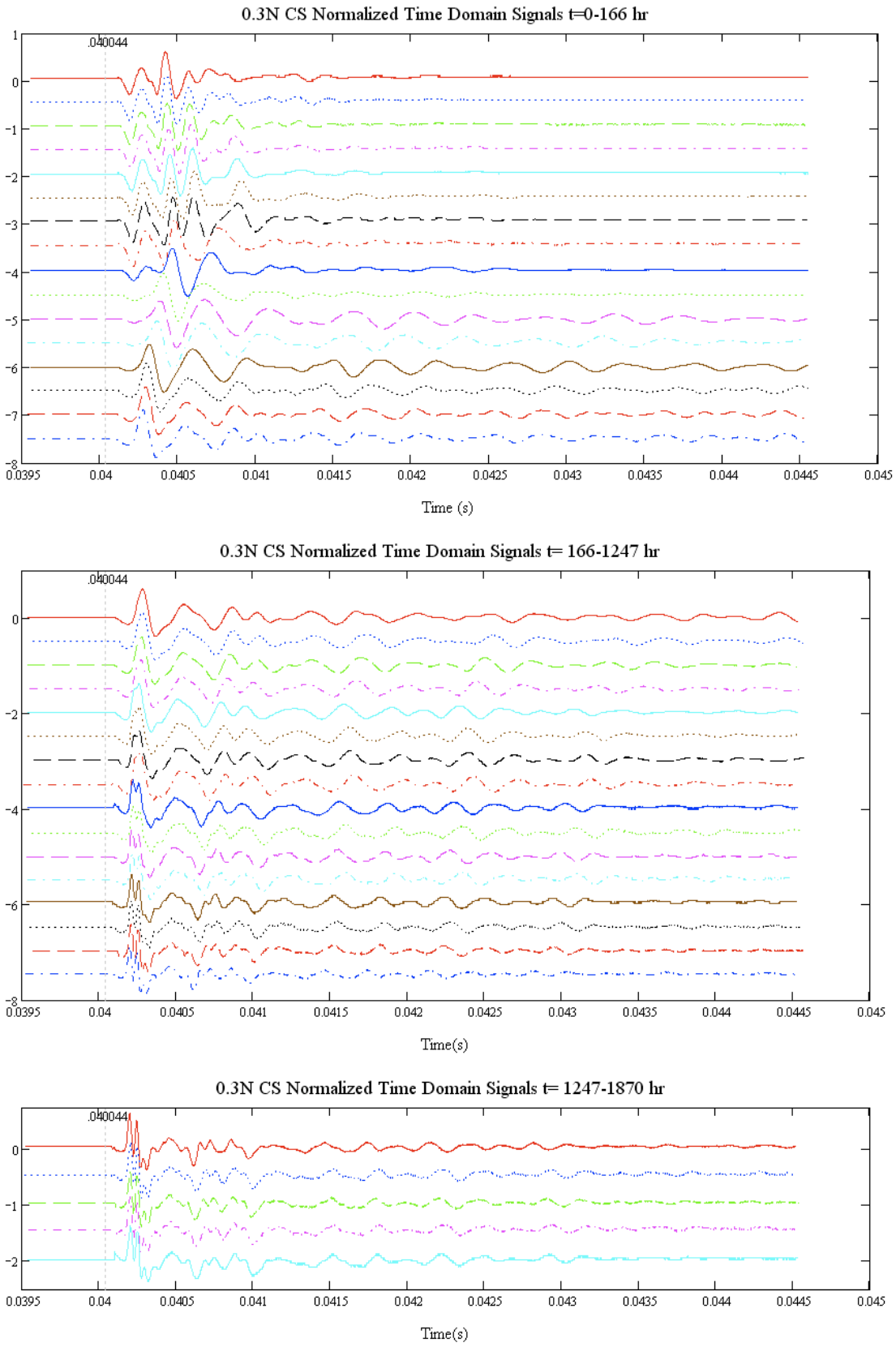

Figure B.3 Output signal time histories over time of Sample 3

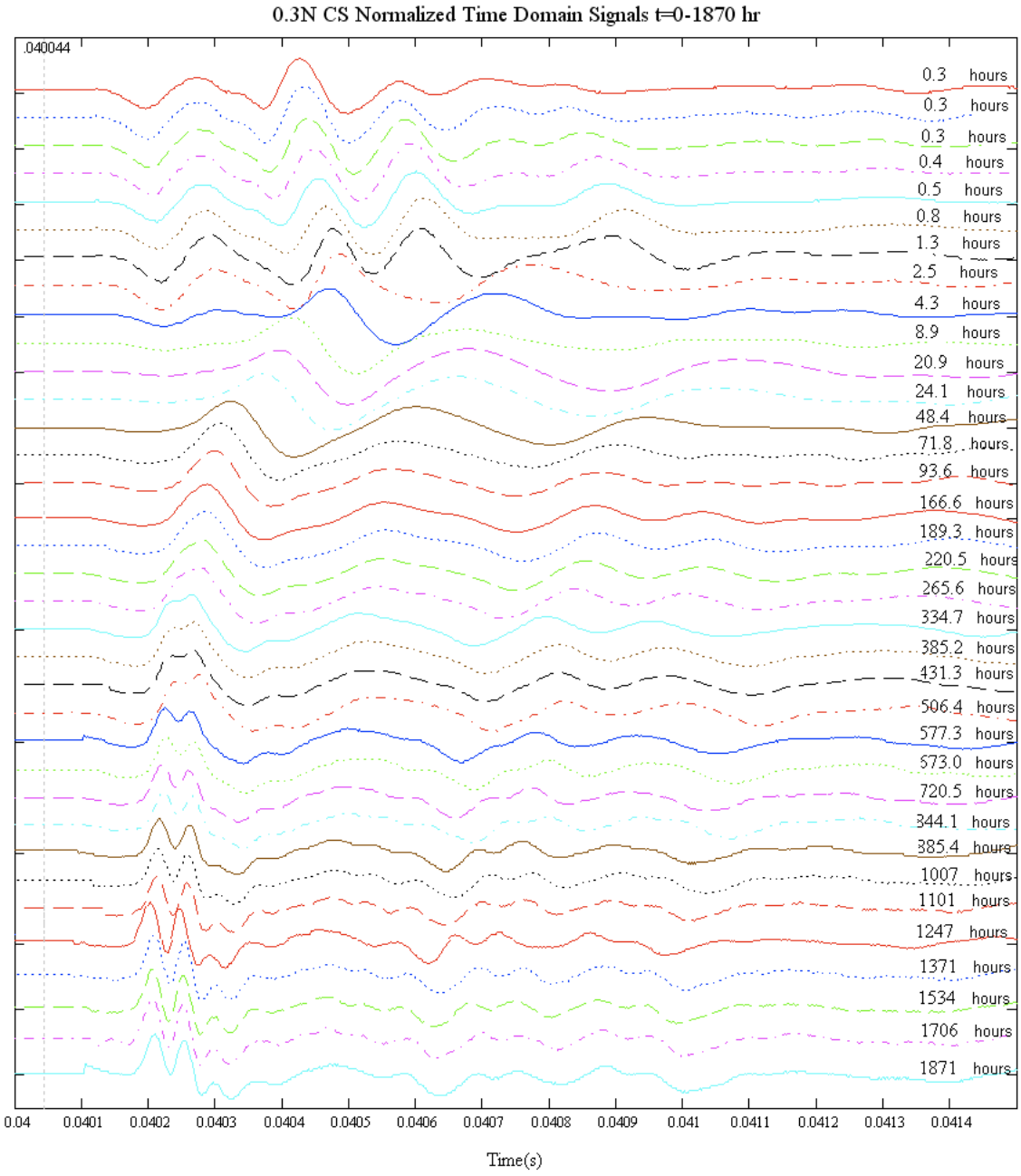

Figure B.4 Close up of shear wave arrival over time of Sample 3

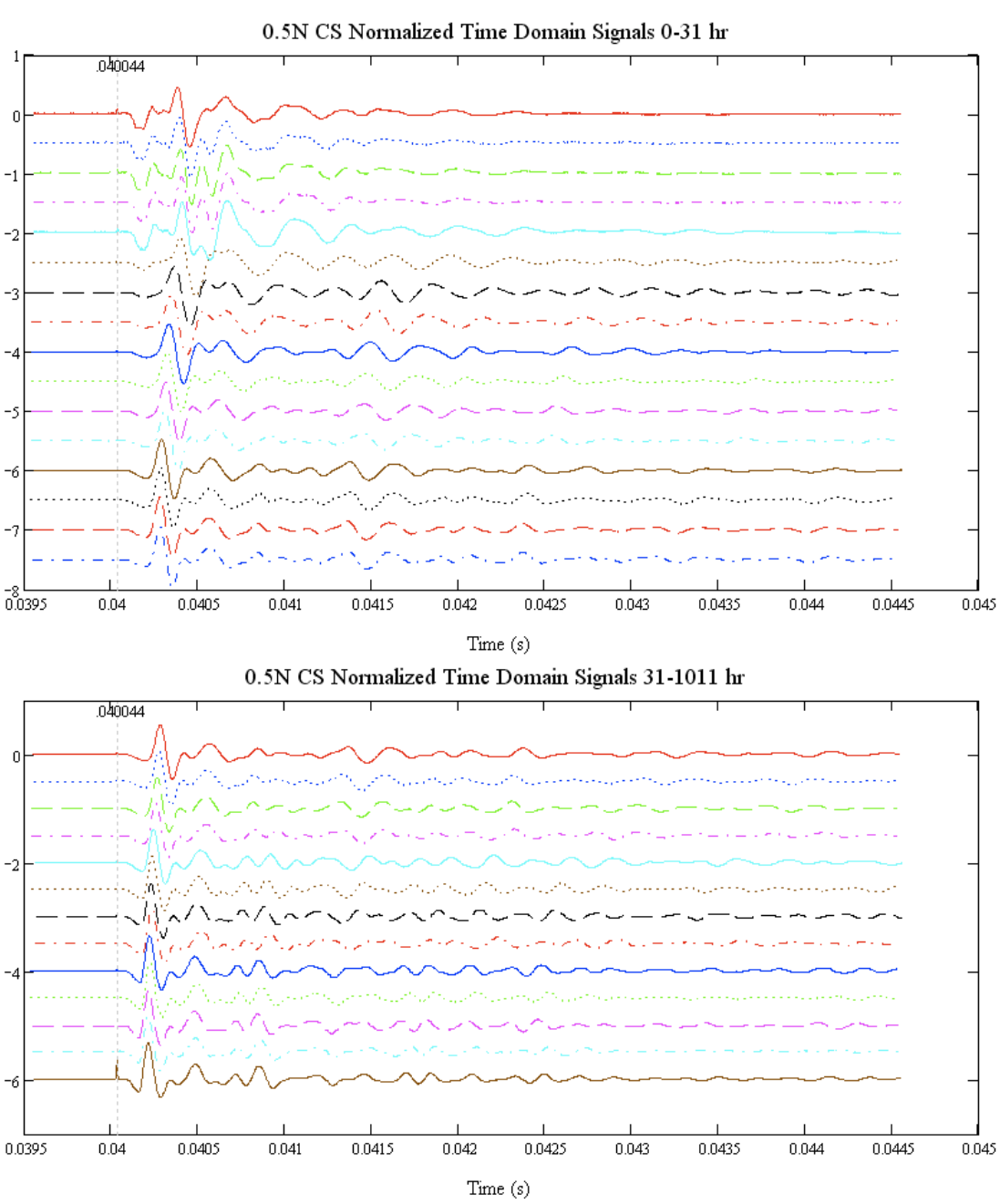

Figure B.5 Output signal time histories over time of Sample 4

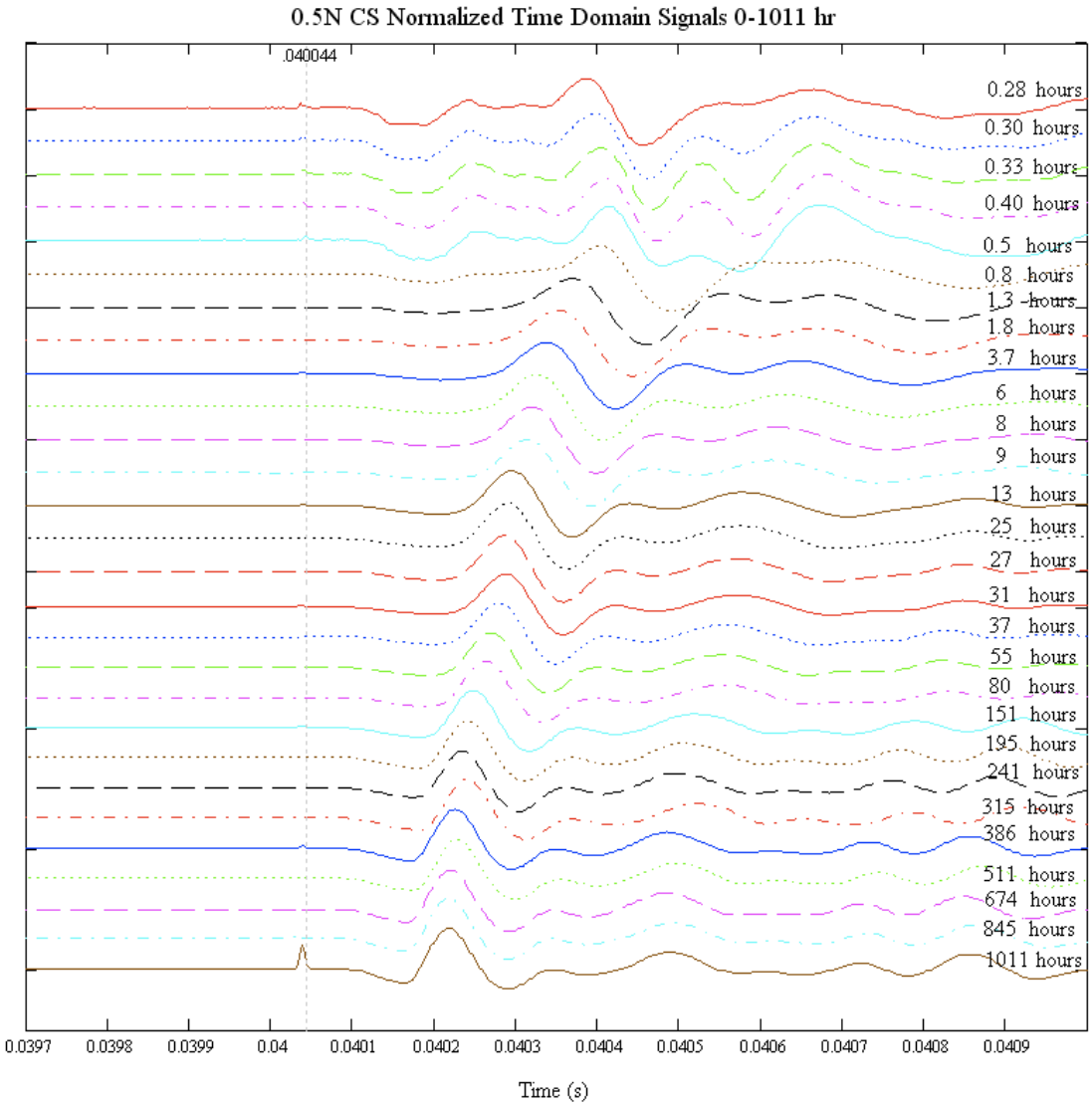

Figure B.6 Close up of shear wave arrival over time of Sample 4

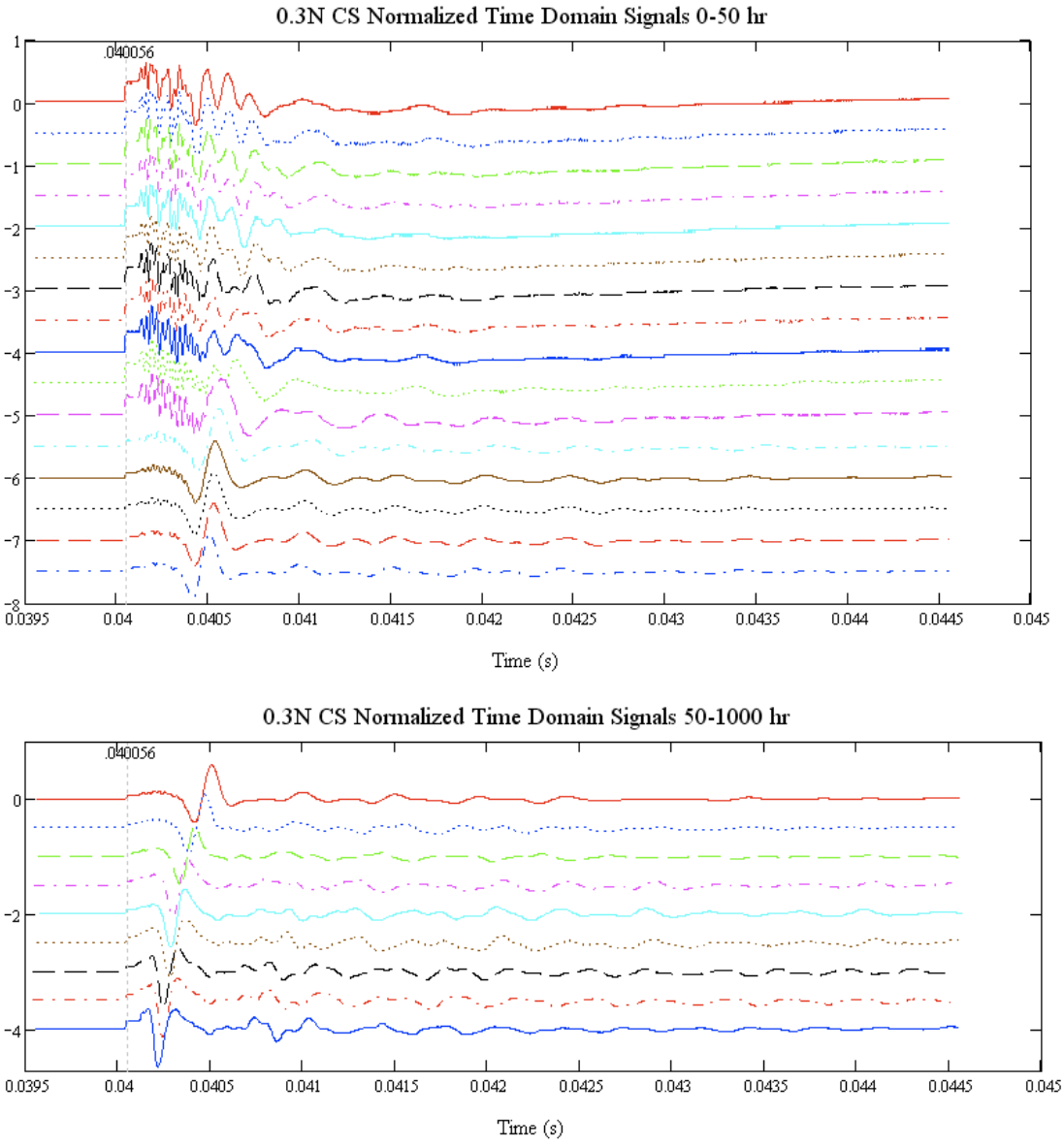

Figure B.7 Output signal time histories over time of Sample 5

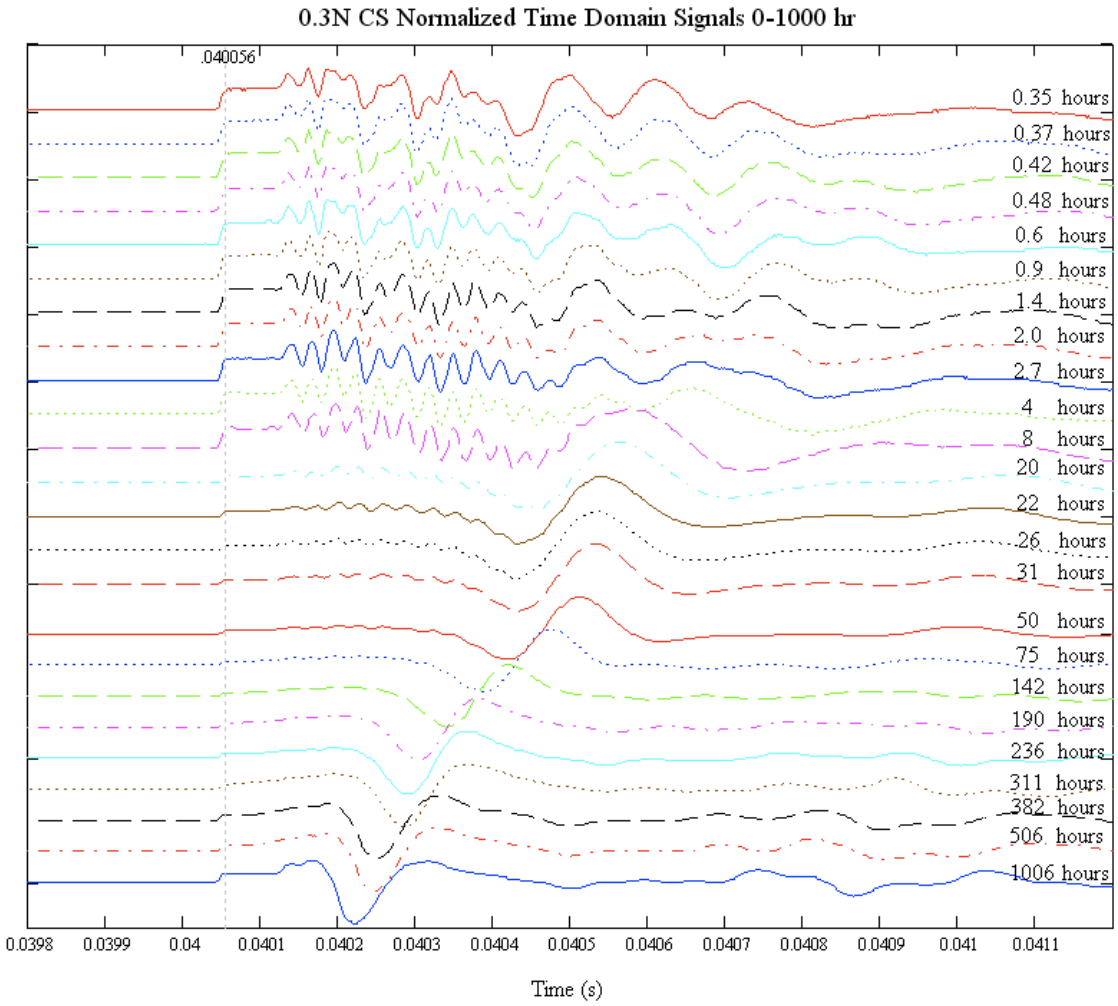

Figure B.8 Close up of shear wave arrival over time of Sample 5

APPENDIX C SHAKING TABLE PHOTOS AND DATA

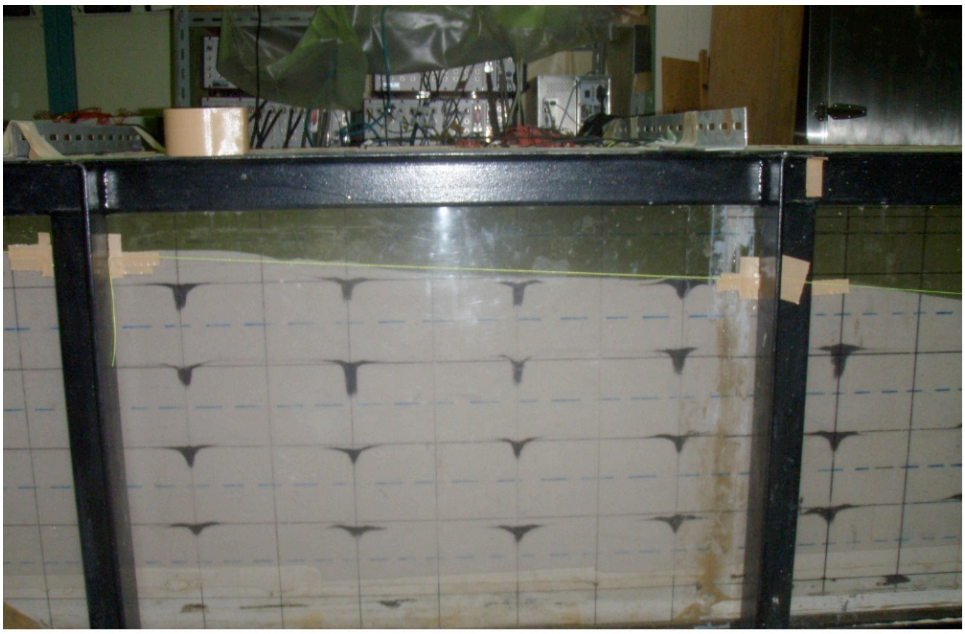

Figure C.1 Test 1 sample before shaking

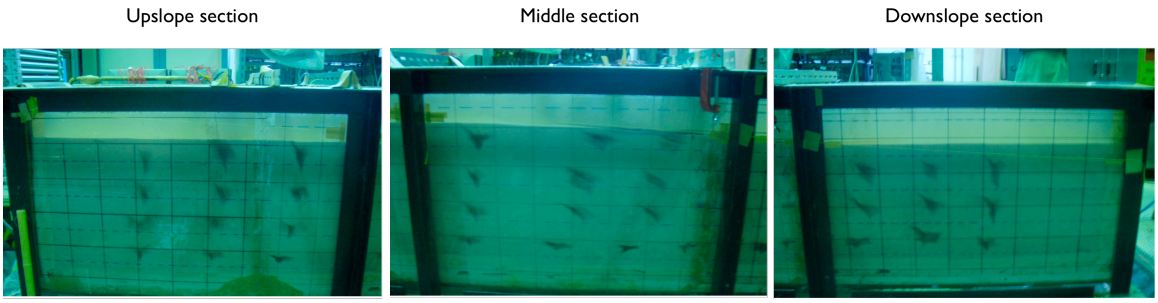

Figure C.2 Test 1 sample after shaking

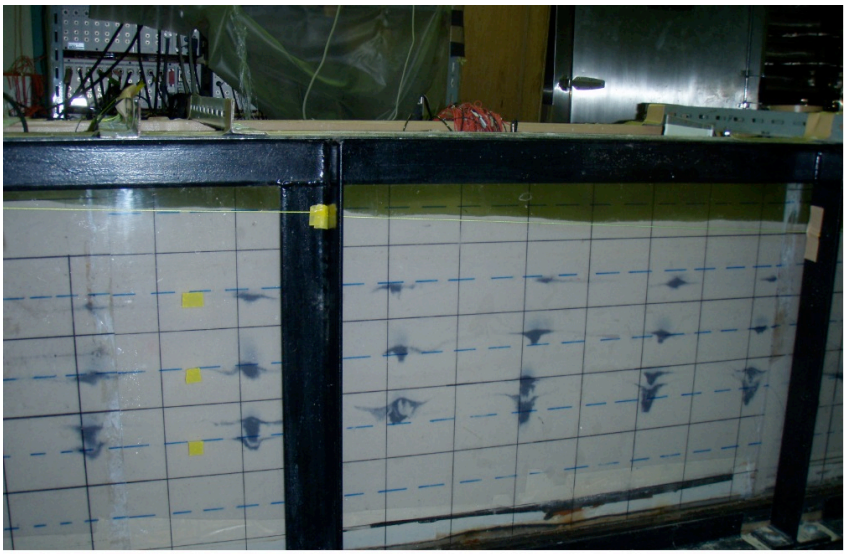

Figure C.3 Test 2 sample before shaking

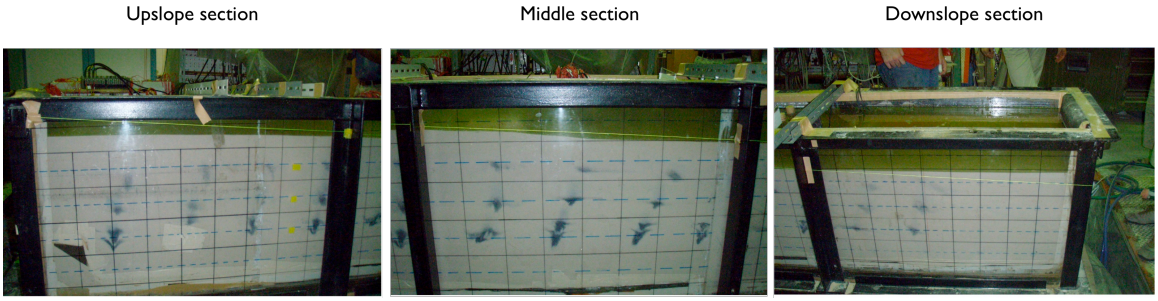

Figure C.4 Test 2 sample after shaking

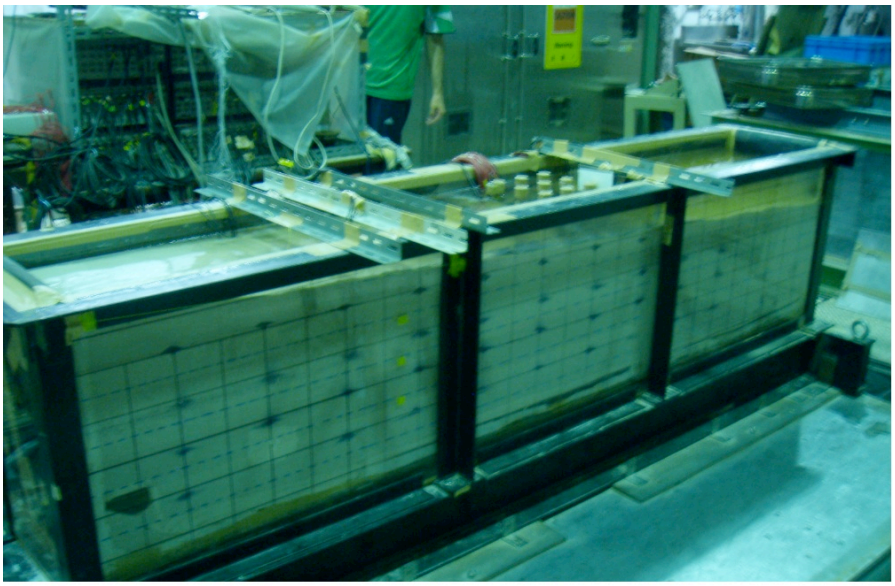

Figure C.5 Test 3 sample before shaking

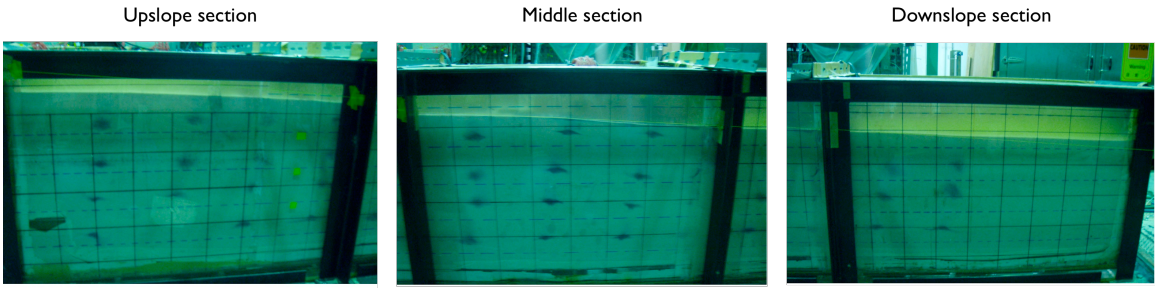

Figure C.6 Test 3 sample after shaking

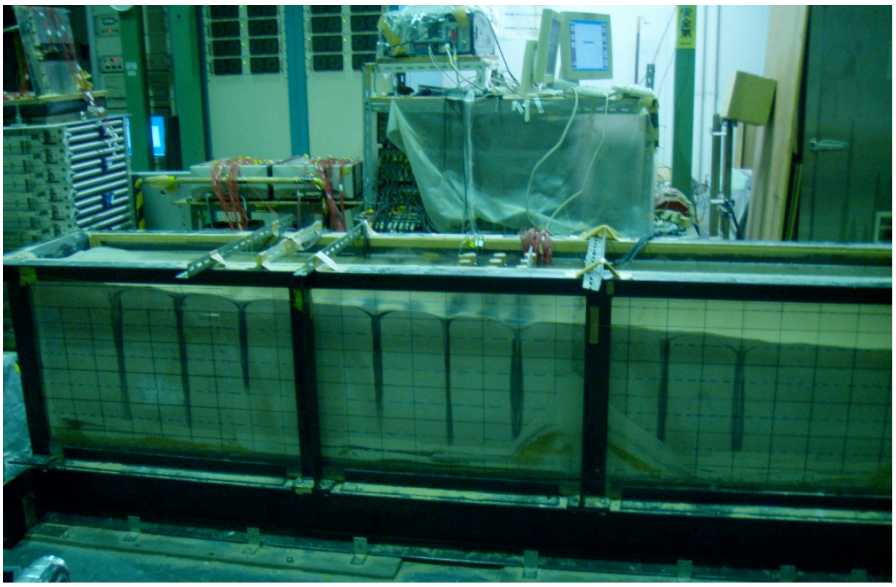

Figure C.7 Test 4 sample before shaking

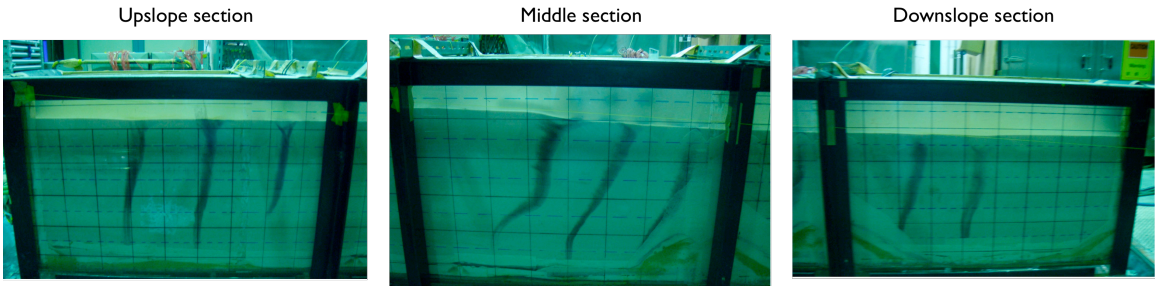

Figure C.8 Test 4 sample after shaking

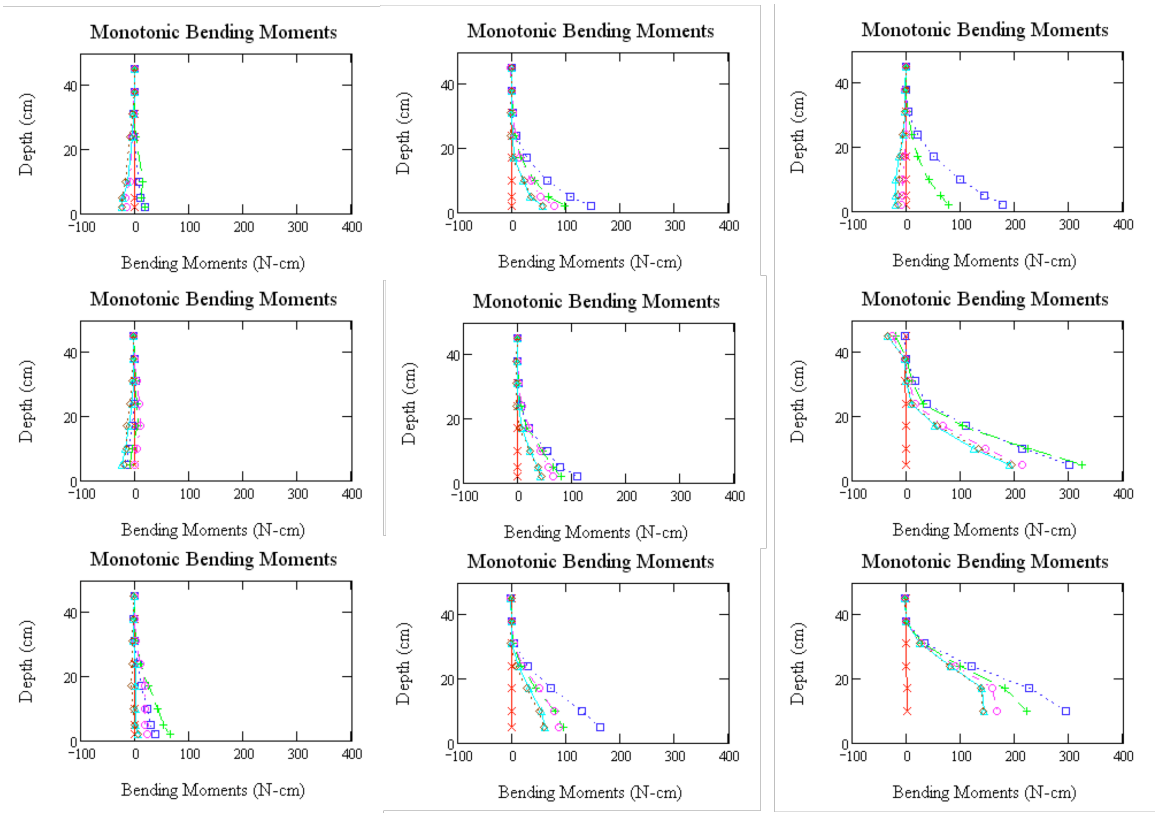

Figure C.9 Monotonic bending moments for Test 1

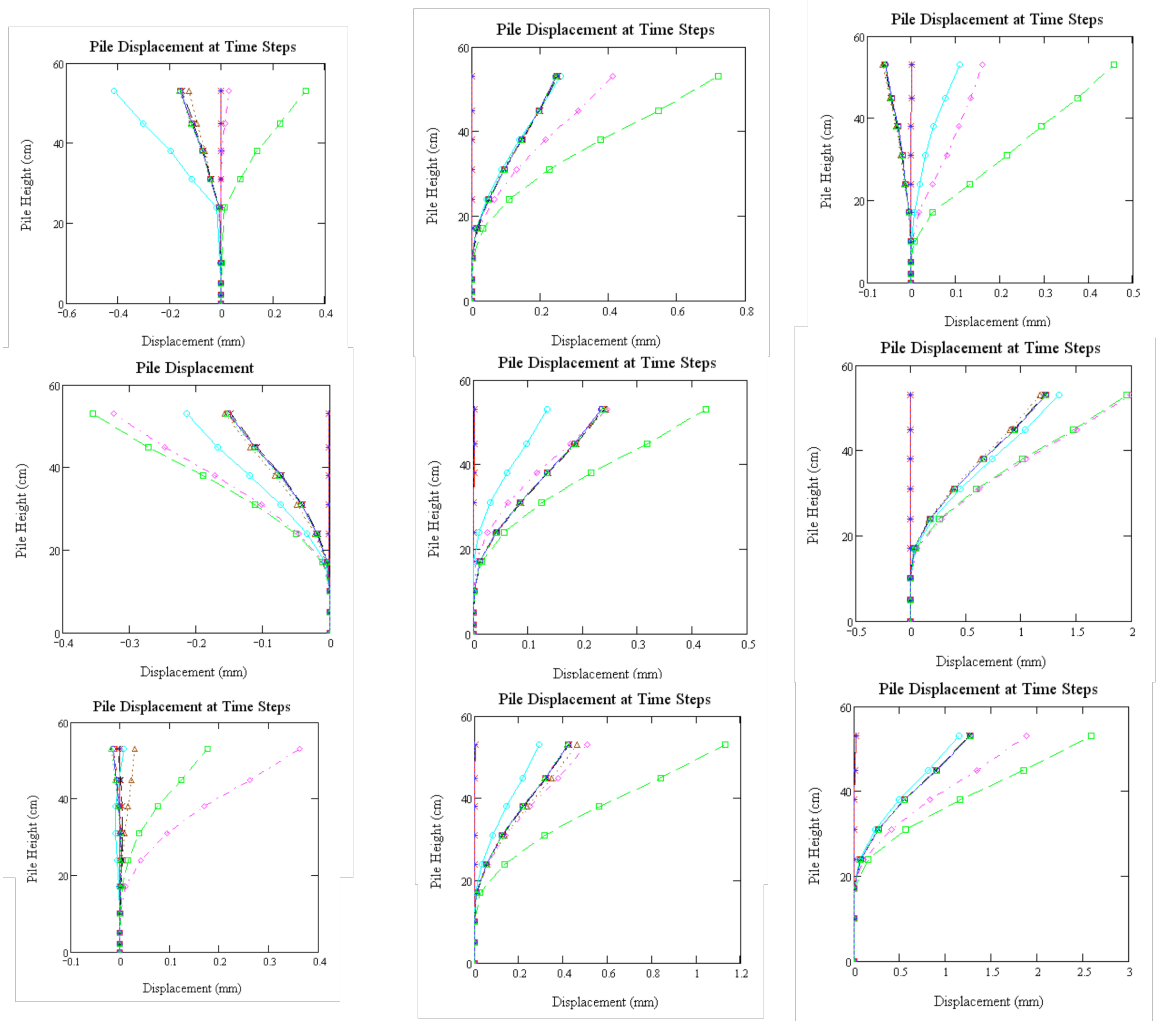

Figure C.10 Calculated pile displacements for Test 1

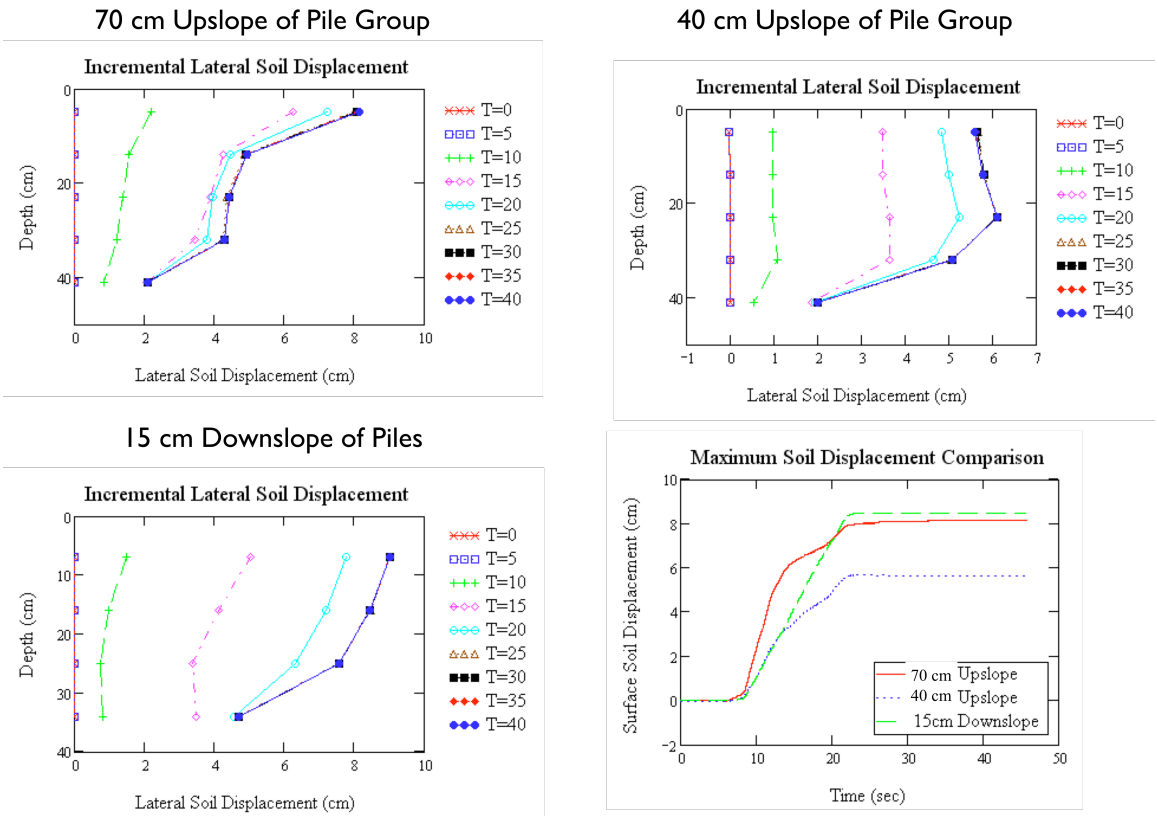

Figure C.11 Inclinometer response for Test 1

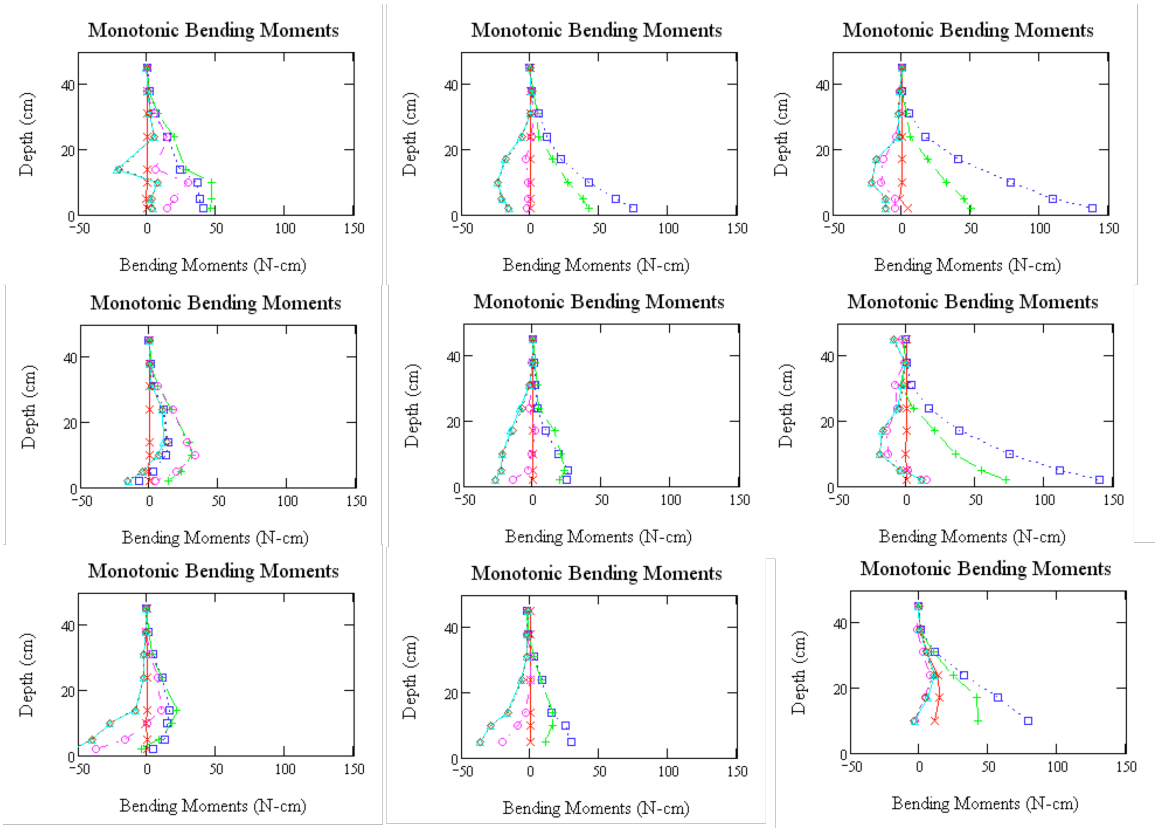

Figure C.12 Monotonic bending moments for Test 2

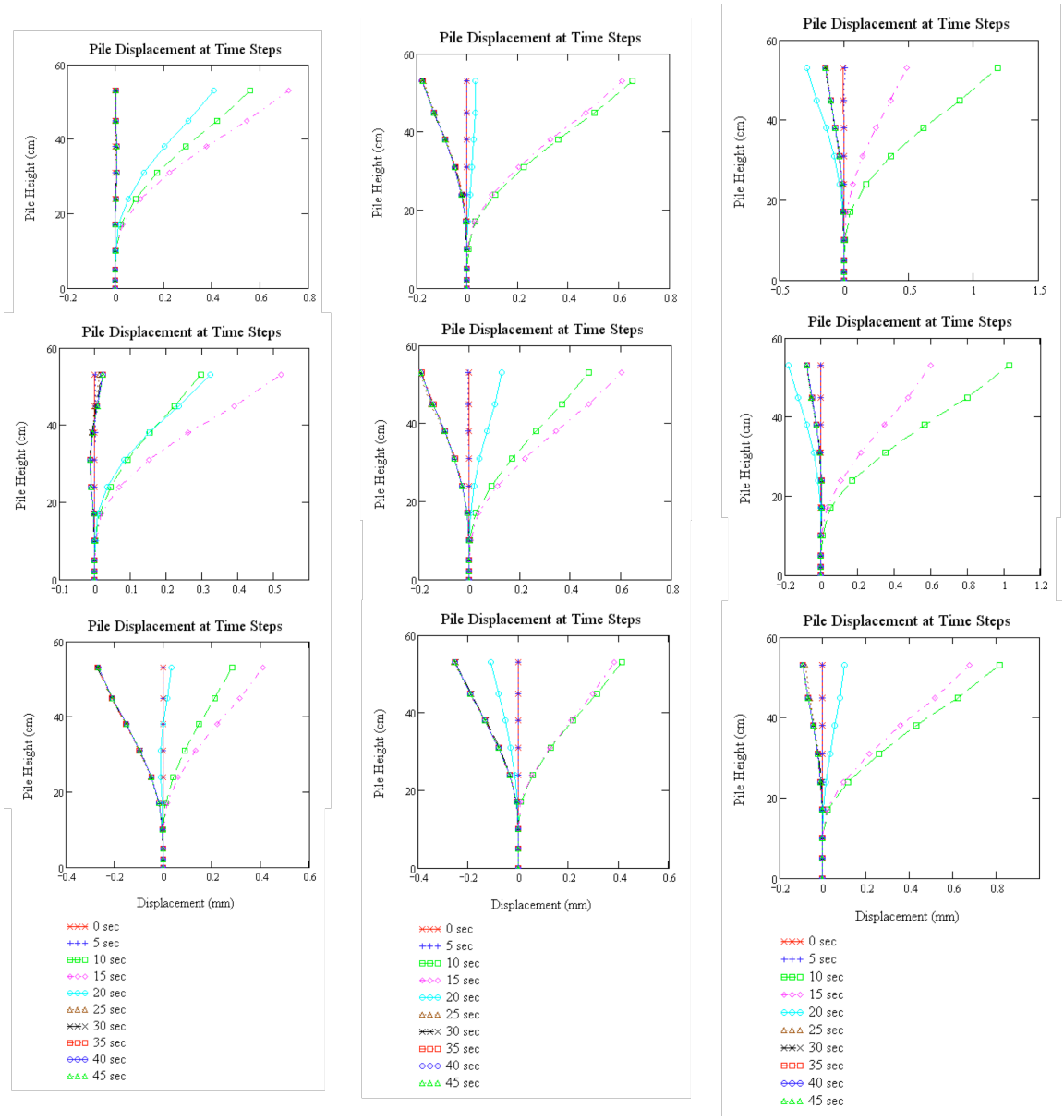

Figure C.13 Calculated pile displacements for Test 2

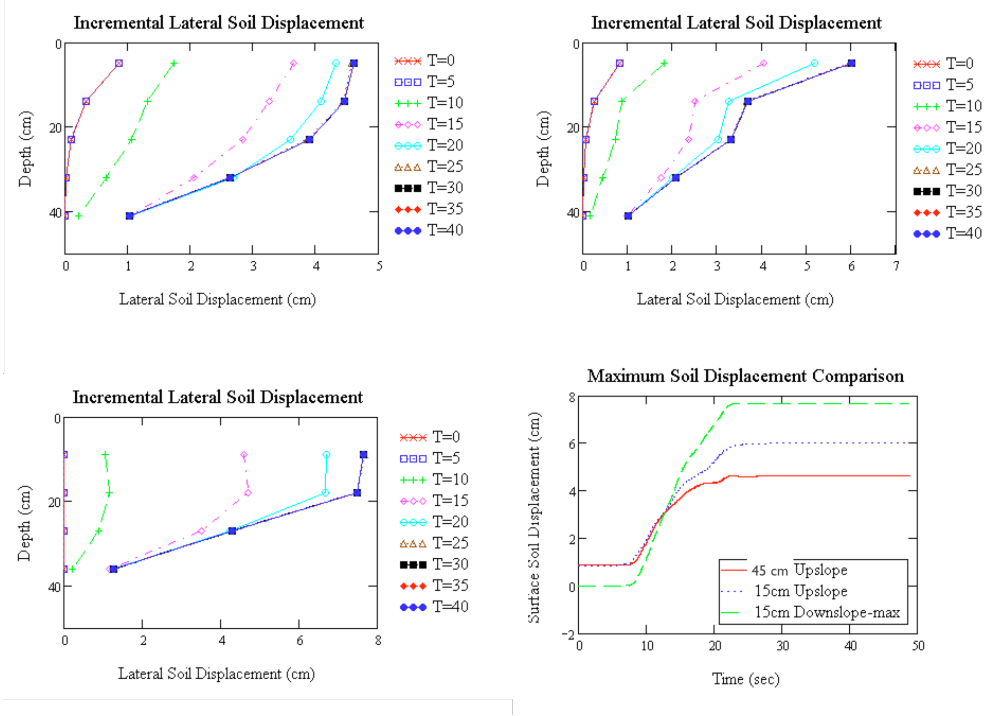

Figure C.14 Inclinometer response for Test 2

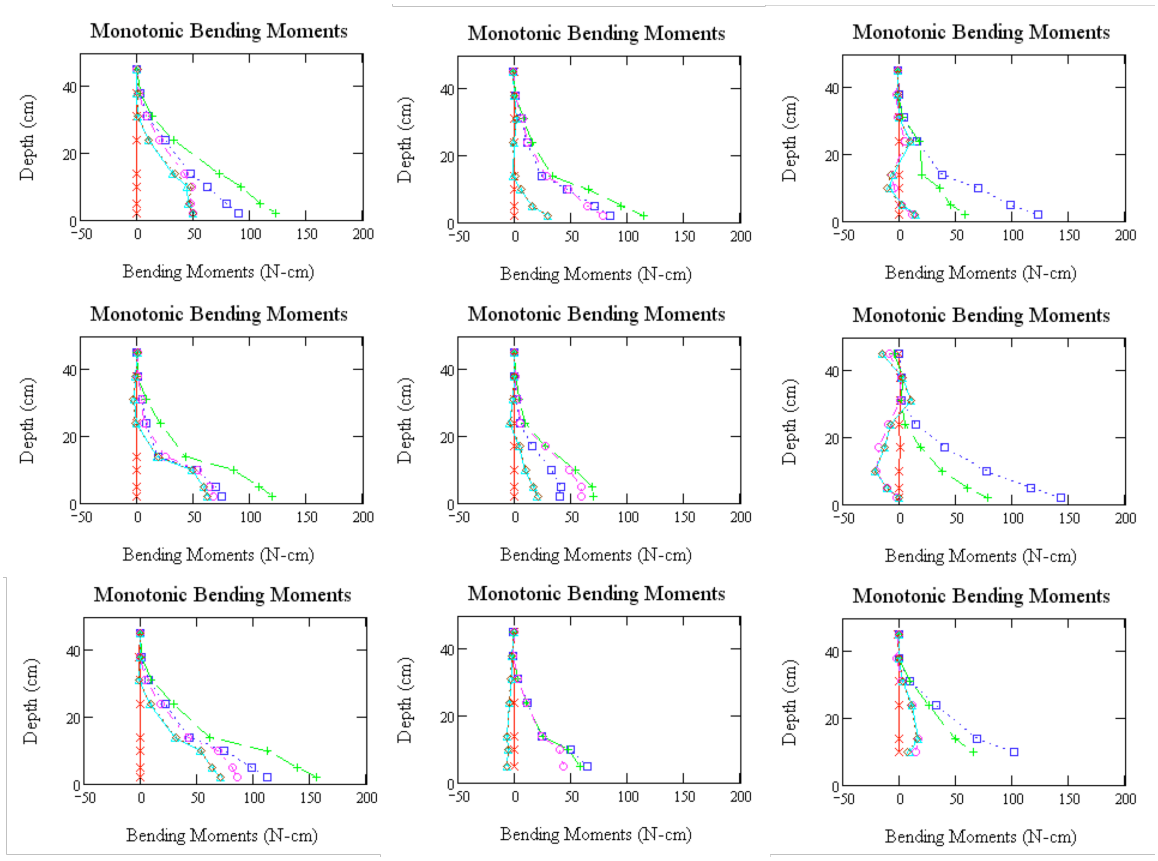

Figure C.15 Monotonic bending moments along the length of the piles of the 3 by 3 pile group for Test 3

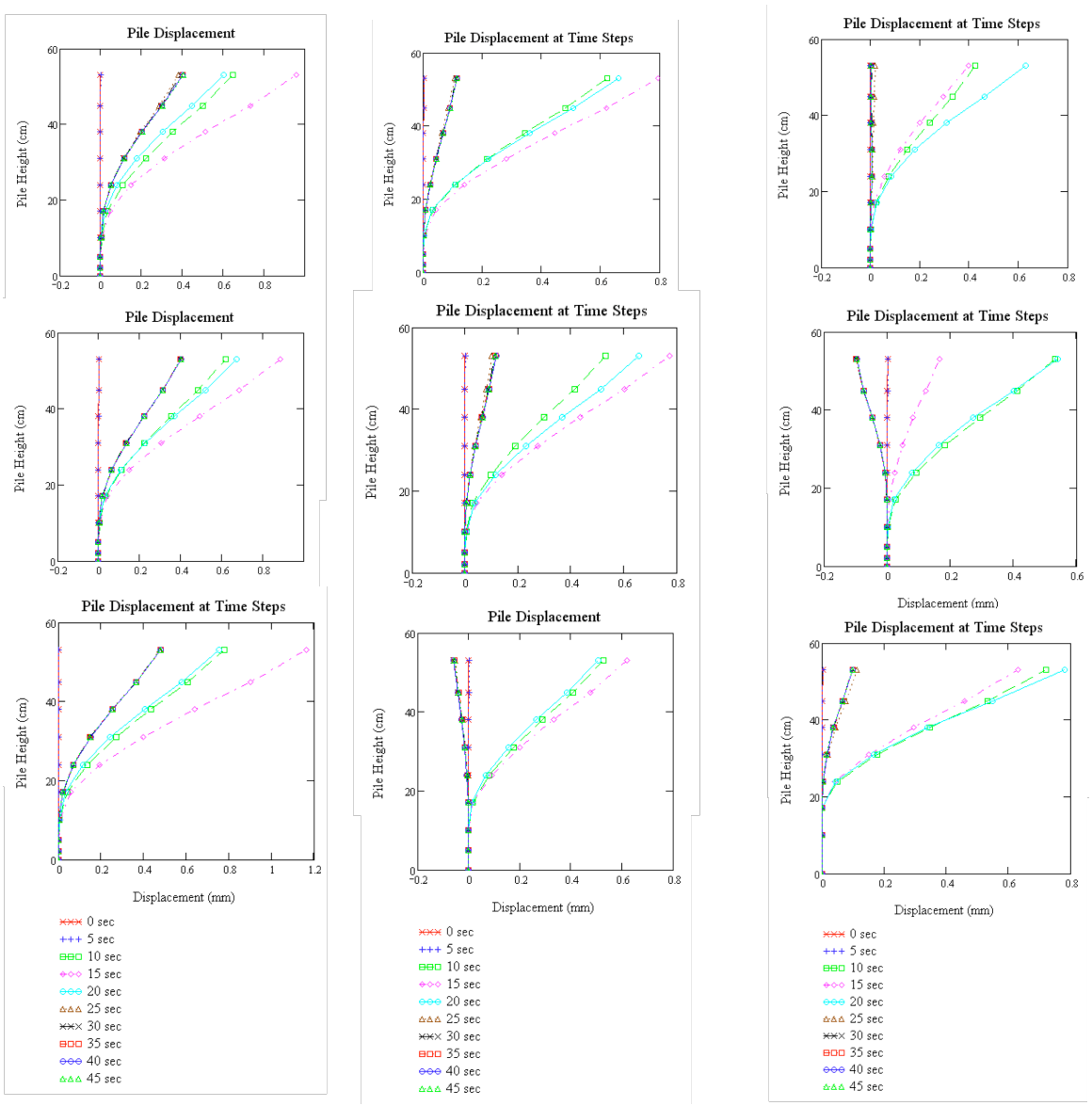

Figure C.16 Pile displacement calculations of the 3 by 3 pile group for Test 3

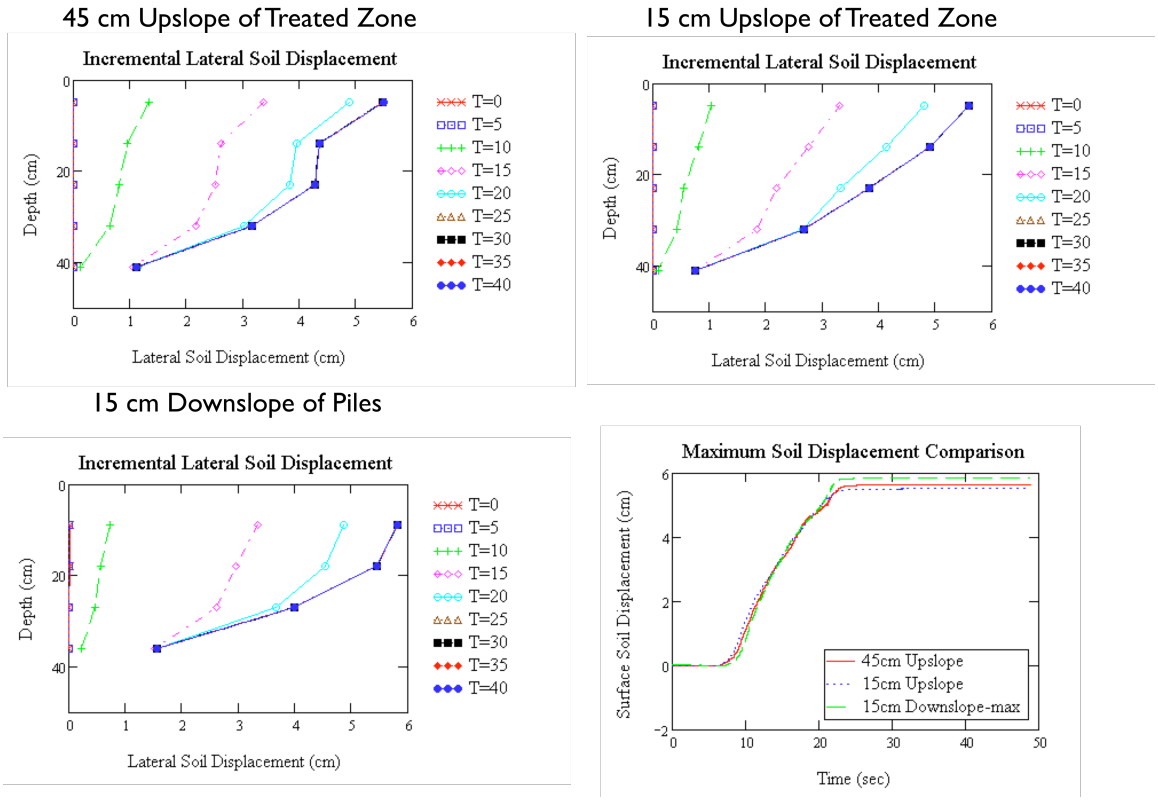

Figure C.17 Inclinometer response for Test 3

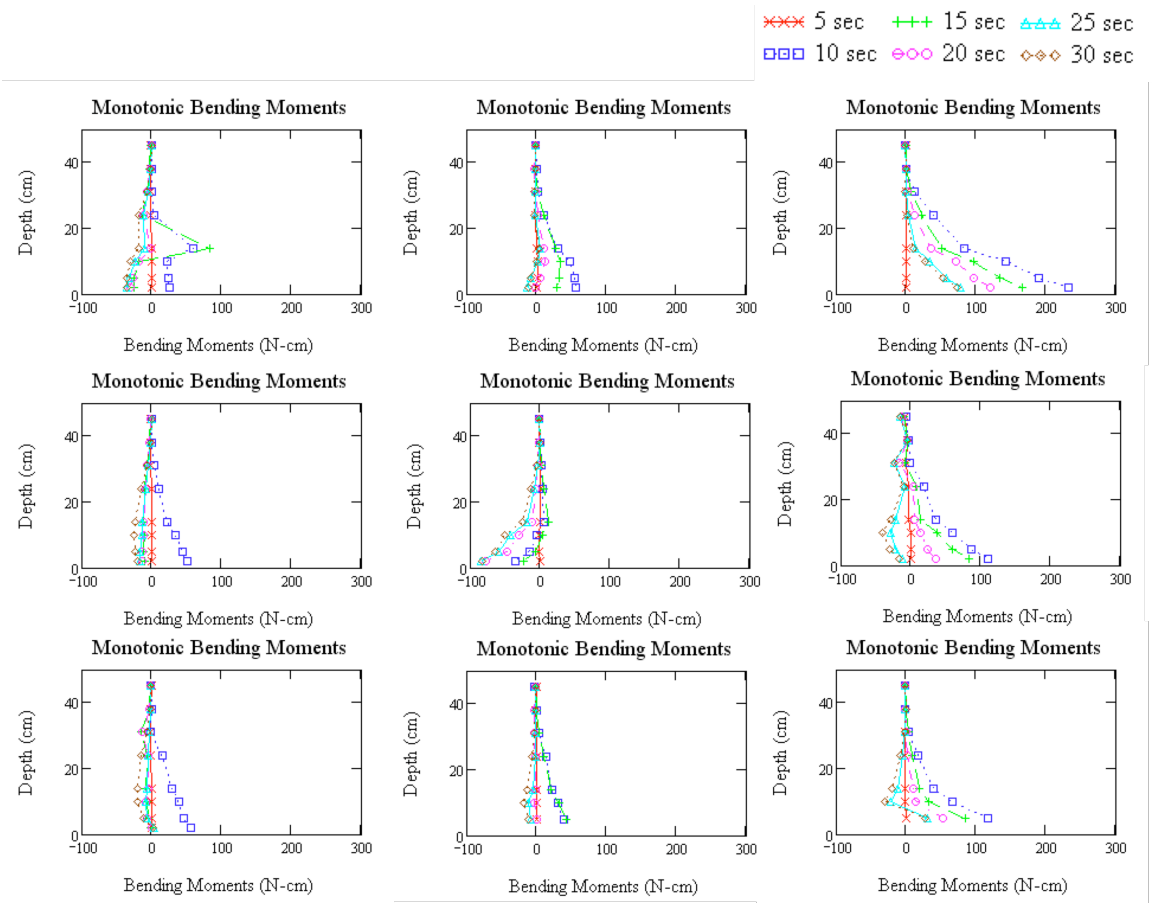

Figure C.18 Monotonic bending moments of the 3 by 3 pile group for Test 4

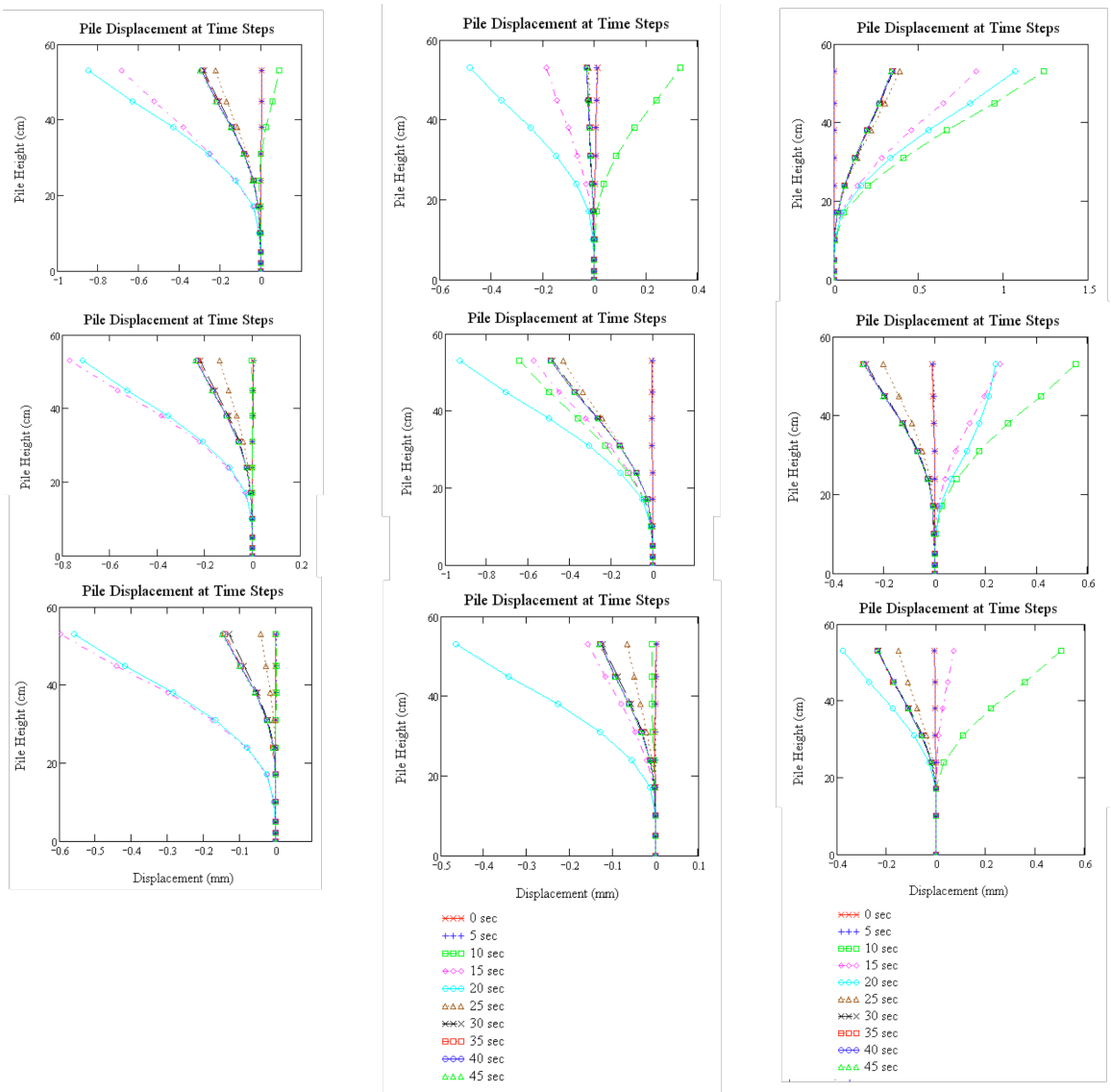

Figure C.19 Pile displacement response for Test 4

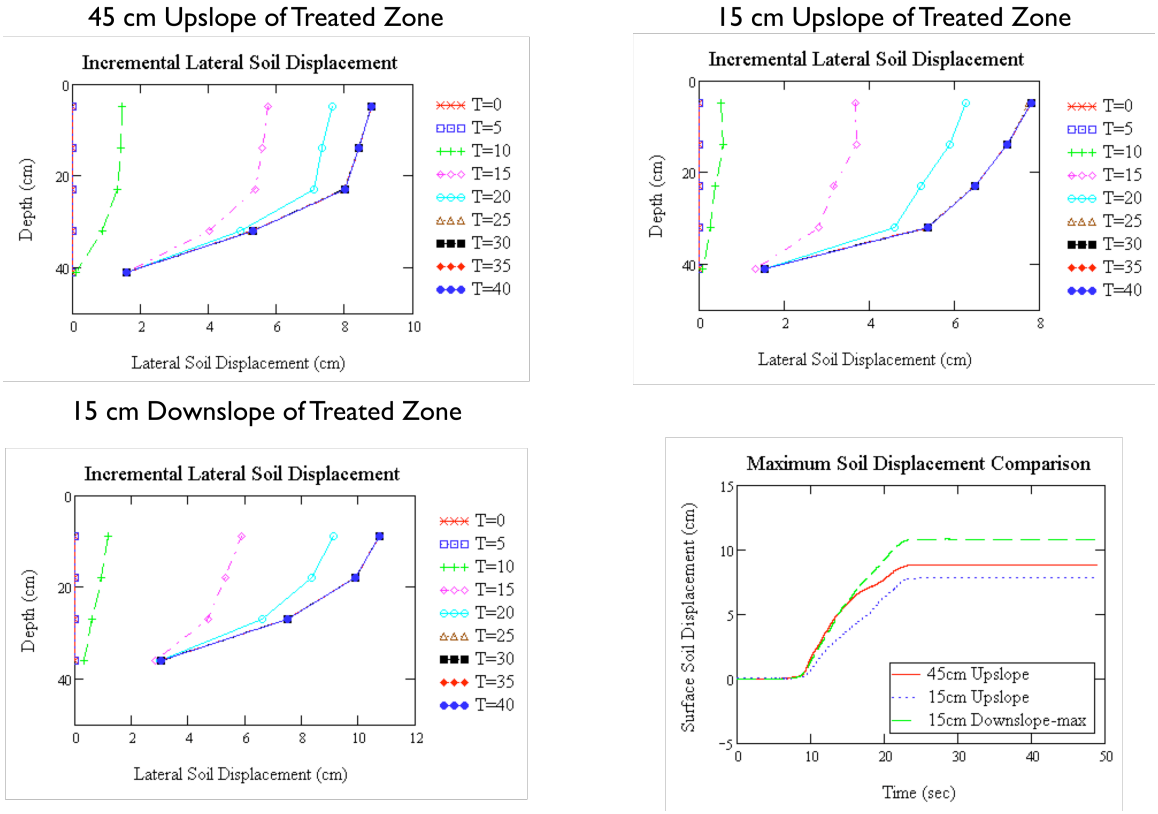

Figure C.20 Inclinometer lateral soil displacement of the three inclinometers for Test 4

REFERENCES

Abdoun, T., Dobry, R., O'Rourke, T. D., and Goh, S. H. (2003). "Pile response to lateral spreads: centrifuge modeling." *Journal of Geotechnical and Geoenvironmental Engineering*, 129(10), 869-878.

Abdoun, T. H., Dobry, R., Zimmie, T. F., and Zeghal, M. (2005). "Centrifuge research of countermeasures to protect pile foundations against liquefaction-induced lateral spreading." *Journal of Earthquake Engineering*, 9(1), 105-125.

Alarcon-Guzman, A., Chameau, J. L., Leonards, G. A., and Frost, J. D. (1989). "Shear modulus and cyclic undrained behavior of sands." *Soils and Foundations*, 29(4), 105-119.

Anderson, D. G., and Stokoe II, K. H. (1978). "Shear modulus, a time-dependent soil property." Dynamic Geotechnical Testing (ASTM STP 654), ASTM, Philadelphia, 66-90.

Arroyo, M., Muir Wood, D., and Greening, P. D. (2003). "Source near-field effects and pulse tests in soil samples." *Geotechnique*, 53(3), 337-345.

Arroyo, M., Muir Wood, D., Greening, P. D., Medina, L., and Rio, J. (2006). "Effects of sample size on bender-based axial Go measurements." *Geotechnique*, 56(1), 39-52.

Arulnathan, R., Boulanger, R. W., and Riemer, M. F. (1998). "Analysis of bender element tests." *Geotechnical Testing Journal*, 21(2), 120-131.

Ashford, S. A., Juirnarongrit, T., Sugano, T., and Hamada, M. (2006). "Soil-pile response to blast induced later spreading I. Field test." *Journal of Geotechnical and Geoenvironmental Engineering*, 132(2), 152-162.

Atkinson, J. H. (2000). "Non-linear soil stiffness in routine design." *Geotechnique*, 50(5), 487-508.

Axelsson, M. (2006). "Mechanical tests on a new non-cementitious grout, silica sol: A laboratory study of the material characteristics." *Tunnelling and Underground Space Technology*, 21, 554-600.

Baird, J. C., and Walz, J. Y. (2006). "The effects of added nanoparticles on aqueous kaolinite suspensions I. Structural effects." *Journal of Colloid and Interface Science*, 297, 161-169.

Baird, J. C., and Walz, J. Y. (2007). "The effects of added nanoparticles on aqueous kaolinite suspensions II. Rheological effects." *Journal of Colloid and Interface Science*, 306, 411-420.

Baxter, C. D. P., and Mitchell, J. K. (2004). "Experimental study on the aging of sands." *Journal of Geotechnical and Geoenvironmental Engineering*, 130(10), 1051-1062.

Bergna, H. E., and Roberts, W. O. (2006). *Colloidal Silica: Fundamentals and Applications*, CRC Taylor & Francis, Boca Raton, FL.

Berryman, J. G. (1999). "Origin of Gassmann's equations." *Stanford Exploration Project*, Report 102, 187-192.

Blewett, J., Blewett, I. J., and Woodward, P. K. (1999). "Measurement of shear-wave velocity using phae-sensitive detection techniques." *Canadian Geotechnical Journal*, 36, 934-939.

Blewett, J., Blewett, I. J., and Woodward, P. K. (2000). "Phase and amplitude response associated with the measurements of shear wave velocity in sand by bender elements." *Canadian Geotechnical Journal*, 37, 1348-1357.

Boulanger, R. W., Kutter, B. L., Brandenberg, S. J., Singh, P., and Chang, D. (2003). "Pile foundations in liquefied and laterally spreading ground during earthquakes: Centrifuge experiments and analyses." University of California.

Chang, W.-J., Rathje, E. M., II, K. H. S., and Cox, B. R. (2004). "Direct evaluation of effeciveness of prefabricated vertical drains in liquefiable sand." *Soil Dynamics and Earthquake Engineering*, 24, 723-731.

Chung, R. M., Yokel, R. Y., and Drnevich, V. P. (1984). "Evaluation of dynamic properties of sands by resonant column testing." *Geotechnical Testing Journal*, 7(2), 60-69.

Ciz, R., and Shapiro, S. A. (2007). "Generalization of Gassmann equations for porous media saturated with a solid material." *Geophysics*, 72(6), A75-A79.

Corral, G., and Whittle, A. (2007). "Cyclic direct shear testing." G. J. Rix and L. M. Spencer, eds., Atlanta, GA.

Cubrinovski, M., and Ishihara, K. (2006). "Assesment of pile group response to lateral spreading by single pile analysis." *Seismic Performance and Simulation of Pile*

Foundations in Liquified and Laterally Spreading Ground, Geotechnical Special Publication No 145 242-254.

D4015, A. (2001). "Standard test methods for modulus and damping of soils by the resonant-column method. Designation D-4015.", A. B. o. A. Standards, ed., ASTM.

Delfosse-Ribay, E., Djeran-Maigre, I., Cabrillac, R., and Gouvenot, D. (2004). "Shear modulus and damping ratio of grouted sand." *Soil Dynamics and Earthquake Engineering*, 24, 461-471.

Dobry, R., and Vucetic, M. "Dynamic properties and seismic response of soft clay deposits." *International Symposium on Geotechnical Engineering of Soft Soils*, Mexico City, 51-87.

Drabarek, E., Bartlett, J. R., Hanley, H. J. M., Woolfrey, J. L., and Muzny, C. D. (2002). "Effect of processing variables on the structural evolution of silica gels." *International Journal of Thermophysics*, 23(1), 145-160.

Drabeck, E., Bartlett, J. R., Hanley, H. J. M., Woolfrey, J. L., and Munzy, C. D. (2002). "Effect of processing variables on the structural evolution of silica gels." *International Journal of Thermophysics*, 23(1), 145-160.

Dumas, J., Quinson, J. F., Bovier, C., Baza, S., and Serughetti, J. (1986). "Correlations between textural and mechanical properties in wet silica gels." *Journal of Non-Crystalline Solids*, 82, 220-224.

DuPont. (1997). "Ludox Colloidal Silica: Properties, Usage, Storage and Handling." Product Information, DuPont, Wilmington, DE.

Dyvik, R., and Madshus, D. "Lab measurements of Gmax using bender element." *ASCE Convention on Advances in the Art of Soil under Cyclic Conditions*, 186-196.

Ferreira, C., Fonseca, A. V. d., and Santos, J. A. (2007). "Comparison of simultaneous bender elements and resonant column tests on Porto residual soil." Soil Stress-Strain Behavior: Measurement, Modeling and Analysis, H. I. Ling, L. Castillo, D. Leshchinsky, and J. Koseki, eds., Springer, 523-535.

Frith, W. J., Pichot, R., Kirkland, M., and Wolf, B. (2008). "Formation, stability, and rheology of particle stabilized emulsions: Influence of multivalent cations." *Industrial and Engineering Chemistry Research*, 47, 6424-6444.

Gallagher, P. M. (2000). "Passive site remediation for mitigation of liquefaction risk," PhD, Virginia Polytechnic Institute, Blacksburg, VA.

Gallagher, P. M., Conlee, C. T., and Rollins, K. M. (2007). "Full-scale field testing of colloidal silica grouting for mitigation of liquefaction risk." *Journal of Geotechnical and Geoenvironmental Engineering*, 133(2), 186-196.

Gallagher, P. M., and Koch, A. J. (2003). "Model testing of passive site stabilization: A new grouting technique." Geotechnical Special Publication 120, Grouting and Ground Treatment, L. F. Johnson, D. A. Bruce, and M. J. Byle, eds., ASCE, New Orleans, LA, 1478-1489.

Gallagher, P. M., and Lin, Y. (2005). "Column testing to determine colloidal silica transport mechanisms." Geotechnical Special Publication 136, Innovations in Grouting and Soil Improvement, ASCE.

Gallagher, P. M., and Mitchell, J. K. (2002). "Influence of colloidal silica grout on liquefaction potential and cyclic undrained behavior of loose sand." *Soil Dynamics and Earthquake Engineering*, 22, 1017-1026.

Gallagher, P. M., Pamuk, A., and Abdoun, T. H. (2006). "Stabilization of liquefiable soils using colloidal silica grout." *Journal of Materials in Civil Engineering*.

Gallagher, P. M., Pamuk, A., Koch, A. J., and Abdoun, T. H. "Centrifuge modeling of passive site remediation." *7th U.S. National Conference on Earthquake Engineering*, Boston, MA.

Gonzalez, L., Abdoun, T., and Dobry, R. (2009). "Effet of soil permeability on centrifuge modeling of pile response to lateral spreading." *Journal of Geotechnical and Geoenvironmental Engineering*, 135(1), 62-73.

Hamada, M., Isoyama, R., and Wakamatsu, K. (1996). "Liquefaction-induced ground displacement and its related damage to lifeline facilities." *Soils and Foundations*(special), 81-97.

Harada, N., Towhata, I., Takatsu, T., Tsunoda, S., and Sesov, V. (2006). "Development of new drain method for protection of existing pile foundations from liquefaction effects." *Soil Dynamics and Earthquake Engineering*, 26, 297-312.

Hardin, B. O., and Black, W. L. (1966). "Sand stiffness under various triaxial stresses." *Journal of the Soil Mechanics and Foundations Division*, 92(SM2), 27-42.

Hardin, B. O., and Black, W. L. (1968). "Vibration modulus of normally consolidated clay." *Journal of the Soil Mechanics and Foundations Division*, 95(SM2), 353-369.

Hardin, B. O., and Drnevich, V. P. (1972). "Shear modulus and damping in soils: design equations and curves." *Journal of the Soil Mechanics and Foundations Division*, 98(SM7), 667-692.

Hardin, K. O., Drnevich, V. P., Wang, J., and Sams, C. E. "Resonant column testing at pressures up to 3.5 MPa." *Dynamic Geotechnical Testing II*, San Francisco, 222-233.

Hdach, H., Woignier, T., Phalippou, J., and Scherer, G. W. (1990). "Effect of aging and pH on the modulus of aerogels." *Journal of Non-Crystalline Solids*, 121, 202-205.

Hench, L. L., and West, J. K. (1990). "The sol-gel process." *Chemical Reviews*, 90(1), 33-72.

Howie, J. A., Shozen, T., and Vaid, Y. P. (2002). "Effect of ageing on stiffness of very loose sand." *Canadian Geotechnical Journal*, 39, 149-156.

Huang, H., You, B., Zhou, S., and Wu, L. (2007). "Rheological behavior of aqueous organosilicone resin emulsion stabilized by colloidal nanosilica particles." *Journal of Colloid and Interface Science*, 310, 121-127.

Hwang, S. K. (1997). "Dynamic properties of natural soils," PhD Thesis, University of Texas at Austin, Austin, TX.

Iai, S. (1989). "Similitude for shaking table tests on soil-structure-fluid model in 1g gravitational field." *Soils and Foundations*, 29(1), 105-118.

Iler, R. K. (1979). *The Chemistry of Silica: Solubility, Polymerization, Colloid and Surface Properties, and Biochemistry*, John Wiley & Sons.

Indraratna, B., and Chu, J. (2005). *Ground Improvement- Case Histories*, Elsevier.

Isenhower, W. M. (1979). "Torsional simple shear/resonant column properties of San Francisco bay mud," MS, University of Texas at Austin, Austin, TX.

Ishihara, K. (1996). *Soil Behavior in Earthquake Geotechnics*, Oxford University Press.

Iwasaki, T., Tatsuoka, F., and Takagi, Y. (1978). "Shear modulus of sands under cyclic torsional shear loading." *Soils and Foundations*, 18(1), 39-56.

Jang, D.-J. (1997). "Quantification of sand structure and its evolution during shearing using image analysis," PhD, Georgia Institute of Technology, Atlanta, GA.

Jang, J., and Hamada, M. (2007). "A study on loads on foundation piles from flowing liquefied soil." *Structural Engineering/Earthquake Engineering*, 24(2), 92-101.

Jovicic, V., and Coop, M. R. (1997). "Interpretaion of bender elements - discussion." *Geotechnique*, 47(4), 875.

Kodaka, T., Oka, F., Ohno, Y., Takyu, T., and Yamasaki, N. (2005). "Modeling of cyclic deformation and strength characteristics of silica treated sand." Geotechnical Special Publication 143, Geomechanics: Testing, Modeling and Simulation, J. A. Yamamuro and J. Koseki, eds., ASCE, Boston, MA, 205-216.

Kramer, S. L. (1996). *Geotechnical Earthquake Engineering*, Prentice-Hall, Inc., Upper Sadle River, NJ.

Lee, J.-S., and Santamarina, J. C. (2005). "Bender elements: Performance and sinal interpretation." *Journal of Geotechnical and Geoenvironmental Engineering*, 131(9), 1063-1070.

Li, N., and Woods, R. D. (1987). "Dynamic behavior of grouted sand." Soil-structure Interaction, A. S. Cakmak, ed., Elsevier, 221-241.

Li, X. S., and Yang, W. L. (1998). "Effects of vibration history on modulus and damping of dry sand." *Journal of Geotechnical and Geoenvironmental Engineering*, 124(11), 1071-1081.

Maher, M. H., Ro, K. S., and Welsh, J. P. (1994). "High strain dynamic modulus and damping of chemically grouted sand." *Soil Dynamics and Earthquake Engineering*, 13, 131-138.

Martin, J. R., Olgun, C. G., Mitchell, J. K., Hon, M., and Durgunoglu, H. T. (2004). "High-modulus columns for liquefaction mitigation." *Journal of Geotechnical and Geoenvironmental Engineering*, 130(6), 561-571.

McVay, M., Zhang, L., Molnit, T., and Lai, P. (1998). "Centrifuge testing of large laterally loaded pile groups in sands." *Journal of Geotechnical and Geoenvironmental Engineering*, 124(10), 1016-1026.

Meng, J. (2003). "The influence of loading frequency on dynamic soil properties," Ph.D., Georgia Institute of Technology, Atlanta, Georgia.

Meng, J., and Rix, G. J. (2003). "Reduction of equipment-generated damping in resonant column measurements." *Geotechnique*, 53(5), 503-512.

Mesri, G., Feng, T. W., and Benak, J. M. (1990). "Postdensification penetration resistance of clean sands." *Journal of Geotechnical Engineering*, 116(7), 1095-1115.

Miller, E. A., and Roycroft, G. A. (2004). "Compaction grouting test program for liquefaction control." *Journal of Geotechnical and Geoenvironmental Engineering*, 130(4), 355-361.

Mitchell, J. K., and Hon, M. "Mitigation of liquefaction potential of silty sands." *From Research to Practice*, New Orleans, LA.

Motamed, R. (2007). "Shaking table tests on pile group subjected to liquefaction-induced large ground deformation," PhD, University of Tokyo, Tokyo, Japan.

Motamed, R., and Towhata, I. (2010). "Shaking table model tests on pile groups behind quay walls subjected to lateral spreading." *Journal of Geotechnical and Geoenvironmental Engineering*, 136(3), 477-489.

Ni, S. (1987). "Dynamic properties of sand under true triaxial stress states from resonant column/torsional shear tests," The University of Texas at Austin, Austin, Texas.

Pamuk, A., Gallagher, P. M., and Zimmie, T. F. (2007). "Remediation of piled foundations against lateral spreading by passive site stabilization technique." *Soil Dynamics and Earthquake Engineering*, 27, 864-874.

Park, J.-Y. (1999). "A critical assessment of moist tamping and its effect on the initial and evolving structure of dilatant triaxial specimens," PhD, Georgia Institute of Technology, Atlanta, GA.

Persoff, P., Apps, J., Moridis, G., and Whang, J. M. (1999). "Effect of dilution and contaminants on sand grouted with colloidal silica." *Journal of Geotechnical and Geoenvironmental Engineering*, 125(6), 461-469.

Richardson, M. D., Williams, K. L., Briggs, K. B., and Thoros, E. I. (2002). "Dynamic measurement of sediment grain compressibility at atmospheric pressure: acoustic applications." *IEEE Journal of Oceanic Engineering*, 27(3), 593-601.

Santamarina, J. C., and Fam, M. A. (1997). "Interpretation of bender element tests - discussion." *Geotechnique*, 47(4), 873-875.

Santamarina, J. C., and Fratta, D. (1998). *Introduction to Discrete Signals and Inverse Problems in Civil Engineering*, American Society of Civil Engineers, Reston, VA.

Santamarina, J. C., Klein, K. A., and Fam, M. A. (2001). *Soils and Waves*, John Wiley & Sons, Ltd, Chichester, England.

Santamarina, J. C., Klein, K.A., and Fam, M.A. (2001). *Soils and Waves*, John Wiley & Sons, Inc.

Sawangsuriya, A., Biringen, E., Fratta, D., Bosscher, P. J., and Edil, T. B. "Dimensionless limits for the collection and interpretation of wave propagation data in soils." *GSP 149: Site and Geomaterial Characterization. 2006 GeoShanghai International Conference*, Shanghai, China, 160-166.

Scherer, G. W. (1988). "Aging and drying of gels." *Journal of Non-Crystalline Solids*, 100, 77-92.

Scherer, G. W. (1989a). "Effect of shrinkage on the modulus of silica gel." *Journal of Non-Crystalline Solids*, 109, 183-190.

Scherer, G. W. (1989b). "Mechanics of syneresis I. Theory." *Journal of Non-Crystalline Solids*, 108, 18-27.

Scherer, G. W. (1996). "Influence of viscoelasticity and permeability on the stress response of silica gel." *The ACS Journal of Surfaces and Colloids*, 12(5), 1109-1116.

Scherer, G. W., Pardenek, S. A., and Swiatek, R. M. (1988). "Viscoelasticity in silica gel." *Journal of Non-Crystalline Solids*, 107, 14-22.

Scott, R. P. W. (1993). *Silica Gel and Bonded Phases: Their production, properties and use in LC*, John Wiley & Sons, New York, NY.

Seed, H. B., Wong, R. T., Idriss, I. M., and Tokimatsu, K. (1986). "Moduli and damping factors for dynamic analyses of cohesionless soils." *Journal of Geotechnical Engineering*, 112(11), 1016-1032.

Shani, C., Weisbrod, N., and Yakirevich, A. (2008). "Colloid transport through saturated sand columns: Influence of physical and chemical surface properties on deposition " *Colloids and Surfaces A: Physicochemical and Engineering Aspects*, 316(1-3), 142-150.

Stokoe, K. H., Lee, S. H. H., and Knox, D. P. "Shear modului measurements under true triaxial stresses." *Advances in the Art of Testing Soils Under Cyclic Conditions*, 166-185.

Towhata, I. (2008). "Mitigation of liquefaction-induced damage." Geotechnical Earthquake Engineering, W. Wu and R. I. Borja, eds., Springer, Berlin, 684.

Toyoto, H., Towhata, I., Imamura, S., and Kudo, K. (2004). "Shaking table tests on flow dynamics in liquefied slope." *Soils and Foundations*, 44(5), 67-84.

Valdes, J. R. (1999). "Simultaneous determination of frequency dependent modulus and damping from resonant column tests," Georgia Institute of Technology, Atlanta, GA.

Vega, A. J., and Scherer, G. W. (1989). "Study of structural evolution of silica gel using (1)H and (29)Si NMR." *Journal of Non-Crystalline Solids*, 111, 153-166.

Verdugo, R., and Ishihara, K. (1996). "The steady state of sandy soils." *Soils and Foundations*, 36(2), 81-91.

Vipulanandan, C., and Ata, A. (2000). "Cyclic and damping properties of silicate-grouted sand." *Journal of Geotechnical and Geoenvironmental Engineering*, 126(7), 650-656.

Vucetic, M. (1994). "Cyclic threshold shear strains in soils." *Journal of Geotechnical Engineering*, 120(12), 2208-2228.

Wang, Y.-H., and Tsui, K.-Y. (2009). "Experimental characterization of dynamic property changes in aged sands." *Journal of Geotechnical and Geoenvironmental Engineering*, 135(2), 259-270.

Warlus, S., Ponton, A., and Leslous, A. (2003). "Dynamic viscoelastic properties of silica alkoxide during the sol-gel transition." *The European Physical Journal*, 12, 275-282.

Woods, R. D. "Laboratory measurements of dynamic soil properties." *Dynamic Geotechnical Testing II*, San Francisco, CA, 165-190.

Youn, J. U., Choo, Y. W., and Kim, D. S. (2008). "Measurement of small-strain shear modulus Gmax of dry and saturated sands by bender element, resonant column, and torsional shear tests." *Canadian Geotechnical Journal*, 45, 1426-1438.